Data Analysis of the High-Energy Ion Tail in Earth's Plasmasphere

by

Lois Keller Smith

A dissertation submitted in partial fulfillment
of the requirements for the degree of
Doctor of Philosophy
(Atmospheric, Oceanic and Space Sciences)
in The University of Michigan
2016

Doctoral Committee:

Professor Michael W. Liemohn, Chair
Professor David Dowling
Professor Roxanne Katus, Eastern Michigan University
Professor Mark Moldwin
Associate Professor Shasha Zou

This thesis is dedicated to my parents, Lindsey and Gail Smith. You have both given me everything again and again for so many years, and, finally, I am just starting to appreciate it all. More than a dedication, this thesis exists because of what you both sacrificed to give Keller and me: the best possible education, a strong work ethic, and a desire to leave things better than we found them. I hope you are as proud of us as we are of you.

ACKNOWLEDGEMENTS

At this point in my life, I am humbled to have had so *many* wonderful people in my life that have brought about the development of this thesis. Although the memories we share are what bring me the most happiness, I relished writing this acknowledgement page because it is finally a chance to begin to say thank you for everything. Years from now, this is the part of my thesis I will read over to remember what an impact each one of you had on this time in my life and how fortunate I am to have met so many caring, hard working, and positive people.

AOSS/CLASP

AOSS/CLASP has been a nurturing and welcoming environment from the start for me. For my space science graders - Rona, Meng, Zhenguang, and Dmitry - thank you for the time, the laughs, and the advice. First year graduate students need that kind of support and brotherly kindness, and we are so lucky to have you all as graders (even though you're a liar Meng!). For my first year space science cohort - Doga, Judit, Casey, Manan, Nathan, and John, I am so glad we had each other to lean on despite the pressure. For my qual exams study group - Mary and Juan - I can not even begin to thank you for your support and honesty during probably the most difficult time in my life. For my office mates - Shaosui, Doga, Roxanne, Abby, Alicia, John, Alex, Sinh, Blake, and briefly Shannon - thank you for putting up with my loud dance music, random sing alongs in the early morning, random crying, and sleeping

in the office for 3 months. It takes some special people to tolerate such behavior.

There are also many students in CLASP who went out of their way to nurture friendships and lend a helping hand. Tremendous thanks to Kai for the dedication he put into being the Magnetospheres grader. Thanks to Ryan for tea and pie parties. Special thanks to Micah who walked me through a thesis timeline and has always set a great example for other students to follow. For Justin and Willow - I appreciated your visits and I am so glad you both decided I wasn't completely crazy. For Alicia, Abby, Sergio, Alex, Erik, Kali - I loved being your grader and loved seeing your growth in class. Thanks to Greg, Motjaba, Jamie, Weijie, Jie, Xiangyun, Nick, Alex, Micah, Matt, Patrick, Josh, Annarelli, Jonathan, and many more for the laughs and happy times around CLASP throughout the years. Thank you to Tom for the support and understanding during thesis writing and simultaneous job hunting. Thank you especially to Nicole and Fiona for reaching out to me and looking past their own problems to make sure the next generation of scientists were doing OK; you both are truly exceptional people, and I am so lucky to be a reciepient of your strength and kindness in graduate school.

I would also like to thank the CLASP support staff for years of smiles, love, and support. For the IT group - Faye, Darren, and Bryan - you all are *actually* the greatest and your patience, skill, and kindness is something to be truly admired. Sometimes it was that friendly smile in the morning that genuinely made the department a brighter place. For Allison Shafer - you light up a department with your sense of community and love of life. We have been so lucky to have you in CLASP! For Marti Moon - I can't begin to thank you enough for the small candies and your huge smiles over the years... You have brought so much joy and made things like water main breaks seem small, and you are truly perfect for your job. For Eidilia, Laura, Jan, Deby, and

Kristi - thank you so much for your support, love, enthusiasm, and brightness over the years. I like to think that I was special for each of you because you all were definitely special to me; Eidilia the crocheting talks, Laura the lunch time chats about books, Jan the department gossip, Deby the amazing cakes, and Kristi remembering I was vegetarian and always with a big smile! For the night time cleaning staff - I loved our late night chats and I am immensely grateful for the on-point response when I accidentally ate a cookie that had been soaked in isopropyl alcohol at 10 PM in the office. All of you were such an integral part of what became this thesis.

There are many professors and research scientists at Michigan who have shaped my development as both a researcher and a person. Professor Mark Flanner is one of the kindest people I have met, and his enthusiasm and knowledge of atmospheric physics is not only impressive but inspiring. Special thanks to Dan Welling for letting me be his first grader and all the honest talks over the years - although I'm disappointed you didn't wear a monocle at AGU, you brought a lot of laughter into our group meetings and kept pushing our computational skills. For the MITHRAS group - Raluca, Natasha, Andy, and Chris - thank you for your comments, insights, encouragement, and discussions over the years. For Jim Raines, I am so lucky to have had a scientist in our department like you that I could come and talk to honestly. For Sue and Justin, thank you for the talks and ENTJ/INTJ support and encouragement! For Jim Slavin, thank you so much for Magnetospheres Journal Club; I learned so much by coming every week, and I am so glad you started that program in CLASP.

SANSA

During my time in graduate school, I was given an amazing opportunity to work at the South African National Space Agency (SANSA) for 4 months. During this

time, I learned a tremendous amount about cultural relations, space science, ballroom dancing, and, on a deeper level, myself. I am indebted to SANSA and to the NSF and US-AID programs for funding this life-changing experience. I would like firstly like to thank Professors Leanne McKinnel and Michael Kosch for hosting and guiding me through my project at SANSA and to Anita for organizing everything and making sure Hermanus was a second home for me.

To my co-workers at SANSA, you made the place I worked a place I looked forward to going everyday. Thank you to my South African office mates - Amore' and Niguisse - for putting up with daily trolling and my spamming of Mike Kosch, which severely limited our productivity (oops!). Thanks also to my room mate Helen who was an amazing travel companion the first month of my stay at SANSA. Thank you also to Teboho, Carsten, Simeon, Catherine, Kate, Zolile, Rhendani, Suney, Nicola, Gert, Barry, Patricia, and others whose bright dispositions made SANSA a place I'll remember as being full of fun and happiness. Thanks also to YY for his relentlessly cheerful disposition while we were in Norway.

During my stay at SANSA, I went on many hikes, played a lot of frisbee, and danced a great deal of Ballroom. I would like to thank Lani Nel for her support, love, and enthusiasm about ballroom which got me hooked on ballroom dancing. She, Paula, Henk, Dylan, Louisille, Tinus, and several others often gave me ride homes from dancing, which allowed me to go to dancing every week. To Tinus Horn, I am immensely grateful for our friendship and your conversations; your ideas helped me see clearly the path ahead, and for that, I am forever grateful.

Friends

I have so many friends that have each played a crucial component in the construction of this thesis. I hate to distill you each down to one or two lines, so please know that if I could write a paragraph about each of you and still defend my thesis in a reasonable time frame, I would. Although my family is my bulwark, my friends are the ones who I experience things with and help provide the guidance I need.

To the elementary school/high school friends who have celebrated the successes and been there for the lows - the Rices, Elizabeth Cofrancesco, Aimee, and Stephanie. For the Rices, you have been a second family to me for years, and you make Buffalo still feel like home after years. For L^3 - it's always like no time has passed when we reunite, from sushi nights to wine nights, I am so lucky to have you both by my side as I have grown up. Aimee, you are an inspiration to everyone and you remind me of what it is to pursue a dream wholeheartedly. Stephanie, I am so immensely proud of everything you have become and you are the greatest little sister a girl could hope to be assigned as a reading partner in 4th grade. Jamee, I don't know where to put you, but I'm going to put you here - thank you for an amazing time in Juneau and for being a friend where years can pass and we just find ourselves more similar.

To the co-workers who became best friends - Amore', Anthony, Shaosui, Doga, Abby, Roxanne - my heaven would be an office with all of us in it. For Amore', you went out of your way to make sure I had a good time in South Africa and I am *lucky* with how effortlessly our friendship developed. Without you in Norway, I think I would have gone crazy, and you pushed me to make positive changes in my life rather than wallowing in self-pity; for these things, I can never thank you enough. Anthony - although you didn't talk to me the first 3 months we were office mates, what great luck that we ended up having so much in common and became hiking, party, tea time, and conferencing buddies. You have given me a place to stay when I needed

it so many times, and I love you so much for your patience, good nature, and fun outlook on life.

For Shaosui and Roxanne, you both are my role models and my hero-worship for both of you was probably a source of great amusement for everyone over the years. You both provided a level of support and love when I very badly needed it. You support sometimes was the boost I needed to get up and try again. Without you both, I could not have made it through graduate school, and the fact that we have becomes friends is an amazing thing to me. Thank you so much to both of you.

To Doga, you have always been there (somehow!) when I'm alone crying at my desk and been the first one to drop everything to be there and give a hug. These are not things one forgets, and I count you as one of my closest friends for your love and support during these times. For Abby, you're like the jelly to my peanut butter. It's brought me so much joy to have you as an office mate and be able to have late night talks ranging from where to buy long pants to all the problems of the world we want to fix. It's really rare to find someone with as much passion and motivation as someone like you, and I hope I have been as good for you as you have been for me.

For the colleagues who made conferences way more fun - Suzanne, Amy, Anthony, Cristian, Jason, Colby, Colin, Prayash, Charles, Narges, Rishi, Joel, Erica, Ian, Blake, Russell, Paul, Hong, Shan, Ryan, Emily, Glyn, Austin, Nataliyia, Victoriya, Bea, Chao, Emma, and many more. Thank you so much for the good times - the karaoke nights, the games of Capitalism (Lois! Stop Cheating!), the frisbee throwing, Egyptian rat screw, charades, drawing pictures in each other's notebooks. Even more, thank you to those who became more than colleagues - the serious conversations, the needed boost, the snapchats, and the encouragement through the years.

I have been extremely fortunate to have you all to look forward to at conferences and you all are what made conferences such a high point in my graduate career.

To the conference friends who became best friends - Nadine and Kristie - you two are so precious to me. Kristie, I still am amazed that we were randomly paired together that first GEM. You've been a part of all my major mile stones in graduate school, and you are the definition of a supportive and loving friend; thank you so much for everything. For Nadine, I love how easy our companionship has been; getting to know you has been like going on a walk and suddenly finding someone in step beside you with a huge smile. You both encompass all the things I value the most - a love of life and fun, intelligence, and strength, and I am so grateful I have both of you to give an honest opinion when difficult decisions need to be made.

To my Los Alamos friends - Dave, Lucas, Sheng, Addy, Scott, Lucas, Ben, Sara, Buff Chris, Max, Wendy, Clare, Nadine, Katie, Ravi, Jinhie, Benigno, and all of Santa Fe and Los Alamos Frisbee. Thank you so much for being part of what was an absolutely amazing summer for me - between hiking, bears, campfires, rainbows, Smith's ice cream, honey filled sopapillas, rafting, wine painting nights, and (most importantly!) Tuesday karaoke nights. Special thanks to Dave who can always cheer me up by insulting me, Scott for all the Boulder-life inspiration, Katie for breakfasts in Albuquerque, and Addy and Sheng for the amazing nights with Bow-Bow and ukeleles. You all made it such an amazing summer - thank you so much!

My Insight Friends - what an unbelievable summer it has been. I have never felt so vulnerable with a group of random people who I've never actually met before. When I fell, I found 15+ people ready to catch me and help me get back on my feet. Special thanks to Swetha, Melanie, Amelia, Jimmy, and Natalie who took time aside

from their own projects to help me figure out my (inordinate) number of problems I seemed to encounter with my project. Our 2 AM happy hour is something I will always remember fondly. Special thanks to Katie and Jen - without their support and dedication to their jobs, I don't think I would have made it through the Insight program (problem child #1). There was so much love in this program, and I am glad to have made so many 'real' friends while working out of a closet. Special thanks to my special friend Jimmy - I'm not sure what we actually have in common, but you've been an amazing friend and I love that we have to beat each other to punch lines because the other person is already thinking of the same joke.

In my final Ann Arbor summer, I've been extremely lucky to get more involved with the Ann Arbor bike community and live with some awesome people. Thanks to Mary, Diane, Bill, Sarah, Kathleen, Kat, LeslyAnne, Jeremy, and Kate for the awesome rides and encouragement ('you get some real pedals girl and you'll fly'). You all have been a part of something I have very much looked forward to several times a week. Thanks to some fantastic housemates too - Ian, Vivien (I'm counting you Vivien), Nick, and Seong-Hee for an awesome summer with a lot of smiles and laughter.

Boyfriends

There are five men who really shaped my graduate school experience and played an integral role is the completion of this thesis - Ryan, Alex, Brian, Liam, and Harvey. To Ryan, thank you for helping me transition into life in Ann Arbor and for holding my hand through the nights after I had failed and thought my world was over. To Alex, thank you for showing me fun and how to set boundaries in graduate school; I laughed till I cried so many times with you. To Brian, you gave me everything

you could, and I am truly grateful for having you in my life during my second year of graduate school. You patiently stood by as I was angry, despondent, mean, and scared about my upcoming exams, and in return, you offered your love and the simple joys of life. You are an amazing and brilliant person, thank you so much.

For Liam, our time together truly changed me. You planted the seed that led to this thesis, and your love and support gave me the confidence to thrive and the happiness to love myself. Without you, I would not have found the courage to leave my first undergraduate university, to struggle through the transition to Boulder, to choose Michigan for graduate school, and to fight for myself and my research. You have been a huge part of my graduate school experience, even if just implicitly. I am so lucky to have you as a friend now, and I am forever indebted to you for what you gave me. Thank you, Liam.

Harvey - it has been incredible having you appear in my life at the end of my time as a graduate student at Michigan. It's like I've been running by myself for years not sure where I was going or why I was pushing myself so hard, and then you appeared and it all made sense. Falling into step with you has been electrifying and beautiful, with everyday starting with a mutual smile. I have never had someone so completely upend my life yet simultaneously be a glue that can bring together all that I am. Your support, love, and energy has brought me nothing short of euphoria during a crazy transition period. I look at you and see such bright things in our future together - cabins, mountain climbs, bike rides to nowhere, hikes in the woods, skis from hut to hut, runs on the beach, diving for frisbees, the good, the bad, and the in between. But more than that is the support - the hand holding, the encouragements, the honesty, and the sharing of burdens that has made me realize that I don't want to do things alone, I want you there. Although I would have finished this thesis

without you (sorry!), it's this new life after graduate school where you are absolutely irreplaceable. So here it is in writing Harvey, immortalized in the Michigan thesis archive: I love you and with you, day by day, all of my dreams are becoming reality. Thank you for a level of happiness I never thought existed and for a life filled with so much.

Role Models, Co-Authors, and Thesis Committee

Obviously, I did not do this work alone; in fact, I feel mostly like the connector of many ideas from many people that manifested in multiple publications. I also did not blaze a trail for tall and/or dark haired women who have a knack for solving problems and writing python code. Everything I have done has been built on the work of others, and sometimes a boost from those people to keep answering difficult questions in science.

For my thesis committee, Shasha, Mark, David, Roxanne, and Mike, you all have been supremely accommodating of my (sometimes) irrational behavior and attempt to bite off more than I can chew. Shasha, I am extremely grateful for that first meeting you had with me at AGU in 2012, and I have always looked to you as who/where I wanted to be in my future. Mark, thank you so much for the random office drop ins that ranged from questioning the basis of my results (someone needed to!) to being a vent for me when I was in a bad place. David, as ridiculous as this may sound, thank you for your love and extremely energetic enthusiasm for what you do. I can definitely say that you are the reason I don't totally hate fluid mechanics, and I have been so lucky to have you on my committee to offer guidance and support. Roxanne, what would I have done without you to talk me down from crazy ideas like doubling the length of my thesis? You have been so amazingly good for me over the years, and

I count myself extremely lucky to have been able to follow in your (physically but not metaphorically much smaller) foot steps along the way.

To my early mentors - my Aunt Jane, Mrs. Tahk, and Ms. Casper - you catalyzed a love for research that blossomed into a dissertation in space physics. Aunt Jane, growing up, you were my role model and your encouragement of intellectual pursuits and creativity was what I needed to chase after Physics, Latin, and a PhD. Mrs. Tahk, your relentless enthusiasm and energy during Future Cities gave me an opportunity to find what I loved about science and engineering. It also gave me a chance to bond with my dad and class mates, which was incredibly valuable to an awkward pre-teen girl who was trying to find where she fit in. For Ms. Casper, my goodness, your energy and love of physics was amazing. I loved having you as a physics teacher, and the support you've shown me. Nardin Academy was an amazing institution to have completed my high school studies at, and I continue to realize the benefits now years later. Thanks also to Miss Podd who has followed how I'm doing for years and cheered along the way at each step.

To my undergraduate research mentors - Erik Richard, Ning Wu, Tiago Ribiero, and Cora Randall - thank you for giving me the time and encouragement to develop skills that would serve me well in graduate school. Each one of you took me on as a student and helped me become a stronger and more competent research. Special thanks to Cora Randall - there were so many times in graduate school where I would ask 'What would Cora do?' and whatever that answer was, it was the one I pursued. Thank you for taking on an undergraduate student when you did not have time to - I can definitely say it had a huge impact on my life and decisions.

To the scientists who took a genuine interest in not only my work but also in me

as a person - Steven Morley, Greg Cunningham, Steve Fuselier, Jerry Goldstein, Phil Valek, Tom Moore, Barbara Giles, Dennis Gallagher, Jichun, Yiqun, John Lyon, Weichao Tu, Delores Knipp, Eric Donovan, Seth Claudepierre, Martin Snow,and Matina. Sometimes students just need a little acknowledgement from someone outside their university to realize that their work does have impact. In so many ways, you all have implicitly (or explicitly) echoed what Seth told me at my first GEM which was 'Stick to your guns girl, you have something here'. Thank you for all being excellent scientific role models.

For the women in space physics who made time to talk with me and offer their encouragement - Liz MacDonald, Alexa Halford, Kelly Korreck, Marilia, Shannon Curry, Gina DiBraccio, and Michelle Thomsen - you all are these incredible rock stars in my mind and the 'version of me' who I needed to see succeed to believe I could do it myself. I'm going to try to keep this paragraph short of unabashed hero-worship, but it might go that way anyway. Liz, thank you for making time for me on your trip to LANL and offering me professional and emotional support over the course of many conferences and discussions. With your dedication to education, love of the outdoors and adventure, and immense respect in space science, you made realize that it is possible to have all of those things and maybe a life (!) in graduate school. For Alexa, thank you so much for our honest discussions and heart felt support - your trust and confidence in me along with a huge smile at conferences has been a blessing! Marilia, you and my 'nephew' have brought me so much joy - thank you so much for the big smiles and the unyielding support since we first found our missing 'sister' at GEM.

Kelly, thank you for specifically making time on your visits to Michigan to get a coffee with me and talk about what it's like to be a woman in science. That says so much about your character and your commitment to making sure others succeed,

and I am excited to watch you thrive as you become a leader in space physics. For Shannon and Gina, you two really are rockstars - by being open about your successes and failures and offering honest advice, you both have helped me tremendously over the years, even when you weren't at Michigan. Michelle - thank you for the phone calls, the encouragement, the protection at times, the happy lunch time discussions, and the enthusiasm for excellent work that has kept me moving forward and pushing myself over the years. You've been such a positive driving force for women in the field over the years, and I know I am not alone in that feeling.

To my infinitely patient co-authors - Ruth, Brian, Geoff, Ondrej, Craig, George, Steve, Aaron, Mike Rietveld, Tim(e), and John - you all have been an integral part of my graduate student experience by teaching me how to properly conduct research through your example. You have all taught me how to respond to reviewer comments and how to prove my points with proper grammar and colorbars. Special thanks to Ruth Skoug... do I win the award for most difficult graduate student? You have been a huge part of my graduate student experience and forcibly (with considerable resistance on my part) made me into a great scientist who pushes herself to submit only the best quality of research and writing. I truly appreciate how much time and effort you spent on me the past three years to shape this thesis, despite the mental anguish it might have caused (me, and probably you) at the time. Thank you for teaching me many things about myself and my potential Ruth, it's something I'll carry with me beyond this thesis.

To Mike Kosch, thank you for taking me on as a 'graduate student on loan' for 4 months and hosting me at SANSA. You gave me an amazing opportunity to travel the world and to see a different style of thinking, both inside and outside of work. I really appreciated your work ethic and your ability to help me turn a paper from

a few figures to a submitted, high quality manuscript in a few weeks. In a way, our time together was like a 'mini-post doc' and it helped me to realize what is best for my long-term future.

To Mike Liemohn... I think one time I bought you a coffee and when you said I did not need to, I said something like 'the debt a graduate student owes their (good) advisor is unpayable'. After years of impromptu meetings, skype calls, discussions of 'well, I did everything wrong', paper revisions, and successes, I still feel the same. It's been quite the rollercoaster, right? From my random application to things not related to thesis work or me asking you for advice and doing the exact opposite only to come back with my tail in-between my legs months later, I think you know better than anyone else that I have not been an easy nor always a likeable graduate student. It is a huge testament to your patience, perseverance, and brilliance that you continued to guide me through all the rough patches and all the projects that weren't exactly in your specialty. Your ability to shepherd me to a coherent dissertation and combine all of the best parts of me into this work is truly astounding. You have also shown your graduate students unyielding trust and support throughout the years, and I **truly** could not have asked for a better graduate advisor, both in research and in personal dilemmas, over the past three years. I absolutely needed your balance to even out my scatterbrained energy and lack of work-life boundaries. Your optimistic support of me and what I do to make it through the difficult periods in graduate school. You really made this thesis and my future as a data scientist possible, so what all started a Michigan reception (which I snuck into) is hitting a break point where you've helped me realize my own potential and strength enough that I can stand alone. Mike, thank you so much for everything.

Family

I am so fortunate to have a close family dispersed throughout the world. To the Sarno clan, you are the ultimate support network - the first ones to congratulate the successes and the ones who have encouragement of my pursuit of Physics for years now. From pepper frys to hugs at funerals, it is an amazing thing to be a part of a family where your second and third cousins are there for you at every turn. To the Smith family, we are more spread out, but the Smiths are the drivers in my life, always pushing me to realize my full potential and cheering when I make it.

To the Cowans - I am very lucky to have you all as such as active part of my life and to set an incredibly high bar. To my Aunt Jane, you have always supported every academic achievement I have pursued, from reading books to Latin, and I needed that when I was young to lay the foundation for my higher education. To Uncle David, I am extremely grateful for the frank talks we have had about graduate school over the past few years. To my cousins - Margaret, Peter, Joe, Mark, and Jessica - you are all truly amazing people. Truly. I love each of you so much and I am so grateful that you all have offered your love and support for me, whether it was through graduate school or in backpacking adventures.

To the Sarnos - Uncle Jim, Aunt Deedee, Sam, and Abby - you are my family that is cheering at the finish line first, always. From nights talking about Star Wars to serious conversations about life choices, I feel like I am truly a part of your family and I appreciate the opportunities you have given me to travel to see you. To Uncle Jim - thank you so much for all the joy you've brought me over the years, from holding me upside down inside out to our trips in Ethiopia. To Aunt Deedee, thank you for all the supportive gchat messages for the past three years in graduate school - they often brought a badly needed smile to my face on many mornings, and I hope I can pass

on what you have given me to another young girl pursuing her goals. For Sam and Abby, thank you for your continued unconditional love and spunky attitudes/dance parties in kitchens that remind your 'old-but-not-too-old' cousin how to have fun. Thank you to Harry John also for his (remote) support of his 'genius' god-daughter, especially when I was in Africa.

To the Zehrings, thank you so much for hosting me over the years and supporting my academic pursuits. To my Aunt Nancy, your resilience and willingness to adapt to new situations has been a huge inspiration for me, and I am so proud/lucky to have you as my aunt (I do brag about you quite a bit). To Uncle Brad, your resolute positive outlook and enthusiasm for my research over pancakes (which you made!) was much appreciated at a time where I definitely needed a smile. Madi, I am glad to have a cousin with so many interests and who always has a big smile on her face whenever I get to see her.

To Isabelle, you are my best friend and certainly a large portion of the emotional-support necessary for this thesis. How many times I called you near tears or distressed over little/big things throughout this thesis? How many times have you talked me through things and offered the support I needed to wake up the next day and continue on? I think you, better than anyone else, know how many times I wanted to leave graduate school. Thank you Isabelle - I really don't think I could have done it without you.

To my grandparents, those alive and those who are not, thank you so much for the love that you have given my parents, my aunts/uncles, my cousins, my brother, and me. We are all so very lucky to have had you all in our lives. For my Grandma Smith - you were the definition of tenacity. Although the skills you taught me (Spite-

n-Malice, hooking) are something I cherish now as a way of remembering our time together, it was the moments where you taught me to pay attention to the details and how to persevere that helped to shape my decisions today. To my Grandpa Sarno, it's been years since you passed and I still can't think of you without missing you so much I cry (even quite embarrassingly on a plane while I write this). You taught me how to be a leader, so when I started pursuing leadership positions in graduate school, I could just think of you and step naturally into the position. You also were a living example of love for one's family, and your dedication to your family helped us all to mimic such strong bonds with each other. To my Grandma Sarno, you have always been there for me at every milestone, to the point it's almost something I take for granted to know you'll be at my thesis defense. Your love and support have been unwavering throughout the years and your pride in my choices and pursuit of education have been an invaluable bulwark against my own self-doubt and insecurities.

To Keller – you're my one and only brother! We needed each other to get through childhood and survive multiple moves. I was mostly obnoxious growing up, but I am glad that we've been able to come to terms with each other more as adults. I am so proud of all of what you have achieved, and I am so glad to have had someone so close and kind setting the bar higher and higher for me to try to match. Thank you Keller for the years we've had and the years together ahead.

To my mom and dad, you have been the best cheerleaders I could have asked for. You both have been more proud and more happy with some of my accomplishments than I have, but you both also never let me settle or say that something was good enough. I know I have been your surprise child in so many ways (Quitting Volleyball? Physics? Latin? Transferring colleges across country? Finishing college? Vegetarian? PhD? Did you dye your hair again?), but I am so immensely grateful that you

all always offered reasonable advice and then supported and respected (sometimes not gladly!) my final decisions. This trust along with the love and dedication you both showed is the most a child could ever ask for from their parents, and you both have always been excellent parents in this regard. The extras, like helping me with laundry, fixing my car, and cooking me meals during graduate school, are additional ways you both have shown your encouragement of my pursuit of a doctorate. I am so incredibly lucky to have been born as your child, and this thesis is dedicated to you both for the years of love you both have given to me. Above all else, I have you both to thank most for the completion of this dissertation.

TABLE OF CONTENTS

LIST OF FIGURES

Figure

LIST OF APPENDICES

Appendix

ABSTRACT

Data Analysis of the High-Energy Ion Tail in Earth's Plasmasphere

by

Lois Keller Sarno-Smith

Chair: Michael W. Liemohn

We examine the ion high-energy (1-10 eV) tail of the cold plasmasphere and it's interaction with plasma waves using data from the Van Allen Probes Mission. The plasmasphere controls wave activity and subsequent particle acceleration, so changes in the plasmasphere can result in consequences such as increased radiation and damage to spacecraft. We statistically analyzed Van Allen Probes Helium Oxygen Proton Electron (HOPE) data from February 2013 to April 2015, looking at quiet times with a Kp index of less than 3. We investigated the high-energy population of the plasmasphere, which consists of ions at energies between 1 and 10 eV and contains approximately 5% of total plasmaspheric density. Both the fluxes and partial plasma densities over this energy range show H^+ is depleted by over two orders of magnitude in the post-midnight sector (1-4 magnetic local time).

Then, we explored the source of the 1-10 eV H^+ ion depletion by developing an algorithm to classify 26 months of pitch-angle distributions measured by the HOPE instrument. We corrected the HOPE low-energy fluxes for spacecraft potential using

measurements from the Electric Field and Waves (EFW) instrument. These results characterize the nature of the dearth of the near 90^o pitch angle 1-10 eV ion population in the near-Earth post-midnight sector. We also show low-energy HOPE differential number fluxes corrected for spacecraft potential and 1-10 eV H^+ fluxes at different levels of geomagnetic activity.

The diurnal variation of equatorially mirroring 1-10 eV H^+ ions between $2 < L < 3$ is connected with similar diurnal variation in the electric field component X-mode (linearly polarized) wave measurements from the Van Allen Probes Electric and Magnetic Field Instrument Suite and Integrated Science (EMFISIS) instrument. A combination of simple models based on quasi-linear theory and equations of motion for thermal ions demonstrate a strong correlation between heating rate from harmonic cyclotron resonance and 1-10 eV H^+ partial densities. This ion-wave resonance creates a suprathermally heated equatorially mirroring dayside H^+ population. The suprathermal ion population attenuates from Coulomb scattering, charge exchange, and pitch angle and energy diffusion across the dusk sector leading to a density minimum in the post-midnight sector. Ultimately, we conclude that the 1-10 eV ion depletion is due to linearly polarized plasma waves suprathermally heating thermal H^+ ions, which then Coulomb scatter across the nightside, leading a minimum in the post-midnight sector. Although this depletion only occurs in less than 5% of the total plasmaspheric density, it can have wide-spread impact in the global magnetospheric system by impacting wave propagation and plasmaspheric temperatures.

CHAPTER I

Introduction

1.1 The Plasmasphere

Discovered in 1963 through analysis of whistler wave data, the plasmasphere is a torus of cold, dense plasma that extends from 1.2 to 6 Earth radii away from Earth's surface (*Carpenter*, 1963; *Carpenter et al.*, 1969; *Inan and Bell*, 1977; *Lemaire et al.*, 2005). The plasma within the plasmasphere is trapped on closed field lines that co-rotates with Earth. The boundary of the plasmasphere, the plasmapause, is demarcated by where electric fields generated by the motion of charged particles dominates low energy particle motion over co-rotation (*Nishida*, 1966; *Carpenter and Park*, 1973). The average temperature of the plasmasphere is approximately 1 eV (11,600 K) (*Chappell*, 1972) and an overview of the layers of the atmosphere/ionosphere/plasmasphere is shown in Figures 1.1 and 1.2.

Recent satellite missions have explored the plasmasphere in much greater detail, including the Imager for Magnetosphere-to-Aurora Global Exploration (IMAGE), Cluster, the Combined Release and Radiation Effects Satellite (CRRES), and the Dynamic Explorer (DE) mission (*Burch et al.*, 2001; *Fu et al.*, 2010; *Darrouzet et al.*, 2009; *Carpenter et al.*, 2000; *Horwitz et al.*, 1990; *Chappell et al.*, 1981). There are currently two main discussion topics in regards to the plasmasphere: wave activity

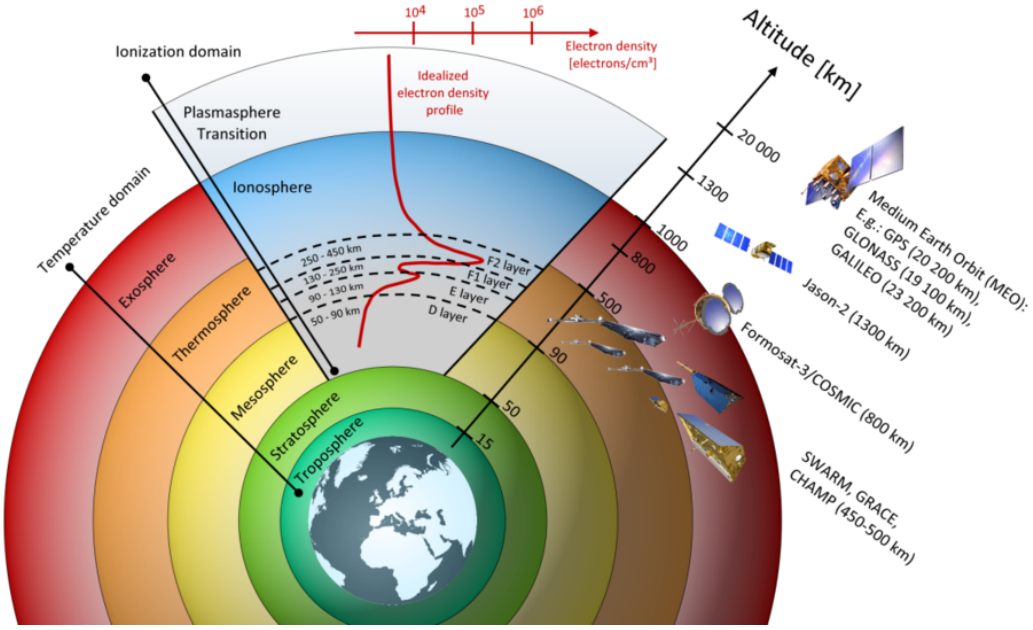

Figure 1.1: The layers of the atmosphere, ionosphere, and plasmasphere and their relative dependence on the temperature (left), on the degree of ionization (middle), and vertical variation of the electron density within the ionosphere. Orbital heights from selected satellites and satellite missions are shown on the right. This image is reproduced from: http://www.dgfi.tum.de/en/research/cross-cutting-research-topics/atmosphere/.

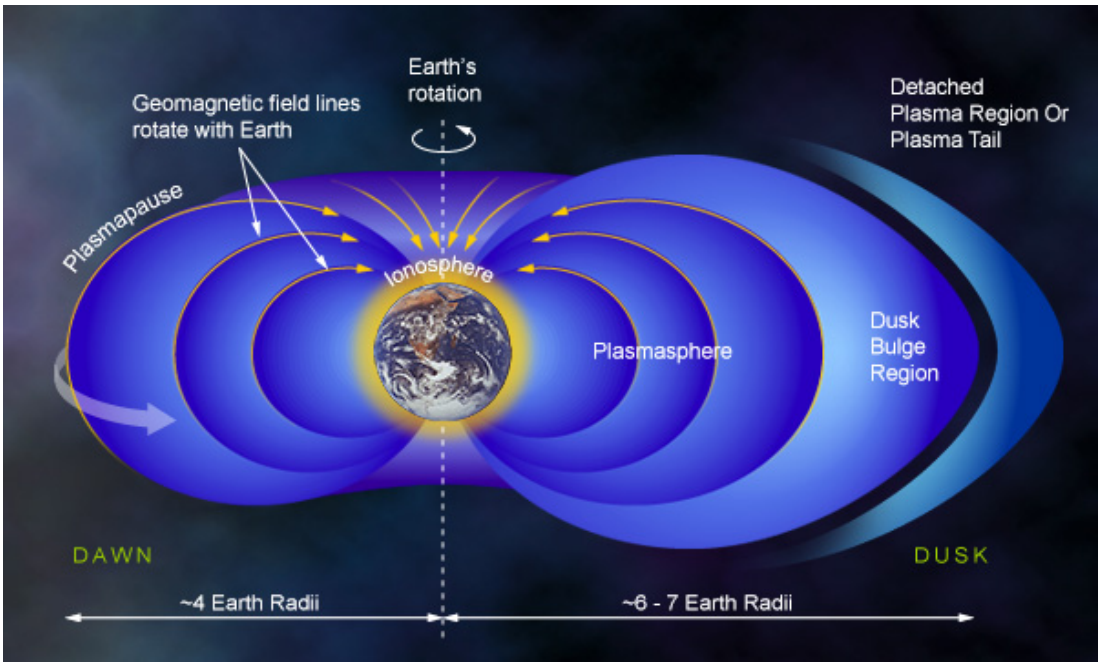

Figure 1.2: The layout of major regions of the plasmasphere and relative distance from Earth. This image is reproduced from: https://www.windows2universe.org/janet/.

modulation and plasmapause studies.

1.1.1 Plasmasphere as Wave Activity Thermostat

The plasmasphere acts as a stable medium for plasma waves to propagate through but also damps/distorts some of the plasma waves that pass through (*Liemohn et al.*, 2006). For example, plasmaspheric hiss is a kHz frequency, fast magnetosonic wave that is created when inward propagating chorus waves hit the plasmapause. At this boundary where density abruptly increases, the magnetosonic waves become incoherent, large amplitude plasmaspheric hiss (*Bortnik et al.*, 2008).

The plasmasphere also serves as a preferred region for plasma wave development. For example, electromagnetic ion cyclotron (EMIC) waves form near the plasmapause and then have favorable propagation in regions of dense plasma, such as the duskside

plasmasphere (*Kozyra et al.*, 1984; *Fraser and Nguyen*, 2001). EMIC waves are not the only waves found in the plasmasphere; ULF, ion cyclotron, whistler, and VLF waves are also commonly found in the plasmasphere (*Fraser et al.*, 1986; *Moullard et al.*, 2002; *Summers et al.*, 2007).

There are still many unresolved topics concerning plasmasphere-wave interactions. For instance, how much energy the various plasmaspheric waves contribute the net energy of the plasmasphere and wave damping coefficients are still unquantified. Some work has been done to explore wave damping rates in regards to plasma density fluctuations (*Lanzerotti et al.*, 1975). How plasma waves decay and connecting expected dispersion rates with satellite observations is still poorly understood, although some progress has been made in this regard in laboratory plasmas (*Walker et al.*, 2015).

1.1.2 Plasmapause Detection

The plasmapause marks the end of dense, low energy co-rotating plasma around Earth (*Nishida*, 1966). It is also a boundary with increased wave activity, which makes it important for inclusion in models (*Imhof et al.*, 1989; *Fraser and Nguyen*, 2001). There has been much debate recently on the importance on the plasmapause in regards to wave propagation and plasmaspheric refilling (*Liu et al.*, 2013; *Clausen and Glassmeier*, 2014; *Gallagher and Comfort*, 2016).

However, defining where this boundary lies is subject to much debate. *Carpenter and Anderson* (1992) described the plasmapause via empirical formula dependent on the Kp index, which ranks geomagnetic activity on a scale of 0 to 9. *Moldwin et al.* (2002) defined the plasmapause boundary as a sharp density gradient of a drop in density of a factor of 5 in less than 0.5 L-Shell. Others have used a density cut off of

100 particles cm^{-3} to determine the plasmapause (*Carpenter*, 1967; *Chappell et al.*, 1970). *Katus et al.* (2015) used images of the plasmasphere and the sharpest gradient within a defined density range to determine a plasmapause boundary based on extreme ultraviolet (EUV) intensity (a proxy for density) scattered from resonant He^+.

1.2 Van Allen Probes Mission

The Van Allen Probes, launched in 2012, are a pair of near equatorial satellites that orbit within geosynchronous orbit (*Mauk et al.*, 2014). The goal of the Van Allen Probes was to better understand the mechanisms behind radiation belt particle acceleration and energy transfer in the inner magnetosphere (*Lanzerotti*, 2013), and recent studies utilizing the Van Allen Probes suite of instruments have augmented our understanding of radiation belt and storm time physics (*Reeves et al.*, 2013; *Baker et al.*, 2013; *Usanova et al.*, 2014). The Van Allen Probes measurements are also leading to new understanding of the plasmasphere (*Li et al.*, 2013; *Jordanova et al.*, 2014).

The Van Allen Probes satellites have an apogee of 5.8 Earth Radii and an orbital period of approximately 8 hours. The spacing between the satellites changes depending on time of mission, and a full procession is about 20 months. In this thesis, we primarily use three instruments onboard the Van Allen Probes satellites: Helium, Oxygen, Proton, Electron (HOPE), Electric Field and Waves (EFW), and Electric and Magnetic Field Instrument Suite and Integrated Science (EMFISIS) (*Funsten et al.*, 2013; *Wygant et al.*, 2014; *Kletzing et al.*, 2014).

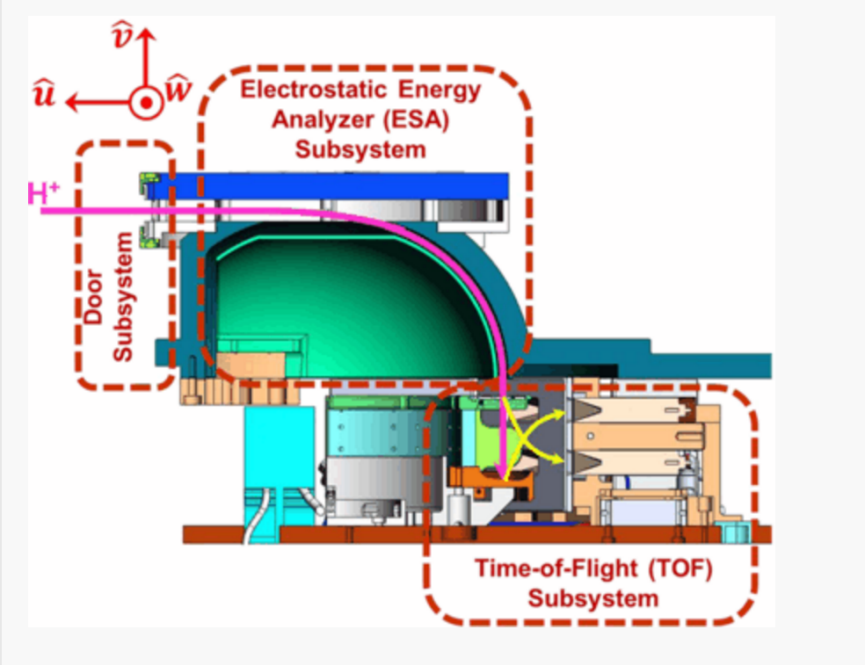

Figure 1.3: Cross section of the HOPE mass spectrometer illustrating the three sensor subsystems and the trajectory of a proton through the instrument (magenta) and the trajectories of secondary electrons generated by the impact of the proton with the start foil and stop anode (yellow). The HOPE Electronics Unit (HEU) subsystem is not shown. Figure and caption reproduced from *Funsten et al.* (2013).

1.2.1 HOPE

HOPE is a low energy (1 eV to 50 keV) top-hat electrostatic analyzer that measures H^+, He^+, and O^+ using foil-based time-of-flight (TOF) mass spectrometry with channel electron multiplier (CEM) detectors (*Funsten et al.*, 2013). Five polar pixels coplanar with the spacecraft spin axis provide angular resolution measurements as the spacecraft spins. Up to 16 azimuthal bins are acquired for each polar pixel over time. HOPE makes ion and electron measurements on alternate spacecraft spins. HOPE also gives pitch angle resolved fluxes using spacecraft magnetic field alignment information from EMFISIS. Figure 1.3 is a reproduced figure from *Funsten et al.* (2013) showing the HOPE design.

1.2.2 EFW

EFW, the electric field and waves instrument, uses two pairs of spherical double probe sensors that are spaced approximately 90 m apart in the spin plane to measure potential across the spacecraft (*Wygant et al.*, 2014). The instrument measures the low frequency electric field vector and spacecraft potential at 32 samples/s in a survey mode. Survey mode spectral information allows the continuous evaluation of the peak value and spectral power in electric, magnetic and density fluctuations from several Hz to 6.5 kHz. Figure 1.4 shows the reproduced Figure 7 from *Wygant et al.* (2014) showing the location of EFW on the Van Allen Probes spacecrafts.

1.2.3 EMFISIS

The Electric and Magnetic Field Instrument Suite and Integrated Science (EMFISIS) instrument measures plasma waves between approximately 2 Hz and 12 kHz using three search coil magnetometers and the three Electric Field and Waves (EFW) instrument's electric field antenna (*Wygant et al.*, 2013; *Kletzing et al.*, 2014). EMFISIS also measures the DC magnetic field with onboard magnetometers and high frequency plasma wave measurements with antenna loop between 10 kHz and 400 kHz. Figure 1.5 is a reproduction of Figure 10 from *Kletzing et al.* (2013) showing the EMFSIS DC magnetometer onboard the Van Allen Probes.

Low-energy ions in the plasmasphere can be very difficult to measure accurately. Around 0.15 eV neutrals will 'weakly' ionize, but it's not until > 0.8 eV that the H^+ fully ionizes in the plasmasphere. Under ideal conditions, an electrostatic analyzer like HOPE could use a voltage difference on the order of 0.1 V to measure ions approximately in this energy range. However, with spacecraft charging and motion of the spacecraft, these measurements become dynamic and much more challeng-

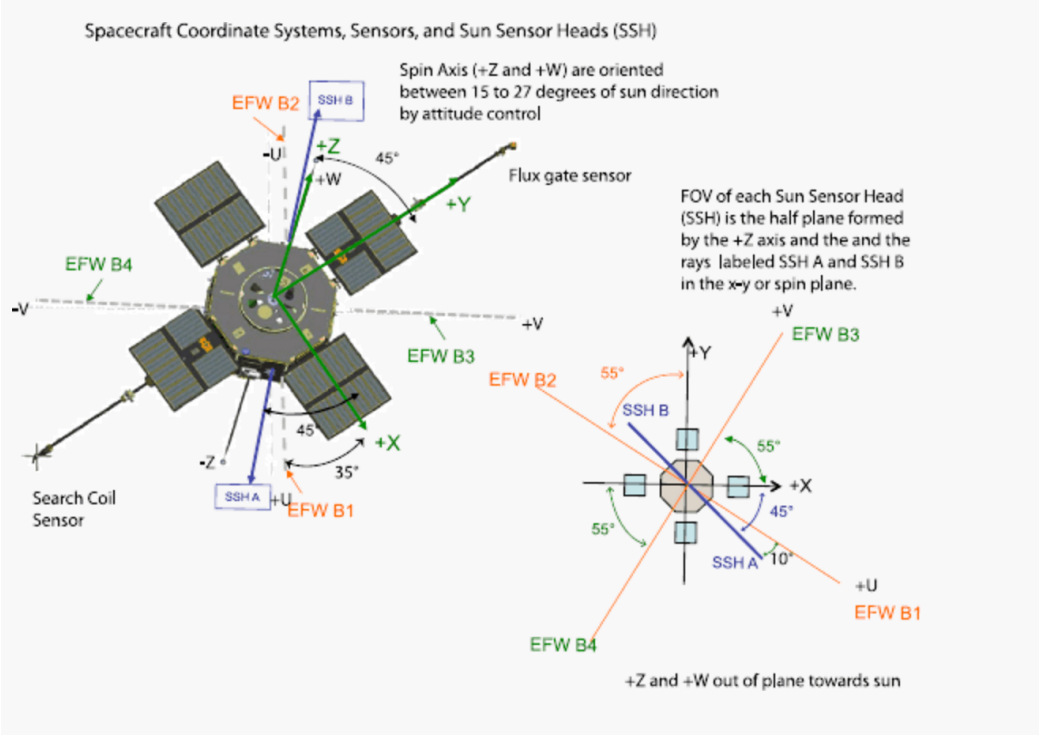

Figure 1.4: Overview picture of Van Allen Probes spacecraft showing orientation of EFW spin plane boom sensors, EFW axial boom sensors, and EMFISIS 3-D Magnetic Search Coil sensors, spacecraft coordinates (xyz) and sensor coordinates (UVW) are indicated. Also shown are the two Sun Sensor Heads (SSH A and B) FOV directions relative to spacecraft coordinates and EFW spin plane booms. Magnetic Search Coil sensors directions and EFW booms are aligned in a common the UVW coordinate system for ease of analysis. Figure and caption reproduced from *Wygant et al.* (2014).

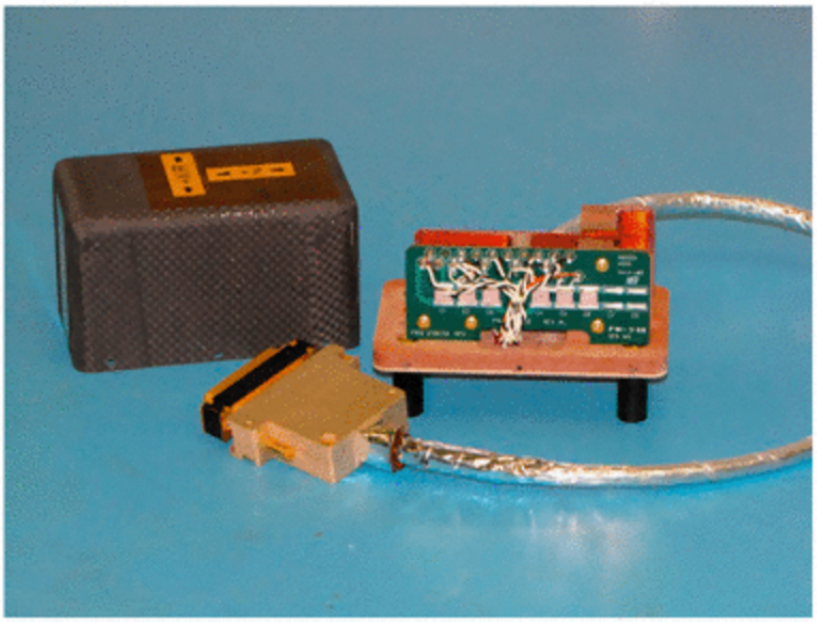

Figure 1.5: EMFISIS Magnetometer sensor with cover and connector. Figure and caption reproduced from *Kletzing et al.* (2013).

ing. For example, if HOPE is calibrated to measure at 0.9 eV, but there is +1 V of charge on the surface of the spacecraft, then HOPE actually measures at 1.9 eV. When examining keV populations, this 1 V of potential is insignificant; however, at 1-10 eV, time varying spacecraft charge makes analysis of this population challenging.

We mitigate this effect in our analysis of the low-energy ion population by accounting for spacecraft potential directly in the measurements. At each time interval, fluxes are adjusted to the appropriate energy channel by adding spacecraft potential and rebinning. We then determined partial densities from the spacecraft potential fluxes.

1.3 Overview of Thesis Work

1.3.1 Chapter 2: Post-Midnight Depletion of the 1-10 eV Ion Plasmasphere Population

The Van Allen Probes Helium Oxygen Proton Electron (HOPE) instrument measures the high-energy tail of the thermal plasmasphere allowing study of topside ionosphere and inner magnetosphere coupling. In Chapter 2, we statistically analyze a 22 month period of HOPE data, looking at quiet times with a Kp index of less than 3. We investigate the high-energy range of the plasmasphere, which consists of ions at energies between 1 and 10 eV and contains approximately 5% of total plasmaspheric density. Both the fluxes and partial plasma densities over this energy range show H^+ is depleted the most in the post-midnight sector (1-4 magnetic local time), followed by O^+ and then He^+. The relative depletion of each species across the post-midnight sector is not ordered by mass, which reveals ionospheric influence. We compare our results with keV energy electron data from HOPE and the Van Allen Probes Electric Fields and Waves (EFW) instrument spacecraft potential to rule out spacecraft charging. Our conclusion is that the post-midnight ion disappearance is due to diurnal ionospheric temperature variation and charge exchange processes.

1.3.2 Chapter 3: Spacecraft Charging Analysis

In Chapter 3, using the HOPE and EFW instruments from the Van Allen Probes, we explored the relationship between electron energy fluxes in the eV and keV ranges and spacecraft surface charging. We present statistical results on spacecraft charging within geosynchronous orbit by L-Shell and magnetic local time. An algorithm to extract the H^+ charging line in the HOPE instrument data was developed to better explore intense charging events. Also, this study explored how spacecraft potential

relates to electron number density, electron pressure, electron temperature, thermal electron current, and low-energy ion density between 1 and 210 eV. It is demonstrated that it is imperative to use both EFW potential measurements and the HOPE instrument ion charging line for examining times of extreme spacecraft charging of the Van Allen Probes. The results of this study show that elevated electron energy fluxes and high-electron pressures are present during times of spacecraft charging but these same conditions may also occur during non-charging times. We also show non-eclipse significant negative charging events on the Van Allen Probes.

1.3.3 Chapter 4: HOPE Pitch Angle Analysis

Chapter 4 explores the source of the 1-10 eV H^+ ion depletion by developing an algorithm to classify 26 months of pitch-angle distributions measured by the HOPE instrument. We correct the HOPE low-energy fluxes for spacecraft potential using measurements from the EFW instrument. A high percentage of low count pitch-angle distributions is found in the post-midnight sector coupled with a low percentage of ion distributions peaked perpendicular to the field line. A peak in loss cone distributions in the dusk sector is also observed. These results characterize the nature of the dearth of the near 90^o pitch angle 1-10 eV ion population in the near-Earth post-midnight sector. We also show in this chapter low-energy HOPE differential number fluxes corrected for spacecraft potential and 1-10 eV H+ fluxes at different levels of geomagnetic activity.

1.3.4 Chapter 5: Plasmaspheric Hiss or Noise?

Previous studies have shown that low-energy ion heating occurs in the magnetosphere due to strong equatorial noise emission. Chapter 5 analyzes the connection

between the depletion in the 1-10 eV ion population in the post-midnight sector of Earth during quiet times at L $<$ 3 and high power spectral density plasma wave emissions in the same region. The diurnal variation of equatorially mirroring 1-10 eV H^+ ions between 2 $<$ L $<$ 3 is connected with similar diurnal variation in the electric field component of plasma waves ranging between 150-600 Hz. Measurements from the Van Allen Probes Electric and Magnetic Field Instrument Suite and Integrated Science (EMFISIS) data set are used to analyze waves of this frequency in near-Earth space. However, when we examine the polarization of the waves in the 150-600 Hz range in the equatorial plane, the majority are right-hand polarized plasmaspheric hiss waves. The 1-10 eV H^+ equatorially mirroring population does not interact with right hand waves, despite a strong statistical relationship suggesting the two are linked. We present evidence supporting the relationship, both in our own work and the literature, but we ultimately conclude that the 1-10 eV H^+ heating is not related to the strong enhancement of 150-600 Hz waves.

1.3.5 Chapter 6: 1-10 eV H^+ Heated by X-mode Waves

In Chapter 6, the diurnal variation of equatorially mirroring 1-10 eV H^+ ions between 2 $<$ L $<$ 3 is connected with similar diurnal variation in the electric field component X-mode (linearly polarized) wave measurements from the Van Allen Probes EMFISIS instrument. A combination of simple models based on quasi-linear theory and equations of motion for thermal ions demonstrate a strong correlation between heating rate from harmonic cyclotron resonance and 1-10 eV H^+ partial densities. This ion-wave resonance creates a suprathermally heated equatorially mirroring dayside H^+ population. The suprathermal ion population attenuates from Coulomb scattering, charge exchange, and pitch angle and energy diffusion across the dusk sector leading to a density minimum in the post-midnight sector.

1.3.6 Conclusions and Future Work

The work contained in this thesis starts at the discovery of the 1-10 eV H^+ depletion in the post-midnight sector of Earth's plasmasphere and resolves why the depletion occurs - linearly polarized equatorial noise resonating with thermal plasma and suprathermally heating them up to 10 eV. To fully understand why the depletion occurs, extensive pitch angle analysis of the 1-10 eV ions, spacecraft surface charging on the Van Allen Probes, and separation of plasma waves with different polarizations at the same frequencies. Ultimately, we demonstrate with models based on particle motion and quasi-linear theory that the plasma waves provide sufficient power spectral densities to effectively heat the low-energy ions.

A natural extension of this work would be to model the balance in pitch angle and energy diffusion and heating of the low-energy ions by plasma waves. Using a test particle simulator, we can establish diffusion coefficients. The calculated diffusion coefficients will then be used to solve the Fokker-Planck equation and combined with charge exchange, Coulomb scattering, and wave heating terms to describe how the distribution function of the 1-10 eV H^+ population evolves in time and ions are lost across the pre-midnight sector. The results of this future project would confirm if the 1-10 eV H^+ depletion seen in Chapter 2 across the pre-midnight sector can be explained via pitch angle and momentum diffusion along with Coulomb collisions and charge exchange processes.

CHAPTER II

Post-Midnight Loss of the 1-10 eV Ion Plasmasphere Population

2.1 Introduction

To motivate the present study of the 1-10 eV ion population of the plasmasphere, we briefly explore other studies examining diurnal temperature and density variation in the plasmasphere and its ionospheric sources. The concentrations of plasmaspheric ions are dependent on energy inputs to the ionosphere, and consequently, ionospheric temperatures. The largest source of sub-auroral ionospheric heating is photoionization. It has been observed that O^+ and H^+ plasma densities behave similarly to ionospheric electron temperatures on the dayside (*Schunk and Nagy*, 1978).

Plasmaspheric refilling has been extensively studied (*Horwitz*, 1987; *Carpenter and Lemaire*, 1997; *Ganguli et al.*, 2000; *Pierrard et al.*, 2009). Transport from the topside ionosphere to the plasmasphere occurs when solar heating of the ionosphere during the day exerts an outward pressure on the topside ionosphere, forcing the ions upward along the flux tubes. Plasma enhancements and depletions with MLT dependence have been modeled in the topside ionosphere (*Heelis et al.*, 1982). This transport of topside ions applies to all three species, suggesting that the MLT depen-

dence of the H^+, O^+, and He^+ densities might also be seen in the plasmasphere.

The absence of solar heating translates into an absence of pressure on the flux tubes. On the night side, plasmaspheric ions flow downward into the ionosphere, enhancing the nightside NmF2 peak, which is the peak in the ionosphere F2 layer density, in the ionosphere (*Singh and Singh*, 1997; *Carpenter and Lemaire*, 1997; *Pavlov and Pavlova*, 2005). Collectively, the movement of the high-energy ions from the ionosphere to the plasmasphere and then back to the ionosphere on the nightside agrees with temperature measurements of ions and electrons in these regions (*Kotova et al.*, 2002).

This diurnal variation is not seen in the thermal core density (< 1 eV) of the plasmasphere. Although many studies and several instruments have explored this region, they have not found a similar result. IMAGE RPI studies looked at fine scale density structures and plasmaspheric electron structures (*Carpenter et al.*, 2002, 2003; *Fu et al.*, 2010; *Denton et al.*, 2012; *Chandler and Chappell*, 1986; *Ozhogin et al.*, 2012), but IMAGE RPI measured total electron number density and was unable to resolve the 1-10 eV energy range to examine density variations. Several physics-based models have also explored plasmaspheric refilling in this region but did not limit their studies to this energy range and did not resolve this diurnal variation (*Guiter and Gombosi*, 1990; *Guiter et al.*, 1995; *Weiss et al.*, 1997; *Liemohn et al.*, 1997, 1999). Extensive whistler wave studies have examined electron number densities in the plasmapshere (*Carpenter and Anderson*, 1992; *Park*, 1970), but these studies capture, once again, the overall behavior of the plasmasphere instead of our focus on the high-energy tail of the plasmasphere. A further discussion of previous measurement techniques of the 1-10 eV plasmasphere population can be found later in the Discussion section.

The Van Allen Probes Mission offers the opportunity to explore the behavior of the high energy (1 - 10 eV) plasmasphere in the L < 4 region at all MLTs to an unprecedented degree. It is critical to study this ion population for understanding magnetosphere-ionosphere coupling and plasmaspheric refilling and for assessing the source, loss, and transport terms between the two regions. The 2-spacecraft Van Allen Probes mission provides an ideal opportunity to study this low energy population of particles, with a short orbital period, a near equatorial orbit, ion composition measurements down to 1 eV, and improved spacecraft potential reduction (*Kirby et al.*, 2014). In our study, we use the Helium Oxygen Proton Electron (HOPE) instrument on board the Van Allen Probes to explore the quiet time 1-10 eV ion population in the near-Earth plasmasphere and the MLT, L-Shell, and compositional dependencies of this population. We observe a species-dependent loss across all three ion species (H^+, He^+, and O^+) in the post-midnight sector near Earth.

2.2 Methodology

This study examines 22 months of quiet time differential number flux measurements from the HOPE instrument on board the Van Allen Probes Mission (*Funsten et al.*, 2013). HOPE measures H^+, He^+, and O^+ from 1 eV to 50 keV using a time-of-flight mass spectrometer with channel electron multiplier detectors. The 72 HOPE instrument energy channels are logarithmically spaced, with measurements in 5 directions relative to the spin axis and at 16 spin angles. Our study spans from January 2013 to November 2014, which covers a full precession of the Van Allen Probes satellites, and uses gyro and spin averaged data. We used HOPE energies from 1 eV to 10 eV in our study.

To capture the quiet time behavior of the plasmasphere, we included HOPE data

collected at times when the Kp Index < 3. The Kp Index, with a 3 hour cadence, is a mid-latitude index that gives insight into magnetospheric convection and overall geomagnetic activity (*Mayaud*, 1980; *Thomsen*, 2004). Traditionally, a Kp of less than 3 is considered quiet time.

We then binned HOPE fluxes into 0.5 MLT and 0.25 L-Shell bins extending from 1 to 6 L-Shell and 0 to 24 MLT. The L-Shell parameter was calculated using the Olson-Pfitzer 77 model (*Olson and Pfitzer*, 1977). The Van Allen Probes are the first satellite pair to provide high-resolution measurements near the equatorial plane with high dwell time inside geosynchronous orbit. Figure 2.1 shows the number of measurements in each L/MLT bin during the period of this study. We included data from both satellite A and satellite B to maximize coverage. In the post-midnight sector, there are more than 1000 points in each bin, with each point corresponding to an 11 second Van Allen Probe spin measurement. This accumulated to several months of data for each bin. We specifically show the 2.2 eV energy channel for each species in this figure, but the distributions for the other energy channels between 1-10 eV were similar. The number of measurements for each species corresponds to the number of non-zero measurements; so H^+ measurements from HOPE are the cleanest whereas O^+ has more zero count measurements.

We used the median differential number flux in each L/MLT bin to represent the ions at that location in space. We then calculated approximate plasma densities in each bin using the formula:

$$n_s = \sum_i 4\pi \frac{1}{\sqrt{\frac{2E_i}{m_s}}} F_s(E_i) \Delta E_i \tag{2.1}$$

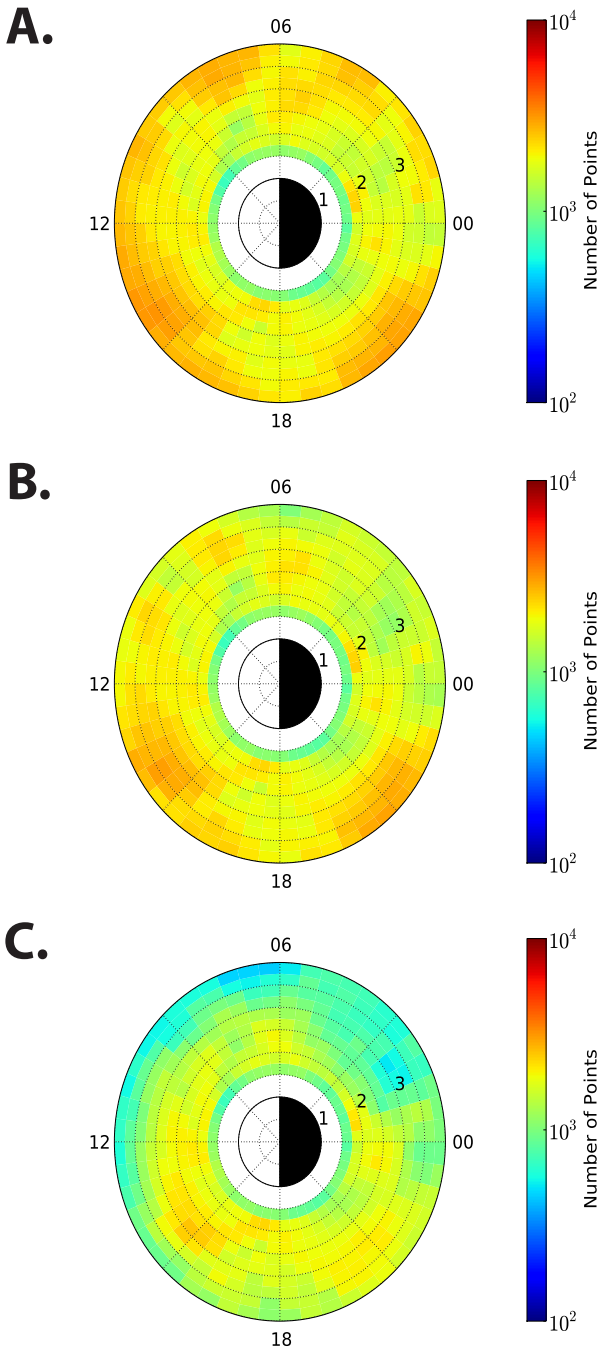

Figure 2.1: Number of measurements for the 2.2 eV energy channel on HOPE during quiet time for A) H^+, (B) He^+ , and (C) O^+ for each MLT and L-Shell bin over the 22 month period covered by our study for satellites A and B combined. The view in these equatorial plane plots is from over the North Pole with the Sun to the left and L values labeling the appropriate concentric L-Shell ring.

where $F_s(E_i)$ is the median differential number flux (cm^{-2} s^{-1} sr^{-1} keV^{-1}), E_i is the median of each HOPE energy channel, ΔE_i represents the range of each energy channel, and m_s and n_s are the mass and number density of each species for H^+, He^+, and O^+. The i in this summation represents the 15 energy channels between 1 eV and 10 eV.

Figure 2.2 shows the median HOPE flux F_s for H^+ ions and electrons as a function of energy and MLT for L=2.5 and Kp < 3. This near-Earth location clearly shows the energy spectrum of the plasmasphere at quiet times. A sharp gradient in flux of several orders of magnitude is seen in Figure 2.2A at approximately 10 eV for most MLTs. This gradient indicates that the plasmasphere is dominated by ions at energies below 10 eV and sets the 10 eV upper boundary for our n_s density calculations. Integration to higher energies, such as 1 keV, did not change the results except to make the density values slightly higher across all MLT and L-Shells.

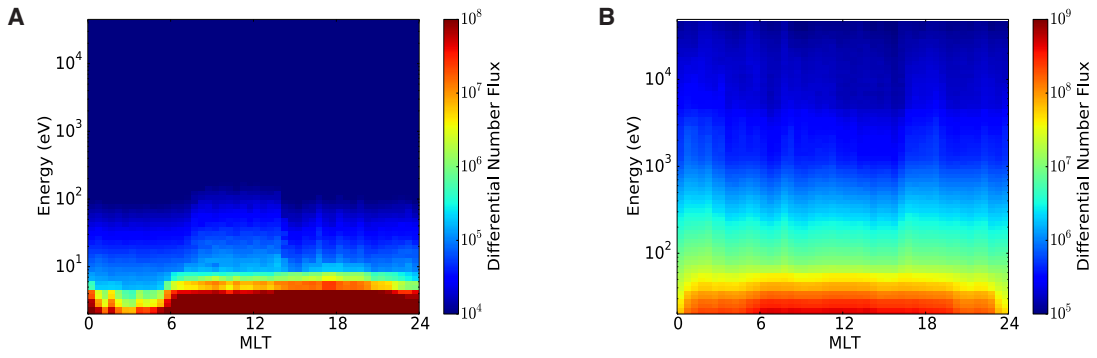

Figure 2.2: Quiet time HOPE H^+ (A) and electron (B) differential number flux at L=2.5 and Kp < 3 as a function of energy and MLT.

It is important to clarify that we are only observing the high-energy range of the plasmasphere ion distribution and make no claims on the behavior of the bulk density of the plasmasphere. Instead, we are looking at the upper 5% (two sigma) of the

energy population in the plasmasphere. The expected two sigma energy population of approximately 10-100 H^+ particles cm^{-3} for the plasmaspheric high-energy tail is consistent with the total plasmaspheric densities given by CRRES data-based models at L=2 (*Sheeley et al.*, 2001). A further discussion of this can be found in Appendix A.1. discussion of spacecraft charging effects on our measurements can be found in Chapter 2.4.2. and is further expanded in Chapter 3.

2.3 Results

When we examine partial plasma densities across all MLTs and L-Shells, we find a significant density depletion across the post-midnight sector. Figure 2.3 shows the median plasma density of quiet time 1-10 eV ions measured by HOPE over a 22 month period. Figure 2.3A shows the H^+ density across all MLTs and L-Shells, Figure 2.3B gives the He^+ density, and Figure 2.3C shows the O^+ plasma density. The density maps on the right are on a logarithmic scale, while the maps on the left are on a relative linear scale for each species to highlight changes. We see in Figure 2.3B that He^+ behaves differently than O^+ and H^+, with a gradual decline and ascent in density over the post-midnight sector. In He^+ density, a local minimum is seen at MLT=14 and is suggested to be from a saturation feedback mechanism (*Galvan et al.*, 2008).

Although the He^+ density decreases post-midnight, it does not drop to the same degree as O^+ and H^+, as evidenced by the percentage each ion species contributes to the total partial plasma density. Figure 2.4 shows the relative contribution of each species to the total ion density in the 1-10 eV energy range. H^+ dominates everywhere (upwards of 60%) except in two regions. One is the post-midnight depletion zone, where He^+ has a strong presence and makes up more than 50% of the total plasma density.

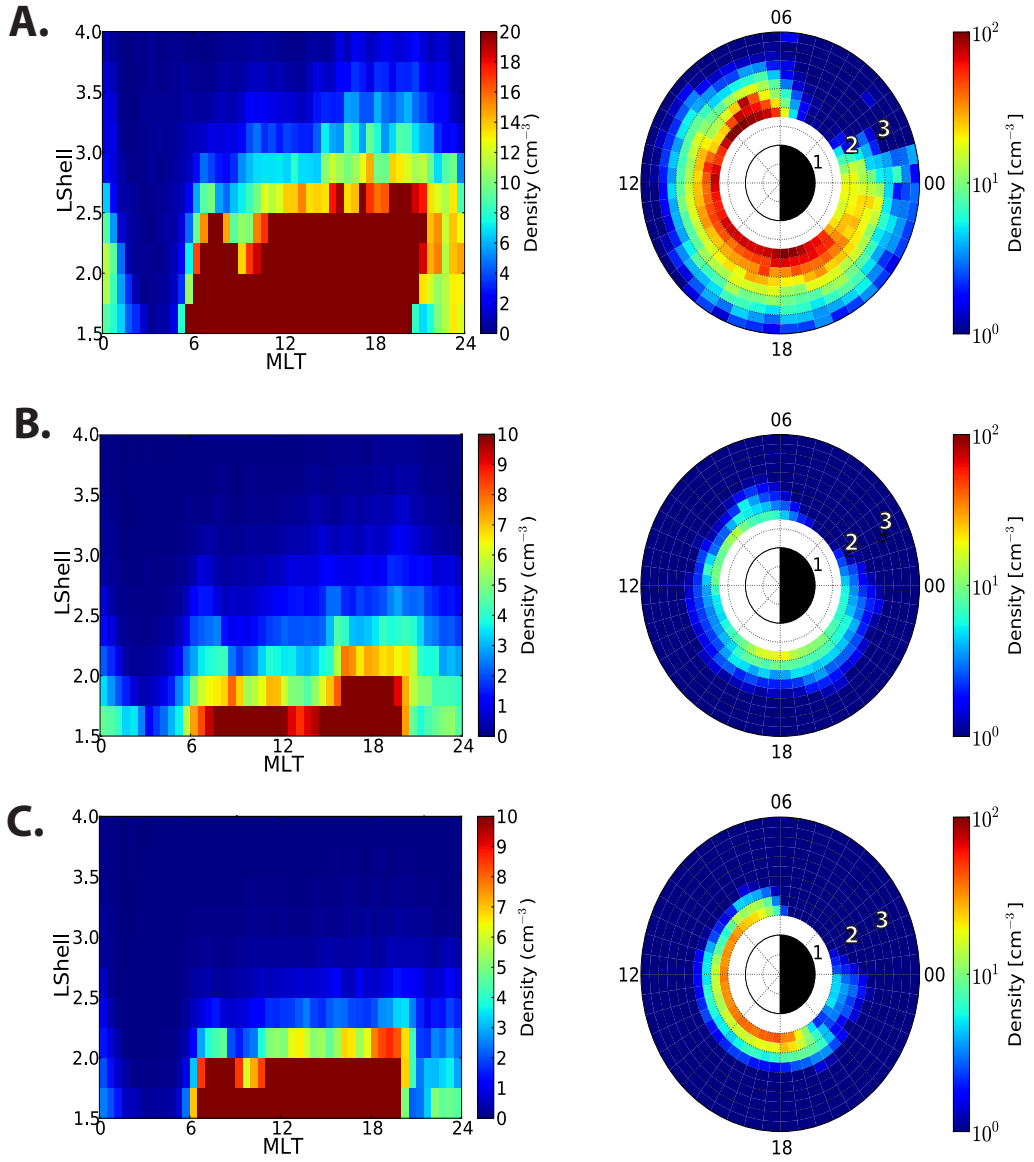

Figure 2.3: Median partial plasma density from 1-4 eV measured by HOPE during quiet times over a 22 month period for (A) H^+, (B) He^+ , and (C) O^+. The density maps on the right are on a logarithmic scale, while the maps on the left are on a relative linear scale dependent on species.

We can see in the ion composition percentages that He^+ dominates the 1-10 eV plasma density at MLT=0-5 and L < 2.5. This result is counterintuitive because He^+ is heavier than H^+ and lighter than O^+, so the effect is not organized by mass in this energy range. To emphasize this result, we examine the partial plasma density gradient across all MLTs at L=2.0. Figure 2.5 shows a line plot of partial densities at L=2.0. Specifically, we calculated the average density values for each species from 2-4 MLT and 14-16 MLT. We found that the H^+ density was 55.8 cm^{-3} at MLT=18 and 0.37 cm^{-3} at MLT=3 (a factor of 150). The He^+ density was 7.18 cm^{-3} at MLT=18 and 0.26 cm^{-3} at MLT=3 (a factor of 28). The O^+ density was 7.74 cm^{-3} at MLT=18 and 0.06 cm^{-3} at MLT=3 (a factor of 122). In He^+, the drop is still distinct, but it is not nearly as great as O^+ or H^+ across the same MLTs. These results demonstrate that there is a depletion in all species, but the effect is most pronounced in H^+ and O^+.

To better understand the variation in the data set, we explore the 33rd and 66th percentile of each flux bin in Figure 2.6 and the relative standard deviation and spread of the data in Figure 2.7. By examining the 33rd and 66th percentile of the 2.2 eV differential number flux, we can see that the post-midnight feature is consistent throughout the data set and the median of each of the flux bins is reflecting the general behavior of the dataset well.

The left column of Figure 2.7 shows the relative standard deviation. Although the relative standard deviation of the post-midnight sector is high compared to other regions, the right column clarifies the spread in the data. The scatter plots in the right column show the differential number fluxes for both satellites for energy channel 2.2 eV of the L = 2.0 bin for MLT=3, 9, 15, and 21. The dayside and pre-midnight MLTs have considerably less variation than MLT=3, but these MLT values also have

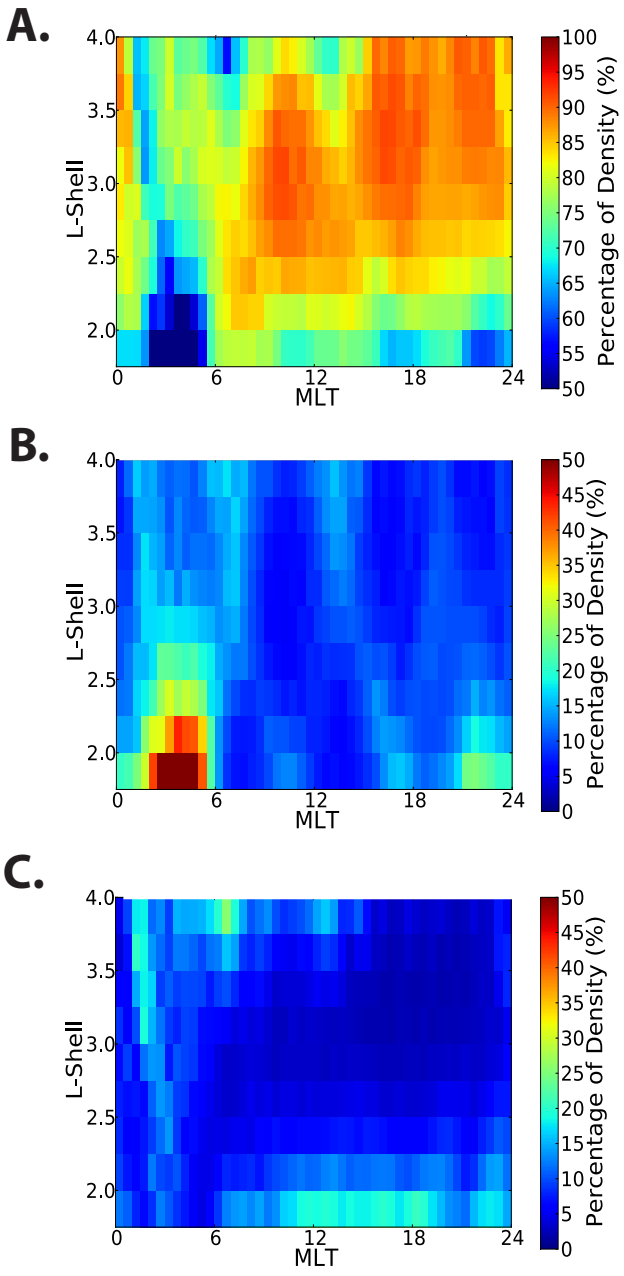

Figure 2.4: Percentage for each ion of the 1-4 eV quiet time partial plasma density at every L-Shell and MLT bin for (A) H^+, (B) He^+, and (C) O^+

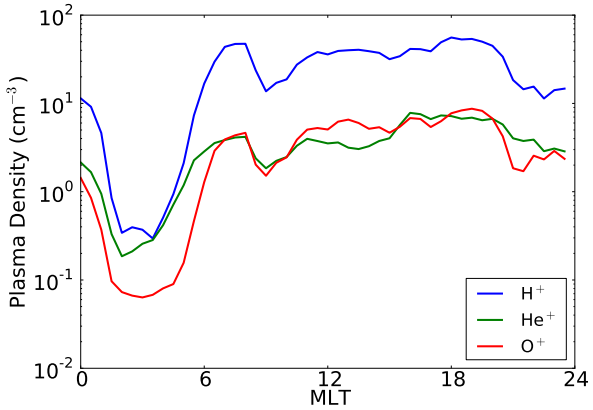

Figure 2.5: Plasma densities at L=2.0 for H^+ (blue), He^+ (green), and O^+ (red). H^+ and O^+ drop by 150 and 122 factors respectively, whereas He^+ drops by a factor of 28 across the same MLTs.

consistently higher flux values than the MLT=3 measurements. The geometric factor for HOPE is 10^{-3} cm^2 sr at 1 eV (*Funsten et al.*, 2013) so the 10^5 flux measurements for HOPE are close to the 1 count level. From Figure 2.7 we can conclude that there is more variation in the post-midnight sector, but the measured fluxes themselves fall within a certain range which is consistently below the dayside and pre-midnight MLTs.

To confirm the statistical results shown in Figures 2.3 - 2.7, we also looked at case studies of individual events. Figure 2.8 shows the HOPE fluxes from 1-7000 eV for a 6 hour period on April 30, 2013. HOPE passes through the post-midnight sector at low L-Shell and sees a drop in flux values for H^+. A dip in flux is seen at all energies up to 10 keV, and the lowered flux measurements are consistent across the satellite transitioning from the inbound to outbound path. The bottom panel of Figure 2.8 shows the spacecraft potential from EFW ranged from 0 V to 0.75 V in the post-midnight, $L < 3$ sector. There is clear sensitivity to spacecraft potential fluctuations in the lower energy channels, but the flux dip in the post-midnight, low L-Shell region is seen at energies above sensitivity to spacecraft charging (e.g., 1 keV). The behavior of the ions shown in the case study suggests that the density drop is indicative of a

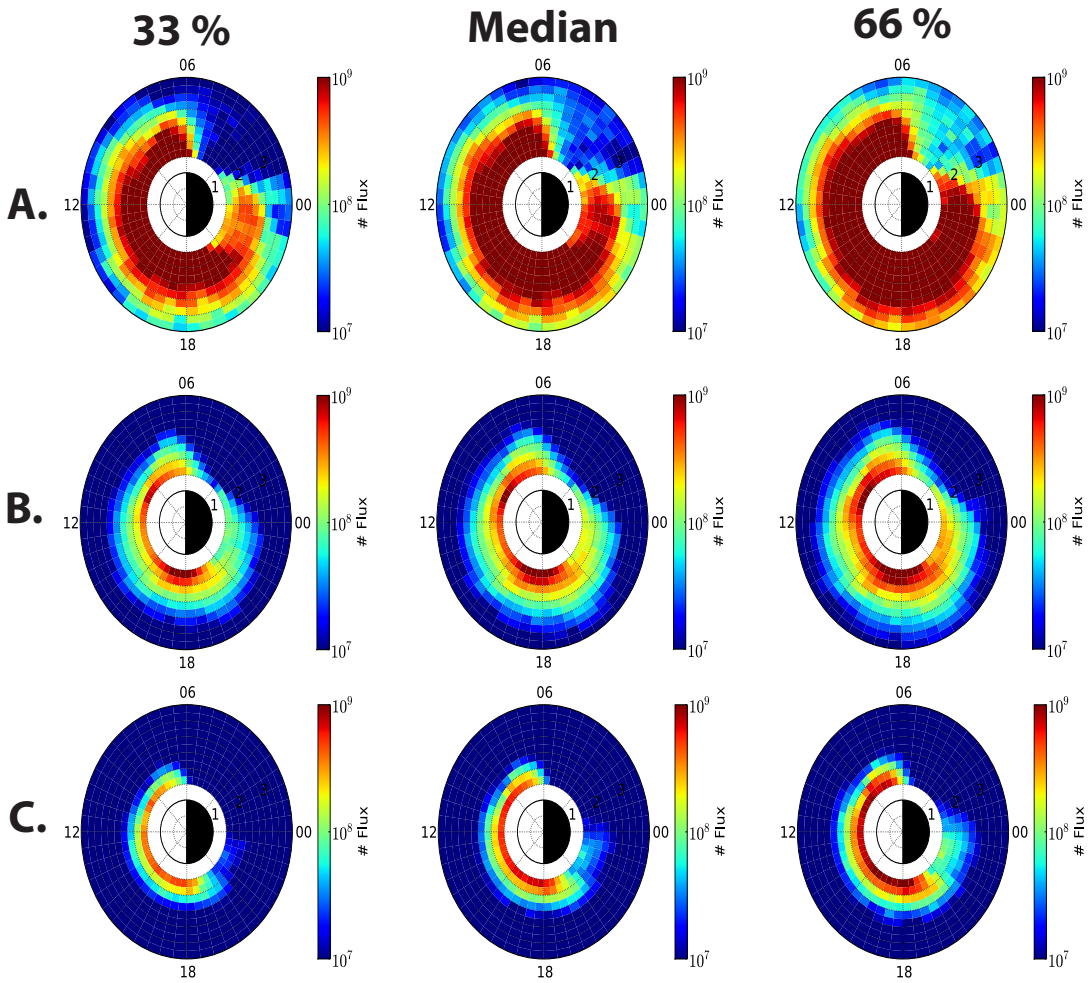

Figure 2.6: 2.2 eV flux maps for (A) H^+, (B) He^+, and (C) O^+. The 33% is the 33rd percentile of the flux measurements made in each MLT/L-Shell bin, the median column is the median flux measurement for each species, and 66% is the 66th percentile of flux measurements.

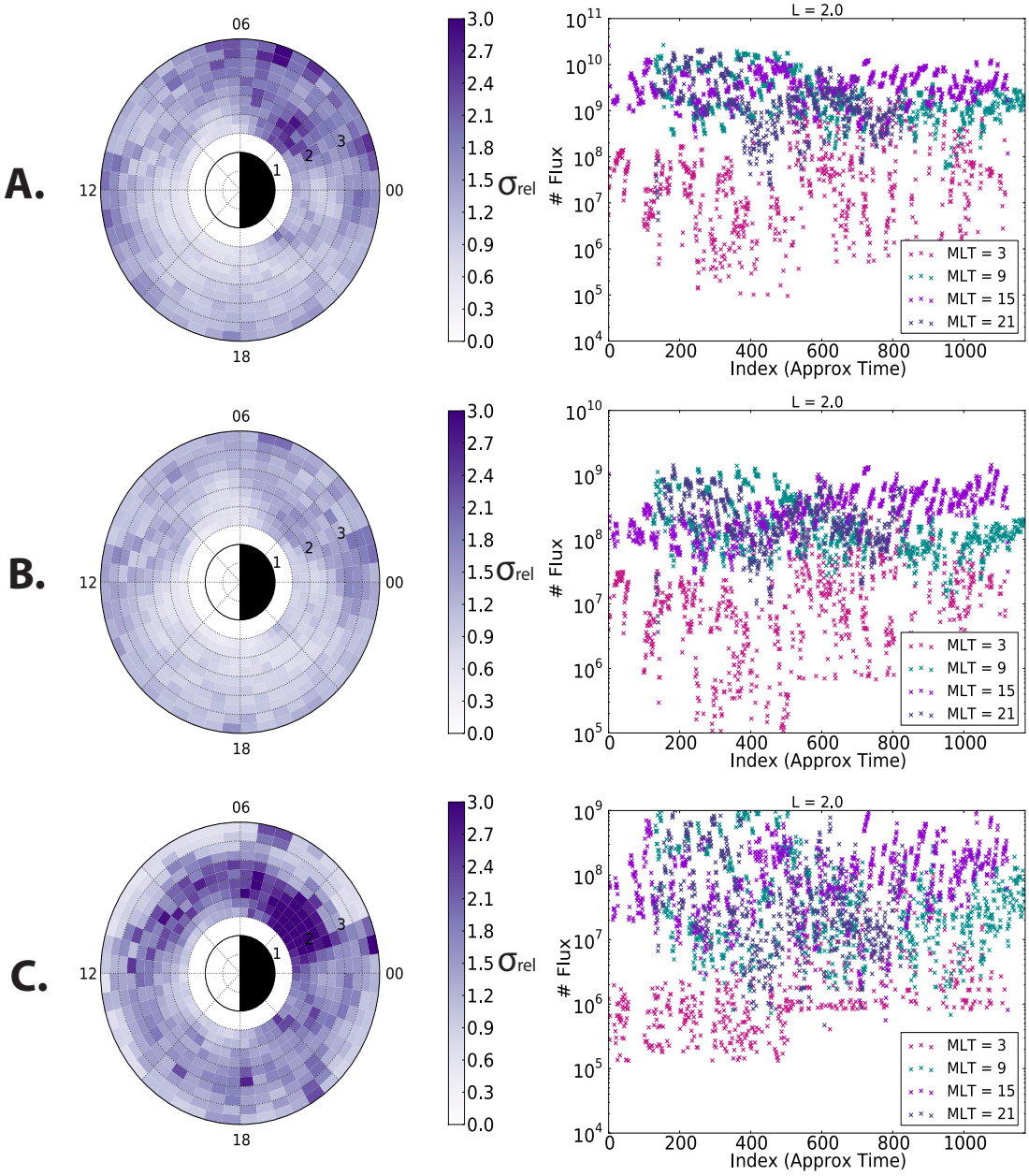

Figure 2.7: The left column gives the relative standard deviation (standard deviation / mean) in the 2.2 eV flux bins for (A) H^+, (B) He^+, and (C) O^+. The right column shows all the HOPE measurements for L=2.0 of MLT=3,9,15,and 21 for each species. Both columns include both satellite A and B data. The flux measurements are ordered in time, so the label Index (Approx Time) refers the relative position of each non-zero measurement in this time ordered array.

dramatic plasma temperature change. This behavior correlates well with ionospheric electron and ion temperatures across the nightside (*Pavlov and Pavlova*, 2005).

To determine whether the post-midnight depletion in the 1-10 eV energy range is a density loss or a cooling effect, we compared the median flux measurements as a function of energy at L=2.0 at MLT=3, 9, 15,and 21. Figure 2.9 shows these results, where the energy values have been shifted by 0.75 eV to account for the average impact of positive spacecraft charging (0.75 eV) on HOPE measurements. The slopes of the lines in Figure 2.9 indicate the change in the distribution with energy and follow an approximately Maxwellian distribution. We find that the distributions from all MLTs have about the same slope, but the MLT=3 median measurements show lower flux. However, based on this limited range (1-10 eV) of the distribution, we are unable to definitely state whether this is purely a temperature change or a density loss.

2.4 Discussion

Through statistical analysis and a case study example, we have demonstrated that there is a depletion across H^+, He^+, and O^+ in the post-midnight sector as seen by the HOPE instrument in the upper end of the thermal distribution of the plasmasphere. Further, the compositional dependence of the nightside loss is that H^+ is depleted the most, followed by O^+, and then He^+; thus the depletion is not ordered by particle mass. A physical explanation of this unusual result is given below, along with an analysis of spacecraft charging, which is an issue of critical importance to the veracity of the findings for the quiet time 1-10 eV population.

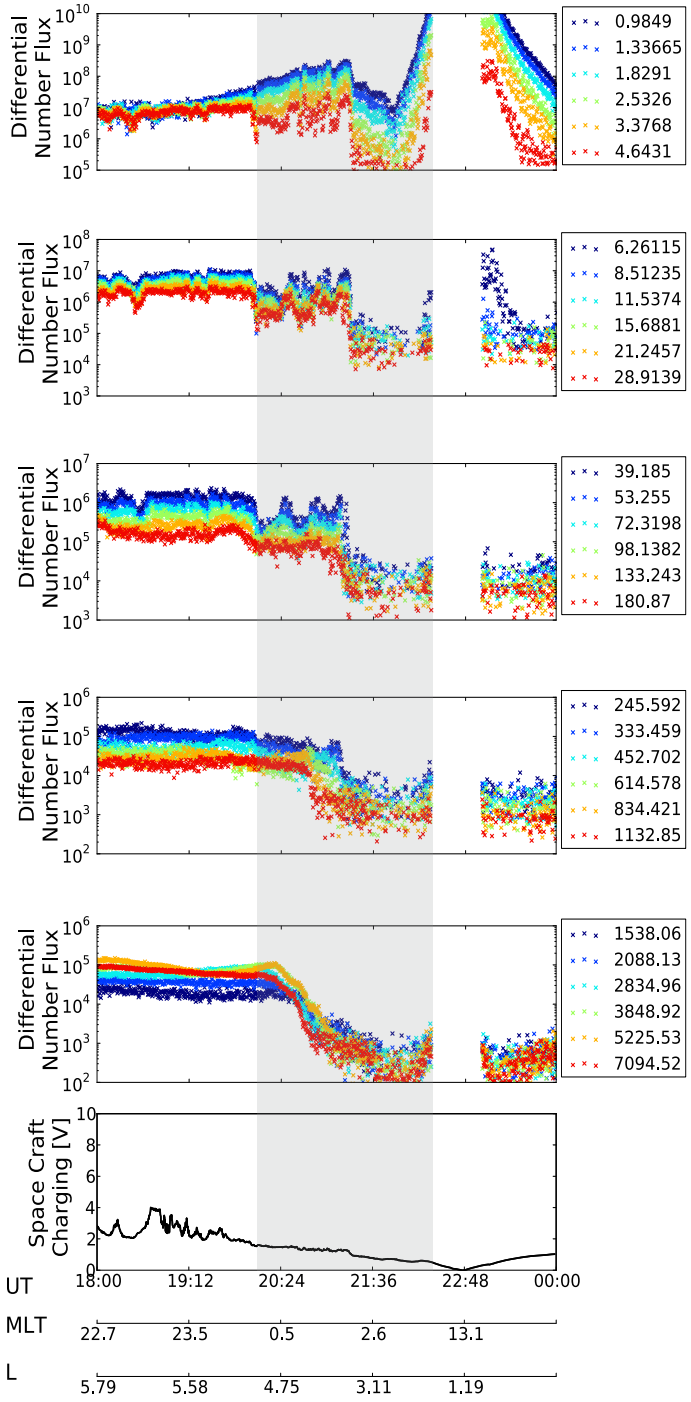

Figure 2.8: HOPE H^+ flux values for a six hour period on April 30, 2013 from 1-7000 eV. The bottom panels show the spacecraft potential in V from the EFW instrument. The gray shaded area highlights the post-midnight sector ($0 < \text{MLT} < 6$).

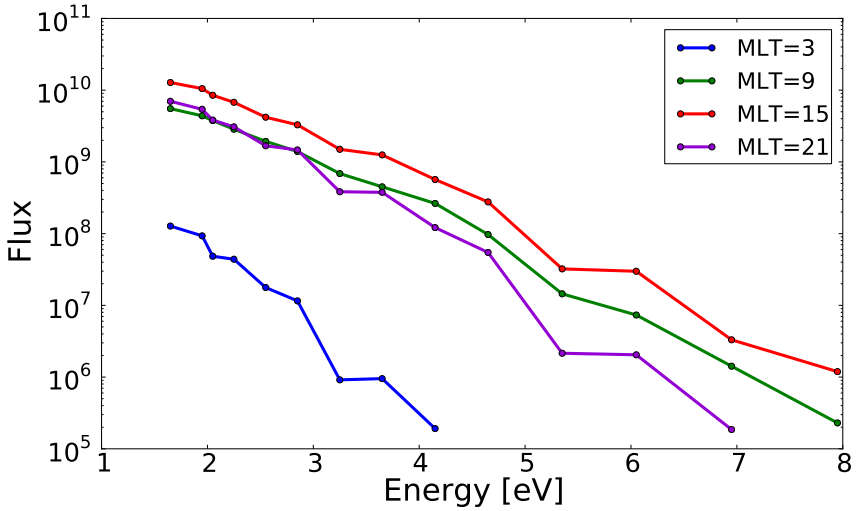

Figure 2.9: Median differential number flux measurement as a function of energy at L=2.0 for MLT=3,9,15,21.

2.4.1 Diurnal Variation Analysis

This variation with species can be explained by observing that plasmaspheric ions at these energies come from the dayside ionosphere (*Chappell et al.*, 1987). The He^+ density profile is similar to the ion temperature profile of the ionosphere (*Roble*, 1975). The double peak feature of He^+ at pre-noon and dusk is similarly seen in the work of *Galvan et al.* (2008). They concluded this feature is due to a local minimum in the topside ionospheric ion density at noon, and thus, with an ionospheric source for 1-10 eV plasma, then the density decrease in plasmaspheric He^+ is consistent.

The MLT dependent behavior of the high energy plasmasphere tail comes from the production of H^+, O^+, and He^+ in the top side ionosphere. H^+ and O^+ have accidental charge resonance,

$$O^+ + H \rightleftharpoons H^+ + O \tag{2.2}$$

This linked reaction is responsible for the tandem behavior of H^+ and O^+ in the high energy portion of the plasmasphere. In particular, S_{H^+}, the source of H^+, is given by,

$$S_{H^+} = m_H \sigma_e \sqrt{\frac{8kT_n}{\pi m_H}} n(\mathrm{O}^+) n(\mathrm{H}) \tag{2.3}$$

where σ_e, the electron collisional cross section, is approximately 2 x 10^{-15} cm^2. So as the neutral temperature, T_n, increases due to heating from photoionization when in the post dawn sector, the H^+ population grows. He^+ is also produced in the ionosphere from solar radiation with $\lambda < 50.4$ nm. The dominant loss mechanism for He^+ is charge transfer with the neutrals O_2 and N_2, which are extremely rarefied in the topside ionosphere.

Since the source of H^+ is sensitive to thermospheric temperature, which is demonstrated in (2.3), and since O^+ is tied to H^+ via (2.4), these populations will naturally decline after the terminator due to the cooling of the atmosphere. He^+ production is sensitive to solar exposure but has a longer loss/gain timescale than that of O^+ and H^+ and consequently shows a less dramatic density depletion.

The diurnal variation of H^+ is seen in the topside ionosphere from previous studies (*Ho and Moorcroft*, 1971; *Richards and Torr*, 1985). The topside ionosphere temperature minimum occurs between 0-4 local time and peaks in the afternoon. This variation supports our claim that near-Earth 1-10 eV plasmasphere ions exhibit similar behavior to topside ionosphere ions.

2.4.2 Spacecraft Charging

Surface spacecraft charging in a lower density and higher energy plasma affects measurements by shifting the energy distribution function of a plasma by the potential energy, eϕ. So, if HOPE makes a measurement at 2 eV, but there is -1.5 V of spacecraft charging, then these measured 2 eV ions would actually have been 0.5 eV ions (2 eV -1.5 eV) because they are accelerated toward the negatively charged satellite. Likewise, if there is a positive potential, the ion population observed by HOPE would appear to be lower energy than the actual distribution (*Garrett*, 1981).

The post-midnight sector is notorious for spacecraft charging effects, particularly for satellites in geosynchronous orbit. *Mizera and Boyd* (1982) explore this topic from an engineering perspective, using the USAF P78-2 satellite to calibrate spacecraft charging based on materials used, Kp, and MLT as a function of percentage of satellite affected. They found that at geosynchronous orbit, spacecraft charging, particularly in the post-midnight sector, is high during times of high and low Kp. For within geosynchronous orbit, a small percentage of the total time ($< 3\%$), there is spacecraft charging in the post-midnight sector; however, an equivalent amount of charging is seen post dawn, in which our results are unaffected.

To calibrate how much spacecraft charging occurs in the post-midnight sector relative to other MLTs and determine if our results might be biased by spacecraft charging, we used the Van Allen Probes Electric and Magnetic Field Instrument Suite and Integrated Science (EMFISIS) instrument (*Kletzing et al.*, 2014), and the Electric Fields and Waves (EFW) instrument (*Wygant et al.*, 2014). Using EFW spacecraft potential for the entirety of the Van Allen Probes Mission (November 2012 to April 2014), we binned spacecraft potential by 0.25 L-Shell and 0.5 MLT and then took the median of each bin, which is shown in Figure 2.10. We did not sort spacecraft

potential by Kp index because very few storms occurred in this time period.

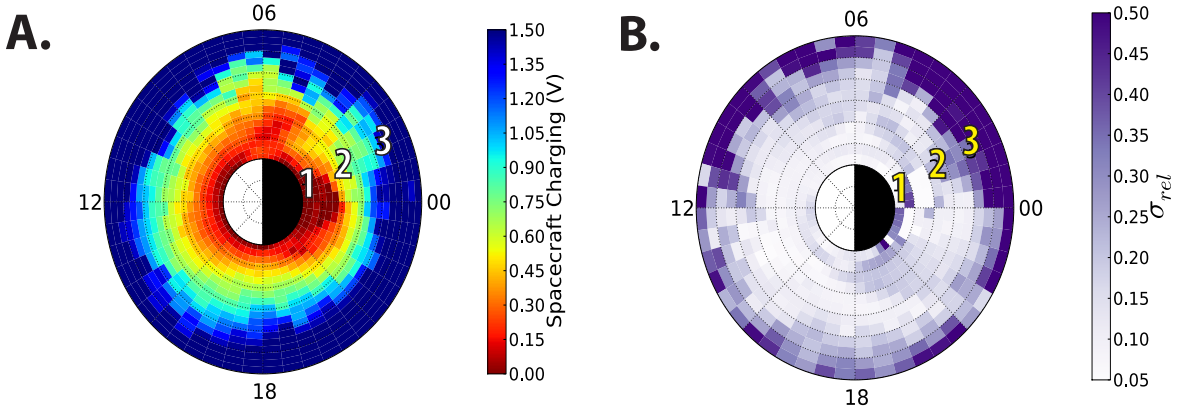

Figure 2.10: (A) is the median spacecraft potential in each 0.25 L-Shell and 0.5 MLT bin from the EFW instrument from November of 2012 to April of 2014. (B) is the relative variation (standard deviation / mean) of the spacecraft potential data shown in A.

In Figure 2.10A, we can see that the spacecraft potential is less positive in Earth's shadow (e.g., at L=2, the median potential is 0.65 V at 18 MLT, but only 0.15 V at 0 MLT). The lower potential indicates that ions near midnight are decelerated by a smaller amount as they approach the detector. Our statistical study of spacecraft potential shows little difference in spacecraft potential between the post-midnight sector and the dusk sector, yet we see a dramatic difference in the partial plasma density maps of Figure 2.3.

We supplement Figure 2.10A with a variation analysis shown in B. The relative standard deviation is the standard deviation of spacecraft potential measurements within a bin divided by the mean spacecraft potential of that bin. The relative standard deviation is approximately constant across low L-Shell MLTs, but at high L-Shells (> 3), there is more variation in the post-midnight sector. This is expected because of the eastward gradient curvature drift of high-energy electrons, which would

increase spacecraft charging. However, this effect does not penetrate to lower L-Shells because the electrons drift eastward before they can reach that close to Earth, especially for the Kp < 3 quiet time data selection filter applied for this study.

Furthermore, Figure 2.11 directly compares the median spacecraft potentials at MLT=3 and MLT=18 with the median densities at these same local times. From L=1.75 to L=2.5, the spacecraft potentials in these two regions are nearly identical, while the densities differ by an order of magnitude with a density of 10 cm^{-3} at MLT=18 and 1 cm^{-3} at MLT=3. Beyond L=2.5, the spacecraft potentials at the two local times diverge with a higher potential observed at MLT=18. However, the density at MLT=3 remains lower than the density at MLT=18 out to at least L=4. This figure directly shows that the ion loss in the post-midnight sector is not related to higher spacecraft potentials in this region.

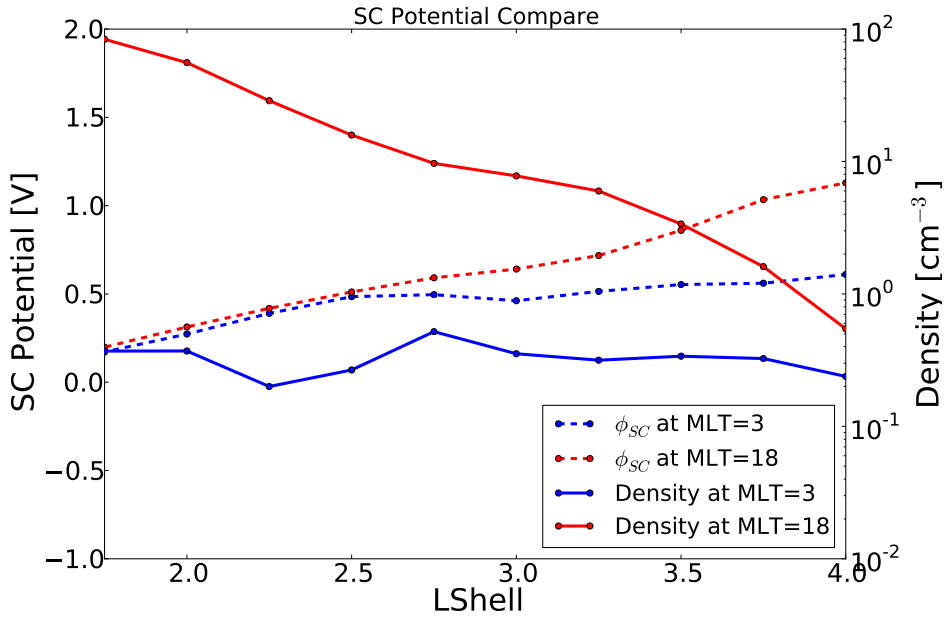

Figure 2.11: Median spacecraft potential (ϕ_{SC}) from L-Shell 1.75 to 4.0 at MLT = 3 and MLT = 18 compared with median partial plasma densities from the same bins.

We also examine the HOPE electron measurements at L=2, shown in Figure 2.2B, for any observable difference in the post-midnight sector compared to other MLTs. We do see a slight increase in median electron flux measurements in the post-midnight sector; however, there is also a comparable sized electron flux augmentation at 15:00 MLT, ruling out this electron intensity increase as responsible for the ion depletion. Also, the HOPE low-energy electron densities are highest at post-dawn, supporting our interpretation that electrons, produced from photoionization in the ionosphere and then scattered at high altitudes on these field lines, mirror and deposit their energy and warm the plasmasphere.

Due to the maximum frequency on EMFISIS of 400 kHz, the EMFISIS electron number density measurements saturate at L < 3, making it impossible to distinguish differences between MLT electron number densities at low L-Shells. This prevents us from determining if the electron number densities also exhibit a similar drop as the ion plasma densities across the post-midnight sector using Van Allen Probes data.

2.4.3 Why This Depletion Has Not Been Previously Observed

In examining the 1-10 eV population in Van Allen Probes data, we questioned why this effect was not observed by previous missions. The uniqueness of the Van Allen Probes mission allowed for clear observation of this post-midnight density loss. In the following section we specifically address why this loss was not observed in other missions and a brief description of those missions.

IMAGE EUV visualized the plasmasphere by counting solar EUV photons resonantly scattered with He^+ (*Sandel et al.*, 2000, 2001), producing vivid pictures of the plasmasphere and highlighting the plasmaspheric plume (*Spasojević et al.*, 2004).

These results are somewhat limited, as IMAGE EUV gives an integrated total density over a line of sight and utilizes an inversion procedure to provide local density values (*Gurgiolo et al.*, 2005). The IMAGE radio plasma imager (RPI) allowed for electron density measurements along plasmaspheric field lines and distributions from the polar cap ionosphere (*Reinisch et al.*, 2000, 2001). However, IMAGE EUV only measured total He^+ densities, which overshadows the plasma loss in the 1-10 eV range.

The Cluster mission offered the advantage of a polar orbit that ultimately transformed into an equatorial orbit (*Escoubet et al.*, 1999) and the Cluster Ion Spectroscopy (CIS) instrument that measured composition (*Reme et al.*, 2001). However, the Cluster CIS-CODIF measured > 40 eV ions, which is above our study's energy range. Also, the Cluster perigee is at approximately L=4, and our study focuses on the region between L=2 and L=3. The Waves of High frequency and Sounder for Probing of Electron density by Relaxation (WHISPER) experiment on board Cluster provided electron density measurements and total plasma density measurements within 0.2-80 cm^{-3} (*Décréau et al.*, 1997), which is useful for understanding plasma distribution outside of an L-Shell of 4.

The Combined Release and Radiation Effects Satellite (CRRES) also provided ample information about the behavior of the plasmasphere. From upper hybrid resonance frequency measurements, CRRES captured the behavior of plasmaspheric electron density exceptionally well, documenting the plasmasphere trough with precision (*Sheeley et al.*, 2001; *Moldwin et al.*, 2002). The mission goals of CRRES were to better understand the radiation environment near Earth and perform several chemical release experiments; however, this satellite was not able to measure low energy plasma due to instrumentation difficulties (*Johnson and Kierein*, 1992) and CRRES did not directly measure ion composition.

The Retarding Ion Mass Spectrometer (RIMS) onboard Dynamics Explorer 1 (DE-1) (*Chappell et al.*, 1981) measured ion composition from 0-50 eV for H^+, He^+, and O^+. With a polar orbit and an apogee at 4 Earth radii, DE-1 provided a wealth of information of near Earth plasma, low energy ion composition, such as the presence of the warm plasma cloak (*Chappell et al.*, 2008) and provided the basis for initial plasmasphere models (*Gallagher et al.*, 1988). This effect was not reported in results of the RIMS data set, but RIMS data could be used to confirm the results seen here. The High Altitude Plasma Instrument (HAPI) onboard DE-1 provided measurements on the velocity space distribution of ion and electrons from 5 eV to 32 keV near Earth (*Burch et al.*, 1981; *Winningham et al.*, 1981).

However, HAPI did not distinguish composition and focused on plasma injections into the polar region (*Burch et al.*, 1982; *Newell et al.*, 1991). DE-2 observations built on our understanding of topside ionospheric electron temperatures (*Kozyra et al.*, 1986). However, the DE-2 satellite was an ionospheric polar orbiter and did not fly at high enough altitudes to see the low energy ion population at $L > 2$.

A combination unique to all of these missions, Van Allen Probes offers high dwell time in the inner magnetosphere, a near equatorial orbit, and the ability to distinguish the 1-10 eV ion population cleanly.

2.5 Conclusions

Using the HOPE instrument data to look at plasma density for H^+, He^+, and O^+ from 1 - 10 eV during quiet time periods, we see strong MLT dependence in the high energy tail of the plasmasphere. Our study has two main findings: there is diurnal

variation across all three ion species in the 1-10 eV range and there is a compositional difference in the amount of loss observed across the post-midnight sector.

We observed that H^+, He^+, and O^+ decrease rapidly, similar to ionospheric temperatures across the nightside. We propose that all three species experience rapid density gains at the dawn terminator because the dayside plasmasphere heats quickly from the magnetic mirroring and energy loss of electrons scattered from photoionization from neutrals. This thermalization of the plasmasphere energizes the ions over the course of a couple of hours, which is what we observe across the dawn terminator in Figure 2.3.

We see that He^+ loss is the smallest, as supported by Figure 2.5. H^+ and O^+ densities follow each other closely because of the charge resonance that exists between these two species. So when H^+ is lost faster than He^+ and O^+ because of its low mass, the net effect is a rapid combined loss of H^+ and O^+ because of their tandem behavior. The enhanced high energy densities from photoionization in these ions remains throughout the day, and then declines slowly after the dusk terminator. The populations almost vanish in the post-midnight sector, with density values dropping a factor of 28 to 150 (Figure 2.5).

He^+ in the high energy plasmasphere tail exhibits different MLT dependence than H^+ and O^+. The source of ionospheric He^+ is photoionization, which peaks in the morning sector and then again at dusk. The increase of dayside He^+ is thought to be from the dayside warm ionosphere exerting a pressure on He^+ ions, pushing them into plasmaspheric flux tubes. The decline in He^+ on the nightside, particularly in the post-midnight sector, is still significant at a factor of 28 but is not as sharp as H^+ and O^+. He^+, although lighter than O^+, has a slower loss rate because of the O^+

charge resonance with H^+.

This study shows the MLT dependence of high energy plasmasphere ions seen in the HOPE instrument on the Van Allen Probes during quiet time intervals. Unanswered questions on the ions in this regime still remain, such as what causes the local minimum of He^+ in the ionosphere and in the high energy ion tail of the plasmasphere. We proceed in the following chapters to focus on H^+ partial densities, so resolving why He^+ and O^+ deplete at different rates and to different degrees remains undone. Also, we have not investigated how periods of high convection or how binning by other indices, such as Dst, the disturbed storm time index, may shed additional light on physics behind the 1-10 eV partial plasma density depletion in the post-midnight sector.

CHAPTER III

Van Allen Probes Spacecraft Charging Analysis

3.1 Introduction

Spacecraft surface charging is a serious concern for satellites near geosynchronous orbit. Spacecraft anomalies have been linked to spacecraft surface charging events, particularly in the post-midnight sector where there are increased electron fluxes (e.g., *Rosen*, 1976; *Grard et al.*, 1983). Spacecraft charging not only affects plasma measurements, but also the operations of telecommunication satellites and solar panels (e.g., *Lanzerotti et al.*, 1998; *Katz et al.*, 1998; *Lanzerotti*, 2001; *Choi et al.*, 2011; *Mazur and O'Brien*, 2012). Our ability to prevent and mitigate spacecraft charging relies on our understanding of spacecraft charging and what causes it.

One of the first reported instances of spacecraft charging was a rocket study where the authors discussed how measured ion peaks from the radio frequency (RF) mass spectrometer onboard could be explained by a -20 V surface potential (*Johnson and Meadows*, 1955). Extreme spacecraft charging conditions on the order of -10,000 V were first recorded by geosynchronous satellites ATS 5 and ATS 6 (*DeForest*, 1972, 1973). ATS 5 and ATS 6 were largely non-conducting satellites, as was the Spacecraft Charging at High Altitude (SCATHA) satellite which also observed extreme charging (*Olsen*, 1981; *Craven et al.*, 1987). Spacecraft surface charging at geosynchronous

orbit has been studied extensively, but conclusions have been varied. Extreme negative spacecraft charging occurs primarily when satellites enter the plasmasheet and are bathed in hot electrons in low density plasma (*Garrett*, 1981). During intense electron flux periods, the electrons generate a strong negative current, overtaking the positive photoemission current on the spacecraft surface and resulting in a net negative current on the spacecraft. One study found that surface charging is so sensitive to location that nearby satellites can not be used to estimate or predict another spacecraft's surface charging (*Koons et al.*, 2006). The variability in both satellite construction and situational evidence has made it difficult to quantify spacecraft charging intensity and the factors that cause spacecraft charging.

It is known that electron fluxes are linked to negative spacecraft surface charging. However, there is still much debate as to exactly how the electron fluxes cause spacecraft charging. Measurements from SCATHA suggested spacecraft charging was produced by the 3 to 30 keV population (*Reagan et al.*, 1981). Yet, another study found that spacecraft charging intensity was caused by the electron population above 30 keV (*Mullen et al.*, 1986). Another study using ATS 6 and SCATHA measurements showed that once a certain threshold of 10 to 20 keV fluxes was reached, spacecraft charging would occur (*Olsen*, 1983). There is also considerable evidence that spacecraft potential is a function of ambient electron temperature around the spacecraft (*Rubin et al.*, 1980; *Laframboise and Kamitsuma*, 1983; *Harris*, 2003).

With data from the Los Alamos National Laboratory geosynchronous (LANL-GEO) satellite program, more studies defining a critical temperature or threshold flux emerged. One such study concluded that, depending on the satellite, charging will only occur when average electron temperatures near the satellite are at least between 400-3000 eV (*Lai and Della-Rose*, 2001). Specifically, for the LANL-GEO

satellites, which were non-conducting satellites, a critical electron temperature between 1 to 2 keV would result in extreme charging events with spacecraft potential below -200 V (*Lai and Tautz*, 2006). A later study found that once a critical threshold of electron energy fluxes within the energy range of 5-10 keV has been satisfied, charging will occur and then the degree of charging was determined by the electron temperature (*Thomsen et al.*, 2013).

The Van Allen Probes satellites, or the Radiation Belt Storm Probes, offer us another way to analyze spacecraft charging. A pair of twin probes launched in 2012 into an approximately 9 hour elliptical orbit, the Van Allen Probes contain two instruments which provide the opportunity to study spacecraft charging on a conducting spacecraft within geosynchronous orbit (*Mauk et al.*, 2014; *Kirby et al.*, 2014).

The first approach used the Helium Oxygen Proton Electron (HOPE) (*Funsten et al.*, 2014) mass spectrometer to extract the ion charging line in the proton spectra, similar to the method used in the analysis of LANL GEO data. The HOPE instrument consists of an electrostatic analyzer followed by central electromagnetic calorimeter (CEM)-based time-of-flight (TOF) pixels that measures 1 eV to 50 keV Helium, Oxygen, and Hydrogen ions along with 15 eV - 50 keV electrons. Angular measurements are derived using five polar pixels (0, +/- 36^o, +/- 72^o) coplanar with the spacecraft spin axis, and up to 16 azimuthal bins are acquired for each polar pixel over time as the spacecraft spins. Ions and electrons are measured on alternating spins. Ion species are determined onboard the spacecraft by the energy dependent TOF bin in which the count falls.

The second method used the Electric Fields and Waves (EFW) instrument (*Wygant et al.*, 2014), which utilized two orthogonal booms in the spin plane with 100 m

tip-to-tip separation to measure potential across each of the Van Allen Probes satellites, similar to other scientific double-probe spacecraft such as Polar (*Harvey et al.*, 1995). The EFW instrument includes three pairs of sensors deployed at the tips of oppositely directed booms. The spacecraft potential is calculated on the ground by averaging probe potentials from sensors on opposite sides of the spacecraft in the spin plane. Summing and averaging removes the differential electric signal from convection, waves, and other ambient plasma processes, leaving the potential of the spacecraft body relative to the ambient plasma.

The EFW sensor is a conducting metal sphere of radius 4 cm coated with DAG 213 in order to minimize work function variations over the sphere. High-input impedance preamplifiers are located in the spheres to limit 'voltage divider effects' in coupling to the ambient plasma sheath, which can have a large source impedance in a low density plasma. The spherical sensor is current biased with a constant bias current which is controlled by the EFW CPU and adjusted to balance the photoemission from the sphere. More specifically, the sensor bias current value is adjusted to have the opposite sign of the photocurrent from the sphere and at about 20-50% of its magnitude. This operating point is determined by periodic bias sweeps that involve stepping the bias current and measuring the output voltage of the sensor.

Sections of the boom near the sphere are voltage biased at constant positive (1-3 V) potential relative to the sphere potential in order to limit spurious photo currents flowing between the sensor and the nearby boom elements. The power supply limits for the sensor pre-amplifier are +/- 200 V. This corresponds to the largest signal that can be measured by the pre-amplifier. Thus if the spacecraft charges to more than 200 V, the pre-amplifiers 'saturate'. In order to limit differential charging of the spacecraft, the spacecraft bus is constructed from conductive materials. The solar

panels include Indium Tin Oxide (ITO) coated cover glasses. The thermal blankets are similarly coated ITO coatings. All conductive surfaces including the backs of the solar panels on the spacecraft are conductively tied together to limit charging between the sunlit and non-illuminated sections of the spacecraft. The purpose of the conductivity specification for spacecraft surfaces was to insure that all surfaces of the spacecraft be conductive such that no differential charging from any two regions on the spacecraft bus with areas larger than approximately 1 cm^2 could exceed one volt when in orbit. This conductivity specification is designed to limit the differential charging believed to play an important role near geosynchronous orbit.

Each method has strengths and weaknesses. The HOPE ion extraction method can only capture times of negative spacecraft charging, and it performs best when charging is below -50 V. The HOPE ion extraction algorithm we use requires that EFW identifies periods of negative charging and then looks for the ion line. On the other hand, the EFW probe potential method measures spacecraft charging at all times both positive and negative, but it saturates due to voltage limitation at +/- 200 V of negative spacecraft potential. This study demonstrates that EFW tends to underestimate times of intense charging lower than -50 V.

EFW is additionally limited since it can not make reliable spacecraft potential measurements while in Earth's shadow because the photocurrents necessary to produce a stable potential reference for the probes are not present (*Wygant et al.*, 2014). The electric field probes are current biased to produce a stable voltage reference. In a low density plasma during times of solar illumination, the two dominant currents are 1) photoemission and 2) a fixed bias current from the sensor that is controlled by the EFW microprocessor. When these two currents are balanced properly, the sensor floats at a nearly constant potential within 1-2 V of the plasma potential at infinity.

When the spacecraft is in Earth's shadow, there is no photoemission current. The current balance lies between the EFW controlled bias current and plasma currents, which can result in large sensor floating potentials and large DC sheath impedances. Thus, EFW and other double probe electric field experiments are not designed to provide accurate electric field measurements during eclipse periods in low density plasmas.

In this study, surface charging was statistically analyzed on the Van Allen Probes satellites as a function of L and magnetic local time (MLT). The relationship between surface charging and electron pressure, electron temperature, thermal electron current, low energy ambient ion density, and electron density was examined. A comparison between the two methods of calculating spacecraft charging, using the HOPE instrument H^+ spectra and EFW potential measurements, was performed. The relationship between thermal current and electron energy fluxes was also examined in this study.

3.2 Observations from EFW

Figure 3.1 shows the distribution of charging occurrences and magnitudes in the Van Allen Probes EFW measurements from February 2013 to April 2015. Combining EFW data from both Van Allen Probes A and B satellites, Figure 3.1A shows that each satellite usually charged within +/- 10 V during this time period. Charging events less than -50 V occurred 4 orders of magnitude less often than +/- 10 V charging times. Figure 3.1B highlights that most of the negative charging events throughout the mission occurred in the first 4 months of 2013 and from August to December of 2014, when the apogee of the satellites was in the post-midnight sector.

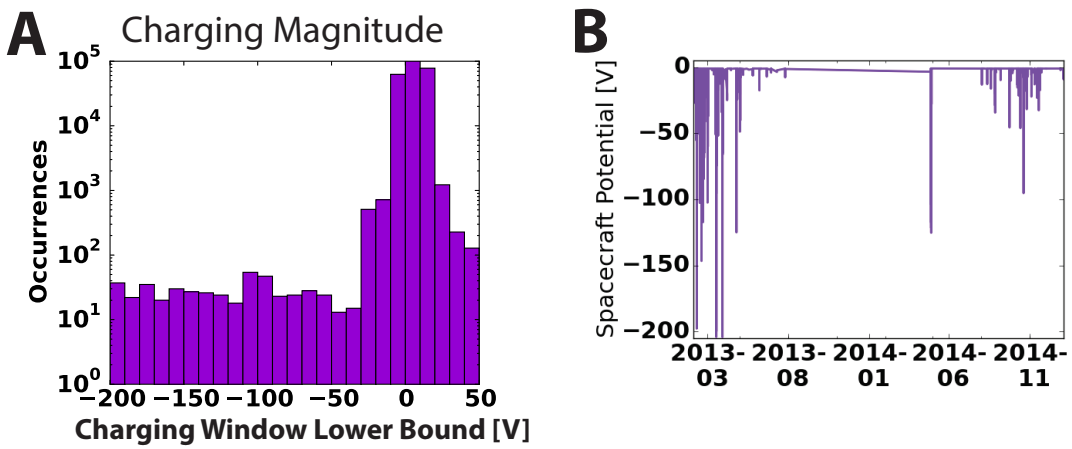

Figure 3.1: A shows the number of EFW charging events from February 2013 to April 2015 over the range of -200 V to 50 V in 10 V windows. The x-axis labels give the lower bound for each window. An occurrence is defined a single measurement by EFW over an 11 second window. B shows the negative spacecraft potential recorded by EFW over the February 2013 to April 2015 time period.

Using times of spacecraft charging between February of 2013 and April of 2015, spacecraft potential from the EFW instrument on both Van Allen Probes A and B was binned by L and MLT. These spacecraft potential measurements were binned by 0.25 L and 0.5 MLT and put into four charging windows: $<$ -10 V, -10 V to 0 V, 0 V to 10 V, and $>$ 10 V. The Olson-Pfitzer 77 model is used to calculate L (*Olson and Pfitzer*, 1977).

Figure 3.2 shows normalized spacecraft potential as a function of MLT and L for each level of charging. The total number of occurrences is used to normalize the results in each L/MLT bin. Most instances of -10 V to 0 V charging occurred at L $<$ 3 at all local times. Times when the spacecraft was in Earth's shadow are identified by nearly 100% likelihood of slight negative charging (-10 V to 0 V). This is because solar driven photoemission is curtailed from lack of sunlight, and as a consequence,

the spacecraft charges slightly negative. Some charging events also occurred in the post-midnight sector at L > 4 in this charging window. The 0 V to 10 V charging window encompasses most of the data from the mission, with small gaps across the nightside, pre-evening sectors, and in Earth's shadow. Only a few < -10 V events are observed, all at L > 4. Most of the events occurred in the post-midnight sector, but some events also occurred at dawn and in the pre-midnight sectors. This is agrees with the results observed by ATS-6 (*Reasoner et al.*, 1976). For > 10 V of positive charging, the majority of events occur at either midnight or pre-midnight at L > 3.

Figure 3.3 highlights times of negative charging on the Van Allen Probes when the spacecraft was not in eclipse. Charging occurrences from both Van Allen Probes A and Van Allen Probes B were included in Figure 3.3. In this situation, the thermal electron current spikes due to the presence of hot electrons and exceeds the photoemission current which usually keeps the spacecraft slightly positive. These times of negative charging in sunlight present a unique situation. Extreme care was taken on the Van Allen Probes satellites to ensure a conducting spacecraft, and previous studies have shown, based on model results, that significant negative spacecraft charging should not occur in sunlight on a conducting spacecraft (*Davis et al.*, 2012; *Kirby et al.*, 2013). In particular, we see from Figure 3.3 in the post-midnight sector at L > 4, there are a large number of negative spacecraft charging events, where hot electrons begin to gradient curvature drift eastward as they enter from the plasma sheet.

We examine the 0-10 V charging window more closely by further dividing this window into 1 V bins; Figure 3.4 shows selected bins. Most observations at L < 4 show 0-1 V charging. By 2-3 V positive potential, there are almost no events at L < 3. Instead, there is a stronger likelihood of these positive events to occur in the dusk

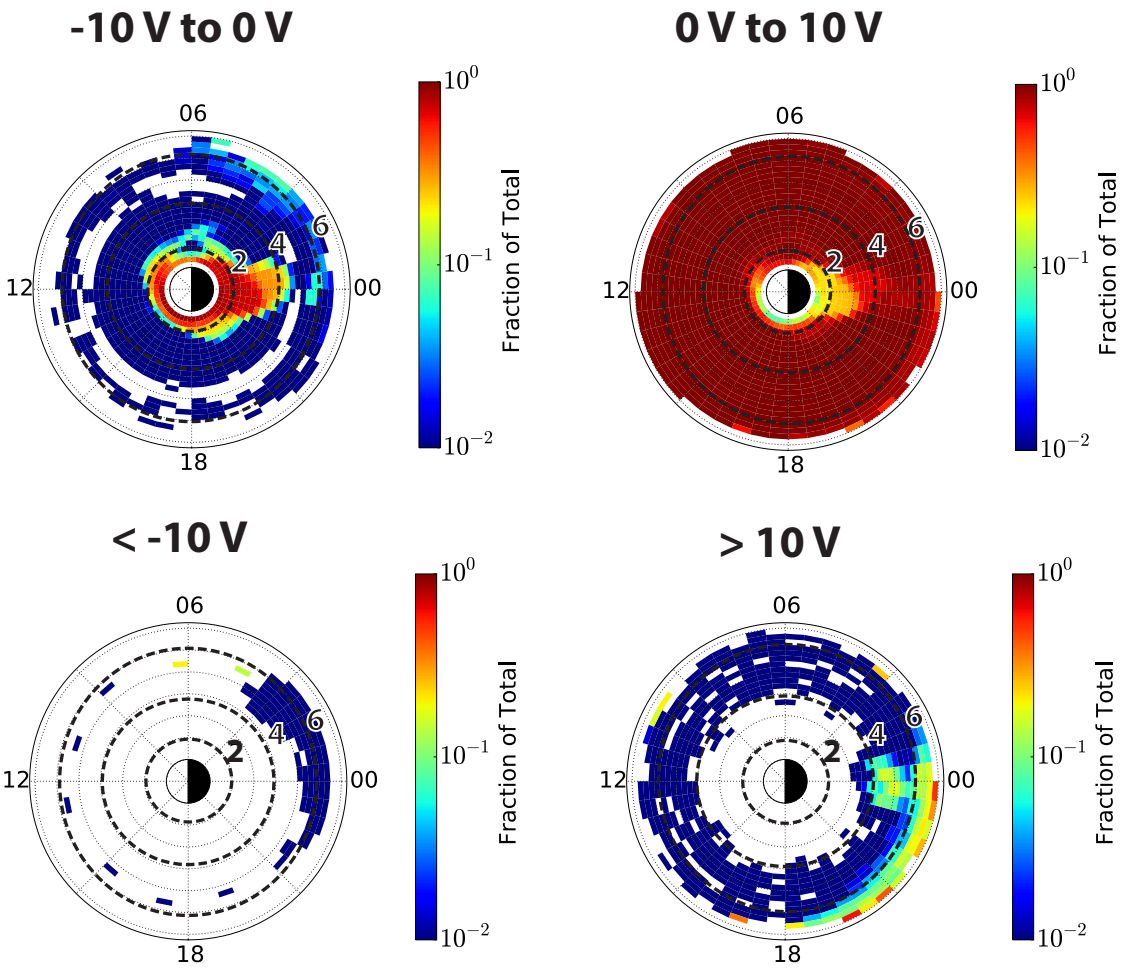

Figure 3.2: EFW Van Allen Probes A and B spacecraft potential categorized as 0 to -10 V, 0 to 10 V, < -10 V, and > 10 V and binned by 0.5 MLT and 0.25 L from February 2013 to April 2015. The fraction reflects the number of 11 second measurements in each charging window and 0.5 MLT/0.25 L bin compared to all the measurements from from that MLT and L. The reddish background in the 0 to 10 V category is because the vast majority of measurements occur in this charging window.

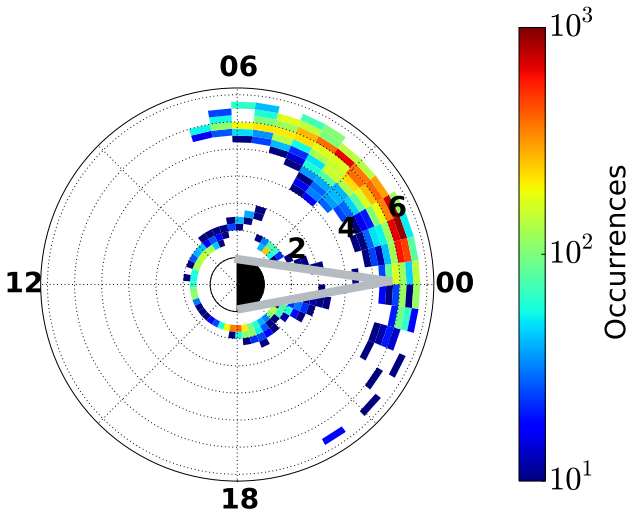

Figure 3.3: Times of negative charging measured by both Van Allen Probes A and B EFW instruments outside of eclipse periods. The spacecraft charge was binned by 0.5 MLT and 0.25 L from February 2013 to April 2015. The silver line shows where we would expect eclipse to be based on average Van Allen Probes satellite orbital parameters.

sector after MLT = 18 between $4 < L < 6$. In the 4-5 V window, charging is most likely to occur at dawn with MLT = 6 just inside of L = 5. There are only a few events in the 8-9 V window, and they most often occur in the pre-midnight sector at $L > 5$. Positive charging appears to be related to the average plasmapause boundary at L=4. Minimal positive spacecraft charging of 0 to 1 V occurs almost 100% of the time within L = 4. More intense positive charging events with charging > 2 V occur outside of L = 4.

3.3 Spacecraft Potential from HOPE Instrument Ion Line Extraction

Two major constraints of the EFW potential measurements are that the instrument saturates at -200 V due to voltage limitations and EFW potential measurements

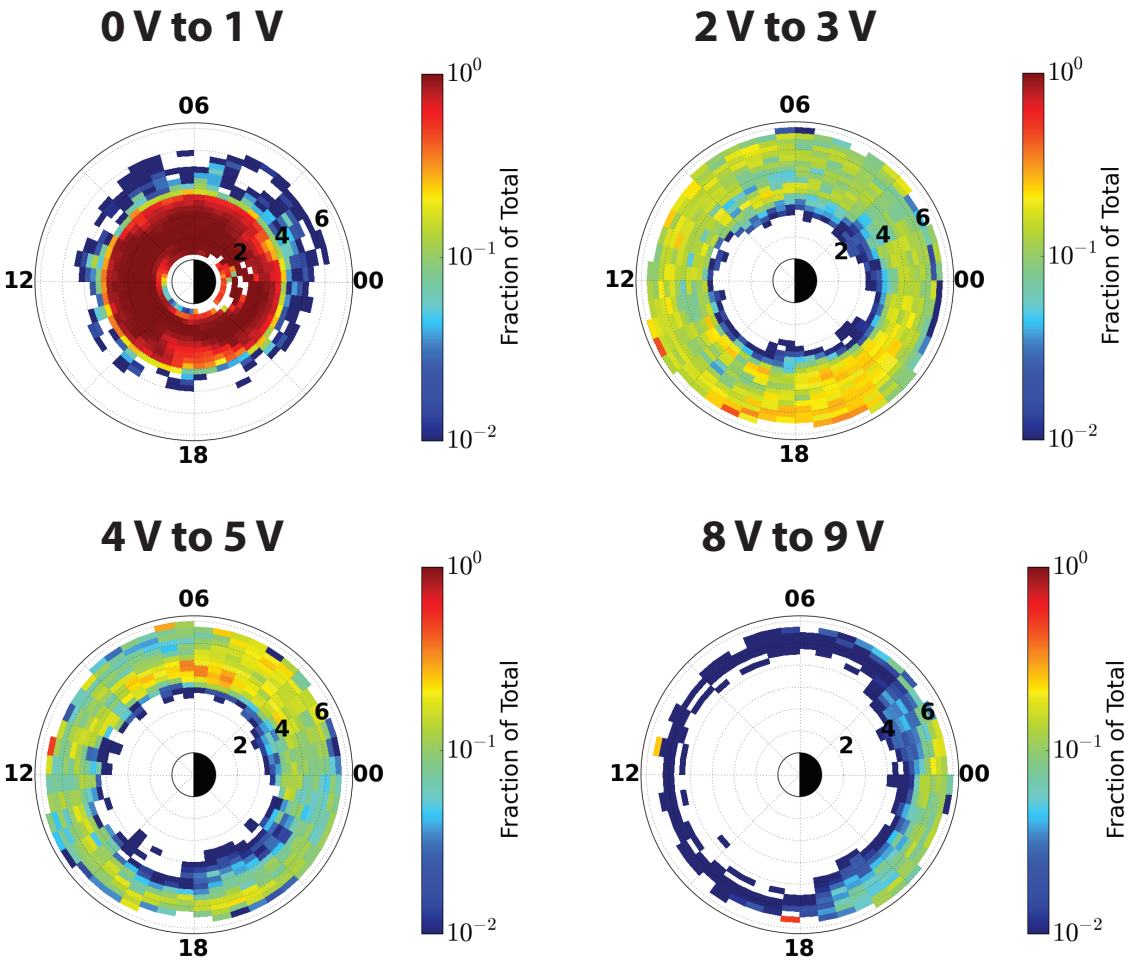

Figure 3.4: Van Allen Probes A and B EFW positive spacecraft potential in selected 1 V charging windows binned by 0.5 MLT and 0.25 L from February 2013 to April 2015 in the same format as Figure 2.

are unreliable during eclipse times when the satellite is in Earth's shadow. However, we can still get a measurement for spacecraft charging during EFW saturation times. We developed an algorithm to extract the charging line from the HOPE instrument H^+ spectra. The charging line occurs when the spacecraft charges negative, and all ions are accelerated by the spacecraft potential as they approach the detector. An ion with an energy of 3 eV would accelerate to 103 eV if the charging on the spacecraft is -100 V. The bulk ion acceleration manifests in the counts spectra as a ribbon of high counts and appears at the level of charging. For -100 V of charging, there would be a line of high counts in the 100 eV measurement bin. In this situation, the detector should observe no ions below 100 eV.

However, at times of significant charging on the Van Allen Probes, there were still counts in the lower energy portion of the spectrum. Therefore, we first employed a base level subtraction technique. To obtain an average base count level, we binned the number of proton counts from 1 eV to 50 keV in the HOPE instrument by 0.1 L between February 2013 to April 2015. Then, for each L and energy bin, the base level counts were defined as the median counts in that bin. The base level counts were highest at low L and at low energies, but above 100 eV were low and usually close to zero.

We subtracted the base count number from each energy bin at each time interval in the HOPE instrument data between February 2013 and April 2015. To identify the charging line was, we looked at times with $L > 5$ and periods where EFW showed negative charging. Based on Figure 3.2, the $L > 5$ assumption is reasonable for times of intense negative charging. During times of charging, the subtracted number of counts was typically negative below the charging line because of the base level subtraction. We then found the three lowest-energy points with non-zero subtracted

counts in each energy spectrum, and determined if these points showed a significant gradient in count rate. If the difference of the first and third non-zero counts was greater than 10, then we concluded that there was a charging line and identified the level of surface charging as the lowest energy with non-zero counts. The minimum gradient of 10 counts worked well at capturing times of high spacecraft charging and identifying the ribbon of accelerated ions. A higher threshold for the gradient excluded low charging events, and a lower threshold made it impossible to distinguish between small fluctuations at mid-energies and times of spacecraft charging. It was necessary to use the gradient method to separate charging times from low count times and events where there were high flux levels at higher energies.

Figure 3.5 shows an example of the results of our algorithm. Figure 3.5 shows the H^+ differential number flux spectrogram for February 8, 2013 between 12:00 to 16:00 UT. This day had a significant charging event where the spacecraft potential reached -198 V according to EFW data and -430 V according to the HOPE ion charging line. There is an uncertainty of 67.8 V on the HOPE ion charging line based on the width of the HOPE energy channel at 430 eV, and this is represented in Figure 3.5 by the width of the silver line. The width of the HOPE energy channels is 15% of the label for that energy channel. The EFW potential probes saturate during the charging event because the spacecraft charge was less than -200 V; thus EFW was unable to accurately determine the charging magnitude. The charging line is clear in the flux spectrogram, and the HOPE instrument ion line extraction algorithm matches this line well.

Figure 3.6 compares the magnitude of charging measured by EFW and determined by the HOPE extraction method at times when both had measurements. The diameter of each point gives the width of the HOPE ion line energy channel. The blue

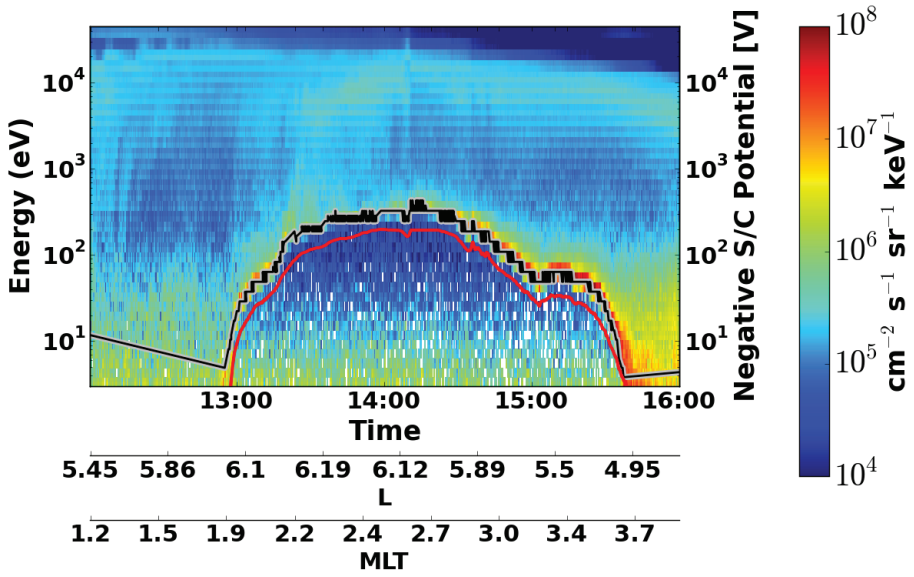

Figure 3.5: Spacecraft charging on February 8, 2013 from Van Allen Probes A, with the red line as the negative EFW spacecraft potential and the black silver edged line as the HOPE instrument charging line from 12:00 to 16:00 UT. The silver line width is the the HOPE energy channel width in eV measuring the H^+ charging line. The spectrogram shows HOPE H^+ differential number flux over the same time period. The satellite was not in eclipse during this charging event.

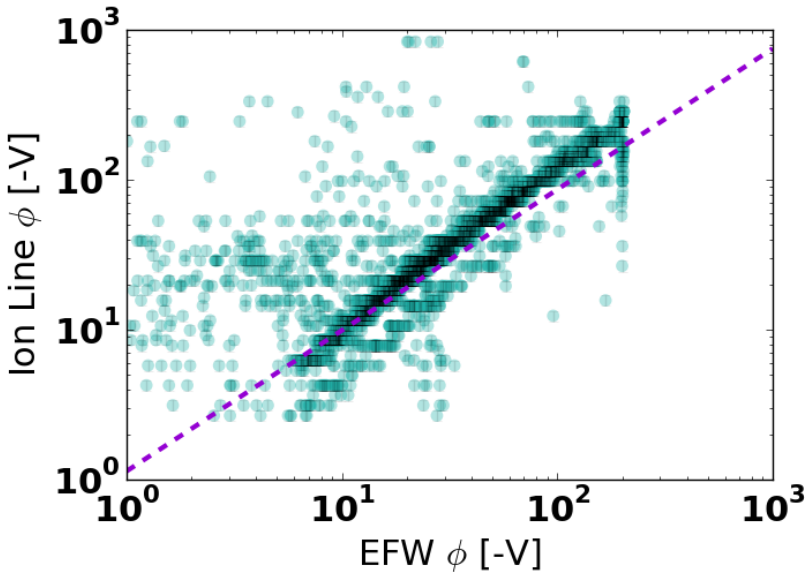

Figure 3.6: The negative spacecraft potential measured by EFW and extracted from the HOPE H^+ line at the same times from February 2013 to April 2015. The diameter of each point is the width of the HOPE energy channel bin (15% of the measured energy) corresponding to that measurement. The purple line is the exponential fit for scatter points within one standard deviation of where EFW ϕ = HOPE ϕ.

dotted line shows the exponential fit of scatter points within one standard deviation of where EFW = HOPE data. For an exponential fit $y = Ae^B$, where A was 1.14 and B was 0 .94, confirming that HOPE measures higher potentials. In Figure 3.6, we can observe that the HOPE extracted ion line measures a higher negative spacecraft potential than EFW particularly during intense charging events, even with error bars taken into account. This is supported by the exponential fit having a slope > 1.

Of the 3284 1-min averaged points with both EFW and HOPE charging measurements, the HOPE potential was larger in 2221 instances. Over all times, EFW potentials were lower than HOPE potentials by a median value of 5.6 V, and a mean difference of 11.2 V. Much of this skew was due to EFW spacecraft potential mea-

surements saturating at -200 V so the instrument was unable to capture times of extreme spacecraft charging. However, even at times of charging below -200 V, EFW tended to underestimate the level of charging. The percentage difference shows that the HOPE potential is typically 25% greater than the EFW potential, with a median difference of 17% over the mission.

It should also be noted that the uncertainty of the spacecraft potential measurement by EFW is on the order of several Volts when the probes provide a stable reference to plasma potential at infinity and when spacecraft potential is less than +/-200 V. The 200 V limitation is from the EFW sensor power supply limits. Further, spacecraft potential may extend over larger distances than the 50 meter boom length; consequently, the booms may not measure the full value of the spacecraft potential. The limits on this error are based on spacecraft potential measured by the shorter 7 meter boom on the axis plane and scaled to the measured value from the 50 m booms.

In order to obtain the best possible depiction of spacecraft charging, it is necessary to use both methods. The extraction of the charging line in the HOPE instrument ion spectra is not a stand alone method, and it is best used by identifying periods of charging and comparing directly with EFW. However, EFW has been shown to underestimate spacecraft potential, saturate at -200 V of charging, and is unable to make spacecraft potential measurements during eclipse. So for certain events where there is extreme charging, using the charging line extraction technique from the HOPE instrument H^+ spectra is necessary. Coupled together, we can get a good picture of the degree of charging and when it is occurring.

3.4 Connection Between keV Electron Energy Fluxes and Charging

Previous studies have shown a connection between keV electron energy fluxes and spacecraft surface charging. These studies found that severe charging events all had keV electron energy flux levels above a certain threshold (*Reagan et al.*, 1981; *Olsen*, 1983; *Thomsen et al.*, 2013). Here we repeat this study with the Van Allen Probes. Both EFW and HOPE spacecraft negative potential measurements were compared with HOPE electron energy flux measurements from February 2013 to April 2015. The data sets were averaged over 1 minute intervals, and we examined times when both EFW and HOPE spacecraft potential measurements were present.

Figure 3.7 shows the magnitude of negative charging measured by EFW and extracted HOPE instrument ion spectra compared to the HOPE energy fluxes at 30 eV, 50 eV, 300 eV, 500 eV, 3 keV, 5 keV, 30 keV, and 50 keV energies. The orange points are the EFW spacecraft potential measurements, which saturate at 200 V. The red points are the HOPE instrument ion charging line extracted results above 10 V of negative surface charging over the same time period. Charging derived using the HOPE spectra reaches 1000 V at times.

Previous studies employed a similar method and found a distinct cutoff where a certain threshold of keV electron energy fluxes was required for large negative charging (*Reagan et al.*, 1981; *Olsen*, 1983; *Thomsen et al.*, 2013). In both the EFW and the HOPE data, we see such a threshold in keV electron energy flux. This cut off also occurs for lower energy fluxes, extending from 1 eV to 5 keV. We define a threshold at 3×10^7 keV cm^{-2} s^{-1} sr^{-1} keV^{-1} in the 3 keV energy channel. Charging occurred at all electron energy flux levels between 10^6 and 10^9 keV cm^{-2} s^{-1} sr^{-1} keV^{-1}

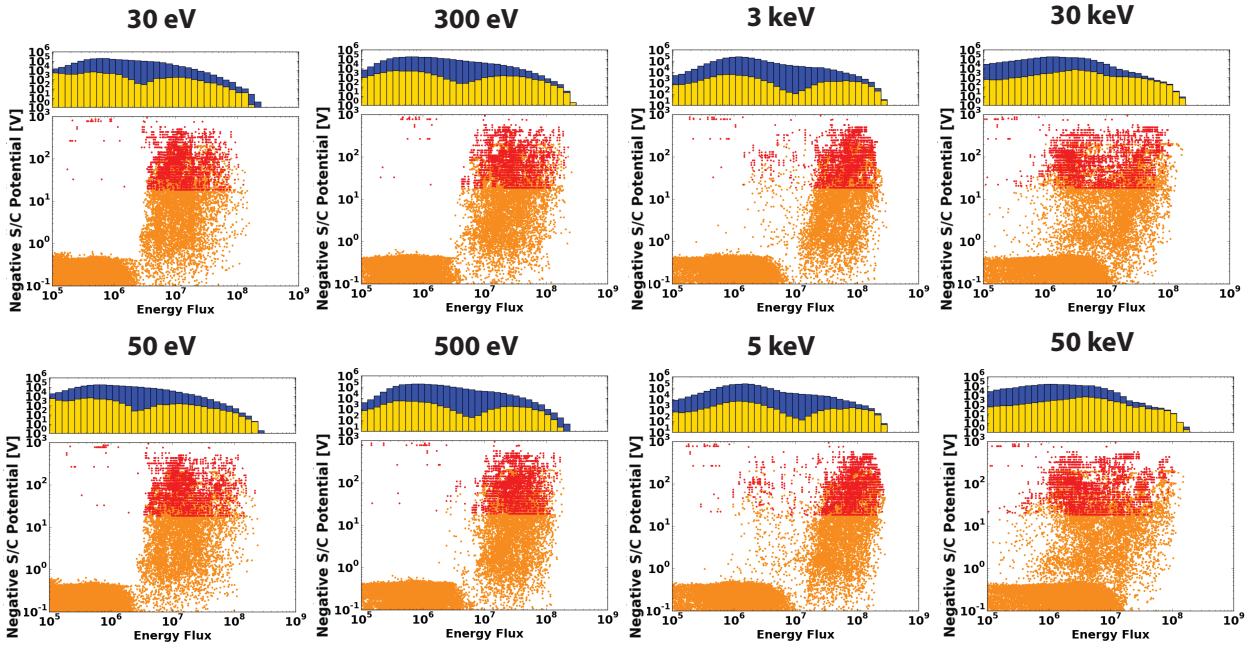

Figure 3.7: The negative spacecraft potential measured by EFW (orange) and HOPE (red) as a function of the electron energy flux (keV cm^{-2} s^{-1} sr^{-1} keV^{-1}) measured by the HOPE instrument. All times of negative charging from both Van Allen Probes from February 2013 to April 2015 are included. The top panels show occurrence histograms of electron energy flux measurements throughout the mission (blue) and negative charging times (yellow).

for all electron energy channels measured by the HOPE instrument. The results in Figure 3.7 confirm that there is a keV electron energy flux threshold that must be satisfied for the most intense negative spacecraft charging to occur and this threshold also occurs in < 5 keV energy channels. It should be noted that there are a few occurrences of spacecraft charging during low keV electron energy fluxes.

3.5 Spacecraft Charging versus Other Parameters

We examined the relationship between spacecraft charging and magnetospheric conditions, including electron temperature, electron pressure, electron density, and low energy ion density. According to other studies, once the electron keV threshold flux at the spacecraft has been met, the overall electron temperature then determined the intensity of surface charging (*Thomsen et al.*, 2013). We averaged all data to a 1-minute cadence, and included only measurements from February to June 2013, where the majority of intense charging events occurred, as can be seen in Figure 3.1. The electron pressure, electron density, and electron parallel and perpendicular temperatures were calculated over the 200 eV to 50 keV range; it is important to note that these parameters were not corrected for spacecraft potential and are partial moments of the quantities they represent. During significant charging, these quantities are less accurate, which adds uncertainty to our following examination of the quantities in regards to charging. The low energy ion density was calculated between 1-210 eV from Chapter 2,

$$n_{H^+} = \sum_i 4\pi \frac{1}{\sqrt{\frac{2E_i}{m_{H^+}}}} F_{H^+} \Delta E_i \tag{3.1}$$

where F_{H^+} is the H^+ differential energy flux (keV cm^{-2} s^{-1} sr^{-1} keV^{-1}). E_i is the measured energy of each energy channel of the HOPE instrument data, begin-

ning with the 1 eV energy channel and ending with the approximately 210 eV energy channel. ΔE_i represents the range of each energy channel. The m_{H^+} and n_{H^+} notations are the H^+ mass and number density. The i in this summation represents the energy channels between 1 eV and 210 eV. We did account for spacecraft potential in the calculation of these partial densities, adjusting flux energy appropriately. During times of more than 200 V of negative charging, the low energy ion density should be approximately 0 due to the acceleration of the ions, so some caution should be taken in the interpretation of the low energy ion density results.

Figure 3.8 examines spacecraft charging as a function of combinations of these variables. We only use EFW data here because we wanted to include times with little or no spacecraft charging (above -10 V), which the HOPE algorithm can not detect. The color of each point represents the degree of spacecraft charging during the measurement, with gold indicating -25 V or lower potential, magenta <-1 V, and blue >-1 V. Figure 3.8A shows the hot (> 200 eV) HOPE partial electron density compared with electron pressure. Times of spacecraft charging tended to occur with electron number densities above 1 cm^{-3} and electron pressure above 0.1 nPa. However, high electron densities and electron pressure do not necessarily indicate that there will be negative spacecraft charging, as there are many non-charging times that have the same density and pressure.

Figure 3.8B shows L and electron temperature. We see that times of spacecraft charging tended to occur above L = 5 and with electron temperatures above 4×10^7 K, or 3.45 keV. However, once again, high L and high electron temperature do not necessarily mean there will be charging. Figure 3.8C displays MLT and the spacecraft potential corrected low-energy ion density using the HOPE instrument protons between 1-210 eV. The method we used to describe spacecraft potential correction in

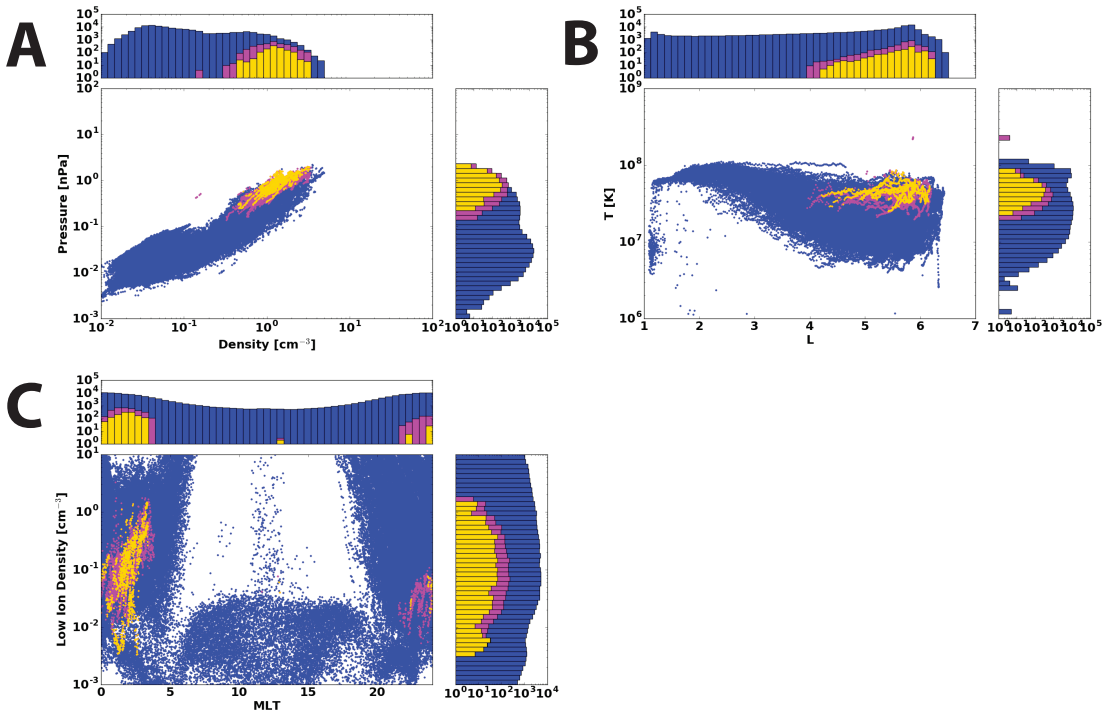

Figure 3.8: Resampled EFW spacecraft potential values, the HOPE instrument electron temperature (T_e), electron density (n_e), spacecraft potential corrected low energy ion density (n_i), electron pressure (p_e), and the ephemeris MLT and L parameters from February 2013 to June 2013. A shows n_e compared to p_e. B is L compared to T_e. C shows low energy ion density compared to MLT. The gold represents charging less than -25 V, the magenta represents charging less than -1 V, and blue represents charging above -1 V. The side panels represent the number of points contained within each interval.

the low energy ion densities can be found in Chapter 4. We see that the most intense charging events involved extremely low-energy ion densities, which is what we would expect because the ions are accelerated. As noted before, some caution must be taken in using this result, however, since charging accelerated low energy-ions to higher energies and make it 'appear' like there was no low-energy ion population. Most intense and moderate charging events occurred in the post-midnight sector between $0 <$ MLT < 5, with a few events also occurring in the pre-midnight sector.

Figure 3.8 demonstrates that electron pressure is more of a controlling factor in intense charging events than any of the other variables. Since pressure is constructed from electron temperature and density ($p_e = n_e k_B T_e$, where k_B is Boltzmann's constant), we can state that in addition to high electron temperatures, high electron densities must be present in order to have surface charging on the Van Allen Probes. This is expected since once a certain threshold current from the electron density on the spacecraft is reached, photoelectron emission current is superseded as the dominant current on the spacecraft surface and the potential runs negative. The amount of negative spacecraft charge is determined by the potential necessary to drive the electron fluxes away from the spacecraft body and restore current balance. The potential is comparable to the electron temperature, so it makes sense that high pressure is a controlling factor in intense charging events. However, high electron densities and temperatures do not necessarily result in negative charging. Also, more intense charging events were related to higher electron pressure, suggesting that pressure may be a controlling factor in the intensity of a charging event, perhaps more than temperature.

Figure 3.9 shows the same variables described above at times when the 3 keV electron energy flux is above 3×10^7 keV cm^{-2} s^{-1} sr^{-1} keV^{-1}. Identical to Figure 3.8, gold is $<$ -25 V, magenta is $<$ -1 V and blue is all other times from February 2013 to

June 2013. We find similar results as Figure 3.8, where electron pressure in panel A seems to be the largest controlling factor in determining if an event will charge negatively. Once again, however, the satellite can measure high electron pressure and high keV electron fluxes, but not show any indication of spacecraft charging in the EFW data set. Most notable about Figure 3.9 is that by excluding times where the electron energy flux is below 3×10^7 keV cm^{-2} s^{-1} sr^{-1} keV^{-1}, many of the non-charging blue points are removed from these plots. Thus, once electron keV energy flux is high, then charging may occur depending on additional unknown circumstances.

The case study shown in Figure 3.10 highlights the relationship between electron density, electron pressure, and temperature with spacecraft potential. We see in the first charging event at 4:00 UT through 7:00 UT on February 14, 2013 on Van Allen Probes A that there was very high density and pressure along with steadily increasing electron temperature during this period. There was a dip in electron pressure at 5:30 UT corresponding with a spacecraft potential drop again to approximately 0 V. Another rise in spacecraft potential occurred at 6:00 UT as electron pressure rose again.

The second spacecraft charging event in Figure 3.10 occurred at 13:30 UT as temperature suddenly spiked in conjunction with a rapid rise in electron density. These three parameters then slowly decreased over the next hour, restoring spacecraft potential to approximately 0 V. In the afternoon, between 16:00 UT and 21:00 UT, we see that electron temperatures were very high, but the electron pressure remained low because the electron density was low. There was no significant charging during this later interval. The magnitude of electron temperature, number density, and pressure does not determine the intensity of the spacecraft charging event.

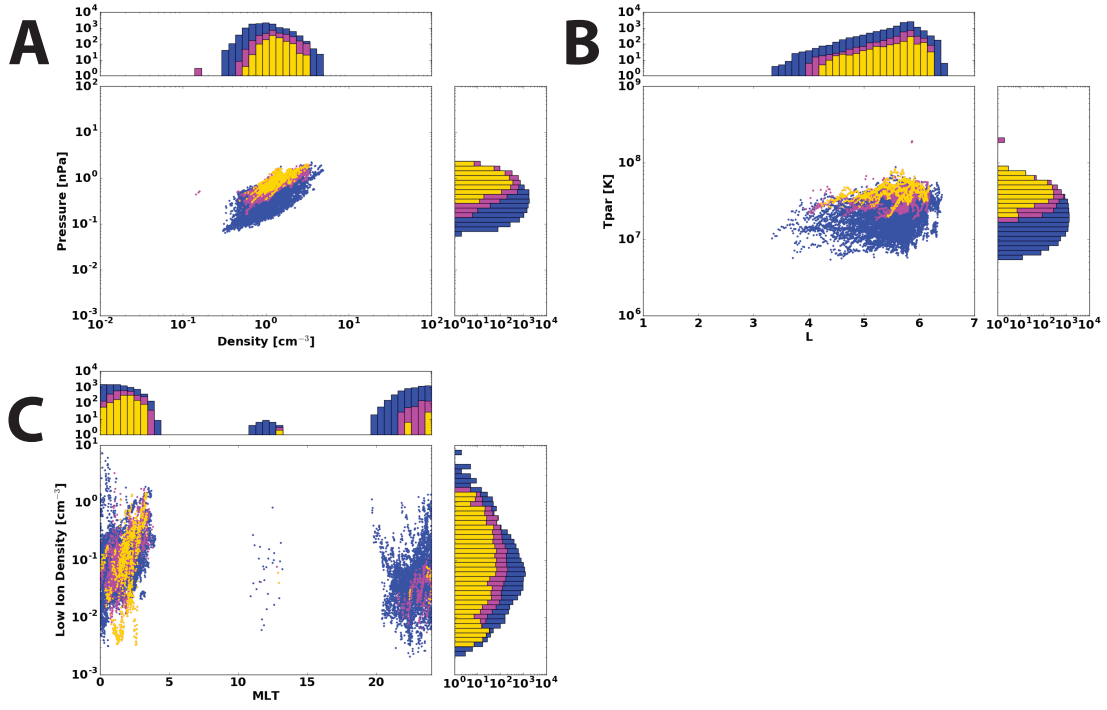

Figure 3.9: Resampled EFW spacecraft potential values, the HOPE instrument electron temperature (T_e), electron density (n_e), spacecraft potential corrected low energy ion density (n_i), electron pressure (p_e), and the ephemeris MLT and L parameters from February 2013 to June 2013 at times where the 3 keV electron energy flux is above 3×10^7 keV cm^{-2} s^{-1} sr^{-1} keV^{-1}. A shows n_e compared to p_e. B is L compared to T_e. C shows low energy ion density compared to MLT. The gold represents charging less than -25 V, the magenta represents charging less than -1 V, and blue represents charging above -1 V. The side panels represent the number of points contained within each interval.

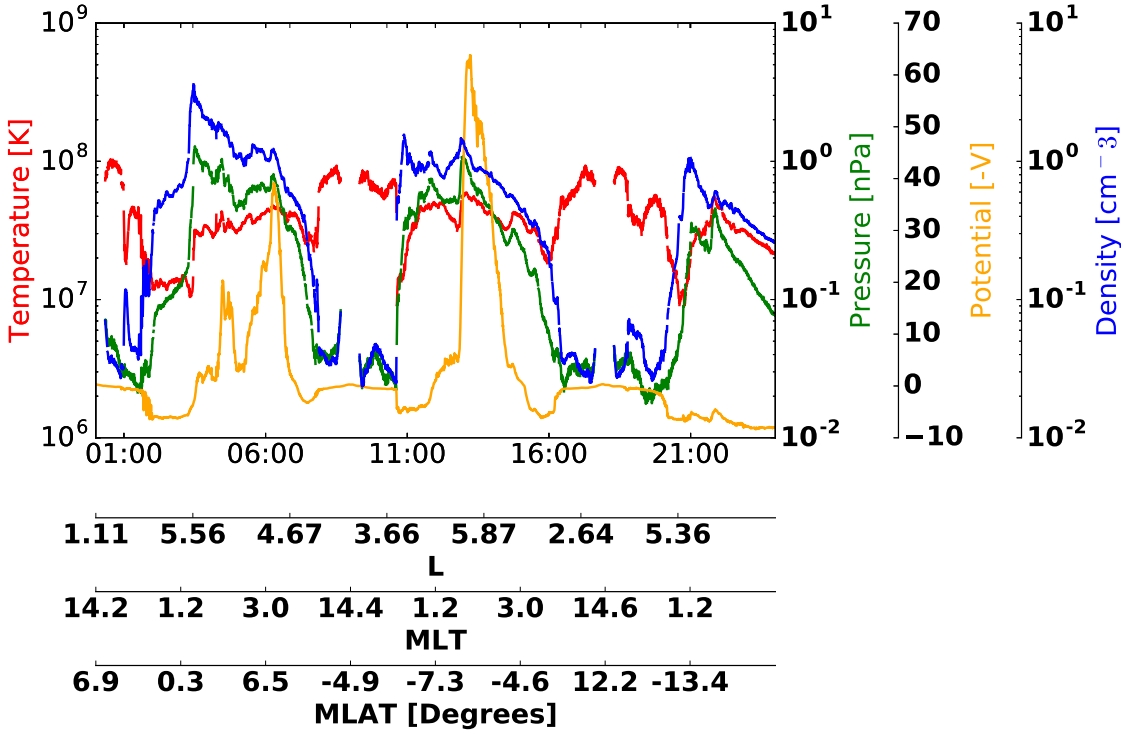

Figure 3.10: An example of negative spacecraft potential (orange) from EFW connected to the HOPE instrument electron temperature (red), electron pressure (green), and 30 eV and above electron number density (blue) on February 14, 2013 from Van Allen Probes A. The satellite was not in eclipse on this day.

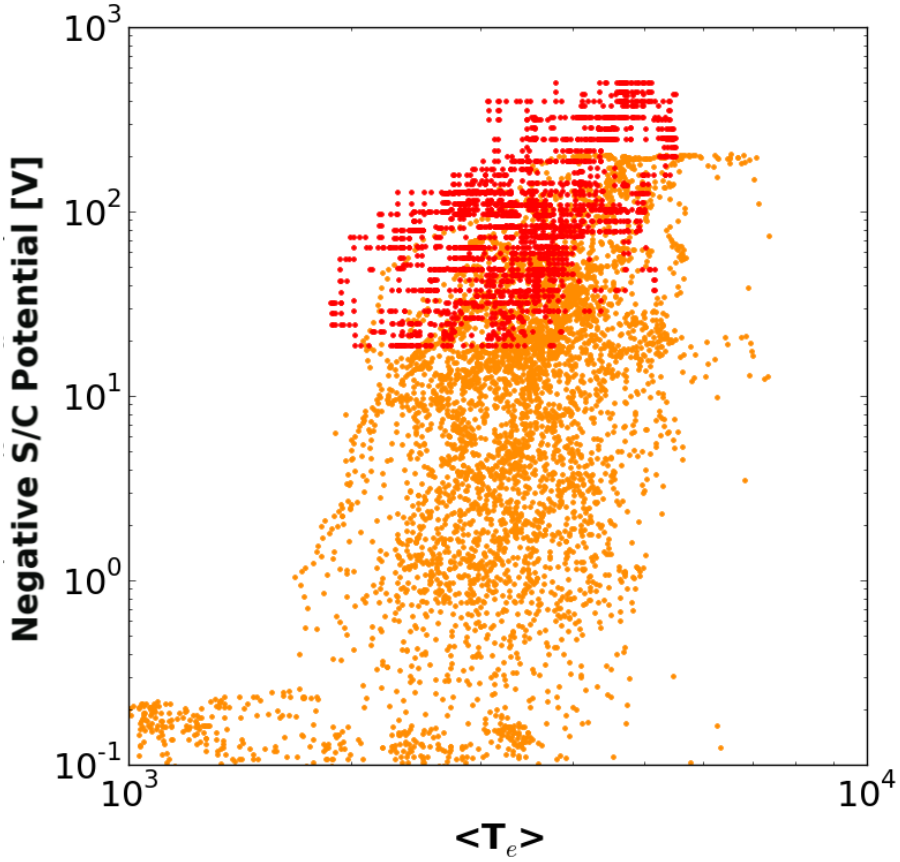

Figure 3.11: Van Allen Probes satellite A average electron temperatures compared to EFW (orange) and HOPE (red) negative spacecraft potentials from February 2013 to June 2013. Average electron temperature is in eV.

Figure 3.11 shows Van Allen Probes A average electron temperature compared to the negative spacecraft potential from EFW and HOPE between February 2013 to June 2013. Average temperature is calculated using an approximation from (*Thomsen et al.*, 2013):

$$< T_e >= \frac{(n_i \times 5) + (n_e T_e)}{n_i + n_e} \tag{3.2}$$

where $< T_e >$ is the average electron temperature, n_i is the low energy ion density from 1-200 eV, n_e is the hot electron density calculated from HOPE differential number electron fluxes above 200 eV, and T_e is the hot electron temperature in eV above 200 eV. The approximation is used because there is backscatter contamination in the low energy electrons, so assuming quasi-neutrality, the measured low energy ion density serves as a more reliable electron density measurement. The factor of 5 is an approximation for the low energy ion temperature of 5 eV. *Thomsen et al.* (2013) had found $< T_e >$ determined the intensity of the spacecraft potential. We do not find a strong or as clear a result here; however we do see that spacecraft potential tends to rise with increasing temperature above a threshold average electron temperature of 2000 K.

Another factor to consider is the thermal electron current compared to the photoemission current. Negative spacecraft charging occurs when the magnitude of the thermal electron currents generated from elevated high energy electron fluxes exceed the photoemission current. Figure 3.12 shows the thermal electron current versus electron pressure and a case study of Van Allen Probes A thermal electron current compared to spacecraft charging on February 8, 2013. Thermal electron current is calculated as:

$$I_{therm} = \beta n \sqrt{T_e} \tag{3.3}$$

where β is a constant of 0.094 that emerges from unit conversion, n is the electron number density above 200 eV in cm^{-3}, and T_e is the electron temperature. The number density and electron temperature were calculated from electron differential number fluxes above 200 eV. Figure 3.12 A shows a statistical study of thermal electron current. Higher thermal electron currents are associated with more intense negative charging, but high thermal electron currents also occur during times of no spacecraft charging. Figure 3.12 shows the thermal electron current from the same day as in Figure 3.10. The highest thermal electron current occurs during the first and less intense charging event on February 14, 2013. However, the thermal electron currents are still high in the second and more intense event. When the position of insulators on the spacecraft is taken into consideration, the thermal electron current difference between the conducting portion of the spacecraft and insulated portions may cause the satellite to charge more negatively at some times (*Davis et al.*, 2012).

3.6 Conclusions

In Chapter 3, spacecraft charging on a conducting spacecraft within geosynchronous orbit was explored. Unlike previous non-conducting satellite missions, spacecraft charging on the conducting Van Allen Probes was not as intense. The Van Allen Probes tended to charge slightly positive; however, times of significant negative charging still occurred in the time period we examined.

We explored statistics based on the distribution of spacecraft charging measured by EFW and its relationship with MLT and L. It was found that most slightly nega-

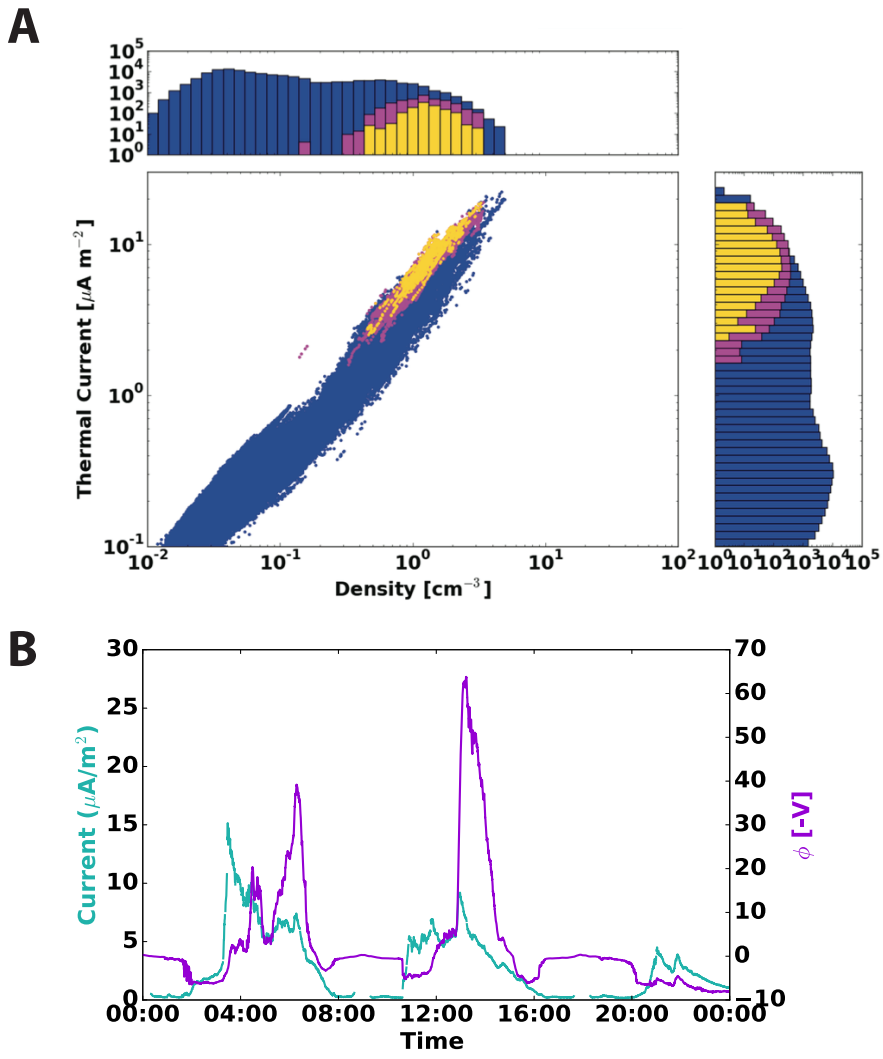

Figure 3.12: A shows the calculated spacecraft thermal electron current (μA m^{-2}) compared to electron pressure from February 2013 to June 2013. The gold represents charging less than -25 V, the magenta represents charging less than -1 V, and blue represents charging above -1 V. The side panels represent the number of points contained within each interval. B shows a case study from Van Allen Probes A of thermal electron current (aqua) compared with negative spacecraft potential (purple), on February 14, 2013. The satellite was not in eclipse on this day.

tive charging occurred at low Ls, at daytime MLTs, and in Earth's shadow. Positive charging occurred at all Ls and MLTs. Strong positive charging occurred across the night-side at high Ls, while strong negative charging occurred primarily at high Ls in the post-midnight sector. This strong negative charging above L > 3 occurred while the spacecraft was not in eclipse. We think the strong positive charging is due to bad data; however, we do not have an explanation of why it is mostly centered around midnight and in the pre-midnight sector.

To obtain spacecraft charging values below the -200 V limit of EFW, we also developed an algorithm to determine the level of spacecraft charging by extracting the charging line seen in the HOPE instrument H^+ spectra. From this technique, we found that EFW underestimated spacecraft charging by approximately 5 V or 17 %. During times when the spacecraft charge reached below -50 V, the two methods provided very similar measurements. However, the charging line extraction method was not a stand alone method, so we concluded that it was best to use both the EFW spacecraft potential measurements and the charging line extraction method to obtain the best understanding of spacecraft charging in the Van Allen Probes.

The connection between keV electron energy fluxes and spacecraft charging was presented in this study. Similar to previous results, we found that for the Van Allen Probes there was a connection between spacecraft charging and keV electron energy fluxes. The connection between high energy fluxes during charging times extended from 1 eV to 5 keV. This study did find an electron energy flux threshold of 3×10^7 keV cm^{-2} s^{-1} sr^{-1} keV^{-1} for 3 keV electrons where intense charging is more likely to occur if this threshold is met; however, there are times the electron energy fluxes reach this threshold and significant negative spacecraft charging does not occur.

Spacecraft charging was compared with electron temperature, pressure, electron density, low energy (1-210 eV) H^+ density, MLT, and L. In times of charging on the Van Allen Probes, electron temperature, electron density, and, consequently, electron pressure were all generally elevated during times of significant charging. The strongest connection was between electron pressure and spacecraft charging. However, high electron pressure did not always correlate with times of negative spacecraft charging, so further exploration of this connection is necessary. *Thomsen et al.* (2013) had found that the intensity of a spacecraft charging event was determined by average electron temperature, but we did not find as strong of a relationship in our study with the Van Allen Probes.

Our results built upon previous work, and we have shown for a conducting spacecraft that there is a keV electron energy flux threshold that once surpassed, increases the likelihood of charging to occur. Future work is necessary to determine exactly what combination of parameters results in intense negative charging on the Van Allen Probes or another similar conducting spacecraft. The extreme care to maximize conductivity on the Van Allen Probes has resulted in a spacecraft that charged negatively infrequently, allowing for low energy ion measurement with greater certainty and reduced arcing potential on the Van Allen Probes.

CHAPTER IV

HOPE Pitch Angle Analysis

4.1 Introduction

The plasmasphere is a region of cold dense plasma with an average energy of 1 eV that co-rotates with Earth (e.g., *Chappell*, 1972). The plasmasphere plays a critical role in inner magnetospheric physics, particularly in modulating wave activity (e.g., *Thorne et al.*, 1973; *Kozyra et al.*, 1984; *Bortnik et al.*, 2008). Changes in plasmaspheric density and composition can lead to changes in the global magnetospheric system. For example, density gradients may change plasmapause location or ion concentrations can disrupt electromagnetic ion cyclotron (EMIC) wave propagation (e.g., *Larsen et al.*, 2007; *Saikin et al.*, 2015).

The high energy tail (1-10 eV) of the inner plasmasphere (L-Shell < 3) ion population exhibits strong local time variation with a minimum in the post-midnight sector (*Lennartsson and Reasoner*, 1978; *Sarno-Smith et al.*, 2015). Although we show the depletion as a partial density loss, it is also likely a temperature effect where the suprathermal tail of the plasmasphere cools in the post-midnight sector. However, without full density or temperature resolution, we are unable to conclude if the depletion is from temperature, density, or combination of both. A previous study suggested that the 1-10 eV plasmasphere depletion might be linked to iono-

spheric outflow in Chapter 2. Here, ionospheric outflow refers to the heating of the topside ionosphere and subsequent transport of plasma to the plasmasphere along flux tubes. Topside ionosphere studies have shown post-midnight sector plasma enhancements from downward flow from the plasmasphere, which suggests that this 1-10 eV ion population flows downward along field lines and charge exchanges in the topside ionosphere (*Pavlov and Pavlova*, 2005). However, the mechanisms leading to the absence of plasma between $2 < L < 3$ remain unresolved.

To further explore the post-midnight depletion of the 1-10 eV ions of the inner plasmasphere, pitch-angle distributions of the suprathermal tail (1-10 eV) inner plasmasphere population are analyzed using the Van Allen Probes. Launched in late 2012, the Van Allen Probes are a pair of near equatorial satellites that orbit within geosynchronous orbit (*Mauk et al.*, 2014). The Helium Oxygen Proton Electron (HOPE) instrument onboard these satellites is a mass spectrometer that measures of H^+, He^+, and O^+ populations of the equatorial inner magnetosphere between 1 eV and 50 keV (*Funsten et al.*, 2014).

The purpose of this study is to determine the cause of the post-midnight sector near-Earth ion depletion and examine the pitch-angle distributions of the HOPE H^+ 1-10 eV plasma. In this study, pitch-angle distributions are calculated over discrete time windows in the HOPE 1-10 eV ion data to determine when ion fluxes are depleting. A pitch angle conveys the motion of an ion or electron on a magnetic field line. Particles with low pitch angles travel further along the field line than 'trapped' particles with high pitch angles, as shown in Figure 4.1. A new algorithm is developed to sort pitch-angle distributions over a 26 month period. If the depletion is from charge exchange in the top side ionosphere, we expect to see strong field aligned 1-10 eV ion flows across the dayside, particularly at dawn, and a residual equatorially

mirroring population that lingers across the night side. For the first time, the results of this study demonstrate that the near 90^o pitch-angle 1-10 eV ion population shows a strong depletion in the post-midnight sector while the H^+ ions at pitch-angles near 0^o and 180^o remain nearly constant. This suggests a steady but weak outward flow from the ionosphere across the nightside. This behavior suggests that physical processes other than charge exchange and ionospheric influence may be involved in the depletion of the post-midnight sector H^+ 1-10 eV ions. The ion depletion may also be the result of a temperature effect, where the 1-10 eV ions are cooled across the post-midnight sector and thus invisible to HOPE. This new data set thus allows a detailed examination of the diurnal behavior of the inner plasmasphere.

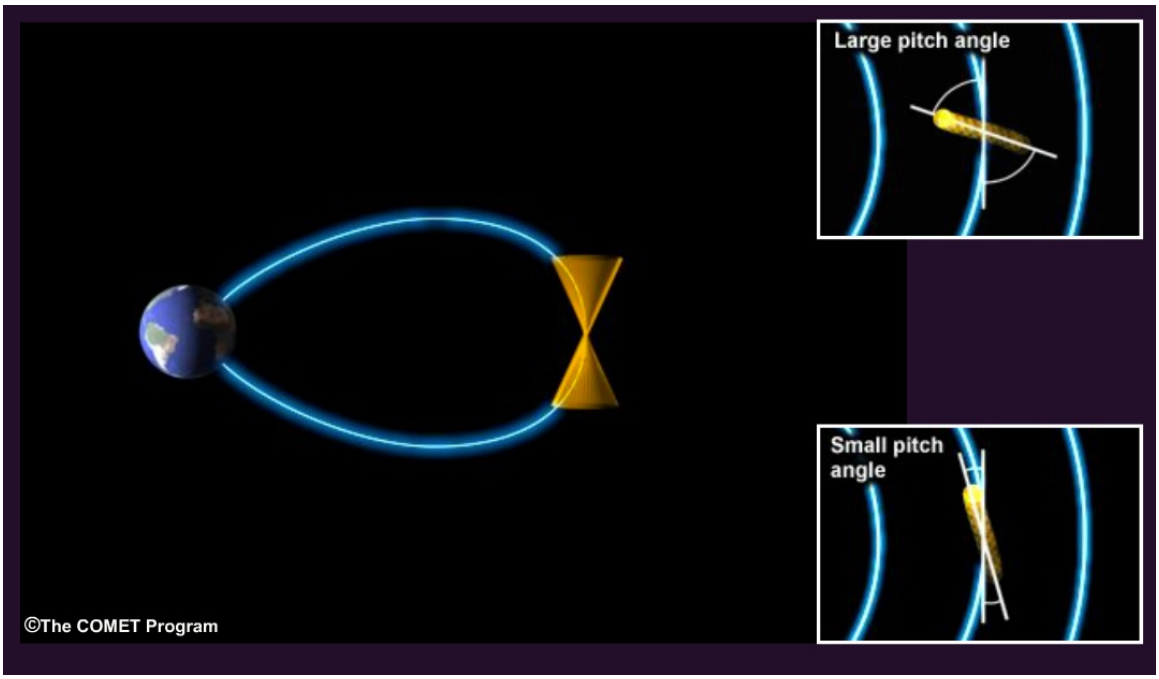

Figure 4.1: Large pitch angles (around 90^o) remain locally trapped whereas particles with low pitch angles (close to 0 or 180^o) travel further along Earth's magnetic field line and can be scattered into the loss cone. This figure is reproduced from http://ffden-2.phys.uaf.edu/.

4.2 Methodology

This study explores the HOPE pitch-angle dependence as a function of MLT and L-Shell during quiet times. To do so, 26 months of HOPE H^+ data from February 2013 to April 2015 were sorted by 0.25 L-Shell and 0.5 MLT bins for each energy channel measured by HOPE between 1-10 eV. This time frame encompassed a full precession of the Van Allen Probes satellites. Only times with Kp less than 3 were examined. The polar-angle resolution on the HOPE instrument is 18 degrees full width and the azimuthal angle is 4.5 degrees full width half maximum, which allowed for resolution of the loss cone at approximately L = 2, where the loss cone is approximately 16 degrees, but not at L = 3, where the loss cone is approximately 8.4 degrees. HOPE data are routinely binned into 11 pitch-angle bins, with centers between 4.5-175.5 degrees. pitch-angle bins are 18 degrees wide, except for 9 degree bins centered at 4.5 and 175.5 degrees. In every spin period of approximately 11 seconds, HOPE differential number flux values were calculated and assigned a pitch-angle designation based on the magnetic field direction as measured by the Electric and Magnetic Field Instrument Suite and Integrated Science (*Kletzing et al.*, 2013).

Plasmapause location varies with activity level and time. In particular, the plasmasphere erodes during geomagnetic storms and the plasmapause can be within L < 2 during times of high convection (*Spasojević et al.*, 2003). However, plasmapause location variability should not significantly affect the results of our statistical study over 2013-2015, which were remarkable years in their absence of storms. In 2013, there are only two storms, March 17, 2013 and June 1, 2013, that are notable and capable of pushing the plasmpause to L < 3. In 2014, there are no significant storms, and in the first part of 2015 (till April), there is only the March 17, 2015 storm. For these dates, we should be concerned about plasmapause location leading to unnaturally low plasma densities between $2 <$ L < 3. However, three days is statistically

insignificant in the context of our larger study of > 600 days. We also have approximately 6 months of dwell time in the post-midnight sector between $2 < L < 3$ for our study.

Figure 4.2 shows the 1.5 eV, 3.0 eV, and 5.3 eV H^+ spacecraft potential corrected average differential number fluxes as a function of pitch-angle and MLT over 26 months at L = 2 (L-Shell and MLT bins are labelled by the lower bound of the bin). HOPE differential number fluxes were corrected for spacecraft potential by using the Electric Field and Waves instrument (EFW) spacecraft potential measurements (*Wygant et al.*, 2014). Both the EFW and HOPE measurements were resampled into 1 minute intervals, and the median spacecraft potential in volts for each interval was added to the energy of each of the 1-10 eV energy channels. The 'new' energy channels and fluxes were then logarithmically interpolated to give flux values at the original HOPE energy channels. Here, logarithmically interpolated means the fluxes were appropriately weighted by the location of the nearest energy channels in log space to the spacecraft potential corrected energy. For example, if there is +0.5 V of spacecraft charge, the HOPE 1.2 eV energy channel actually measures 1.7 eV particles. To calculate the 1.8 eV H^+ fluxes, we logarithmically interpolated the fluxes between the spacecraft potential added energy channels of 1.7 eV and 2.0 eV. We kept only energy channels in the 1-10 eV energy range, even after accounting for spacecraft charge.

Although our study encompasses the 1-10 eV H^+ population, Figure 4.2 highlights three energy channels which reflect the general behavior of the 1-10 eV HOPE energy range. The plot on the left shows the median differential number flux at all MLTs, including a large plasma depletion in the post-midnight sector between $1 < MLT < 4$ in the each of the energy channels. In the post-midnight sector, there was an absence of particles with pitch-angles around 90^o. However, the pitch-angles in the loss cone

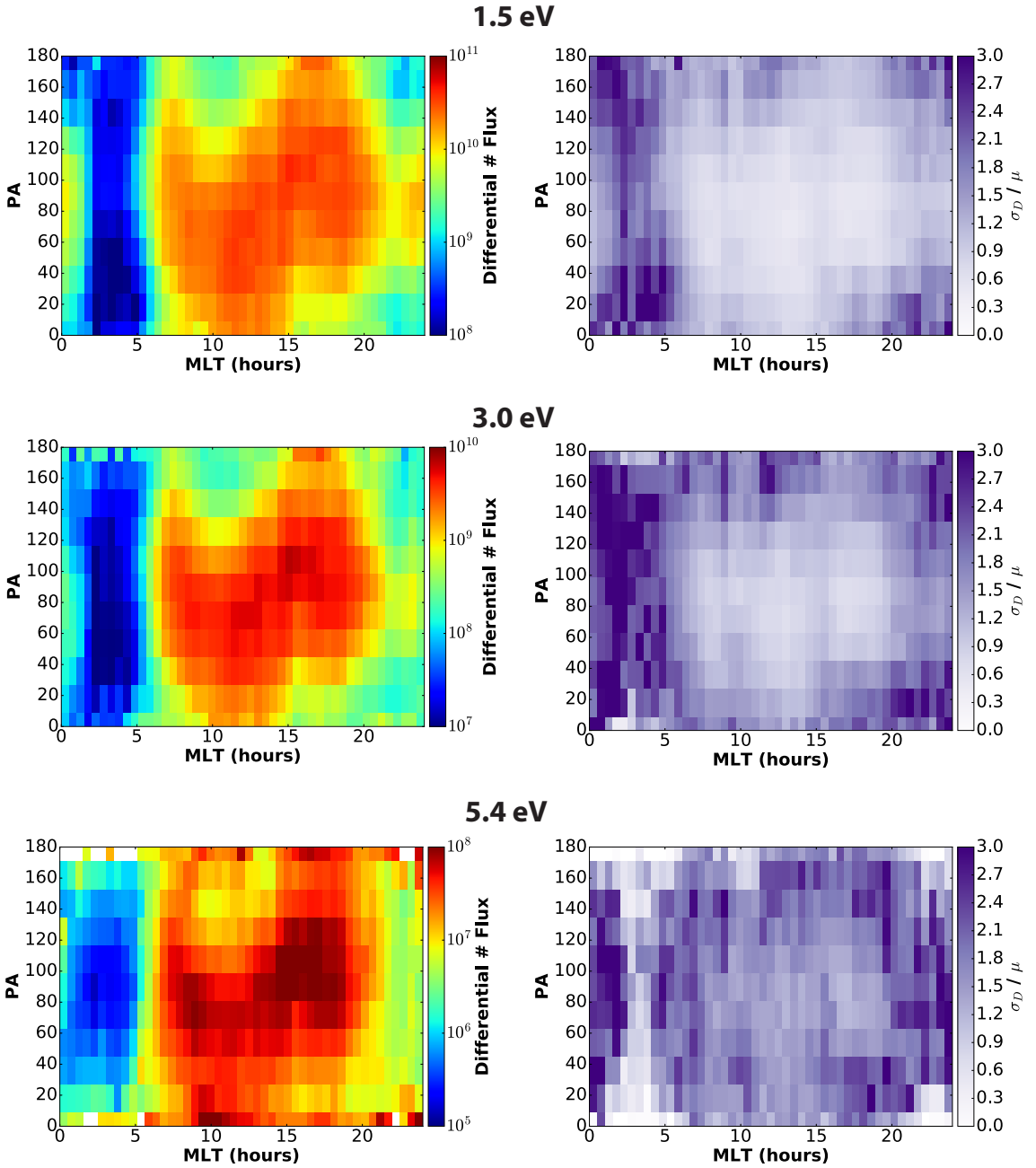

Figure 4.2: Median measured proton differential number fluxes ($cm^{-2}\ s^{-1}\ sr^{-1}\ keV^{-1}$) for 26 months of the HOPE instrument binned by pitch-angle and MLT for the 1.5 eV, 3.0 eV, and 5.3 eV energy channels at L = 2. The plots on the right are the relative variability, which is the standard deviation (σ_D) divided by the mean (μ) of each MLT-PA bin at L = 2 for the 1.5 eV, 3.0 eV, and 5.3 eV energy channels.

show less depletion than the PA=90^o fluxes in the post-midnight sector, particularly at 3.0 and 5.3 eV. This implies that the ionosphere is still acting as a weak source of low energy plasma to the inner plasmasphere in the post-midnight sector, but it remains unclear what causes the significant equatorially mirroring population depletion in this region. Also, in the 1.5 eV and 3.0 eV energy channels, the fluxes significantly change from a peak in the near PA = 90^o population at MLT=0 to MLT=1.5 to a minimum or near-isotropic distribution in the near PA = 90^o population at MLT=2.5.

The plots in the right column of Figure 4.2 show the relative variability, or the standard deviation (σ_D) divided by the mean (μ). For 1.5 eV and 3.0 eV, the relative variability is higher in the post-midnight sector, especially at pitch-angles near 0^o and 180^o. Relative variability is lowest at MLT = 6 to 20 at near PA = 90^o. We expect the post-midnight sector to have more variability for several reasons. For example, the areas of space our bins cover are very large. In the post-midnight sector, some plasma within each bin may not be affected by the mechanisms leading to the depletion of plasma in the post-midnight sector. Thus, there are fluxes with order of magnitude or greater differences contained within each bin, leading to a much higher standard deviation. Interestingly, the relative variability in the post-midnight sector is lowest across all MLTs for the 5.3 eV channel. There are fewer measurements in this energy channel at pitch-angles close to 0^o and 180^o, which may contribute to the lower variability. Outside the post-midnight sector, variability is higher at all MLTs compared to the 1.5 and 3.0 eV energy channels.The results of Chapter 2 also showed similar variability differences at different MLTs but showed in Figure 7 that although the post-midnight sector had higher relative variability, the bulk of the post-midnight sector 1-10 eV fluxes were still significantly below (greater than an order of magnitude) the 1-10 eV fluxes outside the post-midnight sector.

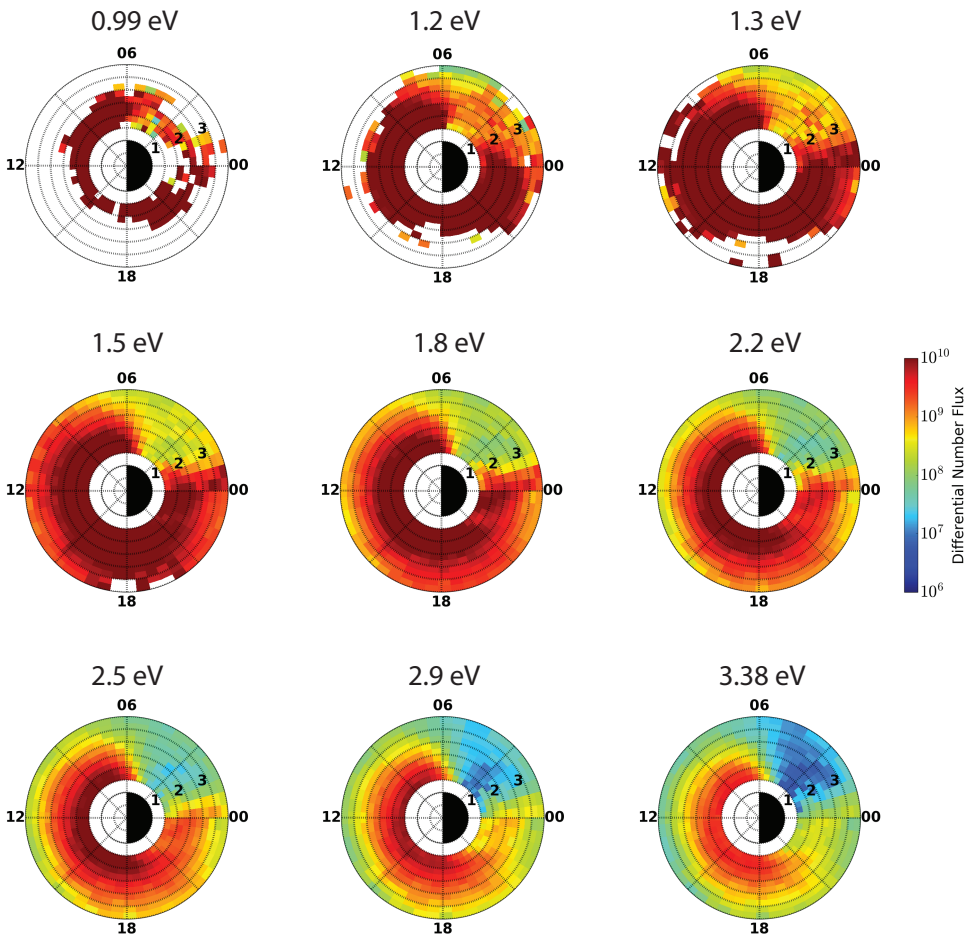

Figure 4.3: Median measured proton differential number fluxes ($cm^{-2}\ s^{-1}\ sr^{-1}\ keV^{-1}$) for 26 months of combined HOPE instrument data binned by L-Shell and MLT for all of the HOPE energy channels between 0.99 eV and 3.38 eV.

Figure 4.3 shows the spacecraft potential corrected fluxes for the 1-10 eV H^+ population binned by L-Shell and MLT from February 2013 to April 2015. The occurrence of the 0.99 eV fluxes is sparse but approximately uniform across all MLTs at L of 2 to 2.5. By 1.5 eV, the occurrence of the 1.5 eV fluxes extends to all L-Shells between 1.5 and 4. The low plasma fluxes in the post-midnight sector are seen in all energies between 1-10 eV, although we only show 0.99 to 3.38 eV here.

Figure 4.4 shows the 1.5 eV, 3.0 eV, and 5.3 eV H^+ median spacecraft potential corrected average differential number fluxes and the relative variability at PA = 90^o

binned by L-Shell and MLT for Kp < 1 and Kp < 3 between February 2013 and April 2015. Activity level does have an impact on the behavior of the 1-10 eV ions, and the difference between the post-midnight sector H^+ differential number fluxes and dayside fluxes is smaller at Kp < 1. Differential number fluxes are higher for the Kp < 1 fluxes, especially for the 1.5 eV and 3.0 eV energy channels within L = 3. The relative variability is highest in the post-midnight sector for both activity level designations. We expect the plasmasphere to be sensitive to geomagnetic activity due to erosion and enhanced convection (*Carpenter*, 1967; *Taylor et al.*, 1970; *Horwitz et al.*, 1990; *Katus et al.*, 2015). However, the general behavior is similar, and we continue to proceed with the designation of Kp < 3 as a definition for quiet time behavior because the distributions are smoother with the increased number of data points.

To better quantify the depletion of the near PA = 90^o population, the 26 months of HOPE pitch-angle distributions were classified by their shape. pitch-angles range from 0 to 180 degrees, where 90^o is a locally mirroring population and 0/180 are field aligned/anti-field aligned particle populations. To ensure a statistically significant number of counts in each bin, the counts of ten consecutive approximately 11 second HOPE measurements, which is approximately 10 spacecraft spins, were summed. However, since the HOPE instrument alternates between measuring ion and electrons, this summing occurred over a 220 second period. The median spacecraft potential over this same period was also used to correct the fluxes for spacecraft potential with the same procedure used in Figures 4.2 and 4.3. This time window was chosen to provide sufficient counts while limiting spacecraft motion to no more than 0.125 L-Shells at L < 3. Times where HOPE was in perigee mode, where HOPE measures only energies above 26 eV due to high O^+ densities, were excluded. The pitch-angle distributions are determined for each energy channel separately without taking into account the pitch-angle distribution classification of other energy channels. This bin-

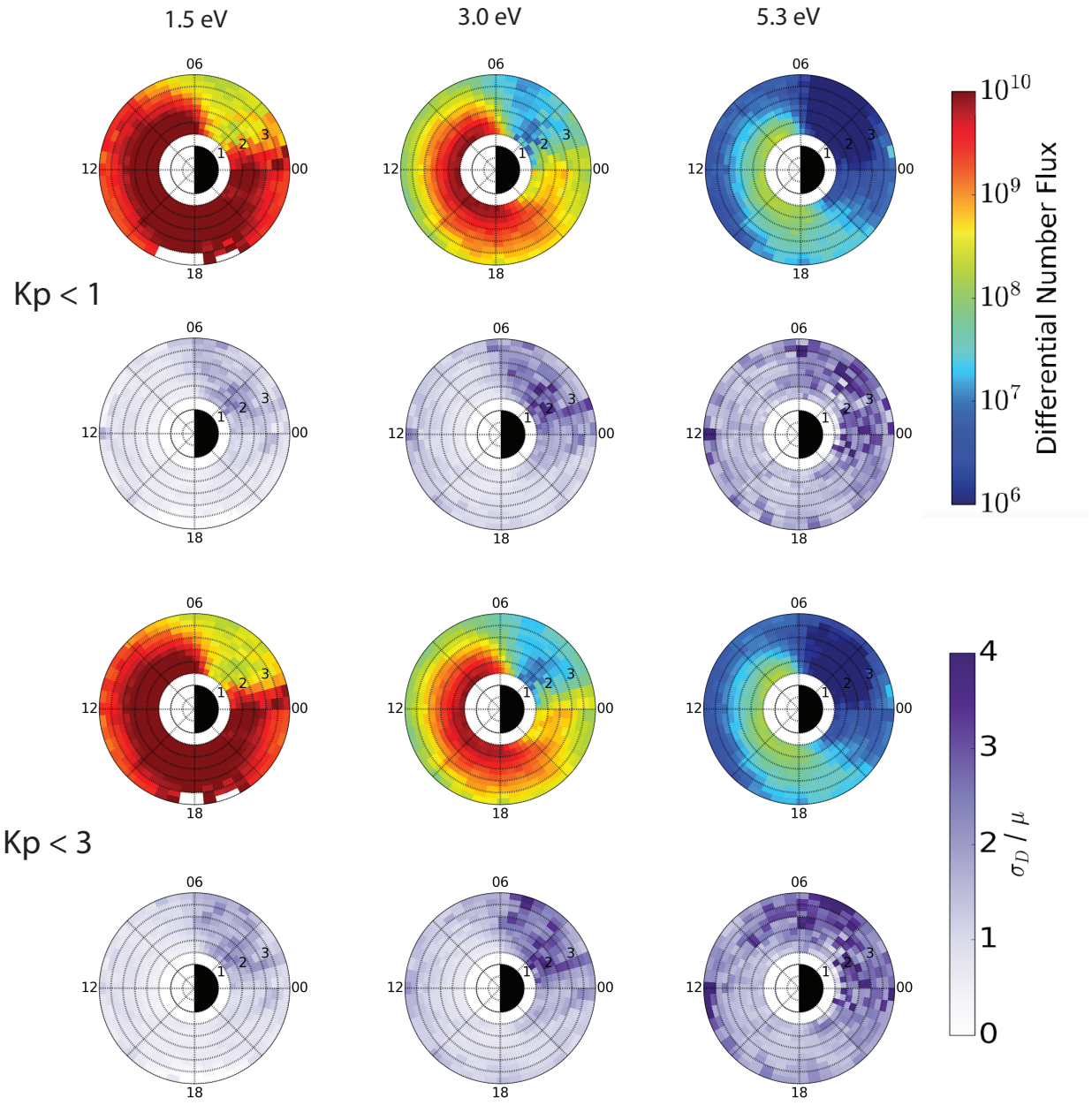

Figure 4.4: The plots with the rainbow color table show the median spacecraft potential corrected HOPE differential number fluxes at PA = 90^o using EFW spacecraft potential from February 2013 to April 2015 binned by MLT and L-Shell for the 1.5 eV, 3.0 eV, and 5.3 eV energy channels at Kp $<$ 1 and Kp $<$ 3. The purple scale plots show the relative variability (standard deviation divided by mean) of each L-MLT bin for the 1.5 eV, 3.0 eV, and 5.3 eV energy channels at Kp $<$ 1 and Kp $<$ 3

ning resulted in a total of 43,309 pitch-angle distributions for spacecraft potential corrected 1.5 eV fluxes, 43,628 pitch-angle distributions for 3.0 eV, and 44,927 pitch-angle distributions for 5.3 eV over the 26 month period in this study.

To calculate the average of each summed pitch-angle distribution, a weighting scheme based on the number of counts in each measurement was used. Over a time window, each pitch-angle bin differential flux measurement was assigned a weighting factor corresponding to the number of counts the detector measured. The weighting factor was the number of counts at measurement divided by the total number of counts for each pitch-angle bin over the time window.

For inclusion in our study, a pitch-angle bin had to have at least 10 total counts across a time window. If a summed pitch-angle bin had fewer than 10 counts, it was considered invalid. If a summed pitch-angle distribution had six or more invalid pitch-angle bins, the entire distribution was labelled as an 'Uncategorized' distribution. However, distributions where all pitch-angle bins were considered invalid in a given spin were discarded. Fewer than 1% of the total number of pitch-angle distributions fell into this category.

To highlight distribution shapes, each summed pitch-angle distribution was normalized by the mean flux value of that pitch-angle distribution. The normalized flux summed pitch-angle distributions were then sorted by a pitch-angle distribution identification algorithm, which was loosely based on the pitch-angle distribution sorting algorithm developed for Mars Global Surveyor electron distributions (*Brain et al.*, 2007). The algorithm presented here was empirically designed to work best for the Van Allen Probes HOPE data set, so modification would be necessary for use with another data set.

Figure 4.5 shows the categories of pitch-angle distributions used for this study and the definitions of each category. Each normalized HOPE pitch-angle distribution was classified either as Isotropic, Butterfly, Inverse Butterfly, Source Cone, Loss Cone, One-sided Cone, or Uncategorized. The first sort was for Isotropic distributions. A pitch-angle distribution is Isotropic if the second highest and second lowest values of the (approximately) 11 point summed distribution were within 20% of each other (2nd max / 2nd min < 1.2). This method provided more consistent results than using the standard deviation because the HOPE instrument measured fluxes could vary up to 3 orders of magnitude across a single pitch-angle distribution. This part of the algorithm was particularly sensitive to changes in the isotropic threshold (2nd max / 2nd min). Lowering the threshold increased the number of partial pitch-angle distributions that fell into the Loss Cone designation. Raising the threshold did the opposite. We ultimately chose a threshold that preferentially sorted these borderline distributions into the Loss Cone designation. Using the second highest and lowest values also reduced algorithm sensitivity to extreme fluxes.

The algorithm then reclassified the 11 pitch-angle bins into five segments. 'End1' is the normalized average of the 4.5 and 18.0 pitch-angle bins, 'Intr1' is the normalized average of the 36.0 and 54.0 bins, 'Middle' is the normalized average of the 72.0, 90.0, and 108.0 bins, 'Intr2' is the normalized average of the 126.0 and 144.0 bins, and 'End2' is the normalized average of the 162.0 and 175.5 bins. The algorithm sorted the normalized summed pitch-angle distributions by the relative peaks and troughs of these five segments.

Then, the algorithm screened for Butterfly distributions, where there are peaks in the intermediate pitch-angles and troughs at the ends and in the middle. Butterfly

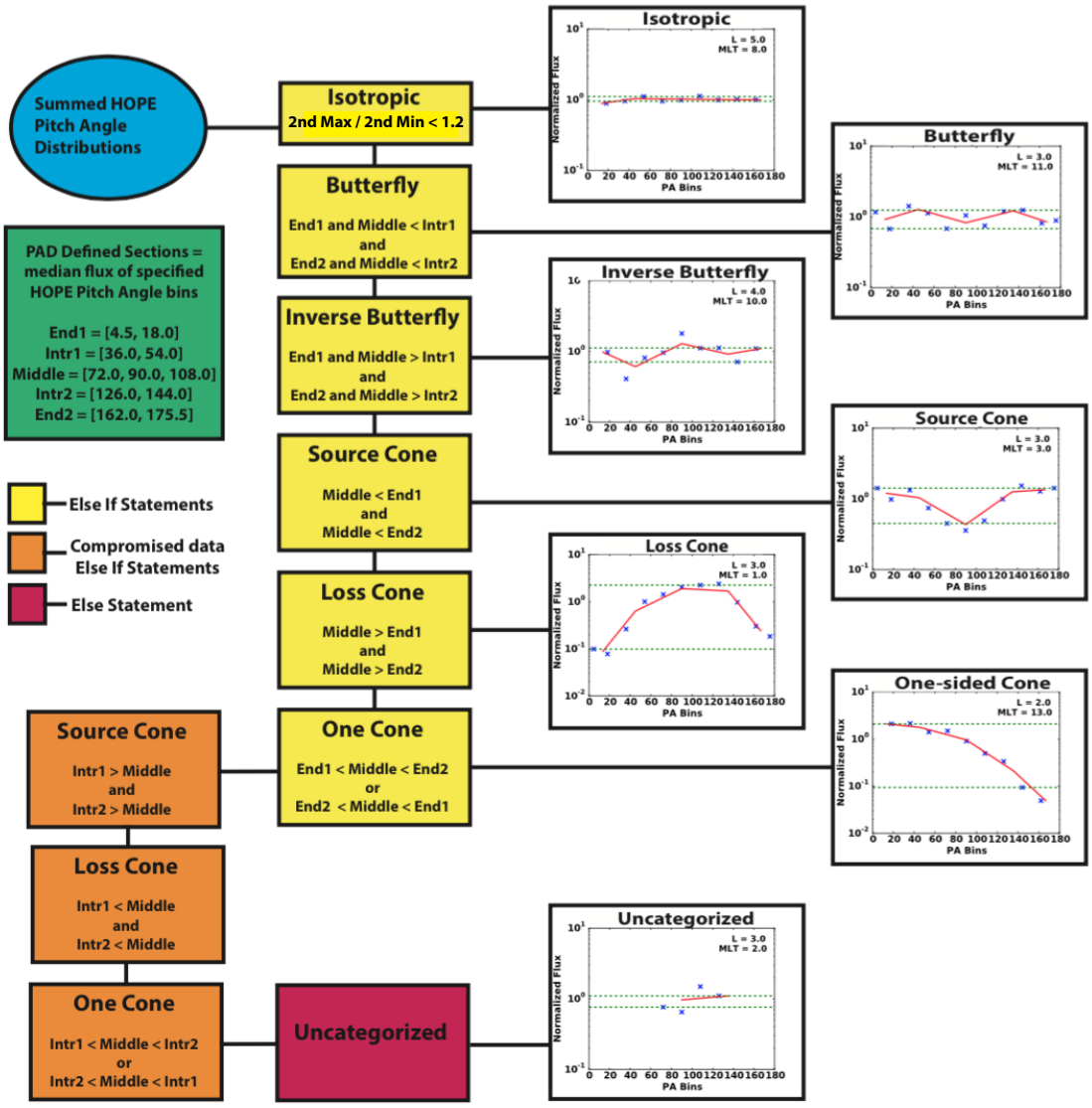

Figure 4.5: Flow chart demonstrating how the HOPE pitch-angle distribution sorting algorithm works and some of its sample output. On the categorized plots, the dotted green line shows the second highest and second lowest normalized flux values in the 11 point summed pitch-angle distribution. The red line shows the 5 segments defined in the green box that the algorithm used to determine pitch-angle distribution shape.

distributions are frequently seen in radiation belt electrons, and it has been proposed that wave particle interactions and magnetopause shadowing are responsible for their formation (*Gannon et al.*, 2007; *Horne et al.*, 2007). In the inner plasmasphere, Butterfly distributions occur when the plasma is in transition between an equatorially mirroring distribution to/from a field aligned population, with peaks in the intermediate portions of the pitch-angle distribution. There are data caveats in the categorization of Butterfly distributions since they required the end points of the pitch-angle distributions, and the end points ($0^o/180^o$) are the most unreliable.

The next type of distribution the algorithm looked for was the Inverse Butterfly Distribution, where the flux is lowest at intermediate pitch-angles. The Inverse Butterfly is an unusual distribution, where particles are simultaneously being lost and flowing into the specified region of space. This distribution was rare and constituted less than 1% of the total number of pitch-angle distributions seen by the HOPE instrument. There are also data caveats in the Inverse Butterfly categorization for the same reasons mentioned previously in the Butterfly distribution classification.

Following Butterfly and Inverse Butterfly Distributions, the algorithm searched for Source Cone distributions, which are peaked at both 0 and 180 degrees. In Source Cone distributions, particles are flowing in or out with pitch-angles close to 0 or 180, but the near 90^o population is at a relative minimum. After sorting for Source Cone distributions, the algorithm selected for its counterpart: Loss Cone Distributions, which are peaked at 90^o. Loss Cone distributions occur when the near 90^o pitch-angle population is at a relative maximum compared to the fluxes at 0^o and 180^o pitch-angles, since the low/high pitch-angle particles have already been lost. Loss Cone distributions are common in the inner magnetosphere, particularly for equatorial H^+ (*Comfort and Horwitz*, 1981; *André*, 1986; *Sagawa et al.*, 1987; *Giles et al.*,

1994).

The algorithm then checked for One-sided Cone distributions, peaked at either 0 or 180 degrees. One-sided pitch-angle distributions, or asymmetric pitch-angle distributions, can occur at times of transition, i.e., crossing a terminator. One-sided pitch-angle distributions can also indicate asymmetric field aligned flow due to hemispheric seasonal differences (*Lockwood et al.*, 1985; *Giles et al.*, 1994). For example, when the northern hemisphere is in summer, this hemisphere will have a larger heated ion concentration than the southern hemisphere. Thus, this seasonal difference between the hemispheres will manifest as increased ion flow from the summer hemisphere into the plasmasphere.

After testing each pitch-angle distribution for each of these 'ideal' classifications, the algorithm then sorts the partial pitch-angle distributions. In these cases, the pitch-angle distributions do not have valid measurements for End1 or End2, for example, but still show an identifiable distribution. A valid partial pitch-angle distribution includes Intr1, Middle, and Intr2 but is missing one or both of End1 and End2. For the partial pitch-angle distributions, the algorithm first sorted for Source Cones, defined now where Intr1 > Middle and Intr2 > Middle. Then, it looked for Loss Cone, now where Intr1 < Middle and Intr2 < Middle. Lastly, the algorithm screened for One-Sided Cones, defined now as Intr1 < Middle < Intr2 or Intr2 < Middle < Intr1. It is important to note that most of the partial pitch-angle distributions were sorted into the 'Loss Cone' distribution. Since visually the partial pitch-angle distribution sorts compared well with the full distributions, they were included in this study.

Lastly, if the algorithm was unable to find a match in any of the above categories, the normalized pitch-angle distribution was sorted as Uncategorized. At 1.5

eV, Uncategorized pitch-angle distributions constituted 11% of the total pitch-angle distributions across all MLTs. For 3.0 eV, Uncategorized pitch-angle distributions were 16% of the total. At 5.3 eV, Uncategorized pitch-angle distributions dominated as 40% of the total pitch-angle distributions across all MLTs. As seen in the example of Figure 4.5 this category comprised mostly severely compromised pitch-angle distributions, where there was large variability or too few of points to make a sensible categorization. The Uncategorized distributions generally occurred in the post-midnight sector where counts were too low to be statistically significant (up to 100% of the distributions in the near-Earth post-midnight sector).

Figure 4.6 shows the number of invalid points in each H^+ sorted pitch-angle distribution between February 2013 and October 2015. The number of counts were summed across all MLTs at L=2.0. The number of complete/near complete pitch-angle distributions with no/few invalid points is highest for the 1.5 eV energy channel. At the higher energy channels around 5.3 eV, the number of invalid point dominated pitch-angle distributions becomes the largest category. In our study, the 1.5-4 eV pitch-angle distributions are more reliable and generally more complete than the higher energy pitch-angle distributions or the pitch-angle distributions below 1.5 eV.

Spacecraft charging is a concern for low energy ion measurements in the magnetosphere. The Van Allen Probes were designed to primarily charge slightly positive. It should be noted that spacecraft potential is a function of total plasma density and temperature; however, this study solely focuses on the 1-10 eV fluxes, so changes in the 1-10 eV fluxes may be independent of spacecraft potential changes. Previous studies found that Van Allen Probes spacecraft potential is about 0.75 V in the 2 $<$ L$<$ 3 region and there are not exceptionally large positive potentials in the post-midnight sector in Chapters 2 and 3. Nonetheless, it is important to remember that

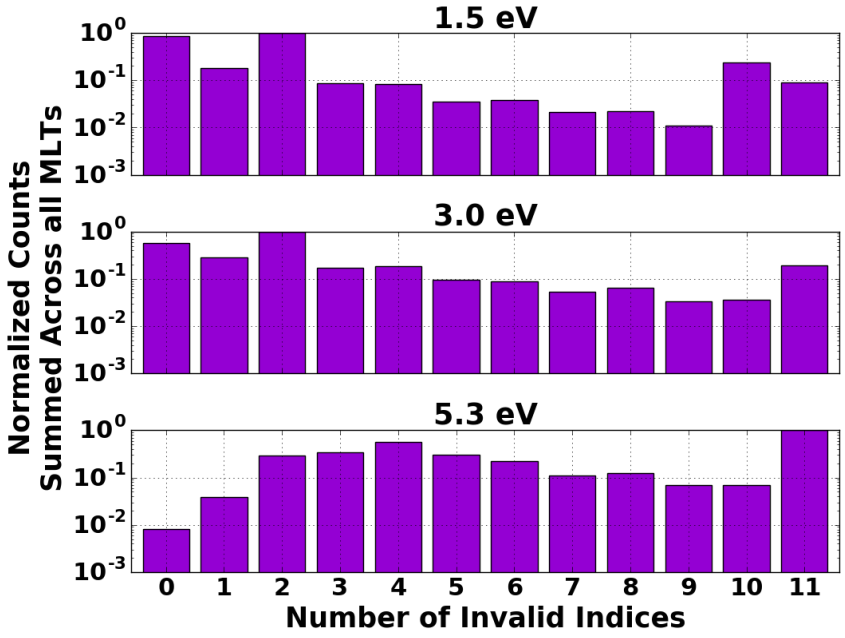

Figure 4.6: The number of invalid points in each classified H^+ pitch-angle distribution from February 2013 to April 2015 for 1.5 eV, 3.0 eV, and 5.3 eV summed across all MLTs at L = 2.0 and then normalized by the maximum number of invalid points at each energy.

this positive potential does add some uncertainty to the aforementioned pitch-angle distributions at all MLTs even with spacecraft potential corrected fluxes.

4.3 Results

The algorithm used in this study successfully sorted the summed pitch-angle distributions into the categories described above. Then the sorted pitch-angle distributions were binned into hourly MLT bins and results from L = 2 to L = 3 were combined to provide more robust statistics. Although this encompasses a large region of space, during quiet times of Kp < 3 this region was most likely within the plasmasphere. Therefore it is reasonable to assume there are no large density gradients between L = 2 to L = 3 and to combine distributions.

Figure 4.7 shows the pitch-angle distribution categorizations for the 1.5, 3.0, and 5.3 eV energy channels between $2 < L < 3$ as a function of MLT. The bar chart on the left depicts the number of total summed pitch-angle distributions in the Loss Cone, One-sided Cone, Source Cone, Low Counting Statistics ('Uncat' or 'Uncategorized'), and Other categories. The 'Other' category includes Isotropic, Butterfly, and Inverse Butterfly distributions. As energy increases, the counting statistics are lower and the Uncategorized pitch-angle contribution becomes larger across all MLTs. The high Uncategorized distribution percentage is further demonstrated by the bar charts on the right which gave the percentage of the total of each of the main categories.

Looking at the plots on the right side of Figure 4.7 and in the post-midnight sector, $1 < \text{MLT} < 4$, the Uncategorized pitch-angle distribution contribution is high at all energies, comprising most of the pitch-angle distributions in the 3.0 and 5.3 eV energy range. The results from these three low energy channels demonstrate how the

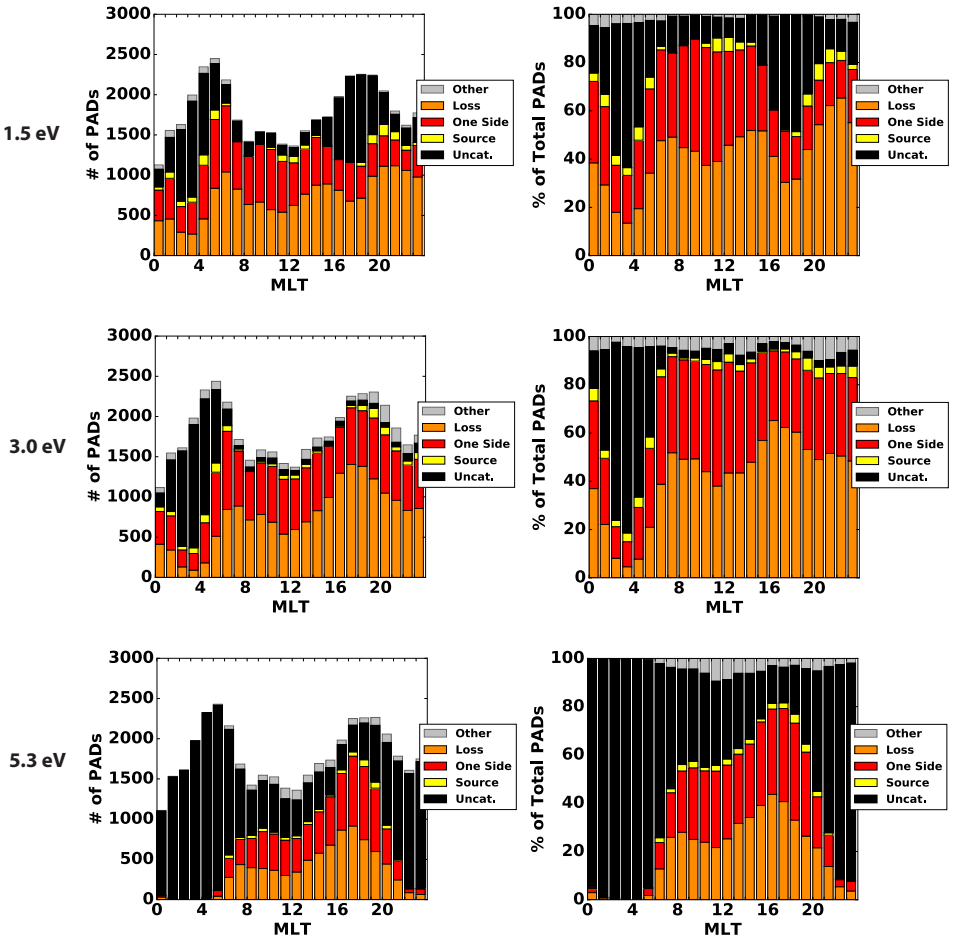

Figure 4.7: Bar charts showing the result of the HOPE pitch-angle distribution sorting procedure for summed pitch-angle distributions in the 1.5, 3.0, and 5.3 eV energy channel bins. These charts show the total summed pitch-angle distributions between $2 < L < 3$ in increments of 1 MLT hour. We highlight the four main summed pitch-angle distribution categories of Loss Cone, One-Sided Cone, Source Cone, and Uncategorized ('Uncat.'). Other includes the Butterfly, Inverse Butterfly, and Isotropic categories. The plots on the left show the total number of pitch-angle distributions contributing to each type of distribution. The plots on the right show the percentage of each type in the specified MLT bin.

post-midnight low energy H^+ depletion becomes more pronounced at higher energies, where the 'Uncategorized' designation dominates. Also notable, the Loss Cone distribution peaks at the dusk terminator (MLT=18) or soon after (MLT = 22) at all energies. In the 1.5 eV pitch-angle distributions, the Loss Cone distribution peaks at close to midnight, contributing almost 60% of the total distributions at this MLT. This peak coincides with the increased number of Uncategorized distributions, suggesting that there is an enhanced Loss Cone in the dusk sector/pre-midnight and at midnight that evolves into uncategorized, or depleted, pitch-angle distributions in the post-midnight sector. Also notable is that in the 3.0 and 5.3 eV energy channels, the Loss Cone peak in the dusk sector occurs earlier, at MLT = 17 for 3.0 eV and at MLT = 16 for 5.3 eV. This suggests the higher energy particles are depleted first across the dusk sector. The One-Sided distribution has a strong and nearly-uniform presence throughout the dayside. The One-Sided distribution is indicative of strong refilling from the summer hemisphere as solar EUV heated the illuminated ionosphere.

The Source Cone distribution was approximately 5% of the total number of pitch-angle distributions between MLT=10-12 and MLT=18-4 in the 1.5 eV and 3.0 eV energy channels. The Source Cone percentage contribution at 5.3 eV is very low across all MLTs. Since the Source Cone populations are indicative of ionospheric outflow, which is usually approximately 1 eV or less, the low percentage of Source Cone distributions at higher energies for all MLTs is expected.

4.4 Conclusions

The 1-10 eV ion population of the inner plasmasphere has been shown to be depleted in the post-midnight sector and reach a minimum at MLT = 3. In this study, pitch-angle distributions of the ion fluxes in the HOPE instrument 1-10 eV energy

channels from February 2013 to April 2015 were examined to determine the cause of the 1-10 eV H^+ depletion in the post-midnight sector of the plasmasphere. It was found that the near 90^o pitch-angle population was severely depleted in the post-midnight sector compared to the field aligned populations. If these lower 1-10 eV fluxes were from pitch-angle diffusion and charge exchange, a weak residual equatorially mirroring population would have been present in the post-midnight sector accompanied by large field aligned flows into the ionosphere.

We also show, for the first time, low energy HOPE differential number fluxes corrected for spacecraft potential using EFW measurements. The flux depletion in the post-midnight sector is still present in the spacecraft potential corrected fluxes. Further, we show that the 1-10 eV plasma depletion in the near-Earth post-midnight sector does exhibit some geomagnetic activity dependence. At $Kp < 1$, the fluxes are higher than at $Kp < 3$ between $2 < L < 3$, particularly in the 1.5 eV and 3.0 eV energy channels.

A new algorithm was developed to categorize summed pitch-angle distributions to better quantify why this loss occurs. A peak in Loss Cone distributions in the pre-midnight sector and strong refilling in the dawn sector were noted in the low energy channels. The Loss Cone peak occurred earlier in the dusk sector for the higher energy particles than the lower energy ones. The post-midnight sector was dominated by Uncategorized distributions at higher energies due to low counting statistics, suggesting plasma depletion occurs before the post-midnight sector due to enhanced dusk and midnight Loss Cone distributions. This result has not been seen before, and it suggests that more than simply charge exchange in the top side ionosphere is responsible for the 1-10 eV lower fluxes.

The pitch-angle sorting algorithm will be a useful tool for the magnetospheric community and applied to classify pitch-angle distributions at higher energy levels. The algorithm could also classify inner magnetosphere electron pitch-angle distributions. For example, one could conduct a study about pitch-angle distributions on ring current pitch-angle scattering or keV particles at L = 4 during substorm injections (e.g., *Lundin et al.*, 1980; *Smith et al.*, 1996). Also, the results of this study emphasize that source and loss processes in the inner plasmasphere are more complicated than previously anticipated and may involve more wave heating aspects.

CHAPTER V

Plasmaspheric Hiss or Noise?

5.1 Introduction

Thermal ions in the plasmasphere have been shown to be transversely heated through ion cyclotron resonance with electromagnetic plasma waves above the ion gyrofrequency and below the lower hybrid resonant frequency. Ion cyclotron resonant heating of thermal ions was demonstrated through observations and modeling of GEOS-1 and GEOS-2 data (*Young et al.*, 1981; *Roux et al.*, 1982; *Perraut et al.*, 1982; *Perraut*, 1982). In particular, He^+ was shown to most strongly resonate with the measured frequencies in the GEOS data. Other studies concluded that cyclotron resonance heats H^+ thermal populations at geosynchronous orbit similar to the He^+ heated population (*Quinn and Johnson*, 1982). These thermal ions require left hand or linearly polarized waves for wave-particle interactions that lead to subsequent heating. However, there is still debate as to which waves are present during times of inner magnetosphere low energy ion heating: equatorial noise or plasmaspheric hiss.

Equatorial noise has been shown to heat thermal ions through cyclotron resonance (*Olsen et al.*, 1987; *Singh and Hwang*, 1987; *Laakso et al.*, 1990). Equatorial noise is a fast magnetosonic, low frequency wave with nearly linearly polarized magnetic field fluctuations generated by unstable energetic proton ring velocity distributions

(*Perraut et al.*, 1982; *Gary et al.*, 2010). Equatorial noise ranges in frequency from approximately 20 Hz to a few hundred Hz and lies below the lower hybrid frequency (*Němec et al.*, 2015; *Boardsen et al.*, 2016). Typically, equatorial noise is found between 2 and 7 Earth radii from Earth's center and within 10 degrees of the magnetic equator (*Russell et al.*, 1970; *Němec et al.*, 2006). Strong diurnal variation has been previously seen in Cluster observations of equatorial noise outside of the plasmasphere, with a peak at MLT = 12 and a minimum in the post-midnight sector between MLT = 0 and 6 (*Hrbáčková et al.*, 2015). Studies of the global wave distribution revealed that equatorial magnetosonic waves inside the plasmapause depended on substorm activity and had larger amplitudes and higher occurrence frequencies on the dayside (*Green et al.*, 2005; *Meredith et al.*, 2008; *Ma et al.*, 2013).

Based on Dynamics Explorer 1 and SCATHA observations, it was proposed that equatorial noise, generated by highly energetic ions in the ring current and/or radiation belt, heats the thermal ion population through cyclotron resonance. Wave-particle interactions elevate the thermal population to a suprathermal population via energy deposition by equatorial noise (10 eV $<$ E $<$ 300 eV) (*Curtis*, 1985). The energy transference could also occur with 1-10 eV He^+ and O^+, albeit on slower time scales. Modeling work also suggests that inward propagating magnetosonic waves produced by proton ring instabilities could cause thermal plasma heating near-Earth (*Horne et al.*, 2000).

However, plasmaspheric hiss occupies a similar region of space as the equatorial noise and typically ranges from 20 Hz to approximately 1000 Hz (*Thorne et al.*, 1973; *Li et al.*, 2015). Plasmaspheric hiss is a broadband incoherent electromagnetic emission that is largely confined to Earth's plasmasphere (*Meredith et al.*, 2009). Plasmaspheric hiss can be generated from magnetospherically reflecting whistler waves or

from inward propagating chorus emissions that lose coherency when they cross the plasmapause (*Draganov et al.*, 1992; *Bortnik et al.*, 2008). Hiss amplification at the equator due to wave turbulence from the electron gyroresonance instability leads to enhanced plasmaspheric hiss in the magnetic equatorial plane (*Thorne and Barfield*, 1976; *Church and Thorne*, 1983; *Solomon et al.*, 1988; *Santolik et al.*, 2001). Unlike equatorial noise, plasmaspheric hiss is right hand polarized and primarily interacts with electrons (*Tsurutani et al.*, 1975; *Li et al.*, 2007; *Summers et al.*, 2007). Without looking at polarization or spectral lines, it is difficult to distinguish between plasmaspheric hiss and equatorial noise (*Gurnett*, 1976; *Santolík et al.*, 2002).

Plasma waves are a likely cause for the observed minimum in the high energy tail (1-10 eV) of the inner plasmasphere (L-Shell < 3) in the post-midnight sector (*Lennartsson and Reasoner*, 1978; *Sarno-Smith et al.*, 2015). A previous study revealed that in the post-midnight sector specifically, the H^+ pitch angle (PA) $= 90^o$ population between $2 < L < 3$ was depleted but plasma was still flowing upward from the ionosphere, which can be found in Chapter 4. Upward flowing plasma in the post-midnight sector suggests that the apparent loss of plasma in the post-midnight sector is not driven by the cooling of plasma in the topside ionosphere. Instead, plasma wave influence may be heating/scattering the particles in such a way to lead to strong diurnal variation in the 1-10 eV population.

Three instruments onboard the NASA Van Allen Probes mission enable further exploration of the connection between 1-10 eV ions of the inner plasmasphere and plasma wave activity. The Van Allen Probes, launched in late 2012, are a pair of satellites that are in highly elliptical, low inclination orbits (*Mauk et al.*, 2014). The Electric and Magnetic Field Instrument Suite and Integrated Science (EMFISIS) instrument measures plasma waves between approximately 2 Hz and 12 kHz using

three search coil magnetometers and the three Electric Field and Waves (EFW) instrument's electric field antennas (*Wygant et al.*, 2013; *Kletzing et al.*, 2014). EMFISIS also measures the DC magnetic field with onboard magnetometers. The plasma wave range we examine is between 150 Hz and 600 Hz, well within the resolution capabilities of EFW and EMFISIS. The Helium Oxygen Proton Electron (HOPE) instrument measures the ion and electron populations of the equatorial inner magnetosphere between 1 eV and 50 keV (*Funsten et al.*, 2014). HOPE also uses the EMFISIS magnetometer measurements to map the observed fluxes into pitch angle space and assign nominal pitch angle bins.

We examine the connection between 150 Hz - 600 Hz waves with the 1-10 eV ion population of the L $<$ 3 inner plasmasphere. As previous studies have found, we find the diurnal variation in the 150 Hz - 600 Hz waves are linked with the 1-10 eV ion equatorially mirroring population growth and loss (*Olsen et al.*, 1987; *Singh and Hwang*, 1987). Polarization analysis reveals that the near-Earth emissions near the equator are primarily plasmaspheric hiss and do not cyclotron resonate with the low energy ions and are not responsible for the ion heating. We corroborate our results with observations from EMFISIS and HOPE, opening up several questions in magnetospheric physics of our understanding of thermal plasma and wave interaction.

5.2 Particle and Wave Statistics

Following the 1-10 eV ion depletion in the post-midnight sector discovery in Chapter 2, we examine the fluxes measured at different pitch angles from February 2013 to April 2015. The polar angle resolution on the HOPE instrument is 18 degrees full width. Pitch angle bins are 18 degrees wide, except for 9 degree bins centered at 4.5 and 175.5 degrees. In every spin period of approximately 11 seconds, HOPE

differential number flux values were calculated and assigned a pitch angle designation based on the magnetic field direction as measured by EMFISIS. Initial analysis of the pitch angle distributions were conducted by Chapter 4, and here the analysis is taken further to examine the evolution of the full velocity-space distribution in both energy and pitch angle.

Figure 5.1 displays the median 1-10 eV H^+ differential number fluxes at L = 2.5 for times where Kp $<$ 3 between February 2013 and April 2015 measured by HOPE sorted by pitch angle, MLT, and energy. The fluxes are corrected for spacecraft charging, and the process is detailed in Chapter 3. We note that the Van Allen Probes tend to charge slightly positive. The L = 2.5 bin spans from 2.375 to 2.625 (0.25 L-Shell). The fluxes are not always centered near-PA = 90^o due to seasonal effects, such as increased upwelling ion fluxes from the summer hemisphere compared to the winter hemisphere. At MLT = 2, the near PA = 90^o population is at a minimum for all energies shown. The flux measurements at near PA = 0^o and near PA =180^o are lower compared with other MLTs for these pitch angle bins but are larger than the near PA = 90^o measurements. The equatorially mirroring population begins to refill for the 1 eV energy channels at MLT = 4, but the near PA = 90^o population minimum is prevalent at the higher energies (energy $>$ 2 eV). MLT = 6 demarcates the transition from a dominant refilling population at 0^o and 180^o to a more equatorially mirroring focused population. Above 6 eV, however, the near PA = 90^o population is still at a relative minimum compared to the 0^o and 180^o degree pitch angle flux measurements or the distribution is isotropic.

A balance is struck between MLT = 8 to MLT =18 where the near PA = 90^o population is still at a relative minimum above 8 eV, but the near PA = 90^o population remains in a steady state throughout the day. MLT = 22 fluxes reveal that

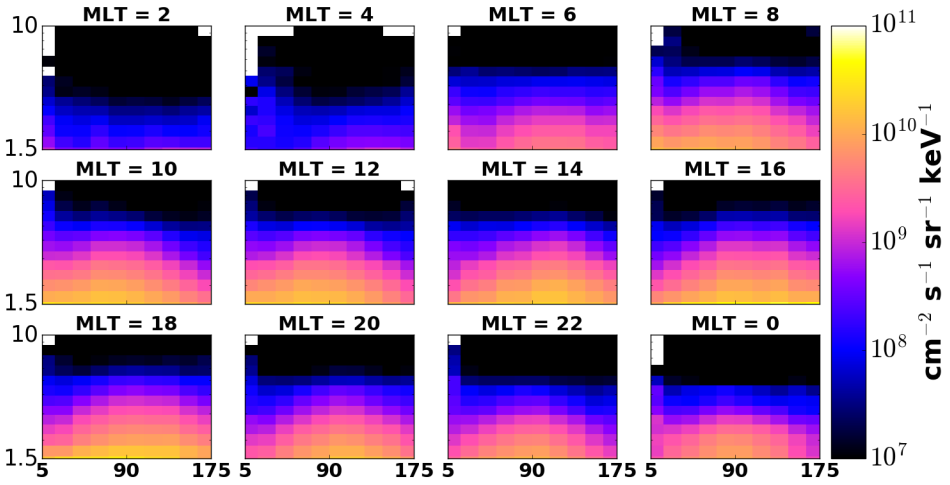

Figure 5.1: Median differential number fluxes corrected for spacecraft potential for 1.5-10 eV H^+ measured by HOPE at L = 2.5 at several MLTs from February 2013 to April 2015. The fluxes were binned by energy channel and pitch angle.

the equatorially mirroring population has begun to recede. While the near PA = 90^o population still dominates below 3 eV, the pitch angle distributions are either refilling (0^o/180^o dominated) or isotropic beyond 3 eV. MLT = 0 exhibits similar behavior, with the last of the near PA = 90^o population at 1.5 eV narrowing.

In Figure 5.1, there are two indications that the loss of the equatorially mirroring population may not simply be a balance of ionospheric outflow and scattering. The first indicator is if the change in 1.5-10 eV plasma in the inner magnetosphere was from ionospheric diurnal variation and consequent transport to the plasmasphere, it would be expected that the higher energy ions should appear first at L = 2.5 and scatter first since they move the fastest. Instead, we see that the lowest energies for PA = 90^o rise the fastest and the higher energies above 8 eV either never have a near PA = 90^o population maximum or take longer than the lower energies. For example, the 2 eV equatorially mirroring population is at a maximum by MLT = 6, but the 8

eV population is not at a maximum until MLT = 8.

The other indication is the depletion in the near PA = 90^o population compared to the near PA = $0^o/180^o$ measurements. While the equatorially mirroring populations have > 2.5 orders of magnitude of variation, the field aligned fluxes show about 2 orders of magnitude diurnal variation. We use the 18^o and 162^o bins to describe the field aligned PA bins because the 175.5^o and 4.5^o bins are smaller and less accurate. Figure 5.2 shows the L = 2.5 spacecraft potential corrected fluxes of 1.55, 1.83, 2.18, 2.53, 2.95, 3.38, 3.94, 4.64, and 5.35 eV normalized by the highest values at each energy at pitch angles of 18^o, 54^o, 90^o, 144^o, and 162^o. For the more field aligned pitch angles, the normalized fluxes show that the high energy H^+ ions rise first at dawn compared to the slower particles. At PA = 90^o, the opposite occurs, with the lowest energy fluxes increasing first.

The PA = 90^o fluxes also show an energy dependent decrease. Starting at MLT = 18, the PA = 90^o fluxes start decreasing. The highest energy ions are depleted first, with over an order of magnitude drop occurring before midnight. The low energy ions (1-3 eV) have a delayed depletion until the post-midnight sector. The steady growth of the PA = 90^o population across the morning to a saturation point at MLT = 10 suggests perpendicular heating the H^+ ions throughout the dayside. The flatness of the curves across the dayside at all pitch angles in Figure 5.2 indicates that the fluxes are in equilibrium, with the wave heating balanced by the scattering and loss.

From Figures 5.1 and 5.2, we can conclude that wave activity, not ionospheric breathing, is responsible for the 1-10 eV ion depletion because of the behavior of the PA = 90^o population. Following the theory of equatorial noise heating thermal plasma from *Olsen et al.* (1987), we explore the possibility of a wave-particle interaction by

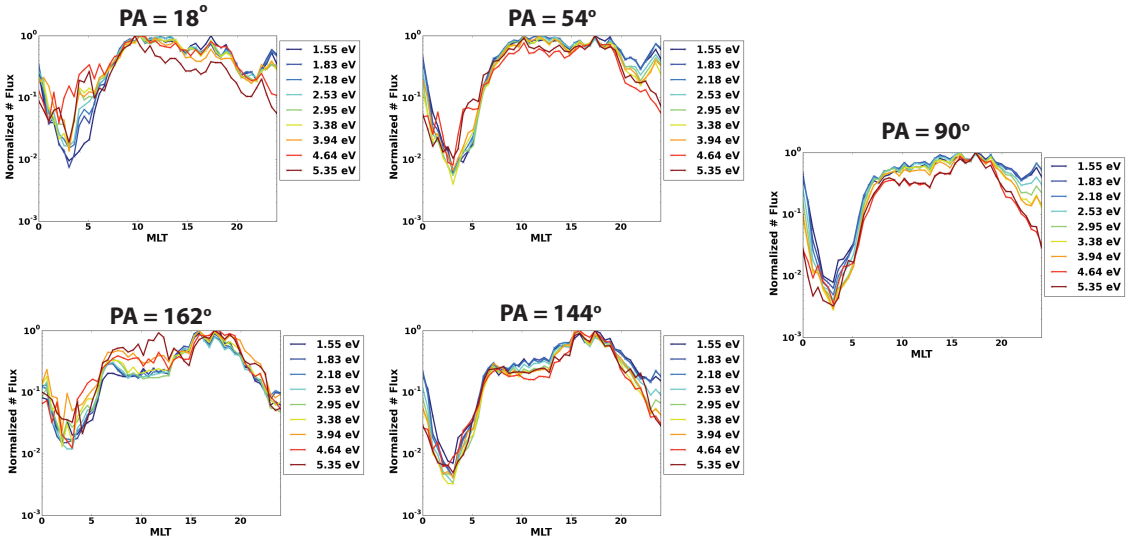

Figure 5.2: Normalized median differential number fluxes corrected for spacecraft potential for 1.5 eV, 1.83 eV, 2.18 eV, 2.53 eV, 2.95 eV, 3.38 eV, 3.94 eV, 4.64 eV and 5.35 eV H^+ measured by HOPE at L = 2.5 from February 2013 to April 2015 for PA=18^o, 54^o, 90^o, 144^o, and 162^o. The median fluxes were normalized based on the maximum value for each energy at all MLTs.

examining the EMFISIS survey mode data over the course of 26 months. The survey mode on EMFISIS includes a set of spectral matrices every 6 seconds (*Kletzing et al.*, 2014). The EMFISIS instrument uses a fast Fourier transform on board to analyze the electric field samples from EFW and the results are telemetered to the ground. The EMFISIS survey mode data are averaged onboard into 65 logarithmically spaced bins between 2 Hz and 10 kHz and binned by 0.5 MLT and 0.25 L-Shell for times when Kp $<$ 3.

To identify peak wave activity, Figure 5.3 shows the relative intensity of EMFISIS WaveForm Receiver (WFR) frequencies as a function of MLT at L = 2.5. Figure 5.3A shows the median power spectral densities from February 2013 to April 2015. Figure 5.3B uses the same binning strategy and displays the normalized power spectral densities. The power spectral densities in each frequency bin are normalized by the

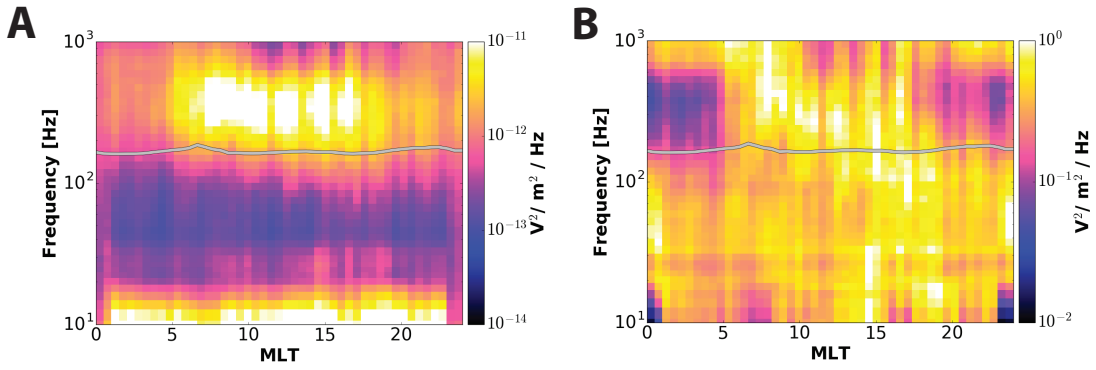

Figure 5.3: A shows the median power spectral density of the electric field component of waves measured from EMFISIS in 0.5 MLT bins and logarithmically spaced frequency bins between 10 Hz and 1 kHz over from February 2013 to April 2015 at L=2.5. B is the power spectral density of the electric field wave component normalized across all MLTs by the max value at each frequency/0.5 MLT bin over the same time period at L=2.5. In both A and B, the silver line is the 6th harmonic of the H^+ cyclotron frequency.

highest power spectral density in that frequency bin. The silver line is the 6th harmonic of the H^+ cyclotron frequency. We use the 6th harmonic of the H^+ cyclotron frequency because it is approximately where we see enhanced power spectral densities. We show the geometric mean lower hybrid frequency instead of the lower hybrid frequency because it is difficult to get a true estimate on plasma density at $L < 3$, where EMFISIS electron number density estimates from the upper hybrid frequency saturate (*Kurth et al.*, 2015). This technique has been used in previous studies to estimate the lower hybrid frequency using only the electron and ion gyrofrequencies (*Olsen et al.*, 1987). It only works under the approximation of dense plasma, otherwise it provides only an upper estimate of the lower hybrid frequency.

Figure 5.3 shows strong diurnal variation in the frequency band above the 6th harmonic of H^+ cyclotron frequency (silver line). The frequencies which show dayside enhancement extend from 150 Hz to 600 Hz. Figure 5.3B highlights the change in

power spectral density with MLT in this range of frequencies with a peak in the morning sector and the lowest values occurring across the night side. This frequency band includes equatorial noise/plasmaspheric hiss. The diurnal variation in plasmaspheric hiss is attributed to keV electron injection into the outer plasmasphere on the dayside in conjunction with substorms and to whistler-mode chorus, which is known to be a source of plasmaspheric hiss, which can not propagate into the plasmasphere on the nightside due to stronger Landau damping caused by higher suprathermal electron flux (*Bortnik and Thorne*, 2007; *Li et al.*, 2013; *Chen et al.*, 2014; *Li et al.*, 2015). Diurnal variation is also common in equatorial noise and proton ring distributions can provide a source of free energy ring velocity (+/- a factor of 2 above or below the Alfvenic speed) and generate equatorial noise (*Chen et al.*, 2010, 2011; *Hrbáčková et al.*, 2015).

Figure 5.4 highlights the power spectral densities for frequencies below 1000 Hz. Using data from February 2013 to April 2015, EMFISIS WFR frequency channels were binned by 0.25 L-Shell and 0.5 MLT for quiet times when Kp $<$ 3. We did not set a limit on the satellite's magnetic latitude in Figure 5.4. The wave amplitudes peak beyond 150 Hz, with a dayside maximum at all L-Shells beginning at f = 200 Hz and continuing through f = 300 Hz. At 1000 Hz, the strong diurnal variation is absent, with a minimum at L $<$ 3 dayside MLTs.

5.3 Quantitative Relationship Between Wave Amplitude and Low Energy Ions

In this section, we show how the Van Allen Probes observations dovetail with a resonant interaction occurring between low energy ions and 150 Hz - 600 Hz waves.

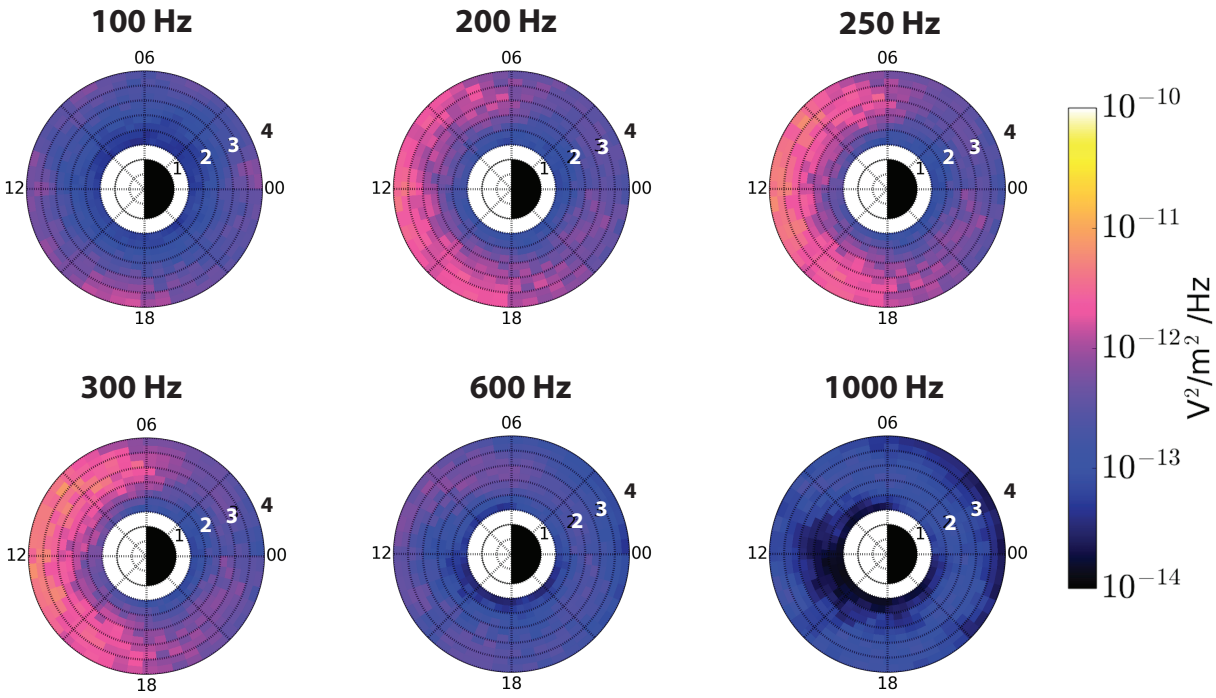

Figure 5.4: Median equatorial noise electric field power spectral densities at different frequency bands from EMFISIS. Each frequency band was sorted by 0.25 L-Shell and 0.5 MLT from February 2013 to April of 2015 at times when Kp < 3.

Figure 5.5 compares the median wave power spectral densities at harmonics of the H^+ cyclotron frequency with median H^+ 1-10 eV partial densities at all MLTs for different L-Shells from February 2013 to April 2015. Figure 5.5A shows L = 2.0, Figure 5.5B shows L = 2.5, and Figure 5.5C shows L = 3.0. For each 4 second measurement of the magnetic field, the gyrofrequency and harmonics of the gyrofrequency were calculated and then the electric field power spectral density at the nearest frequency to the gyrofrequency was extracted and binned.

The partial density and wave power spectral density behave differently at each of the L-Shells. At L = 2.0, The 6th and 10th harmonic wave power spectral density begin to decline at MLT = 14, dropping to approximately 10^{-12} $V^2/m^2/Hz$ between MLT = 19 to MLT = 4. The wave power spectral densities increase in three stages at MLT = 4, 6, and 10 before reaching approximately 10^{-11} $V^2/m^2/Hz$ across the dayside. The 16th harmonic wave power spectral density is largely flat with little diurnal variation. The 1-10 eV H^+ density has a maximum at MLT = 6, beginning to increase at approximately MLT = 4. The density gains and losses do not precisely follow the power spectral densities, but both exhibit general diurnal variation.

For L = 2.5, the 6th, 10th, and 16th harmonic power spectral densities show the most diurnal variation, varying between approximately 10^{-11} $V^2/ m^2/Hz$ from MLT = 6 to MLT = 16 and approximately 10^{-12} $V^2/ m^2/Hz$ from MLT = 17 to MLT = 3. The different harmonic power spectral densities also follow each other closely with very similar power spectral densities at different MLTs. The partial density also shows the most diurnal variation of the three L-Shells shown, peaking from MLT = 6 to MLT = 22. The rise of the 10th and 16th harmonics of the H^+ gyrofrequency occur before the rise in the partial density, although the peak power spectral density occurs after the partial density has risen above 10^1 cm^{-3}.

The L = 3.0 panel shows the least diurnal variation of the 6th, 10th, and 16th harmonic power spectral densities. The heightened dayside power spectral densities occur from MLT = 6 to MLT = 14 and the nightside low extends from MLT = 20 to MLT = 3. The 16th harmonic is strongest at this L-Shell, whereas the 6th and 10th harmonic are much lower. The 1-10 eV density takes much longer to reach the high dayside values at this L-Shell, not reaching peak value until MLT = 9 after a gradual increase starting at MLT = 1.

There are many factors contributing to the partial density increases in Figure 5.5. It is important to note that harmonic cyclotron resonance occurs at multiple frequencies and heats the ions differently based on the degree of the harmonic and the background magnetic field conditions (*Schmitt*, 1976; *Mauk et al.*, 1981). So, in considering how power spectral densities at different harmonics affect the 1-10 eV H^+ partial densities across MLTs, a holistic approach should be taken. For example, at L = 2.5 where all the power spectral densities are high, the cumulative heating impact on the 1-10 eV ions from equatorial noise will be greater than at L = 3.0 where the 16th harmonic has a higher power spectral density dayside value than the other harmonics. Also, at L-Shells closer to Earth, the ionospheric contribution is greater and topside ionospheric plasma is transported into the equatorial plasmasphere faster.

We developed a binary contingency table test to quantify if there was a connection between waves with power spectral density above a certain level and high H^+ fluxes. Figure 5.6 shows the outcome of our threshold test. Each panel of Figure 5.6 shows the percentage of each contingency table element based on MLT and L-Shell location. The grid is divided into 0.25 L-Shell bins between 1.5 and 4 and 0.5 MLT bins between 0 and 24. The threshold bars were 10^8 cm^{-2} s^{-1} sr^{-1} keV^{-1} for H^+ 2.5

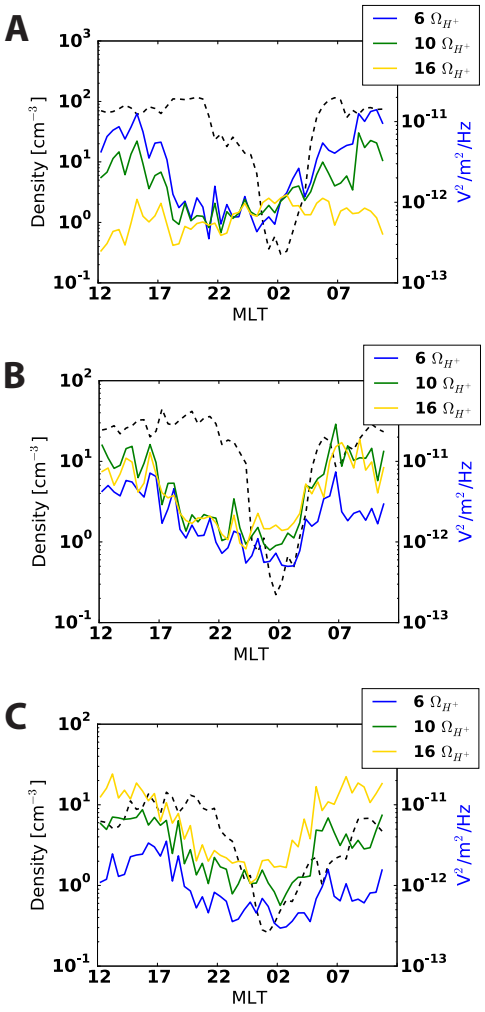

Figure 5.5: The blue, green, and gold lines are the median electric field power spectral density measured by EMFISIS from February 2013 to April 2015 for the 6th harmonic, 10th harmonic, and 16th harmonic of the H^+ gyrofrequency, approximately 100 - 250 Hz. The different panels show different L-Shells, with A at L = 2.0, B at L = 2.5, and C at L = 3.0. The dashed black line is the median H^+ partial 1-10 eV density over the same time period at the same L-Shell. Both the power spectral densities and H^+ partial densities were binned by 0.25 L-Shell and 0.5 MLT.

eV fluxes and 10^{-12} $V^2/$ m^2/Hz for EMFISIS power spectral densities at 250 Hz. The power spectral density boundary is based on the electric field power spectral densities necessary for observable transverse heating of a few eV per hour in the $2 < L < 3$ region (*Singh and Hwang*, 1987). The flux threshold is based on measured HOPE fluxes at all MLTs for this energy channel.

The High Wave and Particle category denotes HOPE H^+ fluxes of 10^8 cm^{-2} s^{-1} sr^{-1} keV^{-1} or greater and a power spectral density of 10^{-12} $V^2/$ m^2/Hz or greater. The Low Wave and Particle section denotes ion fluxes less than 10^8 cm^{-2} s^{-1} sr^{-1} keV^{-1} and power spectral densities less than 10^{-12} $V^2/$ m^2/Hz. Only High Wave occurs where the power spectral densities are greater than 10^{-12} $V^2/$ m^2/Hz but the ion fluxes are less than 10^8 cm^{-2} s^{-1} sr^{-1} keV^{-1}. Only High Particle occurs when power spectral densities are less than 10^{-12} $V^2/$ m^2/Hz and the ion fluxes are greater than 10^8 cm^{-2} s^{-1} sr^{-1} keV^{-1}.

There are several key ideas that emerge from Figure 5.6. When ion fluxes on the dayside are high, in most cases between L-Shells of 1.5 to 3.25 and MLTs between 5 and 20, the EMFISIS power spectral densities will be high and vice versa. This relationship is demonstrated by the High Wave and Particle contingency outcome, where high percentages (> 70 %) are seen in these L-Shell/MLT bins. On the other hand, the Low Wave and Particle category shows us that in the post-midnight region between 0-5 MLT and 1.5 to 3.5 L-Shell, the opposite is seen with approximately equal occurrence frequency; low ion fluxes are accompanied by low power spectral densities.

The Only High Particle and Only High Wave outcomes of the threshold test reveal the areas subject to extenuating factors. The Only High Wave, where ion fluxes are low despite high power spectral densities, occurs at higher L-Shells across many

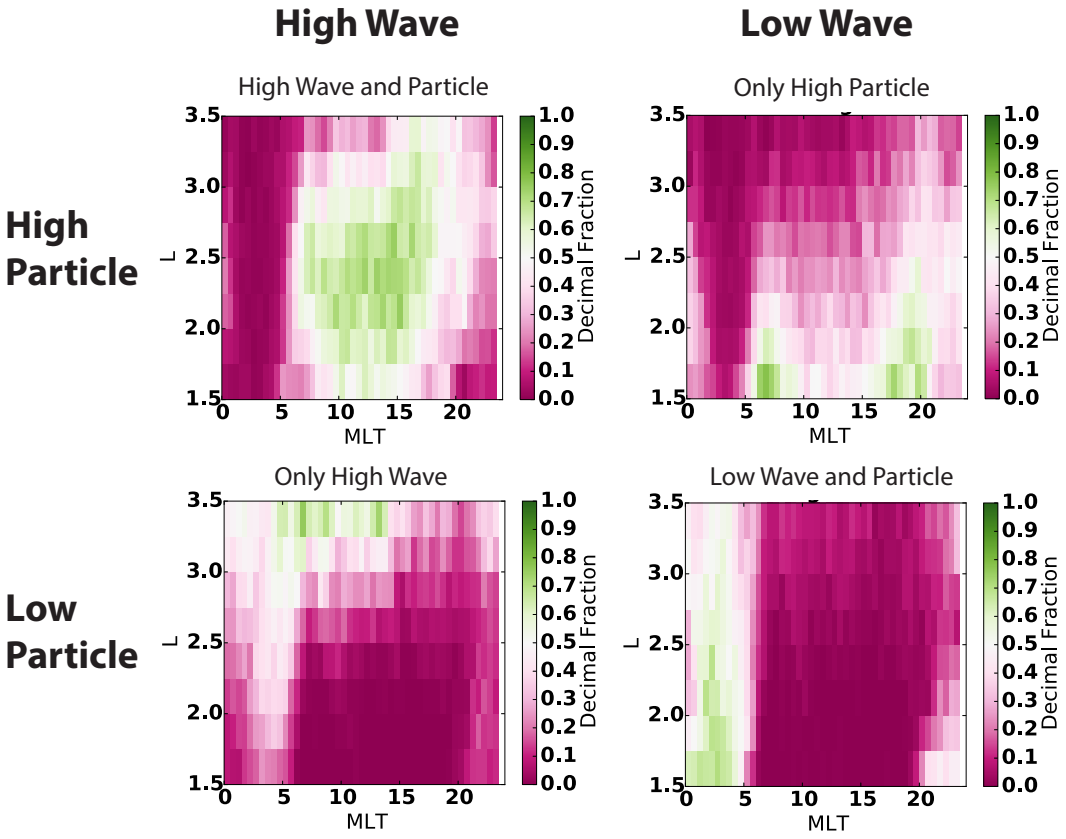

Figure 5.6: Binary contingency table results of median HOPE 2.5 eV fluxes and EMFISIS electric field power spectral densities at 250 Hz. The study used data from February 2013 to April 2015 which was sorted into 0.25 L-Shell and 0.5 MLT bins. The High Wave and Particle category denotes HOPE H^+ fluxes of 10^8 cm^{-2} s^{-1} sr^{-1} keV^{-1} or greater and a power spectral density of 10^{-12} $V^2/m^2/Hz$ or greater. The Low Wave and Particle section denotes ion fluxes less than 10^8 cm^{-2} s^{-1} sr^{-1} keV^{-1} and power spectral densities less than 10^{-12} $V^2/m^2/Hz$. Only High Wave occurs where the power spectral densities are greater than 10^{-12} $V^2/m^2/Hz$ but the ion fluxes are less than 10^8 cm^{-2} s^{-1} sr^{-1} keV^{-1}. Only High Particle occur when power spectral densities are less than 10^{-12} $V^2/m^2/Hz$ and the ion fluxes are greater than 10^8 cm^{-2} s^{-1} sr^{-1} keV^{-1}. The color of each bin reflects the percentage of the bins that lie in each respective category.

MLTs. We attribute this largely to the declining ion densities from the conservation of the second adiabatic invariant at higher L-Shells, so the threshold of 10^8 cm^{-2} s^{-1} sr^{-1} keV^{-1} is no longer a fair threshold mark at $L > 3$. The Only High Particle outcome, where power spectral densities are low but the particle fluxes are high, occurs at high percentages for low L-Shells at MLTs of 5 to 20 and at higher L-Shells around MLT = 18. We attribute this effect to ionospheric influence. From this binary contingency table, we can see that there is a clear connection between wave amplitudes and high H^+ fluxes.

We supplement this statistical result with a case study to show the relationship between dayside 1-10 eV H^+ flux enhancement and high wave amplitudes. Figure 5.7 highlights from 9:00-11:30 UT on July 2, 2013, when the Van Allen Probes A crossed the post-midnight sector between $2 < L < 3$ on the outbound leg of the orbit. Figure 5.7A shows the EMFISIS frequency spectrogram for the electric field component of the waves over the same time period between 100 to 800 Hz. Figure 5.7B is the singular value decomposition (SVD) ellipticity based on the magnetic component of the 250 Hz waves during this time period (*Santolik et al.*, 2003). The ellipticity indicates the polarization of the wave, with -1 as a left hand polarized wave, 1 as a right hand polarized wave, and 0 as a linearly polarized wave. Figure 5.7C is the pitch angle spectrogram from HOPE for the 3.38 eV energy channel. The black line is the 250 Hz power spectral density. In all of the panels, the orange dotted lines highlight the post-midnight sector between $2 < L < 3$ and the pink dotted lines highlight the $2 < L < 3$ afternoon ($15 < L < 18$) sector.

From the panels in Figure 5.7, there is an enhanced population around PA = 90^o between 10:25 - 11:30 UT. At this same time, there are enhanced power spectral densities at or near the sixth harmonic of the H^+ cyclotron frequency. The waves

in the equatorial noise frequency range, however, are primarily right hand polarized, indicating plasmaspheric hiss. In the post-midnight sector, there is also an absence of high power spectral densities and the pitch angle spectrograms reveal a relative minima in the PA = 90^o population in this region. The overall fluxes in the 3.38 eV energy range are severely depleted between 9:00 - 9:45 UT compared to the 10:25 - 11:30 UT 3.38 eV fluxes.

Figure 5.7C also shows relatively low 250 Hz power spectral densities in the post-midnight sector compared to the inbound orbit power spectral densities and a near constant refilling population from the 0^o and 180^o pitch angle fluxes. This case study shows an example of nightside observations of low power spectral densities paired with little to no PA = 90^o H^+ population, as well as dayside observations where both of these values are high. This provides additional evidence supporting the idea that plasma waves could be heating the low energy ions. This theory is supported by previous results in the literature (*Curtis*, 1985; *Olsen et al.*, 1987; *Singh and Hwang*, 1987; *Horne et al.*, 2000).

5.4 Polarization Reveals It's Mostly Plasmaspheric Hiss

However, there is conclusive evidence that these waves between 150 to 600 Hz at $2 < L < 3$ with large power spectral densities are plasmaspheric hiss. Figure 5.8 shows the median magnetic field ellipticity of 614 days of available data from both Van Allen Probes A and B (double counting, so approximately 307 unique days from each satellite) between February 2013 and April 2015 without distinguishing times of low/high Kp. Left Hand waves are defined as having ellipticity < -0.2, Right Hand waves as having ellipticity > 0.2, and Linear Polarization as waves with ellipticity falling between -0.2 and 0.2 (*Santolík et al.*, 2004; *Li et al.*, 2015). We only take times

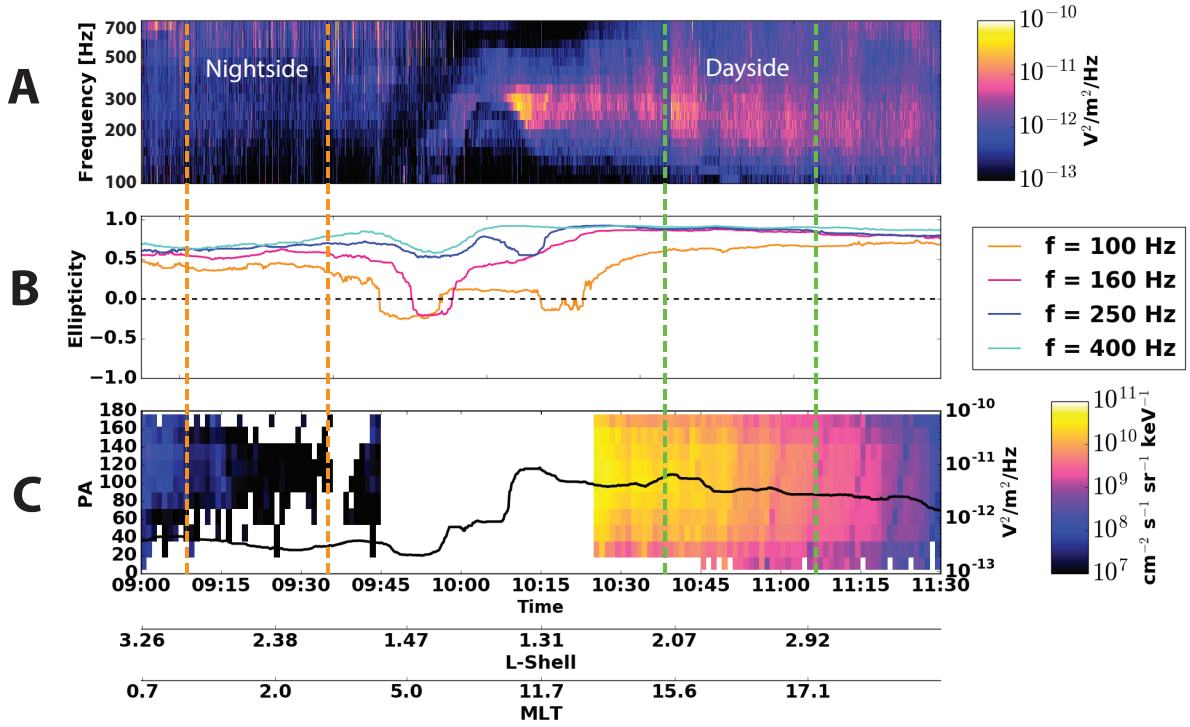

Figure 5.7: Case study on July 2, 2013 from 9 to 11:30 UT with Van Allen Probes A data. Panel A is the EMFISIS WFR spectra between 100 to 700 Hz. Panel B is the ellipticity calculated using singular value decomposition, where +1 indicates right hand polarized waves, 0 is linearly polarized waves, and -1 is left hand polarized waves. Panel C is the H^+ 3.38 eV energy channel differential number fluxes measured in each pitch angle bin over this time interval. The black line is 250 Hz power spectral density. In all panels, the orange dotted lines demarcate where $2 < L < 3$ where $1 < MLT < 4$ and the green dotted lines highlight where $2 < L < 3$ on the dayside between $15 < MLT < 18$.

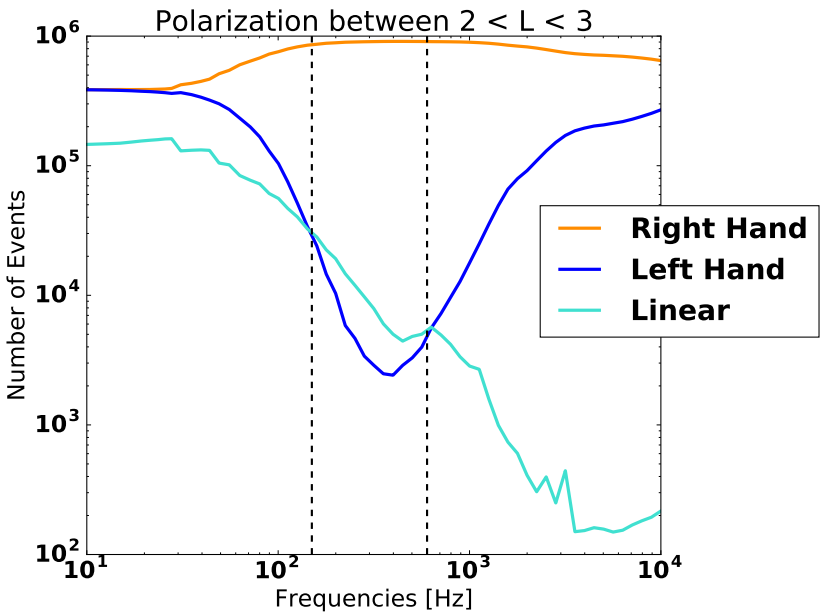

Figure 5.8: Using 614 days of data from both RBSP-A and RBSP-B (double counting, so approximately 307 unique days), we use ellipticity to determine the sense of the waves in addition to the polarization. Left Hand waves are defined as having ellipticity < -0.2, Right Hand waves as having ellipticity > 0.2, and Linear Polarization as waves with ellipticity falling between -0.2 and 0.2. The dotted lines highlight between 150 Hz and 600 Hz, where we see the peak wave amplitudes. Each event is a 1 second measurement between $2 < L < 3$.

where planarity > 0.5. The dotted lines highlight between 150 Hz and 600 Hz, where we see the peak wave amplitudes. Each event is a 1 second measurement between $2 < L < 3$. Figure 5.8 shows that approximately 1% of the wave measurements between $2 < L < 3$ at frequencies of 150 to 600 Hz are linearly polarized or left hand polarized.

Figure 5.9 shows the median polarization and power spectral density of right hand waves versus linearly polarized waves at $L = 2.5$ at MLT = 3, 9, 15, and 21 from February 2013 to April 2015 at times where Kp < 3. The top panel shows the median polarization, or the ellipticity without sense of direction, of all the waves between 0 and 90 degrees. The middle panel shows the power spectral density of waves with

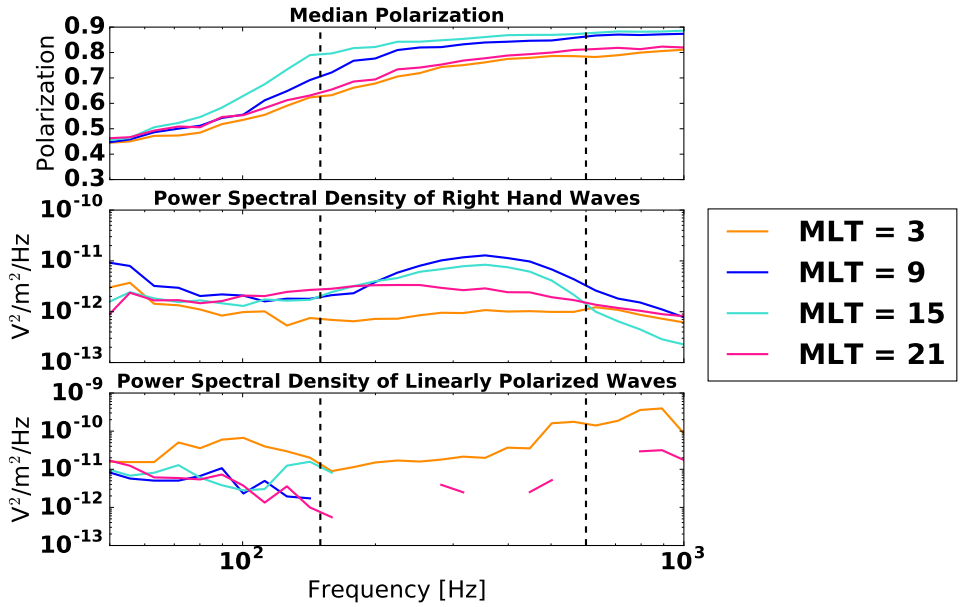

Figure 5.9: These panels show the median polarization and power spectral density of right hand waves versus linearly polarized waves at L = 2.5 at MLT = 3, 9, 15, and 21 from February 2013 to April 2015. The top panel shows the median polarization of all the waves between 0 and 90 degrees. The middle panel shows the power spectral density of waves with polarization greater than 0.7, which here we know from case studies are right hand polarized waves. The lowest panel shows the linearly polarized waves with polarization < 0.2. The dotted lines highlight between 150 Hz and 600 Hz.

polarization greater than 0.7, which we know from case studies and Figure 5.8 are right hand polarized waves. They could be left hand polarized waves since our SVD polarization algorithm can only differentiate between circular and linearly polarized without offering information direction like the limited EMFISIS L4 files can. However, Figure 5.8 confirms that 99% of measurements are right-hand polarized between 150 - 600 Hz, and Figure 5.9 contains analyzed data from every day between February 2013 and April 2015 and was screened based on the Kp index. The lowest panel shows the linearly polarized waves with polarization < 0.2. The dotted lines highlight between 150 Hz and 600 Hz.

From Figure 5.8 and Figure 5.9, we know waves that show high occurrence probability with elevated 1-10 eV populations levels are right hand polarized waves which would not be cyclotron resonant with ions of these energies. Anomalous resonance between the ions and plasmaspheric hiss was considered, as described by *Tsurutani and Lakhina* (1997); *Tsurutani et al.* (1998); *Kozyra et al.* (1994, 1995). However, anomalous resonance requires that the phase velocity of the wave is smaller than the particle parallel velocity, which is in contradiction with our extremely low energy ions with near PA = 90^o and reasonable k vector magnitudes in the inner magnetosphere of 10^{-3} m^{-1} (*Walker et al.*, 2015). Therefore, right hand plasmaspheric hiss, despite evidence in Figure 5.6 and suggestion in previous work (*Curtis*, 1985; *Olsen et al.*, 1987; *Singh and Hwang*, 1987; *Horne et al.*, 2000), is not responsible for the variation in the suprathermal 1-10 eV ion population. Underlying left hand or linearly polarized components of plasmaspheric hiss, however, could be responsible for the ion heating, which will be explored in a follow-up study.

5.5 Conclusions

We have demonstrated that the 1-10 eV H^+ ions measured by the Van Allen Probes exhibit strong diurnal variation in flux measurements with pitch angles near 90^o. In particular, this effect is prominent in lower energy particles as seen in Figure 5.2. Also, when examining pitch angle fluxes against energy, the low energy fluxes at near PA = 90^o rise first and then the higher energy equatorially mirroring H^+ fluxes increase in Figure 5.1. With these factors combined, the depletion of ions described in Chapter 2 is not actually a loss or a transport effect - it is the result of low energy ion heating across the dayside, likely due to wave-particle interactions.

We then demonstrated a possible cause for the 1-10 eV ion heating across the day-

side - higher order cyclotron resonance. Enhanced levels of polarized plasma waves between the ion cyclotron frequency and lower hybrid frequency at $2 < L < 3$ showed similar statistical rises and falls as the 1-10 eV ions in this same region. The binary contingency tables demonstrated that times where waves had amplitudes above 10^{-11} $V^2/ m^2/Hz$ aligned well with times of high low energy ions fluxes. In more than 70% of cases on the dayside at $2 < L < 3$, high power spectral density waves occurred with high particle fluxes. In the post-midnight sector, over 70% of the instances had low power spectral densities and low particle fluxes below $L < 3$.

To further solidify this relationship, a case study was presented where high power spectral densities at 250 Hz occurred when HOPE measured high PA near 90^o populations. In the post-midnight sector, this case study showed that the equatorially mirroring population was at a relative minimum while the 0^o and 180^o pitch angle bins were at a relative maximum. However, this case study also highlights that these high power spectral density waves on the dayside at $2 < L < 3$ are right hand polarized plasmaspheric hiss not linearly polarized equatorial noise. Figures 5.8 and 5.9 confirm that the 150 - 600 Hz waves that exhibit similar diurnal variation to the 1-10 eV ion fluxes are right hand polarized approximately 99% of the time and would not cyclotron resonate with the 1-10 eV ions.

Open questions still remain. Previous studies connected suprathermal ions with the presence of high power spectral density equatorial noise in the equatorial plane; however, the polarization analysis performed in our study reveals that these waves between $2 < L < 3$ are primarily plasmaspheric hiss. Nevertheless, the binary contingency table in Figure 5.6 demonstrated a connection between the 1-10 eV H^+ fluxes and plasmaspheric hiss, so there may be a third variable affecting both plasmaspheric hiss presence and 1-10 eV H^+ energization on the inner plasmasphere dayside. The

potential heating of He^+ and O^+ has not been examined in regards to a connection with plasmaspheric hiss. Also the low energy electrons (< 500 eV) have not been examined in the Van Allen Probes dataset yet in regards to wave activity or in relation to fluctuations in the low energy 1-10 eV population, similar to the findings of *Knudsen et al.* (1998). Our study concludes that contrary to prior evidence (*Curtis*, 1985; *Olsen et al.*, 1987; *Singh and Hwang*, 1987; *Horne et al.*, 2000), large power spectral density right hand waves with frequencies between 150 Hz to 600 Hz in the near-Earth equatorial plane do not interact with the 1-10 eV ion population although they exhibit similar diurnal variation.

CHAPTER VI

1-10 eV H^+ Heated by X-mode Waves

6.1 Introduction

Discoveries from the Van Allen Probes mission have reopened a discussion on how waves interact with thermal plasma. Recent studies that examined the 1-10 eV high energy tail of the thermal ion population in the magnetosphere contradicted previous assumptions that this population was non-interacting with plasma waves. The 1-10 eV H^+ ion population was found to reach a minimum density by a factor of 122 in the post-midnight sector (MLT = 3) compared to dayside partial densities in Chapter 2. In subsequent studies, this partial density minimum was demonstrated to be from wave-particle interactions, although the waves and time scales of the resonances were not identified in Chapters 4 and 5. The remaining open question from these studies was: could the small left hand component of ULF waves (100s of Hz) in the inner plasmasphere resonate with the 1-10 eV H^+ ions and enhance the suprathermal tail of the plasmasphere?

Thermal ions, with temperatures of less than 1 eV, are often neglected in consideration of plasma wave interactions (*Gurnett*, 1976; *LaBelle et al.*, 1988; *Oya et al.*, 2014; *Sicard-Piet et al.*, 2014; *Gallagher and Comfort*, 2016). Especially in models, the thermal ions are often included as a cold and dense medium but not considered

as an energy recepient in wave-particle interactions (*Fok et al.*, 1995; *Bortnik et al.*, 2011). Most plasma waves do not interact with low energy ions. Electromagnetic Ion Cyclotron waves (EMIC) waves, for example, will interact with low energy electrons but typically resonate with keV ions (*Thorne et al.*, 2006).

Equatorial noise heats thermal ions via cyclotron resonance (*Olsen et al.*, 1987; *Singh and Hwang*, 1987; *Laakso et al.*, 1990). Equatorial noise waves are low frequency X-mode, nearly linearly polarized magnetic field fluctuations generated by unstable energetic proton ring velocity distributions (*Perraut et al.*, 1982; *Gary et al.*, 2010). Equatorial noise ranges in frequency from approximately 20 Hz to a few hundred Hz and lies below the lower hybrid frequency (*Němec et al.*, 2015; *Boardsen et al.*, 2016). Equatorial noise is commonly found between 2 and 7 Earth radii and within 10 degrees of the magnetic equator (*Russell et al.*, 1970; *Němec et al.*, 2006). Strong diurnal variation has been previously seen in Cluster observations of equatorial noise outside of the plasmasphere, with a peak at MLT = 12 and a minimum in the post-midnight sector between MLT = 0 and 6 (*Hrbáčková et al.*, 2015).

Three instruments onboard the NASA Van Allen Probes mission allow us to consider possible low energy ion and wave resonance in the inner plasmasphere. The Van Allen Probes mission, launched in late 2012, consists of two satellites that orbit in the near-equatorial plane within 6 Earth radii (*Mauk et al.*, 2014). The Electric Field and Waves (EFW) instrument measures the analog electric field component of plasma waves between 2 Hz and 10 kHz and then this information is transferred to the Electric and Magnetic Field Instrument Suite and Integrated Science (EMFISIS) instrument (*Wygant et al.*, 2013; *Kletzing et al.*, 2014). EMFISIS also me simultaneously measures the wave magnetic field from 2 to 10 kHz using a triaxial search coil magnetometer and the DC magnetic field. The X-mode frequency range we examine

is between 250 Hz to 400 Hz, well within the resolution capabilities of EMFISIS. The Helium Oxygen Proton Electron (HOPE) instrument measures the ion and electron populations of the equatorial inner magnetosphere between 1 eV and 50 keV (*Funsten et al.*, 2014). HOPE also uses the EMFISIS magnetometer measurements to map the observed fluxes into pitch angle space and assign nominal pitch angle bins.

This study explores how enhanced plasmaspheric hiss (*Li et al.*, 2015) in the equatorial plasmasphere masks underlying X-mode equatorial noise (*Russell et al.*, 1970). We determine where linearly polarized waves will contribute to the 1-10 eV ion heating rate between $2 < \mathrm{L} < 3$ and show that the calculated heating rates agree with the observations of 1-10 eV partial H^+ densities.

6.2 Theoretical Support of Cyclotron Heating

To justify this claim that equatorial noise is interacting with the low energy ion plasma population between $2 < \mathrm{L} < 3$, we demonstrate that higher harmonic cyclotron resonance with X-mode waves will appreciably heat the tail of the cold plasma distribution. For plasma waves in the inner magnetosphere, the cyclotron resonance condition is,

$$\omega - k_{||} V_{||} = n\Omega_{H^+} \tag{6.1}$$

where ω is the wave frequency in rad/s, Ω_{H^+} is the cyclotron frequency of H^+, and $k_{||}$ and $V_{||}$ are the wave number and ion velocity parallel components to the background magnetic field. We assume that the magnitude of the k vector is $< 10^{-2}$ due to the long wavelength approximation (described later) and that the ions are nearly

equatorially mirroring with very small parallel velocities. Therefore, we can assume the $k_{||}V_{||}$ term is 0. For H^+ cyclotron resonance in the inner magnetosphere, the resonance condition becomes:

$$\omega_{H^+} = \frac{nqB_0}{m_{H^+}} \tag{6.2}$$

For a sample calculation at L = 2 and n = 1, we would expect a magnetic field of approximately 1200 nT (from the IGRF model - *Finlay et al.* (2010)). When we substitute in values, we find that expected resonance is at 15 Hz. The plasma waves we examine range approximately from 250 Hz to 400 Hz, so we are specifically looking at harmonics where n > 9.

At higher harmonics, particle temperatures do not grow uniformly across a Maxwellian distribution like they do for n = 1 cyclotron resonance. Instead, the higher order harmonics of incoherent heating serve to 'thicken' the tail of the Maxwellian distribution, not affecting the core of the population (*Schmitt*, 1976). For coherent heating, if the wavelength of the electromagnetic wave is long enough, then we can introduce a large wavelength approximation that simplifies the Bessel functions defining particle motion. The large wavelength approximation is applicable when $k_\perp m_i v_\perp$ / $qB_0 << 1$. Here, B_0 is the equatorial magnetic field. For our scenario, a 1 eV H^+ ion with a pitch angle (ϕ) of approximately 90^o in a 1200 nT magnetic field will have a Larmor radius (r_L) of 85 m. In this case, $k_\perp$ will need to be 10^{-2} or less to satisfy the long wavelength approximation we use here. With this reduction, the equations of motion for our system become:

$$\dot{R} = \gamma_n R^{n-1} \cos\psi, \dot{\phi} R = -n\gamma_n R^{n-1} \sin\psi + R\dot{\phi} \tag{6.3}$$

where

$R = k_\perp \, r_L$
$\gamma_n = \gamma/[2^{n-1}(n-1)!]$
$\gamma = k_\perp \, E^*_{LH}/B_0$
$\psi = \phi - n \, \Psi$

and Ψ is a phase offset of the wave, ϕ is the phase of the wave at the guiding center location, E^*_{LH} is the left hand component of the electric field power spectral density at the guiding center location, and n is the degree of the harmonic of the gyrofrequency. In this study, we only examine times where n > 1, so the relaxation time is very large and on the order of R^{1-n}/γ_n. The relaxation time is longer for a slow particle than a fast particle, resulting in heating of the tail of the distribution of particles. To estimate the time it takes for appreciable heating of the tail, from *Schmitt* (1976) we can use:

$$t = \frac{2^{n-1}(n-1)!}{\gamma_n (n-2) R^{n-2}} \tag{6.4}$$

It is critical for appreciable particle heating that the time given in Equation 6.4 is on the order of the time of coherent interaction between the waves and the particles. If this is the case, then the tail of the distribution should heat. Since we do not know the k vector of the waves interacting with the ions, it makes the most sense to solve for k in these equations by setting the time of coherent interaction between the wave and the ions to the bounce period of the nearly equatorially mirroring (PA = 89.9^o) ions (*Roberts and Schulz*, 1968). Rearranging terms, our equation to solve for k is:

$$k = \left(\frac{2^{n-1}(n-1)! B}{\sqrt{E^*_{LH}}(n-2)\tau_B r_L^{n-2}} \right)^{1/(n-1)} \tag{6.5}$$

where B is the local magnetic field and τ_B is the bounce period, :

$$\tau_B = \frac{LR_E}{v_{||}}(3.7 - 1.6\sin(\phi)) \tag{6.6}$$

where L is McIlwain's L-shell number (*McIlwain*, 1961) and ϕ is the pitch angle of the ion.

We can incorporate this solution for k into an analytic model that uses data and spacecraft position to solve for k and then determine if the wave's k vector is small enough for plasma wave and ion resonance to occur. Testing with a 1 eV H^+ ion with a pitch angle of $\phi = 89^o$, we solve for $V_{||}$ and $V_\perp$ from the energy of the particle and it's pitch angle. We then determine the resonant harmonic (n) from Equation 6.2 and the bounce time from Equation 4 using plasma wave frequencies between 250 to 400 Hz and the median measured magnetic field from the EMFISIS magnetometer data from February 2013 to April 2015 binned by 0.25 L-Shell and 0.5 MLT. The model then solves for k using E^*, the median power spectral density of the left hand component of the measurements at each frequency between 250 to 400 Hz from February 2013 to April 2015 binned by 0.25 L-Shell and 0.5 MLT from the EMFISIS instrument.

To determine the X-mode component of the wave, which is the part of the plasma wave resonant with the low energy H^+, we calculate the ratio of the middle to major axis of the polarization ellipsoid using singular value decomposition (SVD) (*Ladreiter et al.*, 1995; *Santolik et al.*, 2003). Using the SVD method, we can determine the wave vector direction in a single hemisphere (without direction along field line), the direction of axes of the polarization ellipse, and the planarity of polarization from the spectral matrices of the magnetic field component available in the EMFISIS level 2 data set. Chapter 5 showed that most of the waves in the 250 - 400 Hz range are plasmaspheric hiss (*Thorne et al.*, 1973; *Bortnik et al.*, 2008), which is an incoherent

right hand polarized wave.

However, these waves are not purely right hand polarized, where the ratio of the middle to major axis of polarization would be 1. Instead, they have ratios of the middle to major axis of polarization between 0.5 to 0.9 because the EMFISIS measurements reflect the superposition of many waves coexisting in the same space. With the cold plasma approximation, which is valid between $2 < L < 3$, there exist only two plasma modes in the 250 Hz to 400 Hz range - right hand circular R mode (parallel to B_0) and linear X-mode (perpendicular to B_0). Thus, we make an assumption that the X-mode component of the waves is (1 - the ratio of the middle to major axis of polarization)/2 (*Chang et al.*, 1986; *André et al.*, 1990; *Crew et al.*, 1990; *Kintner et al.*, 1996). This assumption allows us to calculate the fraction of the power spectral density that is linearly polarized by multiplying the fraction of the X-mode wave component by the total power spectral density for each EMFISIS measurement.

We then calculate the fraction of the linearly polarized wave that would interact with the ions. Linearly polarized X-mode waves can transfer half of their energy to ions and half to electrons, so we define the left hand component, E^*_{LH}, as $E^*_{LH} = 1/2\ E^*_X$ (*Knudsen et al.*, 1998). Figure 6.1 shows the median power spectral density (E^*_{LH}) of the X mode component of the waves at frequencies between February 2013 to April 2015 binned by 0.25 L-Shell and 0.5 MLT. At 250-400 Hz, the power spectral densities are above 10^{-12} $V^2/m^2/Hz$ from MLT = 6 to MLT = 19, and they gradually decrease across the night-side, reaching a minimum at MLT = 3 with power spectral densities closer to 10^{-14} $V^2/m^2/Hz$.

To determine how the power spectral densities affect the low energy ion population at different frequencies, we need to calculate a heating rate. Our analytic model

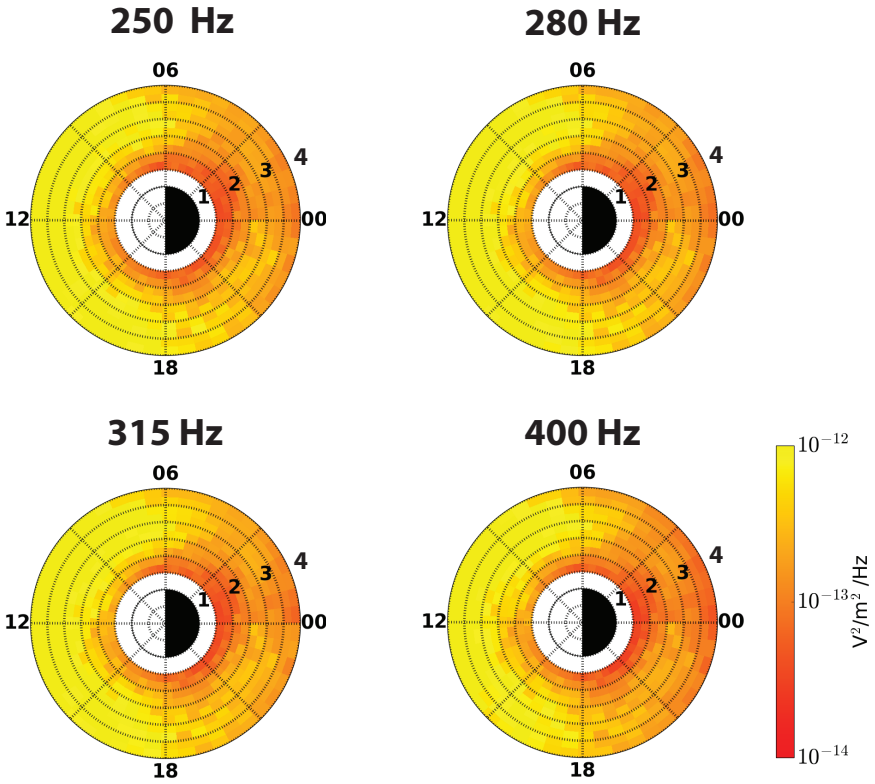

Figure 6.1: The median X-mode component power spectral densities ($E_{LH}{}^*$) from February 2013 to April 2015 calculated from EMFISIS measurements at several frequencies between 250 - 400 Hz.

based on EMFISIS data and the theoretical formulation described above gives us an estimate on the magnitude of the wave k vector. If k is smaller than 10^{-2} and the ratio of the right hand to left hand polarization is greater than $r_L|k|$ (*Schmitt*, 1976), then the plasma wave does not interact with the H^+ ions. If $|k|$ is valid for ion - wave resonance, we can calculate a heating rate from *Singh and Hwang* (1987) derived from quasi linear theory using Equation 6.7:

$$\frac{dW_\perp}{dt} = \frac{1}{2}\frac{q^2 E^*_{LH}}{m_i} \tag{6.7}$$

where $W_\perp$ is the perpendicular energy added to the ions.

6.3 Results

From our derivations, we determined the heating rate based on linearly polarized power spectral densities at different frequencies and then compared this to the changes in low-energy ion differential number flux with MLT. Figure 6.2 shows the results of the heating rate calculated from E^*_{LH} at specific frequency bands. The shaded regions highlight areas where our analytic model calculated k vector magnitudes violated our condition that $|k|$ and the right hand to left hand polarization ratio must be sufficiently small. At 250 and 280 Hz and PA = 89^o, the waves interact with 1 eV ions at all L-Shells within $2 < L < 3.5$ on the dayside. In the post-midnight sector, resonant heating occurs at $2.5 < L < 3.5$. At 315 and 400 Hz, the diurnal variation becomes more pronounced, with resonant heating in the post-midnight sector only occurring between $2.5 < L < 3$ at some MLTs. At all frequencies between 250 and 400 Hz, the post-midnight sector has a low heating rate (approximately 10^{-2} eV/hour) whereas the dayside has a much higher heating rate (approximately 1 eV/hour).

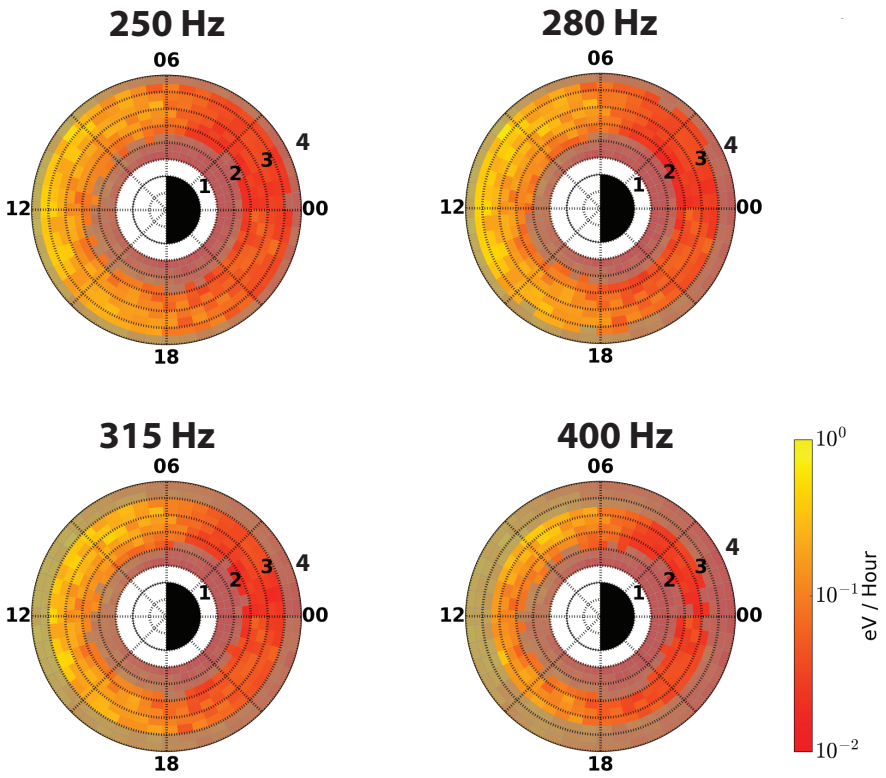

Figure 6.2: Heating rate determined from analytic model for a selected number of frequencies between 250 - 400 Hz using EMFISIS power spectral densities and magnetic field measurements. The gray shaded regions highlight where $|k|$ is not valid based on the left hand to right hand polarization ratios or where the long wave-length approximation is violated. The results were produced using 1 eV H^+ with a pitch angle of 89^o in the analytic model.

Figure 6.3 shows the same heating rate determined from E^*_{LH} at specific frequency bands but highlights relative changes as a line plot. The shaded region highlights where the post-midnight sector MLT values are ($1 < \text{MLT} < 4$). The solid lines indicate where the heating rate has a valid k vector solution based on magnetic field conditions at the satellite measurement location. The dotted lines are where the magnitude of the calculated k vector are too large for the long wavelength approximation. In the line plots at all frequencies between 250 and 400 Hz, the diurnal variation in heating rate is pronounced, with a maximum at MLT = 8 and and minimum at MLT

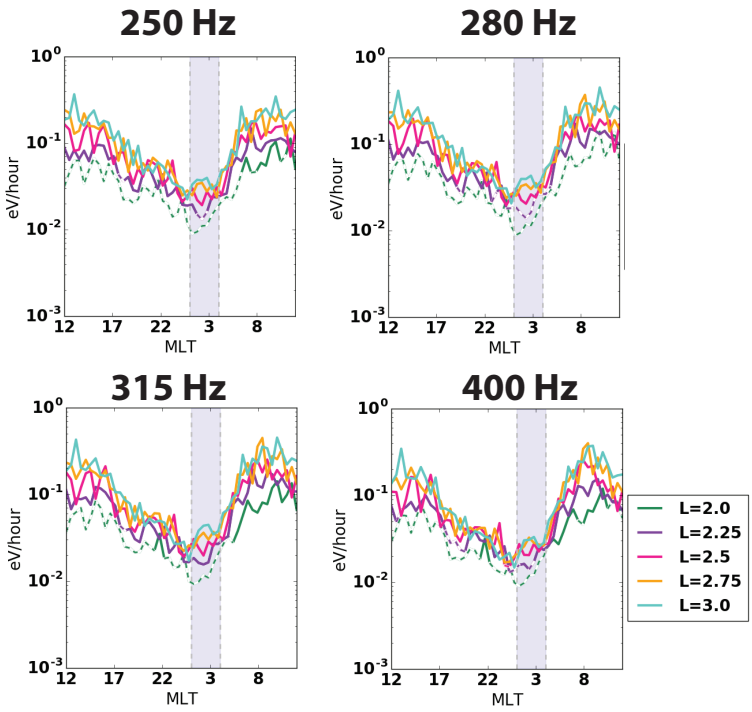

Figure 6.3: Heating rates determined from analytic model for a selected number of frequencies between 250 - 400 Hz using EMFISIS power spectral densities and magnetic field measurements at specific L-Shells. The dotted lines highlight where $|k|$ is not valid based on the left hand to right hand polarization ratios or where the long wave-length approximation is violated. The shaded region highlights the post-midnight sector ($1 < L < 4$).

= 2. The heating rate increases rapidly between MLT = 4 and MLT = 8 and slowly declines across the afternoon and pre-midnight sectors.

The X-mode waves between 250 and 400 Hz contribute differently to the total integrated broadband heating rate. Figure 6.4 shows the median contribution of each frequency to the total heating rate from February 2013 to April 2015 at L = 2.5. The highest heating rate (integrated to $>$ 1 eV/hour) occurs at 200-550 Hz at MLT = 5 to MLT = 9. The frequency band with the lowest heating rate is 2-200 Hz at all MLTs (integrated to $<$ .01 eV/hour). Overall, the most diurnal variation in heating rates is from 250 Hz to 400 Hz, which is why we focus our study on this frequency

space. In this frequency range, the minimum heating rate at all MLTs occurs in the post-midnight sector. Above 500 Hz, the k vectors are too large on the dayside, our long wave length approximation is violated in the model, and the time scales for heating are too long for a significant diurnal influence.

Figure 6.5 gives the median broadband heating rate from the 250 to 400 Hz X-mode waves at L-Shells between $2 < L < 3$. The heating rate is calculated using E^*_{LH} and Equation 6.7. The dotted black line is the HOPE H^+ 1-10 eV median partial density at L = 2.5 over the same range. Figure 6.5a is the broadband heating rate for a 89.9^o, 1 eV particle. The broadband heating rate exhibits the same minimum in the post-midnight sector as the L=2.5 1-10 eV H+ partial density and similar peaks at MLT = 8 and MLT = 13. The low L-Shell heating rates are near the limit for large k vector magnitudes which is why the line is not continuous. The highest heating rates are at L = 3.0.

Figure 6.5b is the broadband heating rate for a particle with PA = 89.9^o at L = 2.5 at different energies. The lower energy particles (< 1.5 eV) are almost continuously heated across all MLTs, with a minimum in the post-midnight sector and a maximum at MLT = 8. Above 1.5 eV, the heating time scales can be much longer than the bounce period of the particle, so heating is more erratic.

Figure 6.5c is the broadband heating rate for a 1 eV particle at L = 2.5 with different pitch angles. Particles with pitch angles above 80^o are most effectively and continuously heated across all MLTs. Particles with pitch angles $< 80^o$ heat effectively on the dayside, but do not heat across the nightside. This is because the bounce times are too long compared to the expected wave-particle interaction time period.

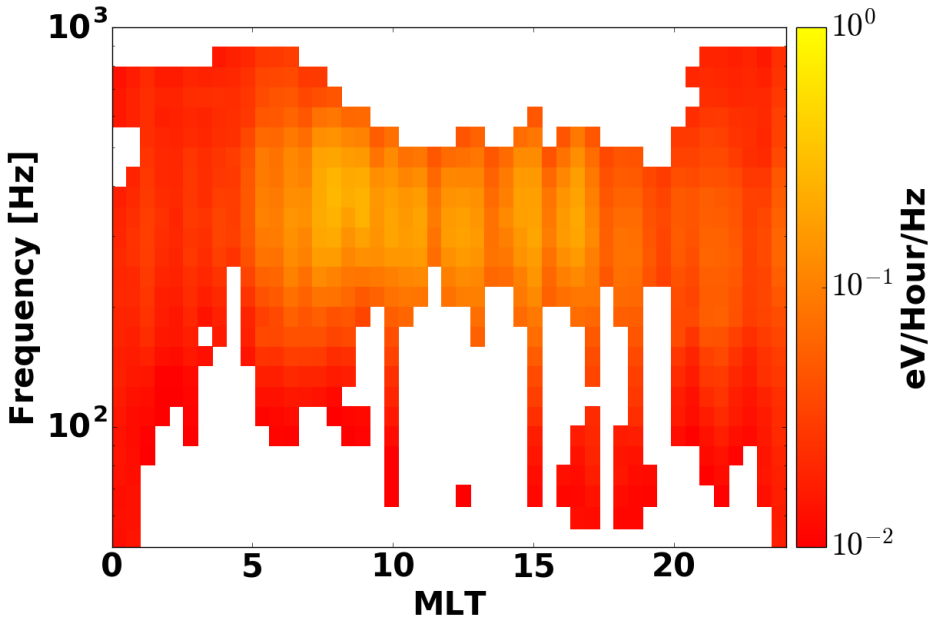

Figure 6.4: Calculated heating rates from analytic model from 20 to 1000 Hz using the X-mode component EMFISIS power spectral densities and magnetic field measurements at L = 2.5 for 1 eV H^+ ions. The white areas represent frequency-MLT space where the model predicts heating will not occur.

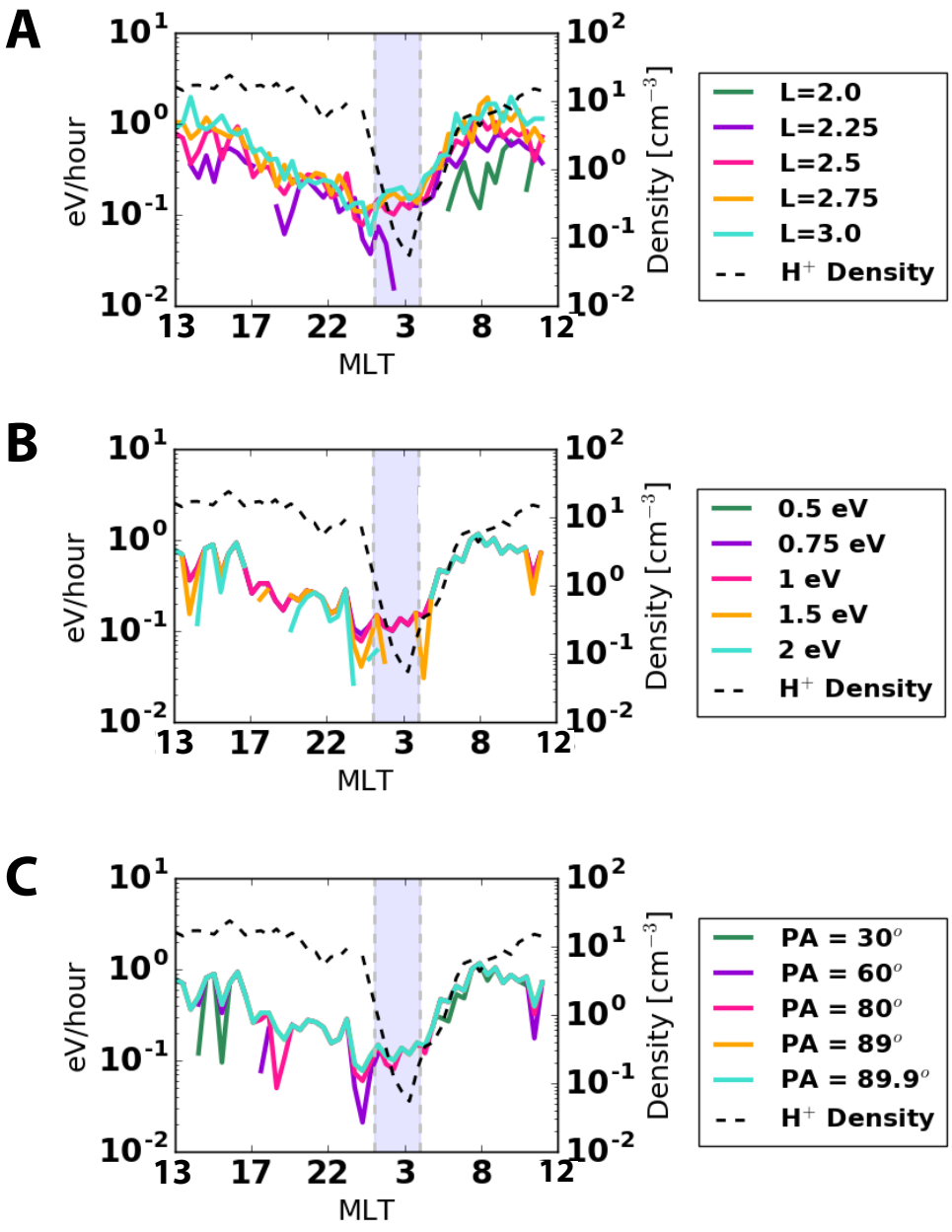

Figure 6.5: Integrated broadband heating rates determined from analytic model from 250 to 400 Hz using the X mode component EMFISIS power spectral densities and magnetic field measurements. Panel A shows the integrated heating rate for different L-Shells for a 1 eV H^+ ion with PA = 89^o, Panel B for different initial energies for a H^+ ion with PA = 89^o at L = 2.5, and Panel C for different initial pitch angles for a 1 eV H^+ ion at L = 2.5.The black dotted line is the H^+ 1-10 eV partial density at L = 2.5 from HOPE. The shaded region highlights the post-midnight sector (1 < MLT < 4).

The minimum of the broadband heating rate at L = 2.5 is 0.27 eV/hour and occurs at MLT = 4 and the minimum in the partial 1-10 eV H^+ density at L = 2.5 is 0.055 particles per cm^{-3} and occurs at MLT = 3. The maximum broadband heating rate at L = 2.5 is 2.76 eV/hour at MLT = 13. The maximum 1-10 eV H^+ partial density at L = 2.5 is 23.8 particles per cm^{-3} and occurs at MLT = 15. The Pearson correlation coefficient (*Sheskin*, 2003) is 0.77 between the broadband wave heating rate and the 1-10 eV H^+ partial density at L = 2.5. A correlation coefficient is considered strong if it is above 0.68 (*Taylor*, 1990). Figure 6.5 demonstrates a very strong connection between the 1-10 eV H^+ ion densities and the broadband heating rate.

Figure 6.6 shows the integrated median broadband heating rate from 250-400 Hz waves for 1 eV H^+ ions with PA = 89^o predicted by the analytic model at L < 4 and at all MLTs. Similar to the previous figures, this dialplot reinforces that there is an enhanced dayside heating rate that declines across the pre-midnight sector and hits a minimum in the post-midnight sector. The dayside heating is primarily confined to $2 < L < 3.5$. Beyond L > 3.5, the k vectors predicted by the analytic model are too large to satisfy our long wavelength approximation. Inside L < 2, the bounce times are too short for interaction between the ions and waves according to the assumptions made by our model. Changes to our requirements for k and the bounce periods would affect at what L-Shells heating will occur, and this should be taken into consideration for future studies.

6.4 Discussion

Although previous studies have explored connections between high-amplitude inner magnetosphere waves and thermal plasma (*Olsen et al.*, 1987), this study, for the first time, shows the connection of the X-mode component of these high-amplitude

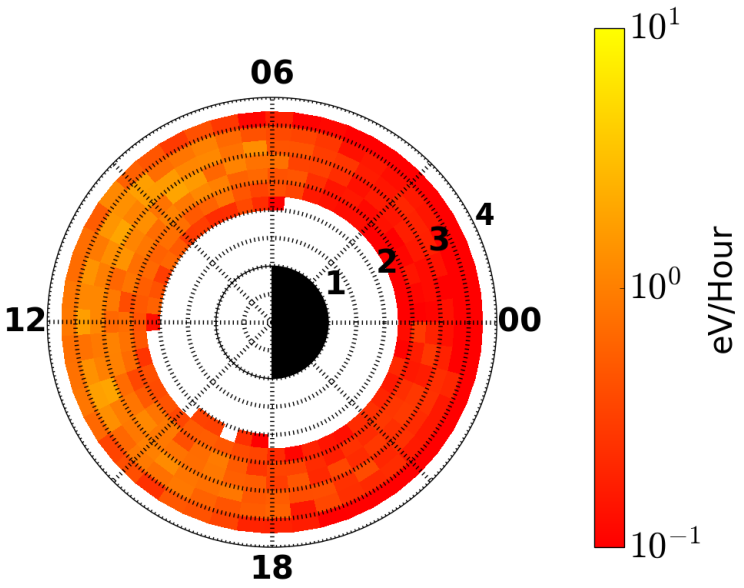

Figure 6.6: Integrated broadband heating rates for 1 eV H^+ ions at PA=89^o determined from analytic model from 250 to 400 Hz using the X mode component EMFISIS power spectral densities and magnetic field measurements shown at all MLTs and at L < 4. The white areas are where there is no heating suggested by the model.

waves and the theoretical support for these waves to heat the ions on probable time scales. The heating rate aligns well with the observed H^+ partial densities from the HOPE instrument in Chapter 2 and are consistent with the diurnal variation (heating) of the approximately PA = 90^o population in Chapter 4.

Chapter 5 results showed that although there was a strong connection between increased plasma wave activity and H^+ 1-10 eV ion fluxes in the Van Allen Probes, the plasma waves in the 100 Hz - 600 Hz range were pre-dominantly right-hand polarized. The results of the current study expand upon the findings of Chapter 5 and show that by treating the waves as a superposition of right-hand and linearly polarized waves, we can determine the component of the waves between 250 - 400 Hz that interact with the 1-10 eV H^+ ions.

However, it is important to note that other factors contribute to the 1-10 eV H^+ population presence. For instance, ionospheric thermal plasma transport does contribute to the partial density, and it could be responsible for the slow attenuation of 1-10 eV H^+ ion densities across the pre-midnight sector compared to the 250 - 400 Hz power spectral densities (*Vickrey et al.*, 1979). Further, in this study we only examine the PA = 89^o H^+ 1 eV heating; however, different energy particles, such as a 5 eV at PA = 70^o, will have different resonance conditions. A kinetic model with pitch angle and energy diffusion is necessary to fully resolve the heating and loss of the suprathermal plasmaspheric tail, such as the one by *Liemohn et al.* (1999).

The results of this work suggest that thermal plasma should be taken into consideration for wave-particle interaction models on a magnetospheric scale and affect how we calculate a distribution function of total ion densities from the 1-10 eV population. For wave-particle interactions, a damping coefficient of X-mode waves should be applied based on energy transferred to the cold H^+ ions. To construct Maxwellian distribution functions from HOPE data, observations from the post-midnight sector should be used since that is the region unaffected by the X-mode wave suprathermal heating.

6.5 Conclusions

We demonstrate that the 1-10 eV H^+ ion can be suprathermally heated by X mode waves in the 250 - 400 Hz frequency range at $2 < L < 3$ using a combination of analytic models based on particle motion and derived from quasi-linear theory. The observed 1-10 eV H^+ partial densities have a 0.77 correlation coefficient with the calculated heating rates from particle interaction with observed X-mode waves. We conclude that there is strong evidence that X-mode waves are heating the 1-10 eV

H^+ across the dayside at $2 < L < 3$ which then attenuates across the pre-midnight sector, hitting a minimum in the post-midnight sector. These results demonstrate that the apparent post-midnight sector minimum in the 1-10 eV partial densities of HOPE is a consequence of suprathermal dayside heating.

CHAPTER VII

Conclusions and Future Work

7.1 Motivation

With increasing reliance on satellites and GPS, it is critical for us to have an excellent understanding of the near-Earth plasma environment. Simple changes in temperature anisotropies, for example, can lead to large scale changes in plasma wave dynamics and lead to spacecraft charging or gaps in GPS coverage. Although not directly responsible for spacecraft charging or damage, the low energy (1-10 eV) ions in the plasmasphere serve as a thermostat - they moderate wave activity and neutralize temperature anisotropies. Changes in the 1-10 eV H^+ ions can lead to larger changes on a global scale.

The work in this thesis focuses on describing a depletion observed in the post-midnight sector of Earth's plasmasphere and proving that this effect is from plasma wave interaction with the thermal H^+ plasma between $2 <$ L-Shell < 3. Chapters contained within the thesis explore spacecraft charging and it's effect on the 1-10 eV ions, pitch-angle distributions of the low-energy ions, distinguishing between different plasma wave types, and demonstrating the energy transfer from equatorial noise to thermal H^+ plasma agrees with what we see. Exploration of H^+ temperatures and ground-based radar observations of thermal electrons in the ionosphere are included

as appendices in the thesis as work done in parallel to the contents of the thesis.

7.2 Summary

In each chapter, a step forward was made in recognizing and explaining the origins the 1-10 eV H^+ depletion in the post-midnight sector between $2 <$ L-Shell < 3. Here, we provide a summary of each chapter.

7.2.1 Summary of Chapter 2

We found strong MLT dependence in the high-energy tail of the plasmasphere using the HOPE instrument data to look at plasma density for H^+, He^+, and O^+ from 1 - 10 eV during quiet time periods. Chapter 2 has two main findings: there is diurnal variation across all three ion species in the 1-10 eV range and there is a compositional difference in the amount of loss observed across the post-midnight sector.

We observed that H^+, He^+, and O^+ decrease rapidly, similar to ionospheric temperatures across the nightside. We propose that all three species experience rapid density gains at the dawn terminator because the dayside plasmasphere heats quickly from the magnetic mirroring and energy loss of electrons scattered from photoionization from neutrals. This thermalization of the plasmasphere energizes the ions over the course of a couple of hours, which is what we observe across the dawn terminator in Figure 2.3.

We see that He^+ loss is the smallest, and H^+ and O^+ densities follow each other closely because of the charge resonance that exists between these two species. Therefore when H^+ is lost faster than He^+ and O^+ because of its low mass, the net effect

is a rapid combined loss of H^+ and O^+ because of their tandem behavior. The enhanced high-energy densities from photoionization in these ions remains throughout the day, and then declines slowly after the dusk terminator. The populations almost vanish in the post-midnight sector, with density values dropping a factor of 28 to 150.

He^+ in the high-energy plasmasphere tail exhibits different MLT dependence than H^+ and O^+. The source of ionospheric He^+ is photoionization, which peaks in the morning sector and then again at dusk. The increase of dayside He^+ is thought to be from the dayside warm ionosphere exerting a pressure on He^+ ions, pushing them into plasmaspheric flux tubes. The decline in He^+ on the nightside, particularly in the post-midnight sector, is still significant at a factor of 28 but is not as sharp as H^+ and O^+. He^+, although lighter than O^+, has a slower loss rate because of the O^+ charge resonance with H^+.

7.2.2 Summary of Chapter 3

In Chapter 3, spacecraft charging on a conducting spacecraft within geosynchronous orbit was explored. Unlike previous non-conducting satellite missions, spacecraft charging on the conducting Van Allen Probes was not as intense. The Van Allen Probes tended to charge slightly positive; however, times of significant negative charging still occurred in the time period we examined.

We explored statistics based on the distribution of spacecraft charging measured by EFW and its relationship with MLT and L. It was found that most slightly negative charging occurred at low Ls, at daytime MLTs, and in Earth's shadow. Positive charging occurred at all Ls and MLTs. Strong positive charging occurred across the night-side at high Ls, while strong negative charging occurred primarily at high Ls in

the post-midnight sector. This strong negative charging above L > 3 occurred while the spacecraft was not in eclipse. We think the strong positive charging is due to bad data; however, we do not have an explanation of why it is mostly centered around midnight and in the pre-midnight sector.

To obtain spacecraft charging values below the -200 V limit of EFW, we also developed an algorithm to determine the level of spacecraft charging by extracting the charging line seen in the HOPE instrument H^+ spectra. From this technique, we found that EFW underestimated spacecraft charging by approximately 5 V or 17 %. During times when the spacecraft potential reached below -50 V, the two methods provided very similar measurements. However, the charging line extraction method was not a stand alone method, so we concluded that it was best to use both the EFW spacecraft potential measurements and the charging line extraction method to obtain the best understanding of spacecraft charging in the Van Allen Probes.

The connection between keV electron energy fluxes and spacecraft charging was presented in this study. Similar to previous results, we found that for the Van Allen Probes there was a connection between spacecraft charging and keV electron energy fluxes. The link between high-energy fluxes during charging times extended from 1 eV to 5 keV. This study did find an electron energy flux threshold of 3×10^7 keV cm^{-2} s^{-1} sr^{-1} keV^{-1} for 3 keV electrons where intense charging is more likely to occur if this threshold is met; however, there are times the electron energy fluxes reach this threshold and significant negative spacecraft charging does not occur.

Spacecraft charging was compared with electron temperature, pressure, electron density, low-energy (1-210 eV) H^+ density, MLT, and L. In times of charging on the Van Allen Probes, electron temperature, electron density, and, consequently, elec-

tron pressure were all generally elevated during times of significant charging. The strongest connection was between electron pressure and spacecraft charging. However, high electron pressure did not always correlate with times of negative spacecraft charging, so further exploration of this connection is necessary. *Thomsen et al.* (2013) found that the intensity of a spacecraft charging event was determined by average electron temperature, but we did not find as strong of a relationship in our study with the Van Allen Probes.

Our results in Chapter 3 built upon previous work, and we have shown for a conducting spacecraft that there is a keV electron energy flux threshold that, once surpassed, increases the likelihood of charging to occur. Future work is necessary to determine exactly what combination of parameters results in intense negative charging on the Van Allen Probes or another similar conducting spacecraft. The extreme care to maximize conductivity on the Van Allen Probes has resulted in a spacecraft that charged negatively infrequently, allowing for low-energy ion measurement with greater certainty and reduced arcing potential on the Van Allen Probes.

7.2.3 Summary of Chapter 4

In Chapter 4, pitch-angle distributions of the ion fluxes in the HOPE instrument 1-10 eV energy channels from February 2013 to April 2015 were examined to determine the cause of the 1-10 eV H^+ depletion in the post-midnight sector of the plasmasphere. It was found that the near 90^o pitch-angle population was severely depleted in the post-midnight sector compared to the field aligned populations. If these lower 1-10 eV fluxes were from pitch-angle diffusion and charge exchange, a weak residual equatorially mirroring population would have been present in the post-midnight sector accompanied by large field-aligned flows into the ionosphere.

We also show in this chapter, for the first time, low energy HOPE differential number fluxes corrected for spacecraft potential using EFW measurements. The flux depletion in the post-midnight sector is still present in the spacecraft potential corrected fluxes. Further, we show that the 1-10 eV plasma depletion in the near-Earth post-midnight sector does exhibit some geomagnetic activity dependence. At Kp $<$ 1, the fluxes are higher than at Kp $<$ 3 between 2 $<$ L $<$ 3, particularly in the 1.5 eV and 3.0 eV energy channels.

A new algorithm was developed to categorize summed pitch-angle distributions to better quantify why this loss occurs. A peak in Loss Cone distributions in the pre-midnight sector and strong refilling in the dawn sector were noted in the low energy channels. The Loss Cone peak occurred earlier in the dusk sector for the higher energy particles than the lower energy ones. The post-midnight sector was dominated by Uncategorized distributions at higher energies due to low counting statistics, suggesting plasma depletion occurs before the post-midnight sector due to enhanced dusk and midnight Loss Cone distributions. This result has not been seen before, and it suggests that more than simply charge exchange in the top side ionosphere is responsible for the 1-10 eV lower fluxes.

The pitch angle sorting algorithm will be a useful tool for the magnetospheric community and applied to classify pitch-angle distributions at higher energy levels. The algorithm could also classify inner magnetosphere electron pitch-angle distributions. For example, one could conduct a study about pitch-angle distributions on ring current pitch-angle scattering or keV particles at L = 4 during substorm injections (e.g., *Lundin et al.*, 1980; *Smith et al.*, 1996). Also, the results of this study emphasize that source and loss processes in the inner plasmasphere are more complicated than

previously anticipated and may involve more wave heating aspects.

7.2.4 Summary of Chapter 5

Throughout this thesis, we have demonstrated that the 1-10 eV H^+ ions measured by the Van Allen Probes exhibit strong diurnal variation in flux measurements with pitch angles near 90^o. In particular, this effect is prominent in lower energy particles as seen in Figure 5.2. Also, when we examined pitch-angle fluxes against energy, the low-energy fluxes at near PA = 90^o rise first and then the higher energy equatorially mirroring H^+ fluxes increase in Figure 5.1. With these factors combined, the depletion of ions described in Chapter 2 is not actually a loss or a transport effect - it is the result of low energy ion heating across the dayside, likely due to wave-particle interactions.

We then demonstrated a possible cause for the 1-10 eV ion heating across the dayside - high-order cyclotron resonance. Enhanced levels of polarized plasma waves between the ion cyclotron frequency and lower hybrid frequency at $2 < L < 3$ showed similar statistical rises and falls as the 1-10 eV ions in this same region. The binary contingency tables demonstrated that times where waves had amplitudes above 10^{-11} $V^2/ m^2/Hz$ aligned well with times of high low-energy ions fluxes. In more than 70% of cases on the dayside at $2 < L < 3$, high power spectral density waves occurred with high particle fluxes. In the post-midnight sector, over 70% of the instances had low power spectral densities and low particle fluxes below $L < 3$.

To further solidify this relationship, a case study was presented where high power spectral densities at 250 Hz occurred when HOPE measured high PA near 90^o populations. In the post-midnight sector, this case study showed that the equatorially

mirroring population was at a relative minimum while the 0^o and 180^o pitch-angle bins were at a relative maximum. However, this case study also highlights that these high power spectral density waves on the dayside at $2 < L < 3$ are right-hand polarized plasmaspheric hiss not linearly polarized equatorial noise. We confirm that the 150 - 600 Hz waves that exhibit similar diurnal variation to the 1-10 eV ion fluxes are right-hand polarized approximately 99% of the time and would not cyclotron resonate with the 1-10 eV ions.

Open questions still remain. Previous studies connected suprathermal ions with the presence of high power spectral density equatorial noise in the equatorial plane; however, the polarization analysis performed in our study reveals that these waves between $2 < L < 3$ are primarily plasmaspheric hiss. Nevertheless, the binary contingency table demonstrated a connection between the 1-10 eV H^+ fluxes and plasmaspheric hiss, so there may be a third variable affecting both plasmaspheric hiss presence and 1-10 eV H^+ energization on the inner plasmasphere dayside. The potential heating of He^+ and O^+ has not been examined in regards to a connection with plasmaspheric hiss. Also the low-energy electrons (< 500 eV) have not been examined in the Van Allen Probes dataset yet in regards to wave activity or in relation to fluctuations in the low-energy 1-10 eV population, similar to the findings of *Knudsen et al.* (1998). Our study concludes that contrary to prior evidence (*Curtis*, 1985; *Olsen et al.*, 1987; *Singh and Hwang*, 1987; *Horne et al.*, 2000), large power spectral density right-hand waves with frequencies between 150 Hz to 600 Hz in the near-Earth equatorial plane do not interact with the 1-10 eV ion population although they exhibit similar diurnal variation.

7.2.5 Summary of Chapter 6

In the final chapter of this thesis, we demonstrated that the 1-10 eV H^+ ion can be suprathermally heated by X-mode waves in the 250 - 400 Hz frequency range at $2 < L < 3$ using a combination of analytic models based on particle motion and derived from quasi-linear theory. The observed 1-10 eV H^+ partial densities have a 0.77 correlation coefficient with the calculated heating rates from particle interaction with observed X-mode waves. We conclude that there is strong evidence that X-mode waves are heating the 1-10 eV H^+ across the dayside at $2 < L < 3$ which then attenuates across the pre-midnight sector, hitting a minimum in the post-midnight sector. These results demonstrate that the apparent post-midnight sector minimum in the 1-10 eV partial densities of HOPE is a consequence of suprathermal dayside heating and align well with observations from the Van Allen Probes. The implications of this work is that the thermal plasmasphere is affected by plasma waves, which can change the composition and energy distribution.

7.3 Future Work

7.3.1 Introduction

Wave-particle interactions play a critical role in the acceleration and loss of energetic particles within Earth's magnetosphere. Plasma waves, which arise from instabilities, resonate with ions and electrons via cyclotron resonance or Landau damping and can lead to dramatic energy and pitch angle (PA) changes on short time scales. For example, chorus wave resonance with relativistic electrons leads to acceleration and particle loss within the radiation belts (*Horne and Thorne*, 1998; *Bortnik and Thorne*, 2007; *Horne et al.*, 2007). These microscale interactions can lead to macroscopic changes, such as enhanced diffuse auroral precipitation (*Ni et al.*, 2008).

In the Van Allen Probes era, community exploration of wave-particle interactions has focused on relativistic scale acceleration and precipitation. However, plasma waves also interact with the cool, dense plasma within the plasmasphere. In 1987, *Olsen et al.* (1987) proposed that thermal ions seen in Dynamics Explorer 1 (DE-1) data were accelerated to suprathermal energies via cyclotron resonance with equatorial noise. Equatorial noise is a fast magnetosonic wave that is confined to the equatorial plane (*Russell et al.*, 1970). Olsen explored low-energy ion and wave interaction between L = 3 and L = 6 but did not look at possible magnetic local time (MLT) dependence. *Singh and Hwang* (1987) found a heating rate derived from quasi-linear theory to explain the existence of a dense warm plasma in the equatorial plane, further confirming interaction between equatorial noise and low-energy ions (*Olsen et al.*, 1987).

Recent work has found MLT variation in the suprathermal ion population near Earth. The results of Chapter 2 used Van Allen Probes Helium Oxygen Proton Electron (HOPE) measurements to show that plasma densities in H^+, He^+, and O^+ were much lower in the post-midnight region from MLT = 0 to ML = 6 at L < 3. The H^+ partial densities between 1-10 eV dropped by a factor of 100 across the post-midnight sector. Similar results have also been found for He^+ and O^+ 1-10 eV partial densities.

Chapter 4 further explored the apparent near-Earth post-midnight sector ion density depletion by examining the fluxes measured by HOPE at different pitch angles. Following the development of a pitch-angle sorting algorithm, the HOPE pitch-angle distributions were classified by shape and statistically analyzed by MLT occurrence. Similar to *Giles et al.* (1994), the authors determined that there was a deficit in the equatorially mirroring population in the post-midnight sector between 2<L<3 and

the percentage of loss cone distributions peaked in the dusk sector. An apparent 1-10 eV plasma loss in Chapter 2 was found to actually represent a depletion of the equatorially mirroring population in the post-midnight region. The results of Chapter 6 showed that the depletion was from suprathermal heating of cold (< 1 eV) plasma via cyclotron resonance on the dayside that then attenuated across the pre-midnight sector from multiple loss processes.

Chapter 6, using measurements from the Van Allen Probes Electric and Magnetic Field Instrument Suite and Integrated Science (EMFISIS), found that equatorial noise in the range of 250 Hz to 400 Hz had strong diurnal variation (*Kletzing et al.*, 2013). The equatorial noise cyclotron resonates with the PA $\approx 90^o$ H^+ ions, increasing their perpendicular energy. The authors demonstrated that a strong relationship exists between enhanced dayside equatorially mirroring ions and equatorial noise. However, they did not explore the loss mechanisms leading to the minimum at MLT = 3, which is left to future studies.

In order to determine the loss mechanism of the enhanced PA $\approx 90^o$ population, we propose to use a Fokker-Planck diffusion coefficient solver to compare diffusion time scales with the known attenuation rate of low-energy ion pitch-angle resolved fluxes measured by the Van Allen Probes HOPE instrument. Fokker-Planck diffusion models for gyro-phase averaged phase space density (PSD) have been used extensively in the past to solve questions of radiation belt electron heating and loss (*Horne et al.*, 2005; *Thorne et al.*, 2013). Solving for Fokker-Planck diffusion coefficients allows us to quantify how much flux is lost due to pitch-angle diffusion and charge exchange/Coulomb collisions. It would also provide timescales for these loss processes.

Future work could use the Fokker-Planck diffusion coefficient solver and a test par-

ticle simulator to determine the timescales of pitch-angle diffusion for the suprathermally heated 1-10 eV H^+ ions. By determining the diffusion coefficients for the resonant interaction of these particles, we can then compare the theoretical results with observations from the Van Allen Probes. We will aim to build a model from these diffusion coefficients that will model how the H^+ distribution function changes with MLT. The main result of this project will confirm whether the H^+ loss across the pre-midnight sector can be explained via pitch angle and momentum diffusion along with Coulomb collisions and charge exchange or will refute the findings of Chapter 6. Our results will also better describe the movement of energy throughout the inner magnetosphere. In particular, an outcome of the model will be to quantify how much energy is lost from the 1-10 eV plasmaspheric ion population to the topside ionosphere. The surplus energy from the 1-10 eV ions heats in the ionosphere, affecting wave propagation and augmenting temperature gradients, leading to terrestrial changes and potential impacts on GPS signal propagation.

7.3.2 Proposed Research Plan

Stage 1: The Fokker-Planck diffusion equation for gyrophase-averaged phase space density (PSD) f ignoring radial diffusion (*Summers*, 2005; *Summers and Ni*, 2008; *Ni et al.*, 2012) is:

$$\left(\frac{df}{dt}\right)_{\mathrm{FP}} = \frac{1}{\sin\,\alpha}\frac{\partial}{\partial\alpha}\Big(D_{\alpha\alpha}\sin\,\alpha\frac{\partial f}{\partial\alpha}\Big) + \frac{1}{\sin\,\alpha}\frac{\partial}{\partial\alpha}\Big(D_{\alpha p}\sin\,\alpha\frac{\partial f}{\partial p}\Big) + \frac{1}{p^2}\frac{\partial}{\partial p}\Big(p^2 D_{p\alpha}\frac{\partial f}{\partial\alpha}\Big) + \frac{1}{p^2}\frac{\partial}{\partial p}\Big(p^2 D_{pp}\frac{\partial f}{\partial p}\Big) \tag{7.1}$$

where t is the time, α is the local pitch angle, and p is the particle momentum. $D_{\alpha\alpha}, D_{\alpha p} = D_{p\alpha}$, and D_{pp} are the local rates of pitch angle diffusion, mixed diffusion, and momentum diffusion. The rates are defined as:

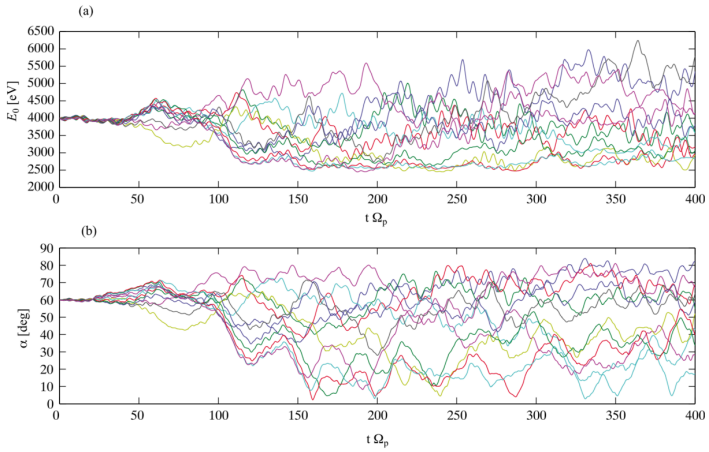

Figure 7.1: Energy (a) and Pitch angle (b) scattering as a function of normalized time for 12 protons, each with different initial Larmor phase, in a test particle simulation from *Bortnik et al.* (2010).

$$D_{\alpha\alpha} = (\Delta\alpha)^2/2\Delta t \qquad D_{\alpha p} = (\Delta\alpha\Delta p)/2\Delta t \qquad D_{pp} = (\Delta p)^2/2\Delta t \tag{7.2}$$

We will begin our modeling work by using a test particle simulation with various pitch angles and background magnetic field conditions to determine the diffusion coefficients. Similar in approach to *Bortnik et al.* (2010) seen in Figure 2, we will use approximately 100 proton test particles in each simulation and expose the test particles to equatorial noise. The test particle simulator will provide $\Delta\alpha$ and Δp which can be used with Equation 2 to calculate the diffusion coefficients. The diffusion coefficients can then be inserted into the Fokker-Planck Equation (Equation 7.1) to solve for $(\frac{df}{dt})_{\mathrm{FP}}$.

There are many parameters that will each require 100 simulation runs for each test. We plan to initiate the simulations with H^+ ions between 1 and 10 eV using 100 log-spaced energy bins within this energy range. Also, runs with varying pitch

angles between 0^o to 90^o will be done in one degree increments. We will also run the test particle simulator under different magnetic field conditions between $2 < \mathrm{L} < 3$ based on data from the Van Allen Probes EMFISIS instrument (*Kletzing et al.*, 2013). Based on the findings in Chapter 6, simulations will be run with 10 different log-spaced k vector magnitudes between 10^{-2} and 10^{-3} and initial wave frequencies of the equatorial noise log-spaced over 100 frequency bins between 250 Hz to 400 Hz. This will require millions of test particle simulation runs to calculate robust diffusion coefficients, which is feasible and will only require a few days of computational run time.

After determining the diffusion coefficients, we can calculate time scales using Equation 7.3:

$$\tau_{\alpha\alpha} = \frac{L_\alpha^2}{D_{\alpha\alpha}} \qquad \tau_{\alpha p} = \frac{L_\alpha L_p}{D_{\alpha p}} \qquad \tau_{pp} = \frac{L_p^2}{D_{pp}} \tag{7.3}$$

where L_α and L_p are the length scales of the wave-particle interaction for pitch angle and momentum diffusion. We can define these length scales by the width of the loss cone for L_α and the maximum energy gain observed by these ions (approximately 5 eV) for L_p. We will compare these timescales to the flux energy gain/loss observed in Chapter 6. If there is a large mismatch and the time scales predicted for pitch-angle diffusion and energy diffusion are infeasible, then the findings of Chapter 6 will be refuted.

Stage 2 Assuming the time scales agree with our previous findings, we will proceed to develop a model that combines the pitch-angle distribution and energy changes $(\frac{df}{dt})_{\mathrm{FP}}$ in Stage 1 with Coulomb collision scattering $(\frac{df}{dt})_{cc}$, charge exchange loss $(\frac{df}{dt})_{ce}$, and expected cyclotron heating effects $(\frac{df}{dt})_{ch}$. The model will be a 1-dimensional model in time and show the evolution of an initial distribution of particles (f) when subjected

to these source and loss processes. At each time step, the model will solve for each of the components, including the Fokker-Planck equation (Equation 7.1). Equation 7.4 summarizes the model we will develop to describe the energy balance of the 1-10 eV near-Earth H^+:

$$\frac{df}{dt} = \left(\frac{df}{dt}\right)_{ch} + \left(\frac{df}{dt}\right)_{\mathrm{FP}} + \left(\frac{df}{dt}\right)_{ce} + \left(\frac{df}{dt}\right)_{ce} \tag{7.4}$$

where the cyclotron resonant heating $(\frac{df}{dt})_{ch}$ will be the source term from perpendicularly heated low energy ions. The pitch angle and momentum diffusion rate $(\frac{df}{dt})_{\mathrm{FP}}$ determined in Stage 1 from the Fokker-Planck equation will change the field alignment and energy of particles. Cyclotron resonant heating is fully described in *Sarno-Smith et al.* (2016) and can be easily incorporated into this model as a source term for energy in the system. Figure 3 summarizes the stages of the project and anticipated inputs to the distribution function model of Equation 7.4 in a flow chart.

The Coulomb collision and charge exchange rates must be calculated. For Coulomb collisions, we will use the empirical formula in Equations 12 and 13 from *Varney et al.* (2012) to calculate $(\frac{df}{dt})_{cc}$. For charge exchange, we can use Equation 18 from (*Fok et al.*, 1993) :

$$\left(\frac{df}{dt}\right)_{ce} = v\sigma_h < n_H > f_H \tag{7.5}$$

where f is the distribution function, v is the particle velocity, σ_h is the cross section for charge exchange of H^+ with neutral hydrogen, and $< n_H >$ is the bounce-averaged neutral hydrogen density. The neutral hydrogen density can be estimated using an empirical relationship given in Equation 13 of *Østgaard et al.* (2003). The appropriate charge exchange cross sections (σ_h) can be found in the technical reports of *Phaneuf*

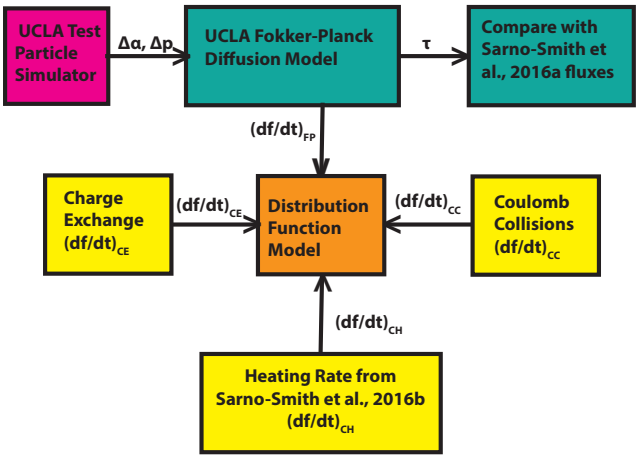

Figure 7.2: Summary of project steps by color, starting with the Test Particle Simulator and ending with the various df/dt inputs to the distribution function model of Equation 7.4.

et al. (1987); *Barnett et al.* (1990) and are the same ones used in *Fok et al.* (1993).

This energy balance model can be used to test how well the theory suggested in Chapter 6 aligns with expected gains and diffusion. We anticipate the model will require additional inputs and losses when run over a long period of time, such as top side ionosphere transport to the plasmasphere.

For instance, if the observed HOPE 1-10 eV H^+ fluxes have similar loss rates to those given by the distribution function model across the pre-midnight sector but disagree for the initial heating in the post-dawn region, we know transport of hot top side ionospheric plasma is contributing to elevated flux levels in the post-dawn region. We can quantify how much plasma is transported by subtracting the fluxes predicted by our model from the observed 1-10 eV H^+ fluxes. This additional input would reveal exactly how pitch-angle diffusion/loss processes affect the 1-10 eV inner plasmasphere ion population versus transport. Overall, the result will be powerful for

describing the motion of low-energy ions and will be useful in modeling the behavior of the high-energy tail of the plasmasphere.

APPENDICES

APPENDIX A

Comparison of HOPE Data to Modeled Plasmasphere Data

A.1 Comparison of HOPE Data to Modeled Plasmasphere Data

Since most plasmasphere particles have low energy (< 1 eV) and the HOPE solid angle has viewing gaps, the HOPE energy range covers only a fraction of the total plasmaspheric distribution. To place the HOPE measurements in the context of previous observations, we wish to confirm that the 1-10 eV quiet time HOPE partial densities are consistent with the total plasma density measured by previous missions by calculating what fraction of the total plasma density distribution the HOPE energy range expects to measure. To do this, we assume that the energy distribution of the plasmasphere can be represented as a Maxwellian,

$$F_m = n_0 \left(\frac{m_s}{kT}\right)^{3/2} 4\pi e^{-E_n/kT} \frac{1}{\sqrt{2m_s E_n}} \frac{2E_n}{m_s} \tag{A.1}$$

where F_m is the differential number flux, m is the mass of the ion species, k is Boltzmann's constant, n_0 is the total number density, T is the plasma temperature,

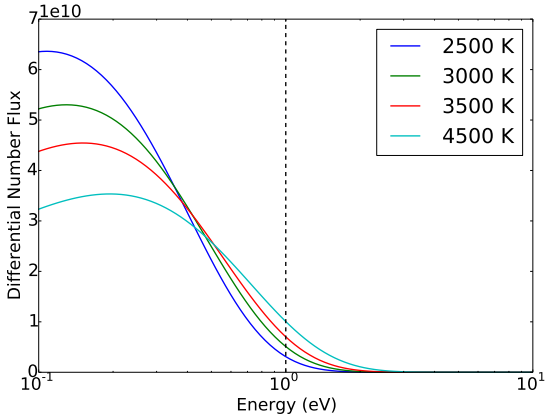

Figure A.1: Differential number flux for a Maxwellian H^+ distribution as a function of energy at different plasmaspheric temperatures. The dotted black line indicates 1 eV, the minimum HOPE measurement energy. We assume a total number density of 1800 cm^{-3} as given by *Chappell* (1972).

and E_n is the plasma energy. We find the partial density of this energy range by integrating over the Maxwell-Boltzmann distribution of ion energies from 1-10 eV,

$$n = \int F_{ms} dE_n \tag{A.2}$$

For simplicity, we perform this calculation at L=2, where the total plasmaspheric H^+ density is approximately 1800 cm^{-3} (*Chappell*, 1972; *Gallagher et al.*, 1988). Also in (A.1), T is the median temperature of the plasmasphere taken from *Comfort et al.* (1985). In Figure A.1, we show the differential number flux for different plasmaspheric temperatures (*Comfort et al.*, 1985). The high energy tail of the plasmasphere is the area under the curve past the dotted black line, comprising approximately 5% of the total density. Our integrating variable, E_n, is the bounding energies of the fraction of the Maxwellian that we want to calculate the density, n, in this case 1 - 10 eV. To confirm this n_0 value we also checked the empirical relationship for electron number densities given in *Carpenter and Anderson* (1992) based on L-Shell value and then using *Gallagher et al.* (2000) to estimate H^+ density as most of the plasmasphere mass at L=2. The value given through this method for n_e at L=2 was 1866 cm^{-3},

which will be approximately equal to n_{H^+}.

APPENDIX B

HOPE 1-10 eV Temperatures

B.1 HOPE Plasmaspheric 1-10 eV Temperatures

During presentations of the work contained in this thesis, a common question asked was 'how do you know this is not a temperature change?'. The answer we returned was that what we have called a partial density loss/gain is simultaneously a temperature cooling/warming. Assuming a Maxwellian distribution for the cold population in the plasmasphere, a change in temperature would result in a shifting of what part of the distribution function HOPE sees. The bulk temperature of plasmasphere is approximately 0.5 eV, and since HOPE's lowest energy channel (with average spacecraft charging accounted for) is 1.5 eV, HOPE does not see the bulk of the plasmasphere. However, if the plasmasphere is 'warmer', the Maxwellian distribution shifts so the bulk energy of the plasmasphere is at, for example, 0.75 eV. In the HOPE measurements, this would manifest as higher fluxes and high densities because HOPE would be viewing closer to the bulk of the plasmasphere.

Calculating temperature, we use equation F3 of *Genestreti et al.* [manuscript in

preparation]:

$$F = \frac{\rho_t - \rho_p}{\rho_t} \tag{B.1}$$

$$\sigma = E_m/(\sqrt{2}\mathrm{erf}F) \tag{B.2}$$

$$T = 2\sigma \tag{B.3}$$

where T is temperature, E_m is the average minimum energy channel seen by HOPE, ρ_t is the total electron density measured by EFW, and ρ_p is the 1-10 eV partial density calculated using the Riemann sum in With this calculation, we determined the median temperature of the 1-10 eV plasmasphere from February 2013 to April 2015 binning by 0.25 L-Shell and 0.5 MLT and show these results in Figure B.1. The lack of measurements in Earth's shadow are because EFW is incapable of making reliable measurements in Earth's shadow. The temperature shows strong diurnal variation at L $<$ 4 and has a minimum of $<$ 0.75 eV in the post-midnight sector and a maximum of 1.3 eV in the dusk sector. The results of our temperature analysis are consistent with the results of the rest of this thesis - the post-midnight sector 1-10 eV plasmasphere is cooler/less dense than the plasmasphere at other MLTs. In this case, as aforementioned, a colder 1-10 eV plasmasphere is the same as a less dense one.

We also check the variability of the calculated temperatures to ensure that results found at 2 $<$ L $<$ 3 are reliable. Figure B.2 shows the calculated standard deviation of the temperatures. The temperature calculations are subject to the most variability ($>$ 1 eV) on the dayside at L $>$ 4. However, in our region of interest at 2 $<$ L $<$ 3, there is nothing exceptional about the variability across at MLTs; in fact, the

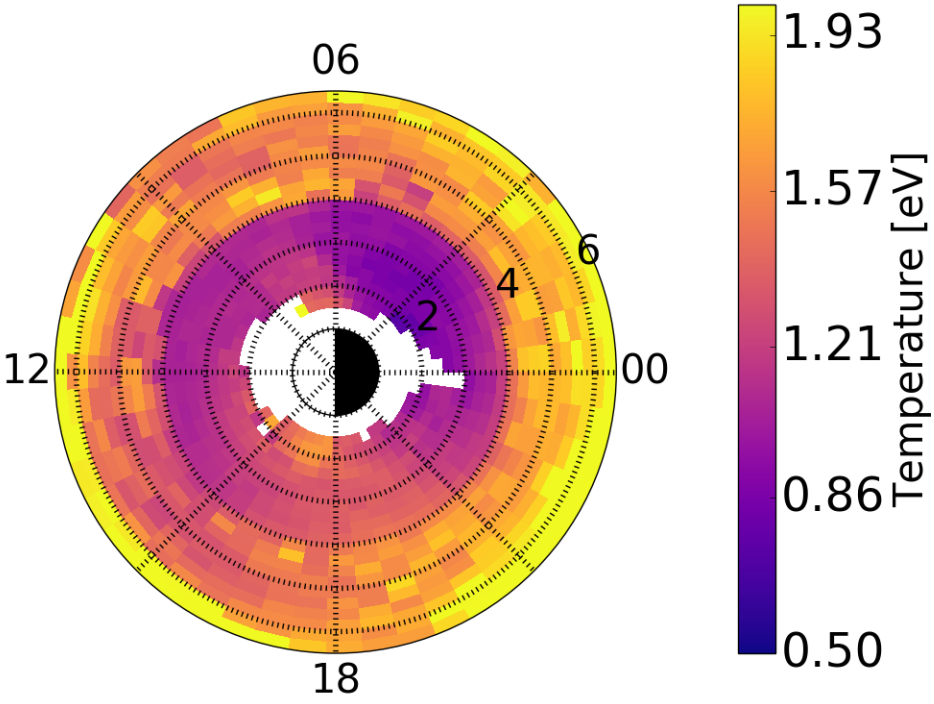

Figure B.1: HOPE 1-10 eV temperatures calculated from February 2013 to April 2015 and binned by 0.25 L-Shell and 0.5 MLT.

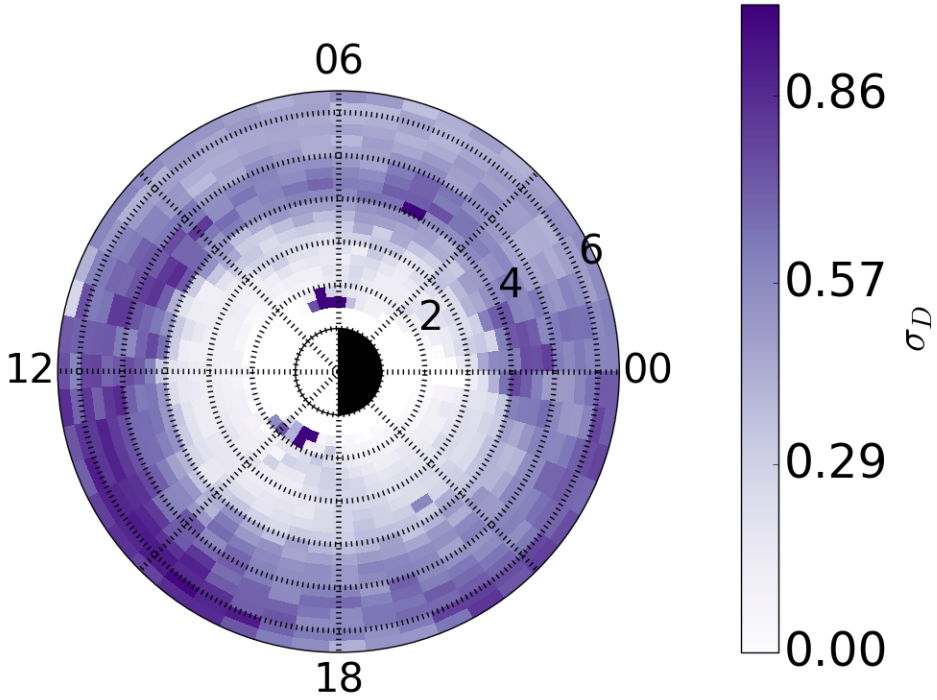

Figure B.2: HOPE 1-10 eV temperatures standard deviations in eV calculated from February 2013 to April 2015 and binned by 0.25 L-Shell and 0.5 MLT.

variability is less than 0.3 eV in this region.

It should be noted that we do differ slight from the method used in *Genestreti et al.* [manuscript in preparation] because we do not subtract the RAM velocity of the spacecraft before calculating temperatures from the HOPE partial densities. Figure B.3 shows the calculated ram velocities for every minute of the entire day of March 28, 2015. We found that the ram energy contribution is minimal and usually below 0.1 eV, even at $2 < L < 3$, and can be neglected in the calculation of temperature, and therefore, we do not include it.

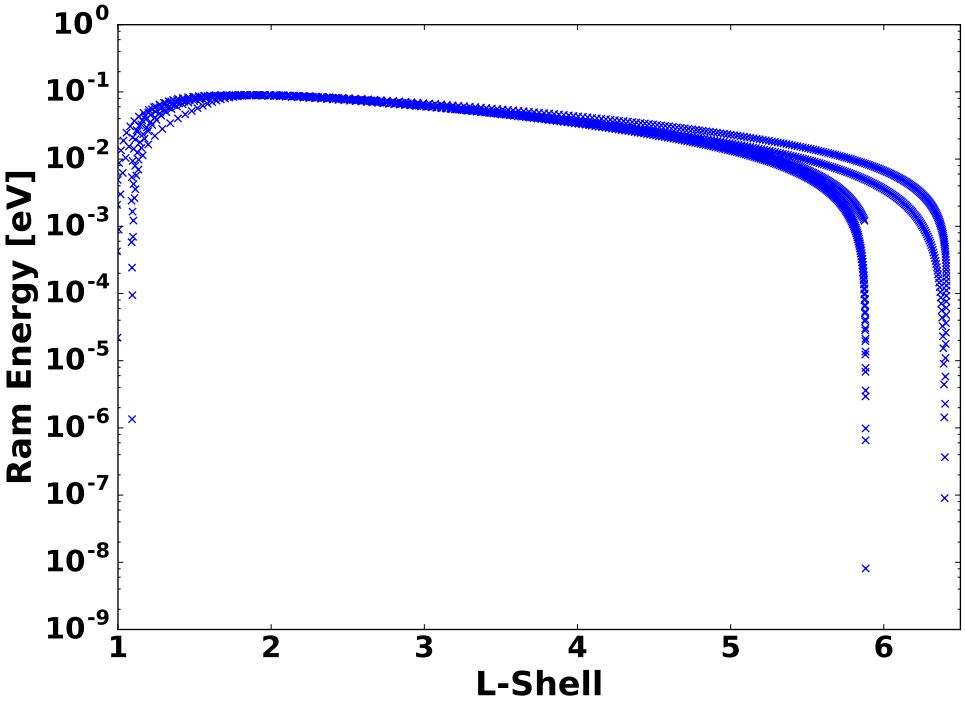

Figure B.3: HOPE ram velocities calculated on March 28, 2015.

APPENDIX C

Comparison of SuperDARN Electron Number Densities to EISCAT

C.1 SANSA Project on SuperDARN Electron Number Densities

C.1.1 Introduction

The Super Dual Auroral Radar Network (SuperDARN) consists of thirty five coherent scatter high frequency (HF) radars stationed throughout the world (*Greenwald et al.*, 1995; *Chisham et al.*, 2007; *Baker et al.*, 2011). SuperDARN radars measure the ionospheric Doppler velocity and can provide large area convection maps of the F region (*Ponomarenko et al.*, 2008; *Thomas et al.*, 2013). However, SuperDARN radars measure velocity with assumption that the index of refraction of the scattering volume is 1.0. In reality, the index of refraction is typically closer to 0.8 (*Gillies et al.*, 2009). This overestimation of the refractive index leads to a consistent underestimation of the Doppler velocity (*Eglitis et al.*, 1998; *Davies et al.*, 1999; *Xu et al.*, 2001).

The index of refraction can be corrected using ionospheric electron number densities (N_e) from models such as the International Reference Ionosphere (IRI) or local ionosonde measurements (*Bilitza*, 2001). Since the scattering volume of each SuperDARN radar is so large (approximately 4×10^6 km^2), direct comparison can lead to ambiguities due to localized irregularities and convection (*Norman et al.*, 2004; *de Larquier et al.*, 2011). A reliable method to calculate the actual index of refraction from SuperDARN observations will lead to better Doppler velocity measurements from backscatter when plasma irregularities are present.

Gillies et al. (2010, 2012) demonstrated that the index of refraction can be calculated from dual frequency observations using SuperDARN. We can subsequently calculate N_e from the plasma frequency. This method is valid as long as the SuperDARN radar shifts the measuring frequency of the radar on a time scale where the ionosphere is stationary and if the difference of ray propagation paths at the two frequencies is small. *Gillies et al.* (2012) showed statistical results of the SuperDARN electron number densities from all the available SuperDARN radars from 1993-2012. However, no direct comparison of plasma density between SuperDARN and another independent method was presented. They also compared the observed line of sight velocities to those measured by the Defense Meteorological Satellite Program (DMSP) and the European Incoherent Scatter (EISCAT) radar. The velocities matched extremely well when the index of refraction was accounted for (0.99 best fit line slope) (*Gillies et al.*, 2012).

Links between ionospheric density irregularities, gravity waves, particle precipitation, and satellite drag prompted the need for large coverage and accurate electron number density measurements (*Drell et al.*, 1965; *Hooke*, 1968; *Robinson et al.*, 1987). Previous work has calculated electron number densities from SuperDARN measure-

ments using ground scatter (*André et al.*, 1998). If SuperDARN can provide reliable N_e measurements, the scientific community will have access to near global N_e coverage. This would, for example, permit quasi-real time global studies of Joule heating in the E-region or F-region (*Kosch and Nielsen*, 1995; *Cierpka et al.*, 2000).

We expand the *Gillies et al.* (2012) study to directly compare the SuperDARN calculated N_e to EISCAT incoherent scatter electron number densities. By generating artificial backscatter with the EISCAT Heater (*Rietveld et al.*, 1993) at Tromsø to create an artificial 'target', we can then use ray tracing to localize the backscatter and directly compare the SuperDARN radar N_e with the EISCAT N_e (*Kosch et al.*, 2004; *Wright et al.*, 2006; *Yeoman et al.*, 2008). The EISCAT N_e are derived from incoherent backscatter power accounting for the electron to ion temperature ratio in a fitting procedure using the Grand Unified Incoherent Scatter Design and Analysis Package (GUISDAP) software (*Lehtinen and Huuskonen*, 1996). Our analysis is the first real test on the accuracy of the SuperDARN-based electron density estimates. The analysis tests credibility of the method for global-scale electron density monitoring for the case of multiple-radar utilization. We use the Co-operative UK Twin Located Auroral Sounding System (CUTLASS) Hankasalmi SuperDARN radar (62.32 N, 26.61 E, geographic coordinates) (*Lester et al.*, 2004) for comparison with EISCAT (69.6 N, 19.2 E, geographic coordinates) (*Rishbeth and Van Eyken*, 1993). CUTLASS offers the unique advantage of simultaneous transmission and reception of two independent signals. This STEREO capability is powerful since it allows the SuperDARN radar to essentially act as two independent radars. Thus, we can calculate electron densities using simultaneous measurements with 1 MHz or more frequency separation (e.g. 15 and 16 MHz). Different frequency rays will propagate to different altitudes along their paths in the F-region. However, it has been shown that pump-induced artificial striations extend 10s of km in altitude (*Senior et al.*, 2004). So, we can reasonably

expect backscatter from similar ranges at different frequencies to come from about the same irregularity regions.

The results of our study demonstrate that calculated CUTLASS N_e measurements are sensitive to the frequencies used to derive the N_e and overestimate N_e compared to EISCAT values. We use two controlled Heater experiments, one at daytime and one in the afternoon/evening, to provide artificial backscatter and narrow spectral widths in the CUTLASS line of sight velocities. We also show that the method using smaller frequency shifts on the kHz scale also overestimates N_e compared to EISCAT.

C.1.2 Methodology

Gillies et al. (2012) showed that the index of refraction, n_s, could be calculated using the plasma frequency f_p and the radar wave frequency f:

$$n_s = \sqrt{1 - f_p^2/f^2} \tag{C.1}$$

and *Gillies et al.* (2011) showed that f_p could be calculated using two radar frequency observations of line of sight velocity, v:

$$f_p^2 = \frac{f_1^2(1 - v_1^2/v_2^2)}{1 - v_1^2 f_1^2/v_2^2 f_2^2} \tag{C.2}$$

Only observations where $v_1/v_2 < 1$ are physically meaningful. From this, we can calculate N_e (m^{-3}) from the f_p in Hz as:

$$N_e = \frac{m_e \epsilon_0}{q^2} 2\pi f_p^2 \tag{C.3}$$

where m_e is the mass of an electron, ϵ_0 is the permittivity of free space, and q is the charge of an electron. SuperDARN mono-frequency radars, by stepping the frequency every few seconds, are able to calculate N_e from f_1 and f_2. With the dual frequency STEREO capability, available on CUTLASS, we operate the radar at two major frequency bands (e.g. 15 and 16 MHz) with incremental steps (kHz) in each band every two seconds.

We use data from two experiments. The first experiment was conducted on March 12, 2015 10:00 to 12:01 UT, or 11:00 to 13:01 LT in Tromsø. During this daytime interval, Kp was at 2+. The CUTLASS Hankasalmi radar (62.3^oN, 26.6^oE) was operated at 15 and 16 MHz sequentially between 10:00 - 11:21 UT. From 11:22 UT to 12:01 UT, the frequency was shifted between three major frequency bands at 16 MHz, 17 MHz, and 18 MHz. For the first case study, the 15 MHz band contained frequencies between 15.0 to 15.1 MHz, the 16 MHz band contained frequencies from 16.2 to 16.7 MHz, the 17 MHz band contained frequencies from 17.9 MHz to 18.1 MHz, and the 18 MHz band contained frequencies from 18.8 to 18.9 MHz. The SuperDARN radar operated on beam 5 with range gates beginning at 480 km and spaced 15 km apart with 1 second integration on each frequency sequentially, i.e. the cycle was either 2 seconds or 3 seconds long.

The EISCAT Heater operated with the beam field-aligned to the local magnetic field at 6.2 MHz between 10:00 - 11:21 UT and then changed to 6.96 MHz between 11:21 - 12:01 UT. The radiation from the Heater was in ordinary polarization mode. Ionospheric pumping was slightly under dense, where the radiation frequency is greater than the peak plasma frequency, throughout the interval. Many past ex-

periments have shown this produces striations (*Leyser et al.*, 1990; *Gurevich et al.*, 1995). The effective radiated power (ERP) was 53 MW between 10:00 - 11:21 UT and 32 MW between 11:21 - 12:01 UT.

The second experiment was conducted on March 3, 2016 from 14:00 to 18:00 UT, or 15:00 to 19:00 LT, with Kp $<$ 2 throughout the experiment. Part of the experiment occurred after sunset (approximately 17:00 UT). The CUTLASS Hankasalmi STEREO radar was operated at 13 and 15 MHz on Channel A throughout the entire interval and with, additionally, 16 MHz between 14:00 to 17:00 UT on Channel B. For the second case study, the 13 MHz band contained frequencies between 13.2 to 13.3 MHz, the 15 MHz band contained frequencies between 15.0 to 15.1 MHz, and the 16 MHz band contained frequencies between 16.2 to 16.7 MHz.The CUTLASS radar operated on beam 5 with range gates beginning at 480 km and spaced 15 km apart on Channel A and the range gates beginning at 180 km and incrementing 45 km on Channel B. Channel A oscillated between 13 and 15 MHz, using 3 second integration with a 6 second cycle time. Channel B measured only at 16 MHz using 3 second integration and also a 3 second cycle time.

The EISCAT ionospheric modification facility operated with the beam field-aligned and between 4.04 MHz to 5.423 MHz with 5.423 MHz between 14:00 to 16:30 UT with an ERP of 180 MW, 4.9128 MHz between 16:30 to 16:38 UT with an ERP of 154 MW, 4.544 MHz from 16:38 to 17:38 UT with an ERP of 131 MW, and 4.04 MHz from 17:45 to 18:00 UT with an ERP of 110 MW. Ionospheric heating was mostly over-dense, where the radiation frequency was lower than the peak ionospheric plasma frequency, during this experiment with the reflection altitude at approximately 220 km. For both experiments, the EISCAT UHF radar observed field-aligned using the 32 x 20 alternating "beata" code with 10 μs sampling. This gives 3 km range resolution, 5

second time integration and covers between 49 and 694 km in range. The EISCAT N_e during both experiments was calibrated with local ionosonde measurements.

Figure C.1A shows the CUTLASS line of sight velocities used in our N_e calculation between range gates 25 and 38 for the March 12, 2015 experiment. Figure C.1 assimilates velocity measurements from 15-18 MHz frequencies. Figure C.1B shows the spectral widths of the respective velocity measurements over the same period. For most of the experiment the velocities are negative and the spectral widths are small (< 50 m/s) which is characteristic of artificially generated backscatter from striations.

Figure C.2 further demonstrates that the velocity distribution for each frequency is largely contained between 0 to -50 m/s. Figure C.2A shows the velocities for 15 MHz, Figure C.2B shows 16 MHz velocities, Figure C.2C is 17 MHz velocities, and Figure C.2D is 18 MHz velocities. The bin widths in the bar plots are 50 m/s. In particular, the 17 MHz frequency velocity distribution is strongly peaked at approximately -50 m/s. The small velocity distribution is consistent with the narrow spectral width and is a feature of artificially generated backscatter.

A ray trace to determine the altitude CUTLASS observes over EISCAT is imperative for our comparison. For the most accurate ray trace, a reliable angle of arrival measurement for CUTLASS is necessary. However, the angle of arrival information for CUTLASS was unavailable during both of our experiments. Figure C.3A shows the ray trace between 5 and 40 degrees elevation angles for the 16 MHz frequency channel on beam 5 for March 12, 2015. The silver lines indicate every 4th range gate starting at 480 km (range gate 0). The black star represents the approximate EISCAT radar location. The horizontal black lines represent a ray for every 2 degrees of elevation angle. Based on where the last ray paths that refract back to Earth are

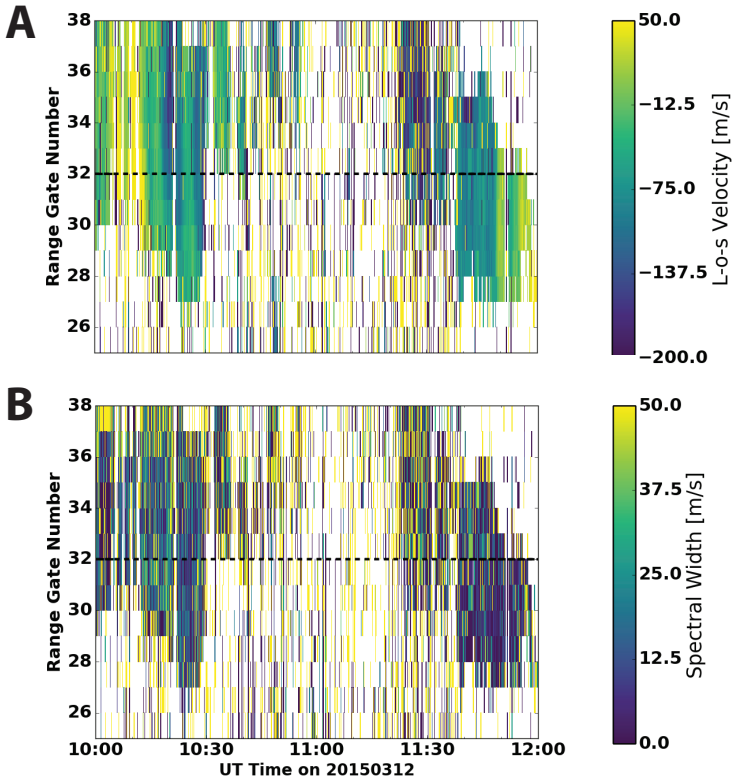

Figure C.1: A is the line-of-sight (L-o-s) velocities from SuperDARN CUTLASS at frequencies of 15 MHz - 18 MHz on March 12, 2015 from 10:00 UT to 12:00 UT at range gates of 25 to 38. The range gates start at 480 km and have 15 km spacing from there. EISCAT is located at approximately range gate 32, where we have placed a black dotted line. B is the SuperDARN CUTLASS spectral widths over the same frequencies and same time period.

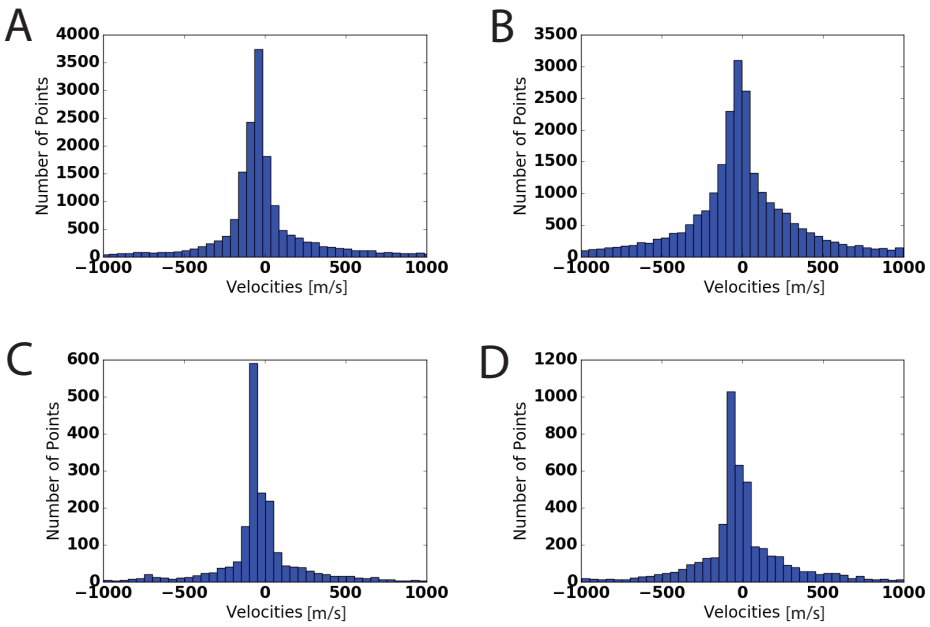

Figure C.2: Velocity distributions of each of the major frequency bands from SuperDARN CUTLASS. A is 15 MHz, B is 16 MHz, C is 17 MHz, and D is 18 MHz for the campaign on March 12, 2015 from 10:00 to 12:00 UT.

over Tromsø, we estimate that SuperDARN observes between 200-260 km, which is consistent with the hmF2 peak from the ionosonde measurements on this day at 240 km. For the following figures, we estimate that CUTLASS observes backscatter from 240 km on this day. When the same elevation angles are compared, higher frequencies probe higher levels of the ionosphere, with a 1 MHz frequency difference producing height differences from 5 km to 50 km. Similar results are obtained for March 3, 2016 (not shown). Here the Heater pump frequency corresponded to the ionospheric plasma frequency at an altitude of approximately 220 km. In Figure C.3B, we show the IRI and EISCAT N_e profiles averaged between 9:30 to 12:00 UT on March 12, 2015 to demonstrate that IRI and EISCAT provide similar N_e values below 300 km. Since the model values from IRI are close to EISCAT, we can trust the ray trace in Figure C.3A which relies on IRI to calculate the index of refraction.

C.1.3 Results

We test two methods to determine if N_e can be reliably calculated from SuperDARN radar data. We make use of the unique STEREO feature of the CUTLASS radar at Hankasalmi, when it is available, which was in our experiment on March 3, 2016. At each measurement, we first average the range gates of backscatter where CUTLASS observes irregularities produced by the EISCAT heater, here defined as range gates 30-35. Then, we resample the data to a 2 minute cadence in each frequency band. Simultaneous comparison and un-averaged measurements from several range gates results in noisy data, which is why we spatially and temporally smooth the data before calculating the velocity ratio between the two frequencies. If $v_1 > v_2$, the N_e values are unphysical because the derivation of Equation 2 from Equation 1 assumes that, because the refractive index is dependent on radar frequency, the velocity measured at the lower frequency (v_1) must be lower than the velocity measured

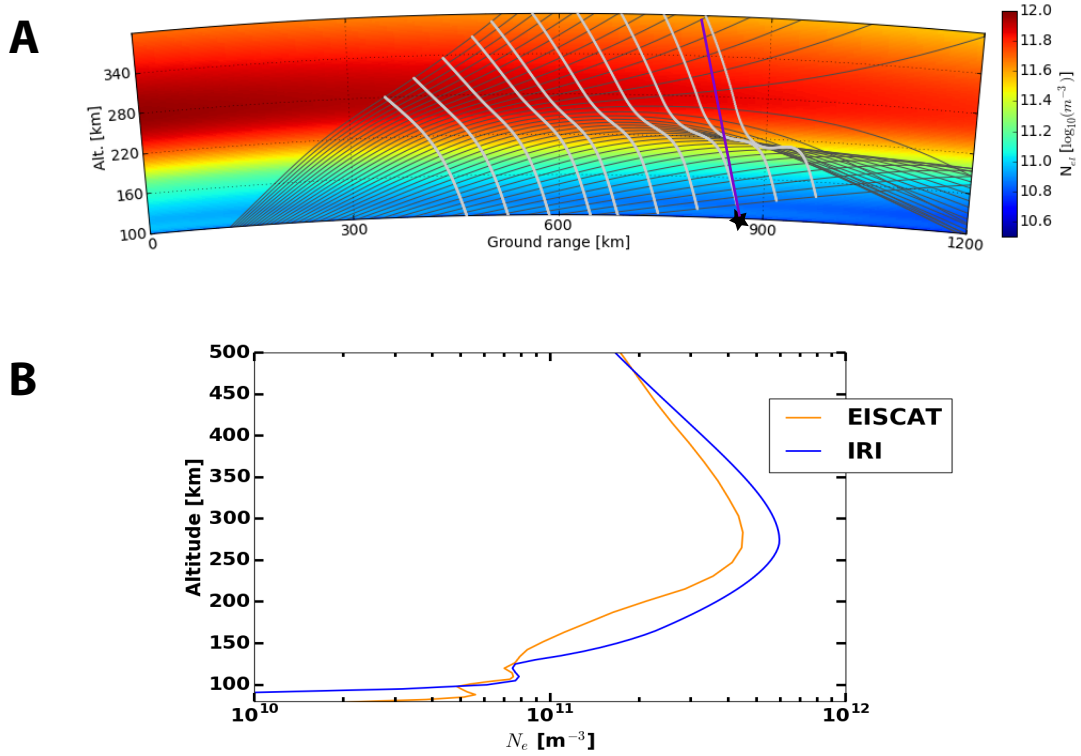

Figure C.3: A shows the SuperDARN ray tracing model output for our experiment at 16 MHz for beam 5 on March 12, 2015. The radar-beam elevation angle ranges between 5 and 40 degrees, with 2 degree increments represented by the black horizontal lines. The silver lines are every 4th range gate (approximately 60 km) starting at 480 km (range gate 0). The background is N_e from the IRI model. The black star represents the approximate distance to the EISCAT Tromsø site. The purple line represents the magnetic field line at Tromsø, indicating the look direction of the EISCAT Heater. B shows the IRI (blue) and EISCAT (orange) N_e profiles averaged between 10:00 to 12:00 UT on March 12, 2015.

at the higher frequency (v_2). Therefore, we remove all data when $v_1 > v_2$.There are 4 bands we compare from the first case study on March 12, 2015: 15-16 MHz, 16-17 MHz, 17-18 MHz, and 16-18 MHz and then 3 bands from the second case study on March 3, 2016 at 13-15 MHz, 13-16 MHz, and 15-16 MHz.

The second method is to use the small frequency shifts of kHz that SuperDARN automatically makes as it scans within a selected frequency range. For instance, in the 15 MHz band we observe an approximate 1 kHz change every 2 seconds. The radar does this to select the quietest frequency of observation, giving the highest signal-to-noise ratio. Our second method uses this frequency shift by averaging the measurements in range gates 30-35 at a given time and then calculating N_e from the average line of sight velocity measurement and slightly shifted frequency two seconds later. We also remove times when $v_1 > v_2$. This method requires assuming ionospheric stability over a 2 second interval but with far smaller frequency shifts. We then resample these data to a 2 minute cadence to reduce the noise of the measurements. The potential advantage of this method is that the dual frequency STEREO mode of CUTLASS is not necessary and this method could be implemented on all SuperDARN radars.

Figure C.4 illustrates the differences in the two approaches for calculating N_e for both case study dates. Figure C.4A shows the CUTLASS data from March 12, 2015. The colored triangles represent the N_e from wide frequency spacing, where red is 15-16 MHz, green is 16-17 MHz, yellow is 16-18 MHz, and blue is 17-18 MHz. The monochrome hexagons represent the small frequency shift (kHz) calculated N_e, with black as the 15 MHz measurements, dark grey is the 16 MHz measurements, light grey is the 17 MHz N_e, and white is the 18 MHz N_e. Figure C.4B shows the SuperDARN data from March 3, 2016 where the red triangles represent 13-15 MHz, green

is 13-16 MHz, and yellow is 15-16 MHz. The gray scale hexagons represent the small frequency shift calculated N_e, with black as the 13 MHz measurements, dark grey is the 15 MHz measurements, and light grey is the 16 MHz N_e.

The most notable feature of this figure is the near constant values the small frequency shift calculated N_e exhibits. For example in Figure C.4A, at 15 MHz, the calculated N_e value barely fluctuates from 2.7×10^{12} m^{-3} while the 16 MHz N_e hovers at 3.7×10^{12} m^{-3}. The N_e calculated from wide frequency spacing, on the other hand, shows some variability and changes in time in a more reasonable manner. The lack of variation in the small frequency shift N_e shows that this method is strongly influenced by the value of f_1 in Equation C.2, which is the measuring frequency of the line of sight velocities. Larger f_1 correspond to larger N_e, with 17 and 18 MHz frequency data being the highest and producing similar values, and this is consistent in Figure C.4B with 16 MHz producing the largest N_e. The small frequency shift method of estimating N_e produces unrealistically static N_e values subject to the radar frequency, which is not consistent with expectation.

Figure C.5 shows the wide-frequency calculated N_e from CUTLASS compared to EISCAT N_e and IRI values. The CUTLASS N_e is approximately an order of magnitude larger than the EISCAT and IRI N_e. The IRI N_e values are calculated on an hourly timescale during the experiment from the Community Coordinated Modeling Center (CCMC). In Figure C.5A, the colored triangles represent the CUTLASS N_e, where red is the 15-16 MHz, green is the 16-17 MHz, yellow is the 16-18 MHz, and blue is the 17-18 MHz observations on March 12, 2015. In Figure C.5B, the colored triangles represent the CUTLASS N_e, where red is the 13-15 MHz, green is the 13-16 MHz, and yellow is the 15-16 MHz on March 3, 2016. In Figure C.5A, the grey diamonds are the 2-minute resampled EISCAT N_e at 240 km and the dotted blue line is

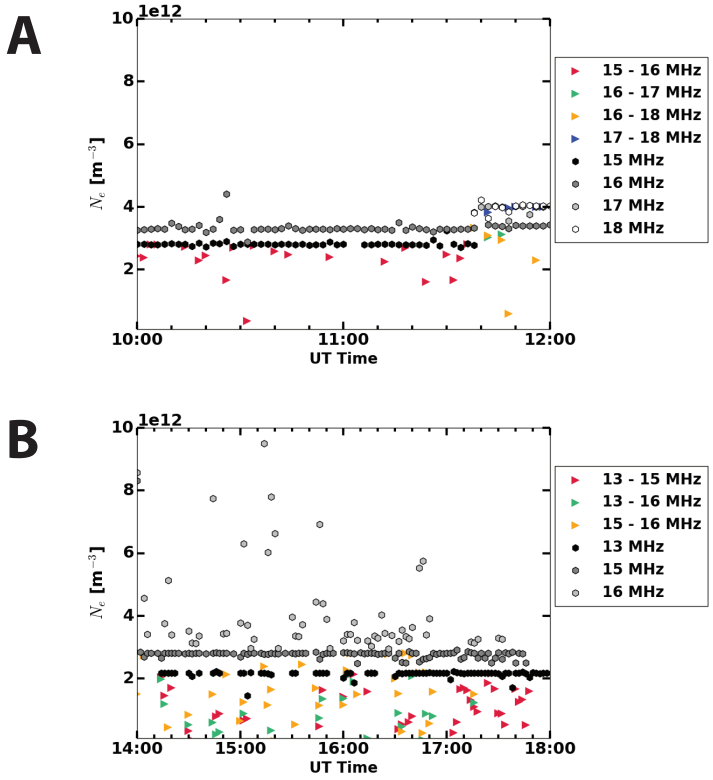

Figure C.4: The colored triangles represent the SuperDARN CUTLASS STEREO mode data resampled on a 2 minute cadence for (A) on March 12, 2015 between 10:00 to 12:00 UT. Red is the calculated N_e from the 15 and 16 MHz measurements, green is the 16 and 17 MHz frequency measurements, Yellow is the 16 and 18 MHz frequency measurements, and blue is the 16 and 18 MHz measurements. The monochrome hexagons represent the small frequency shift (a few kHz) method of calculating N_e using SuperDARN data observations over the same time period. The small frequency shifted N_e are also resampled on a 2 minute cadence. Black represents 15 MHz, dark grey is 16 MHz, light grey is 17 MHz, and white is 18 MHz. (B) is similar, with N_e from March 3, 2016 14:00 to 18:00 UT with red as STEREO mode between 13-15 MHz, green between 13 - 16 MHz, and gold between 15 - 16 MHz. The monochrome hexagons represent small frequency shift N_e calculations, with black as 13 MHz, dark grey as 15 MHz, and light grey as 16 MHz. For both methods in A and B, the mean line of sight velocity over range gates 30-35 at each measurement is used in the calculation.

the IRI data over this time range at 240 km. For Figure C.5B, EISCAT N_e and IRI N_e are taken from 220 km.

The CUTLASS derived N_e does not capture the 1×10^{11} m^{-3} increase that EISCAT measures starting at 10:50 UT in Figure C.5A. Instead, the CUTLASS N_e remains somewhat constant between 10:00 to 11:30 UT and then jumps up by 1×10^{12} m^{-3} when different frequencies are employed. Like the small frequency shift results, this suggests that the dual frequency mode N_e is sensitive to the f_1 used in Equation C.2 and this can affect the results significantly. The IRI and EISCAT N_e agree very well throughout the time period, with IRI slightly higher than EISCAT.

In Figure C.5B, the CUTLASS N_e completely fails to capture the ionospheric N_e decrease in the EISCAT data at 16:00 UT. The results from the March 3, 2016 case study are also more variable than the case study in Figure C.5A, ranging from very close to EISCAT N_e values to being off by a factor of 32. Once again, the IRI and EISCAT N_e values are very close, with IRI slightly lower than EISCAT in Figure C.5B. Overall, the data shown in Figure C.5 demonstrate that deriving N_e from dual frequency measurements is not a reliable method for calculating background N_e from SuperDARN measurements.

We also use linear regression to quantify the correlation coefficient (r) between the 2 minute resampled EISCAT and CUTLASS N_e despite the order of magnitude difference between the data sets. For the first experiment, the r between 15-16 MHz was 0.09, for 16-17 MHz was -0.13, for 16-18 MHz was 0.03, and for 17-18 MHz was 0.17. For the second experiment, the r between 13-15 MHz was -0.049, for 13-16 MHz was -0.015, and between 15-16 MHz was -0.017. All of the linear regression correlation coefficients calculated between the CUTLASS and EISCAT N_e are extremely

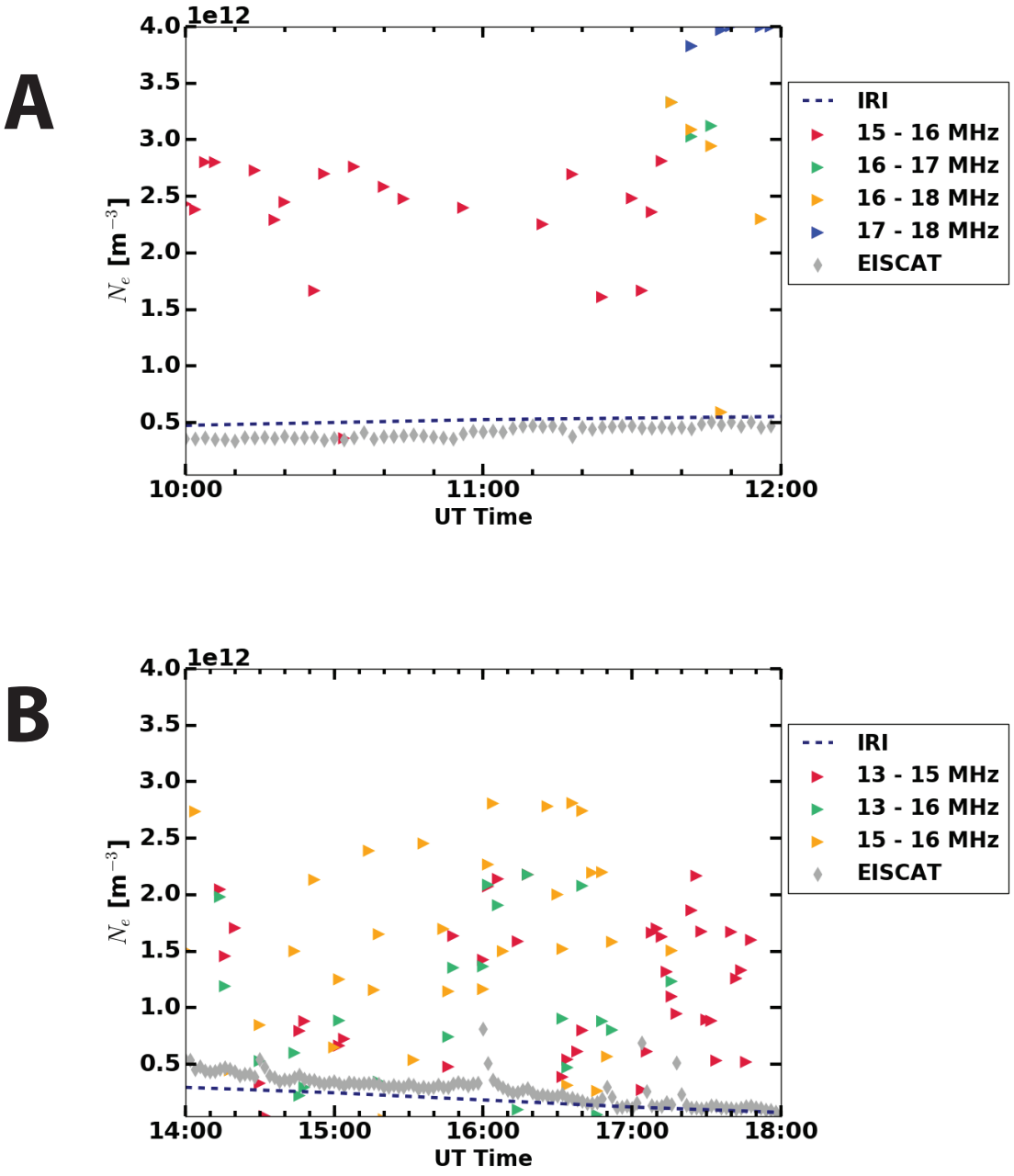

Figure C.5: The colored triangles are the calculated N_e from the CUTLASS STEREO method for (A) March 12, 2015 from 10:00 to 12:00 UT and (B) March 3, 2016 from 14:00 to 18:00 UT. The shaded diamonds are the EISCAT N_e at 240 km for (A) and 220 km for (B). The navy blue dotted line is IRI N_e at 240 km for (A) and 220 km for (B).

low, demonstrating that CUTLASS fails to capture the trends measured by EISCAT. On the other hand, the linear regression r between EISCAT and IRI is 0.97 for the first experiment and 0.99 for the second experiment.

The CUTLASS N_e is approximately an order of magnitude larger than the EISCAT N_e. Figure C.6 shows the CUTLASS N_e divided by the EISCAT N_e at about 240 km, both resampled to the same 2 minute cadence between 10:00 to 12:00 UT on March 12, 2015 and 14:00 to 18:00 on March 3, 2016 at approximately 220 km. The black dotted line represents where the CUTLASS data would match the EISCAT N_e. The colored triangles represent the different frequency bands used to calculate N_e, as previously described. In Figure C.6A, the 15-16 MHz N_e shows the most variation and difference from the EISCAT N_e early in the experiment from 10:00 to 10:30 UT. After 10:30 UT, the CUTLASS N_e measurements, regardless of frequency, are greater than the EISCAT N_e by a factor of 6-10. The least variable ratio is the 17-18 MHz band N_e measurements, clustered around a factor of 8 difference.

In Figure C.6B, all bands (13-15 MHz, 13-16 MHz, and 15-16 MHz) show large variation and are consistently off from the EISCAT N_e. The offset ratio increases throughout the experiment, reaching a maximum of approximately a factor of 15 by 17:00 UT. This is because the CUTLASS calculated N_e do not capture the decrease in the ionosphere as the sun sets and the ionosphere cools.

With a near order of magnitude overestimate of N_e, the CUTLASS measurements do not align well with the EISCAT N_e. The CUTLASS calculated N_e also does not capture the gradual increase in N_e seen by EISCAT after 10:50 UT in the first case study nor the steady decrease of N_e in the second case study as the sun sets.

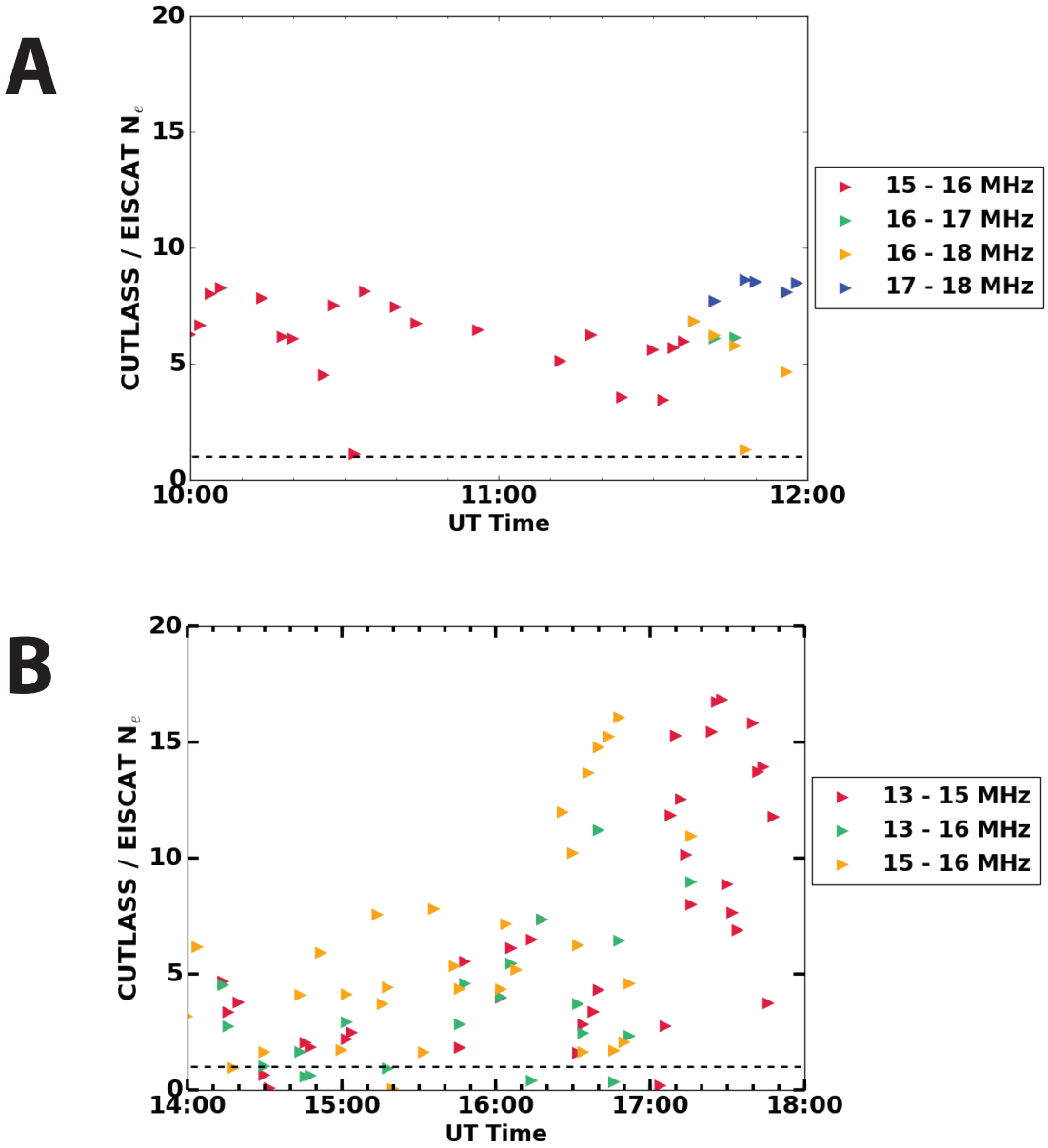

Figure C.6: The ratio of N_e calculated from the CUTLASS and EISCAT radars. The colored triangles are the calculated N_e from the CUTLASS STEREO method resampled into 2 minute periods for (A) on March 12, 2015 from 10:00 to 12:00 UT and (B) on March 3, 2016 from 14:00 to 18:00 UT and divided by the EISCAT N_e at 240 km for (A) and 220 km for (B) at the same times. The black dotted line is where the SuperDARN N_e equals the EISCAT N_e. The color of the triangle indicates what frequency pairs were used to calculate N_e.

C.1.4 Discussion

Theoretically, calculating electron densities from shifts in the CUTLASS line of sight velocities and frequencies should account for the index of refraction and provide reliable electron density calculations. However, our comparison to EISCAT N_e demonstrates that the CUTLASS derived N_e overestimate approximately by a factor 8, which is dependent on the radar frequencies used to calculate N_e. This demonstrates that the dual frequency method is not effective for calculating reliable background N_e from SuperDARN observations.

Gillies et al. (2010) proposed that an overestimation of N_e could be from localized regions of SuperDARN backscatter. For example, dominant scatter could be from a small fraction of the SuperDARN range cell in which conditions for scatter are best. Whereas EISCAT captures the background N_e, CUTLASS is prone to picking up localized structures which produce stronger irregularities and places with higher electron density (*Hosokawa et al.*, 2009). Further, N_e enhancements of up to an order of magnitude due to polar cap patches are likely to occur during the day time, which is when our experiment on March 12, 2015 took place (*Sojka et al.*, 1990; *Pryse et al.*, 2005). Polar cap patches have also been shown to extend in the afternoon and evening, which would overlap with the times of our March 3, 2016 case study (*Moen et al.*, 2007; *Zhang et al.*, 2013). Within a polar cap patch, electron number density can vary by an order of magnitude (*Weber et al.*, 1986). All of this was mitigated in the experiments presented above by running the EISCAT Heater during these two intervals. This produced irregularities over EISCAT and therefore scattering along the line of sight of the CUTLASS radar, making the CUTLASS-EISCAT observations as comparable as possible.

The field aligned density striations themselves could also contribute to the Super-

DARN N_e overestimation. *Gurevich et al.* (1999) showed that bunches of field aligned density striations due to self-focusing of the pump beam in the ionosphere could lead to 10% N_e enhancements. The 10m scale striations observed by SuperDARN are not large, so the density enhancements would not manifest in the EISCAT N_e observations but could be selectively picked out by SuperDARN. Several studies have also shown that these field aligned striations from the EISCAT heating facility produce a strong backscatter response in SuperDARN CUTLASS measurements (*Kelley et al.*, 1995; *Dhillon*, 2002; *Kosch et al.*, 2002; *Gurevich et al.*, 2002; *Rietveld et al.*, 2003). If we could resolve the size of irregularity bunches compared to the scattering volume measured by SuperDARN, it may be possible to reconcile calculated SuperDARN N_e from line of sight velocity measurements at different frequencies to EISCAT N_e. As stated, though, these striations are only a 10% density effect, and the CUTLASS N_e were off by an order of magnitude.

C.1.5 Conclusions

Our experiments on March 12, 2015 and March 3, 2016 compared calculated N_e, derived from the CUTLASS Hankasalmi radar line of sight velocity measurements, to the Tromsø EISCAT UHF incoherent scatter radar derived N_e. Our ray tracing estimates showed that CUTLASS was approximately probing the ionosphere at 240 km over Tromsø on March 12, 2015 and at 220 km on March 3, 2016. We found that the derivation for calculating electron number densities proposed by *Gillies et al.* (2010, 2012) was unsuccessful at determining reasonable background N_e from pump-induced artificial striations over EISCAT. No plasma density at any altitude could provide agreement. We tested the method using near simultaneous dual frequency observations (MHz difference) and by also using the automatic frequency shifts (kHz difference) typical of SuperDARN radars when operating on one frequency band.

Both methods overestimated N_e by approximately a factor of 8, and, in particular, the small frequency shift method resulted in static, frequency dependent results. Neither method captured EISCAT N_e increases or decreases across the experimental window.

We propose that the overestimation of SuperDARN N_e may be due to localized density irregularities dominating the backscatter measured by SuperDARN and resulting in an artificially high N_e based off of these localized irregularities. However, other factors could contribute to the discrepancy between SuperDARN and EISCAT N_e. Future work would involve attempting to reconcile the N_e measurements between SuperDARN and EISCAT by determining the volume of the irregularity back scatter compared to the overall scattering volume.

BIBLIOGRAPHY

BIBLIOGRAPHY

André, D., G. J. Sofko, K. Baker, and J. MacDougall (1998), Superdarn interferometry: Meteor echoes and electron densities from groundscatter, *Journal of Geophysical Research: Space Physics*, *103*(A4), 7003–7015.

André, M. (1986), Electrostatic ion waves generated by ion loss-cone distributions in the magnetosphere, in *Annales Geophysicae, Series A-Upper Atmosphere and Space Sciences*, vol. 4, pp. 241–246.

André, M., G. Crew, W. Peterson, A. Persoon, C. Pollock, and M. Engebretson (1990), Ion heating by broadband low-frequency waves in the cusp/cleft, *Journal of Geophysical Research: Space Physics*, *95*(A12), 20,809–20,823.

Baker, D., et al. (2013), A long-lived relativistic electron storage ring embedded in earth's outer van allen belt, *Science*, *340*(6129), 186–190.

Baker, J. B., J. M. Ruohoniemi, A. J. Ribeiro, L. B. Clausen, R. A. Greenwald, N. A. Frissell, and K. A. Sterne (2011), Superdarn ionospheric space weather, *Aerospace and Electronic Systems Magazine, IEEE*, *26*(10), 30–34.

Barnett, C. F., H. T. Hunter, M. I. Fitzpatrick, I. Alvarez, C. Cisneros, and R. A. Phaneuf (1990), Atomic data for fusion. volume 1: Collisions of h, h2, he and li atoms and ions with atoms and molecules, *NASA STI/Recon Technical Report N*, *91*, 13,238.

Bilitza, D. (2001), International reference ionosphere 2000, *Radio Science*, *36*(2), 261–275.

Boardsen, S. A., et al. (2016), Survey of the frequency dependent latitudinal distribution of the fast magnetosonic wave mode from van allen probes electric and magnetic field instrument and integrated science waveform receiver plasma wave analysis, *Journal of Geophysical Research: Space Physics*.

Bortnik, J., and R. Thorne (2007), The dual role of elf/vlf chorus waves in the acceleration and precipitation of radiation belt electrons, *Journal of Atmospheric and Solar-Terrestrial Physics*, *69*(3), 378–386.

Bortnik, J., R. M. Thorne, and N. P. Meredith (2008), The unexpected origin of plasmaspheric hiss from discrete chorus emissions, *Nature*, *452*(7183), 62–66.

Bortnik, J., R. Thorne, and N. Omidi (2010), Nonlinear evolution of emic waves in a uniform magnetic field: 2. test-particle scattering, *Journal of Geophysical Research: Space Physics (1978–2012)*, *115*(A12).

Bortnik, J., L. Chen, W. Li, R. Thorne, N. Meredith, and R. Horne (2011), Modeling the wave power distribution and characteristics of plasmaspheric hiss, *Journal of Geophysical Research: Space Physics*, *116*(A12).

Brain, D., R. Lillis, D. Mitchell, J. Halekas, and R. Lin (2007), Electron pitch angle distributions as indicators of magnetic field topology near mars, *Journal of Geophysical Research: Space Physics (1978–2012)*, *112*(A9).

Burch, J., J. Winningham, V. Blevins, N. Eaker, W. Gibson, and R. Hoffman (1981), High-altitude plasma instrument for dynamics explorer-a, *Space Science Instrumentation*, *5*, 455–463.

Burch, J., P. Reiff, R. Heelis, J. Winningham, W. Hanson, C. Gurgiolo, J. Menietti, R. Hoffman, and J. Barfield (1982), Plasma injection and transport in the mid-altitude polar cusp, *Geophysical research letters*, *9*(9), 921–924.

Burch, J., et al. (2001), Views of earth's magnetosphere with the image satellite, *Science*, *291*(5504), 619–624.

Carpenter, D., and R. Anderson (1992), An isee/ whistler model of equatorial electron density in the magnetosphere, *Journal of Geophysical Research: Space Physics (1978–2012)*, *97*(A2), 1097–1108.

Carpenter, D., C. Park, H. Taylor, and H. Brinton (1969), Multi-experiment detection of the plasmapause from eogo satellites and antarctic ground stations, *Journal of Geophysical Research*, *74*(7), 1837–1847.

Carpenter, D., T. Bell, U. Inan, R. Benson, V. Sonwalkar, B. Reinisch, and D. Gallagher (2003), Z-mode sounding within propagation cavities and other inner magnetospheric regions by the rpi instrument on the image satellite, *Journal of Geophysical Research: Space Physics (1978–2012)*, *108*(A12).

Carpenter, D. L. (1963), Whistler evidence of a kneein the magnetospheric ionization density profile, *Journal of Geophysical Research*, *68*(6), 1675–1682.

Carpenter, D. L. (1967), Relations between the dawn minimum in the equatorial radius of the plasmapause and dst, kp, and local k at byrd station, *Journal of Geophysical Research*, *72*(11), 2969–2971.

Carpenter, D. L., and J. Lemaire (1997), Erosion and recovery of the plasmasphere in the plasmapause region, *Space Science Reviews*, *80*(1-2), 153–179.

Carpenter, D. L., and C. Park (1973), On what ionospheric workers should know about the plasmapause-plasmasphere, *Reviews of Geophysics*, *11*(1), 133–154.

Carpenter, D. L., R. Anderson, W. Calvert, and M. Moldwin (2000), Crres observations of density cavities inside the plasmasphere, *Journal of Geophysical Research: Space Physics (1978–2012)*, *105*(A10), 23,323–23,338.

Carpenter, D. L., et al. (2002), Small-scale field-aligned plasmaspheric density structures inferred from the radio plasma imager on image, *Journal of Geophysical Research: Space Physics (1978–2012)*, *107*(A9), SMP–22.

Chandler, M., and C. Chappell (1986), Observations of the flow of h+ and he+ along magnetic field lines in the plasmasphere, *Journal of Geophysical Research: Space Physics (1978–2012)*, *91*(A8), 8847–8860.

Chang, T., G. Crew, N. Hershkowitz, J. Jasperse, J. Retterer, and J. Winningham (1986), Transverse acceleration of oxygen ions by electromagnetic ion cyclotron resonance with broad band left-hand polarized waves, *Geophysical Research Letters*, *13*(7), 636–639.

Chappell, C. (1972), Recent satellite measurements of the morphology and dynamics of the plasmasphere, *Reviews of Geophysics*, *10*(4), 951–979.

Chappell, C., K. Harris, and G. Sharp (1970), A study of the influence of magnetic activity on the location of the plasmapause as measured by ogo 5, *Journal of Geophysical Research*, *75*(1), 50–56.

Chappell, C., S. Fields, C. Baugher, J. Hoffman, W. Hanson, W. Wright, H. Hammack, G. Carignan, and A. Nagy (1981), The retarding ion mass spectrometer on dynamics explorer-a, *Unknown*, *1*.

Chappell, C., T. Moore, and J. Waite (1987), The ionosphere as a fully adequate source of plasma for the earth's magnetosphere, *Journal of Geophysical Research: Space Physics (1978–2012)*, *92*(A6), 5896–5910.

Chappell, C., M. Huddleston, T. Moore, B. Giles, and D. Delcourt (2008), Observations of the warm plasma cloak and an explanation of its formation in the magnetosphere, *Journal of Geophysical Research: Space Physics (1978–2012)*, *113*(A9).

Chen, L., R. M. Thorne, V. K. Jordanova, and R. B. Horne (2010), Global simulation of magnetosonic wave instability in the storm time magnetosphere, *Journal of Geophysical Research: Space Physics*, *115*(A11), n/a–n/a, doi:10.1029/2010JA015707, a11222.

Chen, L., R. M. Thorne, V. K. Jordanova, M. F. Thomsen, and R. B. Horne (2011), Magnetosonic wave instability analysis for proton ring distributions observed by the lanl magnetospheric plasma analyzer, *Journal of Geophysical Research: Space Physics*, *116*(A3).

Chen, L., et al. (2014), Generation of unusually low frequency plasmaspheric hiss, *Geophysical Research Letters*, *41*(16), 5702–5709, doi:10.1002/2014GL060628.

Chisham, G., et al. (2007), A decade of the super dual auroral radar network (superdarn): Scientific achievements, new techniques and future directions, *Surveys in Geophysics*, *28*(1), 33–109.

Choi, H.-S., et al. (2011), Analysis of geo spacecraft anomalies: Space weather relationships, *Space Weather*, *9*(6).

Church, S., and R. M. Thorne (1983), On the origin of plasmaspheric hiss: Ray path integrated amplification, *Journal of Geophysical Research: Space Physics*, *88*(A10), 7941–7957.

Cierpka, K., M. Kosch, M. Rietveld, K. Schlegel, and T. Hagfors (2000), Ion-neutral coupling in the high-latitude f-layer from incoherent scatter and fabry-perot interferometer measurements, in *Annales Geophysicae*, vol. 18, pp. 1145–1153, Springer.

Clausen, L., and K.-H. Glassmeier (2014), Enhancement of ultralow frequency wave amplitudes at the plasmapause, *Journal of Geophysical Research: Space Physics*, *119*(11), 9113–9124.

Comfort, R., and J. Horwitz (1981), Low energy ion pitch angle distributions observed on the dayside at geosynchronous altitudes, *Journal of Geophysical Research: Space Physics (1978–2012)*, *86*(A3), 1621–1627.

Comfort, R. H., J. H. Waite, and C. R. Chappell (1985), Thermal ion temperatures from the retarding ion mass spectrometer on de 1, *Journal of Geophysical Research: Space Physics*, *90*(A4), 3475–3486, doi:10.1029/JA090iA04p03475.

Craven, P., R. Olsen, J. Fennell, D. Croley, and T. Aggson (1987), Potential modulation on the scatha spacecraft, *Journal of Spacecraft and Rockets*, *24*(2), 150–157.

Crew, G., T. Chang, J. Retterer, W. Peterson, D. Gurnett, and R. Huff (1990), Ion cyclotron resonance heated conics: Theory and observations, *Journal of Geophysical Research: Space Physics*, *95*(A4), 3959–3985.

Curtis, S. (1985), Equatorial trapped plasmasphere ion distributions and transverse stochastic acceleration, *Journal of Geophysical Research: Space Physics (1978–2012)*, *90*(A2), 1765–1770.

Darrouzet, F., et al. (2009), Plasmaspheric density structures and dynamics: Properties observed by the cluster and image missions, in *The Earths Plasmasphere*, pp. 55–106, Springer.

Davies, J., M. Lester, S. E. Milan, and T. Yeoman (1999), A comparison of velocity measurements from the cutlass finland radar and the eiscat uhf system, in *Annales Geophysicae*, vol. 17, pp. 892–902, Springer.

Davis, V., M. Mandell, N. Baker, M. Brown-Hayes, G. Davis, R. Maurer, and C. Herrmann (2012), Surface-charging analysis of the radiation belt storm probe and magnetospheric multiscale spacecraft, *Plasma Science, IEEE Transactions on*, *40*(2), 262–273.

de Larquier, S., J. Ruohoniemi, J. Baker, N. Ravindran Varrier, and M. Lester (2011), First observations of the midlatitude evening anomaly using super dual auroral radar network (superdarn) radars, *Journal of Geophysical Research: Space Physics*, *116*(A10).

Décréau, P., et al. (1997), Whisper, a resonance sounder and wave analyser: Performances and perspectives for the cluster mission, *Space Science Reviews*, *79*(1-2), 157–193.

DeForest, S. E. (1972), Spacecraft charging at synchronous orbit, *Journal of Geophysical Research*, *77*(4), 651–659.

DeForest, S. E. (1973), Electrostatic potentials developed by ats-5, in *Photon and particle interactions with surfaces in space*, pp. 263–267, Springer.

Denton, R., Y. Wang, P. Webb, P. Tengdin, J. Goldstein, J. Redfern, and B. Reinisch (2012), Magnetospheric electron density long-term (¿ 1 day) refilling rates inferred from passive radio emissions measured by image rpi during geomagnetically quiet times, *Journal of Geophysical Research: Space Physics (1978–2012)*, *117*(A3).

Dhillon, R. S. (2002), Radar studies of natural and artificial waves and instabilities in the auroral ionosphere, Ph.D. thesis, Physics.

Draganov, A., U. Inan, V. Sonwalkar, and T. Bell (1992), Magnetospherically reflected whistlers as a source of plasmaspheric hiss, *Geophysical research letters*, *19*(3), 233–236.

Drell, S., H. Foley, and M. Ruderman (1965), Drag and propulsion of large satellites in the ionosphere: An alfvén propulsion engine in space, *Journal of Geophysical Research*, *70*(13), 3131–3145.

Eglitis, P., T. Robinson, M. Rietveld, D. Wright, and G. Bond (1998), The phase speed of artificial field-aligned irregularities observed by cutlass during hf modification of the auroral ionosphere, *Journal of Geophysical Research: Space Physics*, *103*(A2), 2253–2259.

Escoubet, C., M. Fehringer, and M. Goldstein (1999), Introduction the cluster mission, in *Annales Geophysicae*, vol. 19, pp. 1197–1200, Copernicus GmbH.

Finlay, C., et al. (2010), International geomagnetic reference field: the eleventh generation, *Geophysical Journal International*, *183*(3), 1216–1230.

Fok, M.-C., J. Kozyra, A. Nagy, C. Rasmussen, and G. Khazanov (1993), Decay of equatorial ring current ions and associated aeronomical consequences, *Journal of Geophysical Research: Space Physics (1978–2012)*, *98*(A11), 19,381–19,393.

Fok, M.-C., P. D. Craven, T. E. Moore, and P. G. Richards (1995), Ring current-plasmasphere coupling through coulomb collisions, *Cross-Scale Coupling in Space Plasmas*, pp. 161–171.

Fraser, B., and T. Nguyen (2001), Is the plasmapause a preferred source region of electromagnetic ion cyclotron waves in the magnetosphere?, *Journal of Atmospheric and Solar-Terrestrial Physics*, *63*(11), 1225–1247.

Fraser, B., J. Samson, R. McPherron, and C. Russell (1986), Ion cyclotron waves observed near the plasmapause, *Advances in space research*, *6*(3), 223–226.

Fu, H., J. Tu, J. Cao, P. Song, B. Reinisch, D. Gallagher, and B. Yang (2010), Image and dmsp observations of a density trough inside the plasmasphere, *Journal of Geophysical Research: Space Physics (1978–2012)*, *115*(A7).

Funsten, H., et al. (2013), Helium, oxygen, proton, and electron (hope) mass spectrometer for the radiation belt storm probes mission, *Space Science Reviews*, *179*(1-4), 423–484, doi:10.1007/s11214-013-9968-7.

Funsten, H., et al. (2014), Helium, oxygen, proton, and electron (hope) mass spectrometer for the radiation belt storm probes mission, in *The Van Allen Probes Mission*, pp. 423–484, Springer.

Gallagher, D., and R. Comfort (2016), Unsolved problems in plasmasphere refilling, *Journal of Geophysical Research: Space Physics*.

Gallagher, D., P. Craven, and R. Comfort (1988), An empirical model of the earth's plasmasphere, *Advances in space research*, *8*(8), 15–24.

Gallagher, D. L., P. D. Craven, and R. H. Comfort (2000), Global core plasma model, *Journal of Geophysical Research: Space Physics (1978–2012)*, *105*(A8), 18,819–18,833.

Galvan, D. A., M. B. Moldwin, and B. R. Sandel (2008), Diurnal variation in plasmaspheric he+ inferred from extreme ultraviolet images, *Journal of Geophysical Research: Space Physics (1978–2012)*, *113*(A9).

Ganguli, G., M. Reynolds, and M. Liemohn (2000), The plasmasphere and advances in plasmaspheric research, *Journal of Atmospheric and Solar-Terrestrial Physics*, *62*(17), 1647–1657.

Gannon, J., X. Li, and D. Heynderickx (2007), Pitch angle distribution analysis of radiation belt electrons based on combined release and radiation effects satellite medium electrons a data, *Journal of Geophysical Research: Space Physics (1978–2012)*, *112*(A5).

Garrett, H. B. (1981), The charging of spacecraft surfaces, *Reviews of Geophysics and Space Physics*, *19*(4), 577–616.

Gary, S. P., K. Liu, D. Winske, and R. E. Denton (2010), Ion bernstein instability in the terrestrial magnetosphere: Linear dispersion theory, *Journal of Geophysical Research: Space Physics (1978–2012)*, *115*(A12).

Giles, B., C. Chappell, T. Moore, R. Comfort, and J. Waite (1994), Statistical survey of pitch angle distributions in core (0-50 ev) ions from dynamics explorer, 1: Outflow in the auroral zone, polar cap, and cusp, *Journal of Geophysical Research: Space Physics (1978–2012)*, *99*(A9), 17,483–17,501.

Gillies, R., G. Hussey, G. Sofko, K. McWilliams, R. Fiori, P. Ponomarenko, and J.-P. St-Maurice (2009), Improvement of superdarn velocity measurements by estimating the index of refraction in the scattering region using interferometry, *Journal of Geophysical Research: Space Physics*, *114*(A7).

Gillies, R., G. Hussey, G. Sofko, D. Wright, and J. Davies (2010), A comparison of eiscat and superdarn f-region measurements with consideration of the refractive index in the scattering volume, *Journal of Geophysical Research: Space Physics*, *115*(A6).

Gillies, R., G. Hussey, G. Sofko, P. Ponomarenko, and K. McWilliams (2011), Improvement of hf coherent radar line-of-sight velocities by estimating the refractive index in the scattering volume using radar frequency shifting, *Journal of Geophysical Research: Space Physics (1978–2012)*, *116*(A1).

Gillies, R., G. Hussey, G. Sofko, and K. McWilliams (2012), A statistical analysis of superdarn scattering volume electron densities and velocity corrections using a radar frequency shifting technique, *Journal of Geophysical Research: Space Physics*, *117*(A8).

Grard, R., K. Knott, et al. (1983), Spacecraft charging effects, in *Progress in Solar-Terrestrial Physics*, pp. 289–304, Springer.

Green, J. L., S. F. Fung, S. Boardsen, and H. J. Christian (2005), Distribution and origin of plasmaspheric plasma waves, *Inner Magnetosphere Interactions: New Perspectives from Imaging*, pp. 113–126.

Greenwald, R., et al. (1995), Darn/superdarn, *Space Science Reviews*, *71*(1-4), 761–796.

Guiter, S., and T. Gombosi (1990), The role of high-speed plasma flows in plasmaspheric refilling, *Journal of Geophysical Research: Space Physics (1978–2012)*, *95*(A7), 10,427–10,440.

Guiter, S., T. I. Gombosi, and C. Rasmussen (1995), Two-stream modeling of plasmaspheric refilling, *Journal of Geophysical Research: Space Physics (1978–2012)*, *100*(A6), 9519–9526.

Gurevich, A., K. Zybin, and A. Lukyanov (1995), Stationary striations developed in the ionospheric modification, *Physical review letters*, *75*(13), 2622.

Gurevich, A., H. Carlson, M. Kelley, T. Hagfors, A. Karashtin, and K. Zybin (1999), Nonlinear structuring of the ionosphere modified by powerful radio waves at low latitudes, *Physics Letters A*, *251*(5), 311–321.

Gurevich, A., E. Fremouw, J. Secan, and K. Zybin (2002), Large scale structuring of plasma density perturbations in ionospheric modifications, *Physics Letters A*, *301*(3), 307–314.

Gurgiolo, C., B. Sandel, J. Perez, D. Mitchell, C. Pollock, and B. Larsen (2005), Overlap of the plasmasphere and ring current: Relation to subauroral ionospheric heating, *Journal of Geophysical Research: Space Physics (1978–2012)*, *110*(A12).

Gurnett, D. A. (1976), Plasma wave interactions with energetic ions near the magnetic equator, *Journal of Geophysical Research*, *81*(16), 2765–2770.

Harris, J. T. (2003), Spacecraft charging at geosynchronous altitudes: current-balance and critical temperature in a non-maxwellian plasma, *Tech. rep.*, No. AFIT/GAP/ENP/03-05. AIR FORCE INST OF TECH WRIGHT-PATTERSON AFB OH SCHOOL OF ENGINEERING AND MANAGEMENT.

Harvey, P., et al. (1995), The electric field instrument on the polar satellite, *Space Science Reviews*, *71*(1-4), 583–596.

Heelis, R., J. K. Lowell, and R. W. Spiro (1982), A model of the high-latitude ionospheric convection pattern, *Journal of Geophysical Research: Space Physics*, *87*(A8), 6339–6345.

Ho, M., and D. Moorcroft (1971), Hydrogen density and proton flux in the topside ionosphere over arecibo, puerto rico, from incoherent scatter observations, *Planetary and Space Science*, *19*(11), 1441–1455.

Hooke, W. H. (1968), Ionospheric irregularities produced by internal atmospheric gravity waves, *Journal of Atmospheric and Terrestrial Physics*, *30*(5), 795–823.

Horne, R. B., and R. M. Thorne (1998), Potential waves for relativistic electron scattering and stochastic acceleration during magnetic storms, *Geophysical Research Letters*, *25*(15), 3011–3014.

Horne, R. B., G. V. Wheeler, and H. S. C. Alleyne (2000), Proton and electron heating by radially propagating fast magnetosonic waves, *Journal of Geophysical Research: Space Physics (1978–2012)*, *105*(A12), 27,597–27,610.

Horne, R. B., R. M. Thorne, S. A. Glauert, N. P. Meredith, D. Pokhotelov, and O. Santolík (2007), Electron acceleration in the van allen radiation belts by fast magnetosonic waves, *Geophysical Research Letters*, *34*(17).

Horne, R. B., et al. (2005), Wave acceleration of electrons in the van allen radiation belts, *Nature*, *437*(7056), 227–230.

Horwitz, J. (1987), Core plasma in the magnetosphere, *Reviews of Geophysics*, *25*(3), 579–587.

Horwitz, J., R. Comfort, and C. Chappell (1990), A statistical characterization of plasmasphere density structure and boundary locations, *Journal of Geophysical Research: Space Physics*, *95*(A6), 7937–7947.

Hosokawa, K., K. Shiokawa, Y. Otsuka, T. Ogawa, J.-P. St-Maurice, G. Sofko, and D. Andre (2009), Relationship between polar cap patches and field-aligned irregularities as observed with an all-sky airglow imager at resolute bay and the polardarn radar at rankin inlet, *Journal of Geophysical Research: Space Physics*, *114*(A3).

Hrbáčková, Z., O. Santolík, F. Němec, E. Macúšová, and N. Cornilleau-Wehrlin (2015), Systematic analysis of occurrence of equatorial noise emissions using 10 years of data from the cluster mission, *Journal of Geophysical Research: Space Physics*, *120*(2), 1007–1021.

Imhof, W., H. Voss, J. Mobilia, M. Walt, U. Inan, and D. Carpenter (1989), Characteristics of short-duration electron precipitation bursts and their relationship with vlf wave activity, *Journal of Geophysical Research: Space Physics*, *94*(A8), 10,079–10,093.

Inan, U. S., and T. F. Bell (1977), The plasmapause as a vlf wave guide, *Journal of Geophysical Research*, *82*(19), 2819–2827.

Johnson, C. Y., and E. B. Meadows (1955), First investigation of ambient positive-ion composition to 219 km by rocket-borne spectrometer, *Journal of Geophysical Research*, *60*(2), 193–203.

Johnson, M., and J. Kierein (1992), Combined release and radiation effects satellite (crres): Spacecraft and mission, *Journal of Spacecraft and Rockets*, *29*(4), 556–563.

Jordanova, V., Y. Yu, J. Niehof, R. Skoug, G. Reeves, C. Kletzing, J. Fennell, and H. Spence (2014), Simulations of inner magnetosphere dynamics with an expanded ram-scb model and comparisons with van allen probes observations, *Geophysical Research Letters*, *41*(8), 2687–2694.

Katus, R., D. Gallagher, M. Liemohn, A. Keesee, and L. Sarno-Smith (2015), Statistical storm time examination of mlt-dependent plasmapause location derived from image euv, *Journal of Geophysical Research: Space Physics*, *120*(7), 5545–5559.

Katz, I., V. Davis, D. B. Snyder, et al. (1998), Mechanism for spacecraft charging initiated destruction of solar arrays in geo, *AIAA paper*, pp. 98–1002.

Kelley, M. C., T. L. Arce, J. Salowey, M. Sulzer, W. T. Armstrong, M. Carter, and L. Duncan (1995), Density depletions at the 10-m scale induced by the arecibo heater, *Journal of Geophysical Research: Space Physics*, *100*(A9), 17,367–17,376, doi:10.1029/95JA00063.

Kintner, P. M., J. Bonnell, R. Arnoldy, K. Lynch, C. Pollock, and T. Moore (1996), Scifer-transverse ion acceleration and plasma waves, *Geophysical Research Letters*, *23*(14), 1873–1876.

Kirby, K., et al. (2013), Radiation belt storm probesobservatory and environments, *Space Science Reviews*, *179*(1-4), 59–125.

Kirby, K., et al. (2014), Radiation belt storm probesobservatory and environments, in *The Van Allen Probes Mission*, pp. 59–125, Springer.

Kletzing, C., et al. (2013), The electric and magnetic field instrument suite and integrated science (emfisis) on rbsp, in *The Van Allen Probes Mission*, pp. 127–181, Springer.

Kletzing, C., et al. (2014), The electric and magnetic field instrument suite and integrated science (emfisis) on rbsp, in *The Van Allen Probes Mission*, pp. 127–181, Springer.

Knudsen, D. J., J. H. Clemmons, and J.-E. Wahlund (1998), Correlation between core ion energization, suprathermal electron bursts, and broadband elf plasma waves, *Journal of Geophysical Research: Space Physics*, *103*(A3), 4171–4186.

Koons, H., J. Mazur, A. Lopatin, D. Pitchford, A. Bogorad, and R. Herschitz (2006), Spatial and temporal correlation of spacecraft surface charging in geosynchronous orbit, *Journal of spacecraft and rockets*, *43*(1), 178–185.

Kosch, M. J., and E. Nielsen (1995), Coherent radar estimates of average high-latitude ionospheric joule heating, *Journal of Geophysical Research: Space Physics*, *100*(A7), 12,201–12,215.

Kosch, M. J., M. Rietveld, A. Kavanagh, C. Davis, T. Yeoman, F. Honary, and T. Hagfors (2002), High-latitude pump-induced optical emissions for frequencies close to the third electron gyro-harmonic, *Geophysical research letters*, *29*(23).

Kosch, M. J., M. Rietveld, A. Senior, I. McCrea, A. Kavanagh, B. Isham, and F. Honary (2004), Novel artificial optical annular structures in the high latitude ionosphere over eiscat, *Geophysical research letters*, *31*(12).

Kotova, G., V. Bezrukikh, M. Verigin, and L. Lezhen (2002), Temperature and density variations in the dusk and dawn plasmasphere as observed by interball tail in 1999–2000, *Advances in Space Research*, *30*(7), 1831–1834.

Kozyra, J., T. Cravens, A. Nagy, E. Fontheim, and R. Ong (1984), Effects of energetic heavy ions on electromagnetic ion cyclotron wave generation in the plasmapause region, *Journal of Geophysical Research: Space Physics (1978–2012)*, *89*(A4), 2217–2233.

Kozyra, J., L. Brace, T. Cravens, and A. Nagy (1986), A statistical study of the subauroral electron temperature enhancement using dynamics explorer 2 langmuir probe observations, *Journal of Geophysical Research: Space Physics (1978–2012)*, *91*(A10), 11,270–11,280.

Kozyra, J., C. Rasmussen, R. Miller, and L. Lyons (1994), Interaction of ring current and radiation belt protons with ducted plasmaspheric hiss: 1. diffusion coefficients and timescales, *Journal of Geophysical Research: Space Physics*, *99*(A3), 4069–4084.

Kozyra, J., C. Rasmussen, R. Miller, and E. Villalon (1995), Interaction of ring current and radiation belt protons with ducted plasmaspheric hiss: 2. time evolution of the distribution function, *Journal of Geophysical Research: Space Physics*, *100*(A11), 21,911–21,919.

Kurth, W., S. De Pascuale, J. Faden, C. Kletzing, G. Hospodarsky, S. Thaller, and J. Wygant (2015), Electron densities inferred from plasma wave spectra obtained by the waves instrument on van allen probes, *Journal of Geophysical Research: Space Physics*, *120*(2), 904–914.

Laakso, H., H. Junginger, A. Roux, R. Schmidt, and C. d. Villedary (1990), Magnetosonic waves above fc (h+) at geostationary orbit: Geos 2 results, *Journal of Geophysical Research: Space Physics (1978–2012)*, *95*(A7), 10,609–10,621.

LaBelle, J., R. Treumann, W. Baumjohann, G. Haerendel, N. Sckopke, G. Paschmann, and H. Lühr (1988), The duskside plasmapause/ring current interface: Convection and plasma wave observations, *Journal of Geophysical Research: Space Physics*, *93*(A4), 2573–2590.

Ladreiter, H., P. Zarka, A. Lecacheux, W. Macher, H. Rucker, R. Manning, D. Gurnett, and W. Kurth (1995), Analysis of electromagnetic wave direction finding performed by spaceborne antennas using singular-value decomposition techniques, *Radio science*, *30*(6), 1699–1712.

Laframboise, J., and M. Kamitsuma (1983), The threshold temperature effect in high-voltage spacecraft charging, *Tech. rep.*, YORK UNIV DOWNSVIEW (ONTARIO).

Lai, S. T., and D. J. Della-Rose (2001), Spacecraft charging at geosynchronous altitudes: New evidence of existence of critical temperature, *Journal of spacecraft and rockets*, *38*(6), 922–928.

Lai, S. T., and M. Tautz (2006), High-level spacecraft charging in eclipse at geosynchronous altitudes: A statistical study, *Journal of Geophysical Research: Space Physics (1978–2012)*, *111*(A9).

Lanzerotti, L., D. Mellen, and H. Fukunishi (1975), Excitation of plasma density gradients in the magnetosphere at ultralow frequencies, *Journal of Geophysical Research*, *80*(22), 3131–3140.

Lanzerotti, L., C. Breglia, D. Maurer, G. Johnson, and C. Maclennan (1998), Studies of spacecraft charging on a geosynchronous telecommunications satellite, *Advances in Space Research*, *22*(1), 79–82.

Lanzerotti, L. J. (2001), Space weather effects on communications, in *Space storms and space weather hazards*, pp. 313–334, Springer.

Lanzerotti, L. J. (2013), Van allen probes mission, *Space Weather*, *11*(4), 133–133, doi:10.1002/swe.20037.

Larsen, B., D. Klumpar, and C. Gurgiolo (2007), Correlation between plasmapause position and solar wind parameters, *Journal of Atmospheric and Solar-Terrestrial Physics*, *69*(3), 334–340.

Lehtinen, M. S., and A. Huuskonen (1996), General incoherent scatter analysis and guisdap, *Journal of Atmospheric and Terrestrial Physics*, *58*(1), 435–452.

Lemaire, J. F., K. I. Gringauz, D. L. Carpenter, and V. Bassolo (2005), *The Earth's plasmasphere*, Cambridge University Press.

Lennartsson, W., and D. L. Reasoner (1978), Low-energy plasma observations at synchronous orbit, *Journal of Geophysical Research: Space Physics (1978–2012)*, *83*(A5), 2145–2156.

Lester, M., et al. (2004), Stereo cutlass-a new capability for the superdarn hf radars, in *Annales Geophysicae*, vol. 22, pp. 459–473.

Leyser, T., B. Thidé, H. Derblom, Å. Hedberg, B. Lundborg, P. Stubbe, and H. Kopka (1990), Dependence of stimulated electromagnetic emission on the ionosphere and pump wave, *Journal of Geophysical Research: Space Physics*, *95*(A10), 17,233–17,244.

Li, W., Y. Shprits, and R. Thorne (2007), Dynamic evolution of energetic outer zone electrons due to wave-particle interactions during storms, *Journal of Geophysical Research: Space Physics*, *112*(A10).

Li, W., Q. Ma, R. Thorne, J. Bortnik, C. Kletzing, W. Kurth, G. Hospodarsky, and Y. Nishimura (2015), Statistical properties of plasmaspheric hiss derived from van allen probes data and their effects on radiation belt electron dynamics, *Journal of Geophysical Research: Space Physics*, *120*(5), 3393–3405.

Li, W., et al. (2013), An unusual enhancement of low-frequency plasmaspheric hiss in the outer plasmasphere associated with substorm-injected electrons, *Geophysical Research Letters*, *40*(15), 3798–3803.

Liemohn, M., G. Khazanov, T. Moore, and S. Guiter (1997), Self-consistent superthermal electron effects on plasmaspheric refilling, *Journal of Geophysical Research: Space Physics (1978–2012)*, *102*(A4), 7523–7536.

Liemohn, M., G. Khazanov, P. Craven, and J. Kozyra (1999), Nonlinear kinetic modeling of early stage plasmaspheric refilling, *Journal of Geophysical Research: Space Physics (1978–2012)*, *104*(A5), 10,295–10,306.

Liemohn, M. W., A. J. Ridley, J. U. Kozyra, D. L. Gallagher, M. F. Thomsen, M. G. Henderson, M. H. Denton, P. C. Brandt, and J. Goldstein (2006), Analyzing electric field morphology through data-model comparisons of the geospace environment modeling inner magnetosphere/storm assessment challenge events, *Journal of Geophysical Research: Space Physics*, *111*(A11).

Liu, Y., B. Fraser, and F. Menk (2013), Emic waves observed by cluster near the plasmapause, *Journal of Geophysical Research: Space Physics*, *118*(9), 5603–5615.

Lockwood, M., J. Waite, T. Moore, J. Johnson, and C. Chappell (1985), A new source of suprathermal o+ ions near the dayside polar cap boundary, *Journal of Geophysical Research: Space Physics (1978–2012)*, *90*(A5), 4099–4116.

Lundin, R., L. Lyons, and N. Pissarenko (1980), Observations of the ring current composition at l¡ 4, *Geophysical Research Letters*, *7*(6), 425–428.

Ma, Q., W. Li, R. M. Thorne, and V. Angelopoulos (2013), Global distribution of equatorial magnetosonic waves observed by themis, *Geophysical Research Letters*, *40*(10), 1895–1901.

Mauk, B., C. McIlwain, and m. L. McPherron (1981), Helium cyclotron resonance within the earth's magnetosphere, *Geophysical Research Letters*, *8*(1), 103–106.

Mauk, B., N. Fox, S. Kanekal, R. Kessel, D. Sibeck, and A. Ukhorskiy (2014), Science objectives and rationale for the radiation belt storm probes mission, in *The Van Allen Probes Mission*, pp. 3–27, Springer.

Mayaud, P.-N. (1980), *Derivation, meaning, and use of geomagnetic indices*, vol. 22, American Geophysical Union.

Mazur, J. E., and T. P. O'Brien (2012), Comment on analysis of geo spacecraft anomalies: Space weather relationships by ho-sung choi et al., *Space Weather*, *10*(3).

McIlwain, C. E. (1961), Coordinates for mapping the distribution of magnetically trapped particles, *Journal of Geophysical Research*, *66*(11), 3681–3691.

Meredith, N. P., R. B. Horne, and R. R. Anderson (2008), Survey of magnetosonic waves and proton ring distributions in the earth's inner magnetosphere, *Journal of Geophysical Research: Space Physics (1978–2012)*, *113*(A6).

Meredith, N. P., R. B. Horne, S. A. Glauert, D. N. Baker, S. G. Kanekal, and J. M. Albert (2009), Relativistic electron loss timescales in the slot region, *Journal of Geophysical Research: Space Physics*, *114*(A3).

Mizera, P., and G. Boyd (1982), A summary of spacecraft charging results.

Moen, J., N. Gulbrandsen, D. Lorentzen, and H. Carlson (2007), On the mlt distribution of f region polar cap patches at night, *Geophysical Research Letters*, *34*(14).

Moldwin, M. B., L. Downward, H. Rassoul, R. Amin, and R. Anderson (2002), A new model of the location of the plasmapause: Crres results, *Journal of Geophysical Research: Space Physics (1978–2012)*, *107*(A11), SMP–2.

Moullard, O., A. Masson, H. Laakso, M. Parrot, P. Décréau, O. Santolik, and M. Andre (2002), Density modulated whistler mode emissions observed near the plasmapause, *Geophysical research letters*, *29*(20).

Mullen, E. G., M. S. Gussenhoven, D. A. Hardy, T. A. Aggson, B. G. Ledley, and E. Whipple (1986), Scatha survey of high-level spacecraft charging in sunlight, *Journal of Geophysical Research: Space Physics*, *91*(A2), 1474–1490, doi: 10.1029/JA091iA02p01474.

Němec, F., O. Santolık, K. Gereová, E. Macúšová, H. Laakso, Y. De Conchy, M. Maksimovic, and N. Cornilleau-Wehrlin (2006), Equatorial noise: Statistical study of its localization and the derived number density, *Advances in Space Research*, *37*(3), 610–616.

Němec, F., O. Santolík, Z. Hrbáčková, and N. Cornilleau-Wehrlin (2015), Intensities and spatiotemporal variability of equatorial noise emissions observed by the cluster spacecraft, *Journal of Geophysical Research: Space Physics*, *120*(3), 1620–1632.

Newell, P. T., W. J. Burke, C.-I. Meng, E. R. Sanchez, and M. E. Greenspan (1991), Identification and observations of the plasma mantle at low altitude, *Journal of Geophysical Research: Space Physics (1978–2012)*, *96*(A1), 35–45.

Ni, B., R. M. Thorne, Y. Y. Shprits, and J. Bortnik (2008), Resonant scattering of plasma sheet electrons by whistler-mode chorus: Contribution to diffuse auroral precipitation, *Geophysical Research Letters*, *35*(11).

Ni, B., R. Thorne, and Q. Ma (2012), Bounce-averaged fokker-planck diffusion equation in non-dipolar magnetic fields with applications to the dungey magnetosphere, in *Annales Geophysicae*, vol. 30, pp. 733–750, Copernicus GmbH.

Nishida, A. (1966), Formation of plasmapause, or magnetospheric plasma knee, by the combined action of magnetospheric convection and plasma escape from the tail, *Journal of Geophysical Research*, *71*(23), 5669–5679.

Norman, R., M. Parkinson, P. Dyson, et al. (2004), Comparing hf radar backscatter from the southern ocean with ray-tracing results using the iri model, in *Proceedings of the Workshop on the Applications of Radio Science, Hobart, Tasmania*, pp. 18–20.

Olsen, R., S. Shawhan, D. Gallagher, J. Green, C. Chappell, and R. Anderson (1987), Plasma observations at the earth's magnetic equator, *Journal of Geophysical Research: Space Physics (1978–2012)*, *92*(A3), 2385–2407.

Olsen, R. C. (1981), Modification of spacecraft potentials by thermal electron emission on ats-5, *Journal of spacecraft and rockets*, *18*(6), 527–532.

Olsen, R. C. (1983), A threshold effect for spacecraft charging, *Journal of Geophysical Research: Space Physics (1978–2012)*, *88*(A1), 493–499.

Olson, W., and K. Pfitzer (1977), Magnetospheric magnetic field modeling. annual scientific report, *Tech. rep.*, McDonnell Douglas Astronautics Co., Huntington Beach, CA (USA).

Østgaard, N., S. Mende, H. Frey, G. Gladstone, and H. Lauche (2003), Neutral hydrogen density profiles derived from geocoronal imaging, *Journal of Geophysical Research: Space Physics (1978–2012)*, *108*(A7).

Oya, H., Y. Katoh, and K. Kobayashi (2014), Results of the plasma wave sounder experiments on board the akebono satellite in the topside ionosphere and plasmasphere, in *General Assembly and Scientific Symposium (URSI GASS), 2014 XXXIth URSI*, pp. 1–4, IEEE.

Ozhogin, P., J. Tu, P. Song, and B. Reinisch (2012), Field-aligned distribution of the plasmaspheric electron density: An empirical model derived from the image rpi measurements, *Journal of Geophysical Research: Space Physics (1978–2012)*, *117*(A6).

Park, C. (1970), Whistler observations of the interchange of ionization between the ionosphere and the protonosphere, *Journal of Geophysical Research*, *75*(22), 4249–4260.

Pavlov, A., and N. Pavlova (2005), Mechanism of the post-midnight winter night-time enhancements in nmf2 over millstone hill during 14–17 january 1986, *Journal of atmospheric and solar-terrestrial physics*, *67*(4), 381–395.

Perraut, S. (1982), Wave-particle interactions in the ulf range: Geos-1 and-2 results, *Planetary and Space Science*, *30*(12), 1219–1227.

Perraut, S., A. Roux, P. Robert, R. Gendrin, J.-A. Sauvaud, J.-M. Bosqued, G. Kremser, and A. Korth (1982), A systematic study of ulf waves above fh+ from geos 1 and 2 measurements and their relationships with proton ring distributions, *Journal of Geophysical Research: Space Physics (1978–2012)*, *87*(A8), 6219–6236.

Phaneuf, R., R. Janev, and M. Pindzola (1987), Collisions of carbon and oxygen ions with electrons, h, h 2 and he: Volume 5, *Tech. rep.*, Oak Ridge National Lab., TN (USA).

Pierrard, V., J. Goldstein, N. André, V. K. Jordanova, G. A. Kotova, J. F. Lemaire, M. W. Liemohn, and H. Matsui (2009), Recent progress in physics-based models of the plasmasphere, *Space science reviews*, *145*(1-2), 193–229.

Ponomarenko, P., C. Waters, and F. Menk (2008), Effects of mixed scatter on super-darn convection maps, in *Annales Geophysicae*, vol. 26, pp. 1517–1523, Copernicus GmbH.

Pryse, S., K. Dewis, R. Balthazor, H. Middleton, and M. Denton (2005), The dayside high-latitude trough under quiet geomagnetic conditions: Radio tomography and the ctip model, in *Annales Geophysicae*, vol. 23, pp. 1199–1206.

Quinn, J., and R. Johnson (1982), Composition measurements of warm equatorially trapped ions near geosynchronous orbit, *Geophysical Research Letters*, *9*(7), 777–780.

Reagan, J., R. Nightingale, E. Gaines, R. Meyerott, and W. Imhof (1981), Role of energetic particles in charging/discharging of spacecraft dielectrics, *NASA. Lewis Research Center Spacecraft Charging Technol, 1980 p 74-85(SEE N 82-14213 05-18)*.

Reasoner, D., C. Chappell, and W. Lennartsson (1976), Relationship between ats-6 spacecraft-charging occurrences and warm plasma encounters, *Spacecraft charging by magnetospheric plasmas*, pp. 89–101.

Reeves, G., et al. (2013), Electron acceleration in the heart of the van allen radiation belts, *Science*, *341*(6149), 991–994.

Reinisch, B., et al. (2001), First results from the radio plasma imager on image, *Geophysical research letters*, *28*(6), 1167–1170.

Reinisch, B. W., et al. (2000), The radio plasma imager investigation on the image spacecraft, in *The IMAGE Mission*, pp. 319–359, Springer.

Reme, H., et al. (2001), First multispacecraft ion measurements in and near the earth's magnetosphere with the identical cluster ion spectrometry (cis) experiment, in *Annales Geophysicae*, vol. 19, pp. 1303–1354.

Richards, P., and D. Torr (1985), Seasonal, diurnal, and solar cyclical variations of the limiting h+ flux in the earth's topside ionosphere, *Journal of Geophysical Research: Space Physics*, *90*(A6), 5261–5268.

Rietveld, M., H. Kohl, H. Kopka, and P. Stubbe (1993), Introduction to ionospheric heating at tromsøi. experimental overview, *Journal of atmospheric and terrestrial physics*, *55*(4), 577–599.

Rietveld, M., M. J. Kosch, N. Blagoveshchenskaya, V. Kornienko, T. Leyser, and T. Yeoman (2003), Ionospheric electron heating, optical emissions, and striations induced by powerful hf radio waves at high latitudes: Aspect angle dependence, *Journal of Geophysical Research: Space Physics*, *108*(A4).

Rishbeth, H., and A. Van Eyken (1993), Eiscat: early history and the first ten years of operation, *Journal of atmospheric and terrestrial physics*, *55*(4), 525–542.

Roberts, C. S., and M. Schulz (1968), Bounce resonant scattering of particles trapped in the earth's magnetic field, *Journal of Geophysical Research*, *73*(23), 7361–7376.

Robinson, R., R. Vondrak, K. Miller, T. Dabbs, and D. Hardy (1987), On calculating ionospheric conductances from the flux and energy of precipitating electrons, *Journal of Geophysical Research: Space Physics*, *92*(A3), 2565–2569.

Roble, R. (1975), The calculated and observed diurnal variation of the ionosphere over millstone hill on 23–24 march 1970, *Planetary and Space Science*, *23*(7), 1017–1033.

Rosen, A. (1976), Spacecraft charging by magnetospheric plasmas, *Nuclear Science, IEEE Transactions on*, *23*(6), 1762–1768.

Roux, A., S. Perraut, J. Rauch, C. Villedary, G. Kremser, A. Korth, and D. Young (1982), Wave-particle interactions near ωhe+ observed on board geos 1 and 2: 2. generation of ion cyclotron waves and heating of he+ ions, *Journal of Geophysical Research: Space Physics (1978–2012)*, *87*(A10), 8174–8190.

Rubin, A., H. B. Garrett, and A. Wendel (1980), Spacecraft charging on ats-5., *Tech. rep.*, No. AFGL-TR-80-0168. AIR FORCE GEOPHYSICS LAB HANSCOM AFB MA.

Russell, C. T., R. E. Holzer, and E. J. Smith (1970), Ogo 3 observations of elf noise in the magnetosphere: 2. the nature of the equatorial noise, *Journal of Geophysical Research*, *75*(4), 755–768.

Sagawa, E., A. Yau, B. Whalen, and W. Peterson (1987), Pitch angle distributions of low-energy ions in the near-earth magnetosphere, *Journal of Geophysical Research*, *92*(A11), 12–241.

Saikin, A., J.-C. Zhang, R. Allen, C. Smith, L. Kistler, H. Spence, R. Torbert, C. Kletzing, and V. K. Jordanova (2015), The occurrence and wave properties of h+-, he+-, and o+-band emic waves observed by the van allen probes, *Journal of Geophysical Research: Space Physics*.

Sandel, B. R., R. A. King, W. Forrester, D. L. Gallagher, A. L. Broadfoot, and C. Curtis (2001), Initial results from the image extreme ultraviolet imager, *Geophysical research letters*, *28*(8), 1439–1442.

Sandel, B. R., et al. (2000), The extreme ultraviolet imager investigation for the image mission, in *The Image Mission*, pp. 197–242, Springer.

Santolik, O., M. Parrot, L. Storey, J. Pickett, and D. Gurnett (2001), Propagation analysis of plasmaspheric hiss using polar pwi measurements, *Geophysical research letters*, *28*(6), 1127–1130.

Santolík, O., J. Pickett, D. Gurnett, M. Maksimovic, and N. Cornilleau-Wehrlin (2002), Spatiotemporal variability and propagation of equatorial noise observed by cluster, *Journal of Geophysical Research: Space Physics*, *107*(A12).

Santolik, O., M. Parrot, and F. Lefeuvre (2003), Singular value decomposition methods for wave propagation analysis, *Radio Science*, *38*(1).

Santolík, O., F. Nemec, K. Gereová, E. Macúšová, Y. De Conchy, and N. Cornilleau-Wehrlin (2004), Systematic analysis of equatorial noise below the lower hybrid frequency, in *Annales Geophysicae*, vol. 22, pp. 2587–2595.

Sarno-Smith, L., et al. (2016), Equatorial noise mlt dependence and impact on the 1-10 ev ion population of the inner quiet plasmasphere, *Journal of Geophysical Research, Manuscript in Preparation*.

Sarno-Smith, L. K., M. W. Liemohn, R. M. Katus, R. M. Skoug, B. A. Larsen, M. F. Thomsen, J. R. Wygant, and M. B. Moldwin (2015), Postmidnight depletion of the high-energy tail of the quiet plasmasphere, *Journal of Geophysical Research: Space Physics*, *120*(3), 1646–1660.

Schmitt, J. (1976), Nonlinear theory of rf heating at cyclotron harmonics, *Physics of Fluids (1958-1988)*, *19*(2), 245–255.

Schunk, R., and A. F. Nagy (1978), Electron temperatures in the f region of the ionosphere: Theory and observations, *Reviews of Geophysics*, *16*(3), 355–399.

Senior, A., M. T. Rietveld, N. Borisov, M. Kosch, T. Yeoman, and F. Honary (2004), Multi-frequency hf radar measurements of artificial f-region field-aligned irregularities.

Sheeley, B., M. Moldwin, H. Rassoul, and R. Anderson (2001), An empirical plasmasphere and trough density model: Crres observations, *Journal of Geophysical Research: Space Physics (1978–2012)*, *106*(A11), 25,631–25,641.

Sheskin, D. J. (2003), *Handbook of parametric and nonparametric statistical procedures*, crc Press.

Sicard-Piet, A., D. Boscher, R. Horne, N. Meredith, and V. Maget (2014), Effect of plasma density on diffusion rates due to wave particle interactions with chorus and plasmaspheric hiss: Extreme event analysis, in *Annales Geophysicae*, vol. 32, pp. 1059–1071, Copernicus Publications on behalf of the European Geosciences Union.

Singh, N., and K. Hwang (1987), Perpendicular ion heating effects on the refilling of the outer plasmasphere, *Journal of Geophysical Research: Space Physics (1978–2012)*, *92*(A12), 13,513–13,521.

Singh, U., and R. Singh (1997), Study of plasmasphere-ionosphere coupling fluxes, *Journal of Atmospheric and Solar-Terrestrial Physics*, *59*(11), 1321–1327.

Smith, A., M. Freeman, and G. Reeves (1996), Post midnight vlf chorus events, a substorm signature observed at the ground near l= 4, *Journal of Geophysical Research: Space Physics (1978–2012)*, *101*(A11), 24,641–24,653.

Sojka, J. J., R. W. Schunk, and J. Whalen (1990), The longitude dependence of the dayside f region trough: A detailed model-observation comparison, *Journal of Geophysical Research: Space Physics*, *95*(A9), 15,275–15,280.

Solomon, J., N. Cornilleau-Wehrlin, A. Korth, and G. Kremser (1988), An experimental study of elf/vlf hiss generation in the earth's magnetosphere, *Journal of Geophysical Research: Space Physics*, *93*(A3), 1839–1847.

Spasojević, M., J. Goldstein, D. Carpenter, U. Inan, B. Sandel, M. Moldwin, and B. Reinisch (2003), Global response of the plasmasphere to a geomagnetic disturbance, *Journal of Geophysical Research: Space Physics*, *108*(A9).

Spasojević, M., H. Frey, M. Thomsen, S. Fuselier, S. Gary, B. Sandel, and U. Inan (2004), The link between a detached subauroral proton arc and a plasmaspheric plume, *Geophysical research letters*, *31*(4).

Summers, D. (2005), Quasi-linear diffusion coefficients for field-aligned electromagnetic waves with applications to the magnetosphere, *Journal of Geophysical Research: Space Physics (1978–2012)*, *110*(A8).

Summers, D., and B. Ni (2008), Effects of latitudinal distributions of particle density and wave power on cyclotron resonant diffusion rates of radiation belt electrons, *Earth, planets and space*, *60*(7), 763–771.

Summers, D., B. Ni, and N. P. Meredith (2007), Timescales for radiation belt electron acceleration and loss due to resonant wave-particle interactions: 2. evaluation for vlf chorus, elf hiss, and electromagnetic ion cyclotron waves, *Journal of Geophysical Research: Space Physics*, *112*(A4).

Taylor, H., H. Brinton, and A. Deshmukh (1970), Observations of irregular structure in thermal ion distributions in the duskside magnetosphere, *Journal of Geophysical Research*, *75*(13), 2481–2489.

Taylor, R. (1990), Interpretation of the correlation coefficient: a basic review, *Journal of diagnostic medical sonography*, *6*(1), 35–39.

Thomas, E., J. Baker, J. Ruohoniemi, L. Clausen, A. Coster, J. Foster, and P. Erickson (2013), Direct observations of the role of convection electric field in the formation of a polar tongue of ionization from storm enhanced density, *Journal of Geophysical Research: Space Physics*, *118*(3), 1180–1189.

Thomsen, M. (2004), Why kp is such a good measure of magnetospheric convection, *Space Weather*, *2*(11).

Thomsen, M. F., M. G. Henderson, and V. K. Jordanova (2013), Statistical properties of the surface-charging environment at geosynchronous orbit, *Space Weather*, *11*(5), 237–244.

Thorne, R., et al. (2013), Rapid local acceleration of relativistic radiation-belt electrons by magnetospheric chorus, *Nature*, *504*(7480), 411–414.

Thorne, R. M., and J. N. Barfield (1976), Further observational evidence regarding the origin of plasmaspheric hiss, *Geophysical Research Letters*, *3*(1), 29–32.

Thorne, R. M., E. J. Smith, R. K. Burton, and R. E. Holzer (1973), Plasmaspheric hiss, *Journal of Geophysical Research*, *78*(10), 1581–1596.

Thorne, R. M., R. B. Horne, V. K. Jordanova, J. Bortnik, and S. Glauert (2006), Interaction of emic waves with thermal plasma and radiation belt particles, *Magnetospheric ULF waves: synthesis and new directions*, pp. 213–223.

Tsurutani, B., J. Arballo, G. Lakhina, C. Ho, B. Buti, J. Pickett, and D. Gurnett (1998), Plasma waves in the dayside polar cap boundary layer: Bipolar and monopolar electric pulses and whistler mode waves, *Geophysical research letters*, *25*(22), 4117–4120.

Tsurutani, B. T., and G. S. Lakhina (1997), Some basic concepts of wave-particle interactions in collisionless plasmas, *Reviews of Geophysics*, *35*(4), 491–501.

Tsurutani, B. T., E. J. Smith, and R. M. Thorne (1975), Electromagnetic hiss and relativistic electron losses in the inner zone, *Journal of Geophysical Research*, *80*(4), 600–607.

Usanova, M., et al. (2014), Effect of emic waves on relativistic and ultrarelativistic electron populations: Ground-based and van allen probes observations, *Geophysical Research Letters*, *41*(5), 1375–1381.

Varney, R., W. Swartz, D. Hysell, and J. Huba (2012), Sami2-pe: A model of the ionosphere including multistream interhemispheric photoelectron transport, *Journal of Geophysical Research: Space Physics (1978–2012)*, *117*(A6).

Vickrey, J. F., W. E. Swartz, and D. T. Farley (1979), Ion transport in the topside ionosphere at arecibo, *Journal of Geophysical Research: Space Physics*, *84*(A12), 7307–7314.

Walker, S., M. Balikhin, D. Shklyar, K. Yearby, P. Canu, C. Carr, and I. Dandouras (2015), Experimental determination of the dispersion relation of magnetosonic waves, *Journal of Geophysical Research: Space Physics*, *120*(11), 9632–9650.

Weber, E., J. Klobuchar, J. Buchau, H. Carlson, R. Livingston, O. Beaujardiere, M. McCready, J. Moore, and G. Bishop (1986), Polar cap f layer patches: Structure and dynamics, *Journal of Geophysical Research: Space Physics*, *91*(A11), 12,121–12,129.

Weiss, L., R. Lambour, R. Elphic, and M. Thomsen (1997), Study of plasmaspheric evolution using geosynchronous observations and global modeling, *Geophysical research letters*, *24*(5), 599–602.

Winningham, J., J. Burch, N. Eaker, V. Blevins, and R. Hoffman (1981), The low altitude plasma instrument/lapi, *Space Science Instrumentation*, *5*, 465–475.

Wright, D., J. Davies, T. K. Yeoman, T. Robinson, and H. Shergill (2006), Saturation and hysteresis effects in ionospheric modification experiments observed by the cutlass and eiscat radars, in *Annales Geophysicae*, vol. 24, pp. 543–553.

Wygant, J., et al. (2013), The electric field and waves instruments on the radiation belt storm probes mission, *Space Science Reviews*, *179*(1-4), 183–220.

Wygant, J., et al. (2014), The electric field and waves instruments on the radiation belt storm probes mission, in *The Van Allen Probes Mission*, pp. 183–220, Springer.

Xu, L., A. Koustov, J. Thayer, and M. McCready (2001), Superdarn convection and sondrestrom plasma drift, in *Annales Geophysicae*, vol. 19, pp. 749–759.

Yeoman, T. K., G. Chisham, L. Baddeley, R. Dhillon, T. Karhunen, T. Robinson, A. Senior, and D. Wright (2008), Mapping ionospheric backscatter measured by the superdarn hf radars–part 2: Assessing superdarn virtual height models.

Young, D., S. Perraut, A. Roux, C. Villedary, R. Gendrin, A. Korth, G. Kremser, and D. Jones (1981), Wave-particle interactions near ωhe+ observed on geos 1 and 2 1. propagation of ion cyclotron waves in he+-rich plasma, *Journal of Geophysical Research: Space Physics (1978–2012)*, *86*(A8), 6755–6772.

Zhang, Q.-H., et al. (2013), Direct observations of the evolution of polar cap ionization patches, *science*, *339*(6127), 1597–1600.